Finite Element Limit Analysis of Offshore Foundations on Clay

Helen Patricia Dunne

Mansfield College

University of Oxford

A thesis submitted for the degree of

Doctor of Philosophy

Trinity 2017

Acknowledgements

First and foremost, I would like to thank my supervisor Chris Martin. When I started my DPhil, Chris was patient with me, and endeavoured to pass on some of his extensive knowledge. In the latter part of my studies he has pushed me to be a better researcher and writer — I have learned so much from him. I also thank Chris for encouraging me to enter the BGA Cooling Prize competition, the resulting experiences have been some of my most memorable.

Subsea 7 provided the funding which made this research possible. For insight and help along the way I would like to especially thank Neil Brown, Régis Wallerand, Christian Olsen, Mersina Cafi, and Lindsay Muir.

My gratitude goes to my examiners, Chris MacMinn and Susan Gourvenec, whose research I have followed closely throughout my DPhil.

In the department, my gratitude goes to Byron for facilitating my undergraduate teaching and to Alison for having all administrative answers, and to Ross for being so encouraging.

For stimulating discussions and laughter in the middle of the day, I must thank the Wallis room lunch regulars.

I would like to thank my office cohabitee during the writing up phase, William, for lending an ear, and our frequent visitor, Stephen, for lifting my spirits with his habitual enthusiasm, even when discussing LaTeX compilation time and appropriate line spacing. Thanks also go to Stephen for instigating interesting and enjoyable collaborative research, and for providing manifold useful suggestions and insights, particularly in my final year.

My close friends were the glue that held me together when times got tough. Aoife and Seán provided me with a safe haven in London; I am grateful for the many nights out (and in) which helped to clear my mind. My special thanks also go to David Hodge for all of his advice down through the years, and to Hazel and Aideen, for being there when needed.

Finally, I tip my hat to the mighty Dunne clan back in Cork, and in particular to my parents, Ciarán and Patricia. I thank them for always encouraging me to question everything, to think outside the box, and to make my own decisions. It has ultimately given me the courage to take on this task.

Abstract

Finite Element Limit Analysis of Offshore Foundations on Clay

A thesis submitted for the degree of Doctor of Philosophy

Helen Patricia Dunne
Mansfield College, Oxford
Trinity 2017

Capacity analysis is a common preliminary step in the design of offshore foundations. Inaccuracies in traditional capacity analysis methods, and the advancement of numerical modelling capabilities, have increasingly led designers to optimise foundations using more complex methods. In this thesis, the ultimate limit state capacity of a range of foundation types is investigated using finite element limit analysis.

Novel three-dimensional finite element limit analysis software is benchmarked against analytical solutions and conventional displacement finite element analysis. It is then used to find lower and upper bounds of foundation capacity, with adaptive mesh refinement used to reduce the bound gap over successive iterations of the solution. Rigid foundations subjected to short term loading on clay soil are analysed. The undrained soil is modelled as a rigid–plastic von Mises material, and attention is given to modelling any normal and/or shear stress limits at the foundation/soil interface.

Shallow foundations, suction anchor foundations, and hybrid mudmat/pile foundations are considered. Realistic six degree-of-freedom load combinations are applied and results are reported in the form of normalised design charts, and tables, that are suitable for use in preliminary design. Relationships between loading combinations and failure mechanisms are also explored. A number of case studies based on authentic foundation designs are analysed. The results suggest that finite element limit analysis could provide an attractive alternative to displacement finite element analysis for preliminary foundation design calculations.

Contents

Notation

Symbols used in this thesis, excluding those which only appear in one location

A	bearing area of a foundation/cross sectional area
A_i	void area of a perforated foundation
A_o	gross area of a perforated foundation
B	foundation breadth in the x direction
B^*	effective width of a perforated foundation
D	diameter
d	mudmat embedment
d_c, d_q, d_γ	depth factors for general bearing capacity equation
e	eccentricity of horizontal load in the xy plane
e_max	maximum feasible eccentricity of horizontal load
E_u	undrained Young's modulus
F_x, F_y	horizontal loads along the x and y axes
F_{x0}, F_{y0}	uniaxial horizontal capacities
F_z	vetical load
F_{z0}	uniaxial vertical capacity
H	length of a pile when used as part of a hybrid foundation
h	height of a load application
$k_\mathrm{n}, k_\mathrm{s}$	soil stiffness under normal and shear loading respectively
L	foundation length in the y direction, or length of a pile/caisson
L_F	length from the mudline to the load application point for a suction caisson
L_opt	optimal load point for a suction caisson
M_x, M_y	overturning moments about x and y axes
M_{x0}, M_{y0}	uniaxial overturning moment capacities
M_z	torsional moment
M_{z0}	uniaxial torsional moment capacity

N	number of sides in a polygonal pile/caisson section
N_c, N_q, N_γ	bearing capacity factors for general bearing capacity equation
O	load reference point
p_1, p_2, p_3	lever arms from pile centres to hybrid foundation rotation point
q_u	vertical bearing capacity
R	perforation ratio
r_c	peroration factor
s_c, s_q, s_γ	shape factors for general bearing capacity equation
s_u	undrained shear strength
$s_{\mathrm{u,av}}$	average undrained shear strength
s_um	undrained shear strength at the mudline
T	tensile capacity at foundation/soil interface
t	thickness of mudmat skirts or caisson wall, or UINTER subroutine tension capacity input
α	roughness factor at foundation/soil interface
β	inclination of load in the z direction from horizontal
γ'	submerged unit weight of the soil
θ	angle of horizontal load angle from the x-axis
ν_u	undrained Poisson's ratio
ξ	ground inclination
ρ	rate of soil strength change per unit depth of soil
$\sigma_1, \sigma_2, \sigma_3$	soil principal stresses
τ	shear stress
τ_x, τ_y	shear stress components in the x and y directions

Abbreviations used in this thesis

2D	two-dimensional
3D	three-dimensional
ALS	accidental limit state
CPT	cone penetration test
DLO	discontinuity layout optimisation
FE	finite element
FEA	finite element analysis
FELA	finite element limit analysis
FPSO	floating production storage and offloading

LB	lower bound
LE	limit equilibrium
LF	load factor
LP	linear programming
MoC	method of characteristics
NC	normally consolidated
NLP	non-linear programming
PLA	plastic limit analysis
PLEM	pipe line end manifold
PLET	pipe line end termination
RFEA	rigid finite element analysis
SOCP	second-order cone programming
SP	singularity planes (present in mesh)
U	unstructured (mesh)
UB	upper bound
ULS	ultimate limit state

Chapter 1

Introduction

In this thesis, recently developed three-dimensional (3D) finite element limit analysis (FELA) software is benchmarked against analytical solutions and conventional displacement finite element analysis, before it is used as the primary analysis tool for assessing the ultimate bearing capacity of various types of offshore foundation. A range of foundation design problems are investigated, with a focus on undrained soil response and the application of combined loading (vertical, horizontal, moment, torsional) to the foundation. Some noteworthy advantages of FELA in comparison to other analysis methods, such as having a directly quantifiable error measure, are highlighted. Insight is provided into the capacities of offshore foundations under complex loading, with attention also drawn to foundation failure mechanisms.

1.1 Offshore foundations and loading conditions

A wide range of foundations is used in the offshore oil and gas industry and in the offshore wind industry. This thesis considers three foundation types: shallow foundations, caisson foundations (used as suction anchors), and hybrid foundations comprising shallow foundations with short piles at the foundation corners. Offshore foundations are commonly founded in clay. The loading applied to these foundations is often sufficiently rapid that the ultimate undrained capacity is a critical aspect of design.

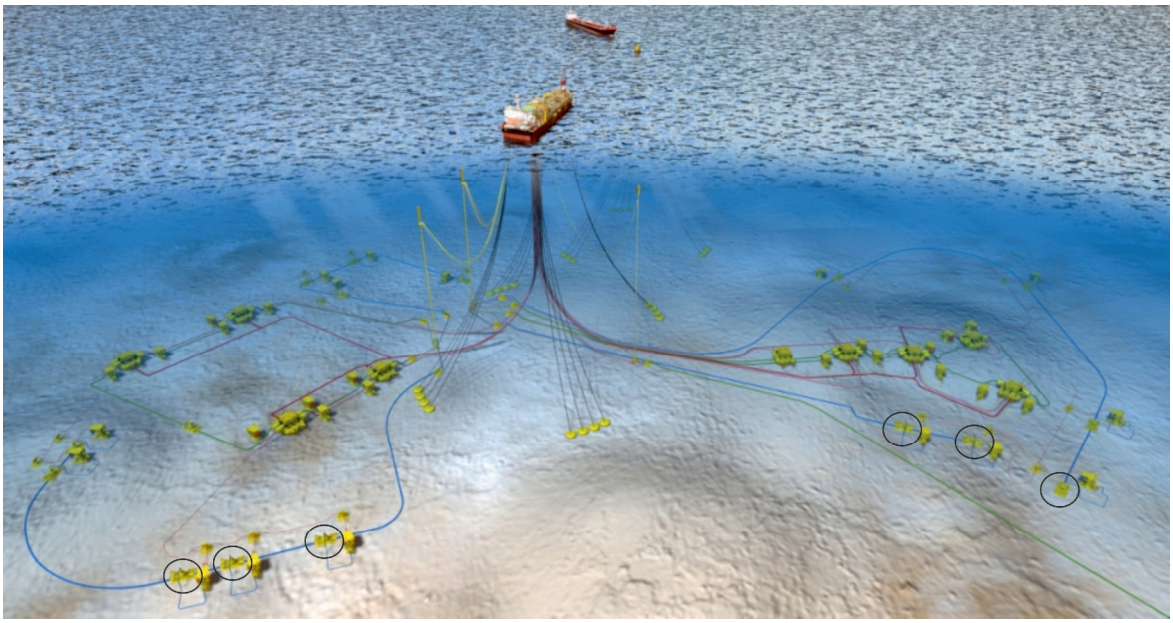

Figure 1.1: Typical offshore arrangement of subsea equipment for an FPSO installation

1.1.1 Shallow foundations

Shallow rectangular foundations, termed mudmats, are frequently used to support subsea infrastructure such as pipeline end terminations and pipeline end manifolds (PLETs and PLEMs). A typical subsea arrangement of flowlines and risers from a floating production storage and offloading (FPSO) installation is shown in Figure 1.1; some items of subsea equipment supported on mudmat foundations are circled in black.

Mudmats used offshore are generally equipped with underbase skirts which penetrate into the soil, confining a soil plug. A mudmat attached to infrastructure being hoisted into position before installation is shown in Figure 1.2(a) and the underbase skirts can be viewed in Figure 1.2(b). Figure 1.2(b) also highlights the size of these foundations; notice workers towards the top of the figure. Typical mudmat dimensions are $5-10$ m in breadth by $10-20$ m in length. The embedment to breadth ratio is typically in the range of $0.025-0.2$, depending on the soil and loading conditions (Feng et al., 2014).

Short pipes, termed jumpers, connect PLETs and PLEMs to pipelines. Jumpers can be situated at a height above the mudmat and are often not aligned along its plan view axes. Jumpers experience horizontal expansion and contraction forces from pipelines as they

(a) (b)

Figure 1.2: Rectangular mudmat foundation: (a) PLEM with mudmat foundation being hoisted before installation; (b) a view of the underbase skirts

undergo temperature changes during operation. Depending on the jumper arrangement, this can induce biaxial horizontal loads in conjunction with biaxial overturning moments and torsional loading on the mudmat. Vertical loading is predominantly due to the self-weight of the supported infrastructure and is typically small compared with the ultimate vertical bearing capacity of the foundation (Feng et al., 2014, 2017). However, sometimes it is necessary to install mudmats on a sloping seabed, and in this case vertical loads, combined with other loads, need consideration (Dunne et al., 2015).

As offshore oil and gas developments move to deeper reservoirs, pipelines are subjected to increasing levels of temperature and pressure change, leading to larger loads for mudmats to resist. In practice, mudmat dimensions are restricted by the size of their installation vessels, thus increasing the importance of accurate bearing capacity analysis.

Larger gravity base foundations used offshore are sometimes designed with a central perforation. Advantages of using a perforated foundation include increased moment capacity per unit bearing area, reduced cost of materials, and easier offshore handling (due to reduced weight). Large perforated foundations can be used to support wind turbines, or oil and gas

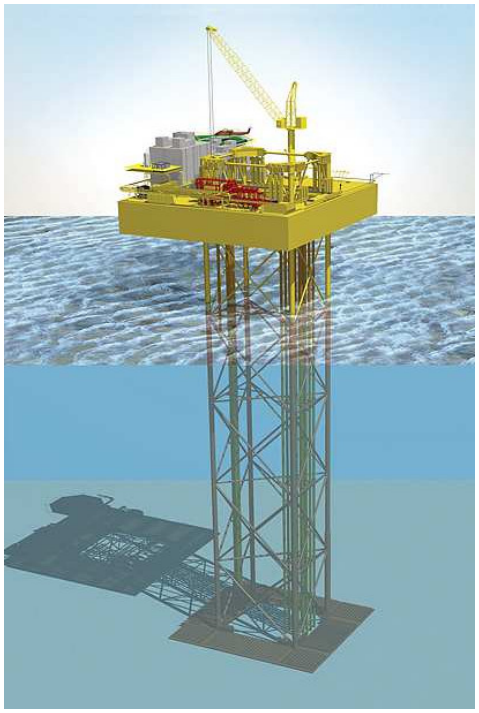

(a)

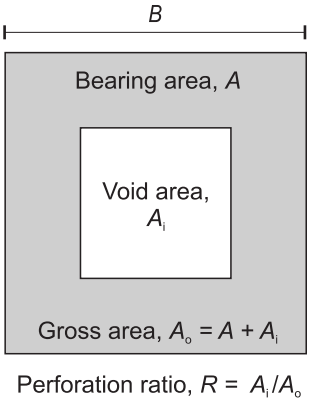

(b)

Figure 1.3: Perforated foundations: (a) the Maari wellhead platform, supported on a gravity base foundation with a central perforation (Arup, 2009); (b) plan view of foundation showing definition of perforation ratio, R

platforms, such as the Maari wellhead platform shown in Figure 1.3(a). Foundations for this type of structure may be in excess of 50 m wide. Like mudmats, these foundations often have steel skirts designed to confine a soil plug, and embedment to breadth ratios typically range from 0.2 – 0.5. A ratio of perforation area, A_i, to gross foundation area, A_o, is often used to help categorise perforated foundations (see Figure 1.3(b)). The perforation ratio, R, is defined as

$$R = A_i/A_o \, . \tag{1.1}$$

1.1.2 Suction caisson foundations

Suction caissons are widely used offshore to anchor floating structures such as spars and FPSOs (Figure 1.4(a)). Also known as suction anchors, or suction piles, they have a thin, typically steel, embedded cylindrical wall and a circular top cap. Self-weight causes a caisson to partially embed when it is lowered into position. Water is then pumped out from inside the caisson through valves in the top cap. This lowers the pressure inside the caisson,

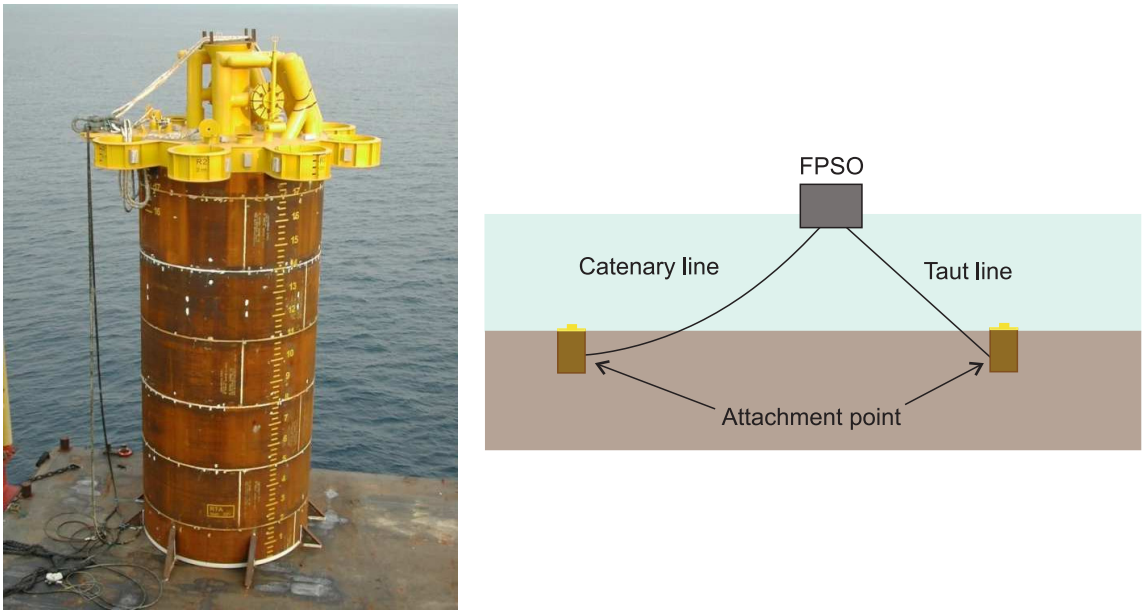

(a) (b)

Figure 1.4: Suction caisson: (a) before installation; (b) loading inclination when used as part of catenary or taut mooring systems

causing a net downwards force and resulting in further embedment. Pumping stops when the desired penetration has been reached, and at this point the valves in the caisson lid are sealed. Caissons are typically 4.5 – 6 m in diameter and their length to diameter ratios can range from one to ten, but are generally less than six (Andersen et al., 2005).

When used as anchors, suction caissons are subject to large mooring loads that are transferred to the caisson at the mooring attachment point (or 'padeye'). The position of the mooring attachment point along the caisson's length can be optimised for maximum holding capacity. The vertical and horizontal components of the mooring load can vary and are particularly dependent on the type of mooring system; loading from catenary mooring systems is predominantly horizontal, while loading from taut and semi-taut mooring systems may have a substantial vertical component (Figure 1.4(b)).

1.1.3 Hybrid mudmat–pile foundations

There are some situations in which a mudmat alone may not provide adequate capacity; in very poor soils, in brownfield sites where space is limited, or where available installation vessels limit foundation size. Recent studies have highlighted that combined horizontal and

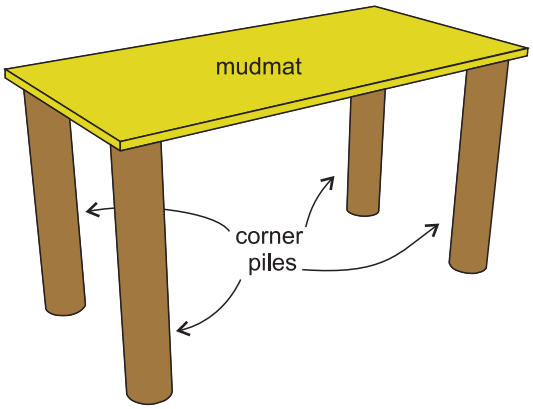

Figure 1.5: Hybrid mudmat–pile foundation

torsional loading of mudmat foundations often represents the governing load case in mudmat design (Martin et al., 2015; Feng et al., 2017; Dunne and Martin, 2017b). Mudmat capacity, particularly under horizontal and torsional loading, can be significantly increased by installing piles at the mudmat corners (sometimes referred to as 'pin piles'), thus resulting in a hybrid mudmat–pile foundation (Figure 1.5).

While piled raft foundations are commonly used onshore, the use of hybrid mudmat–pile foundations offshore is relatively new. Hybrid foundations with pinned mudmat/pile connections can significantly increase horizontal and torsional capacity when compared with mudmats alone (Dimmock et al., 2013). Recent studies have shown that the degree of rotational and translational restraint at the mudmat/pile connection (pile head) can strongly influence the lateral capacity of hybrid foundations (Won et al., 2015; Hossain et al., 2015b).

1.2 Capacity analysis

Capacity analysis is undertaken in order to find the maximum load or combinations of loads that can be applied to a foundation before the soil is expected to fail in shear. For the analysis of offshore foundations, consideration must be given to the rate of load application when compared with the rate of water movement in the soil, as this will determine whether the response of the soil is likely to be drained or undrained. Clays and silts, commonly found in deep waters and considered in this study, typically have low permeability. When foundation loading is sufficiently rapid, it can be assumed that the soil remains undrained for foundation

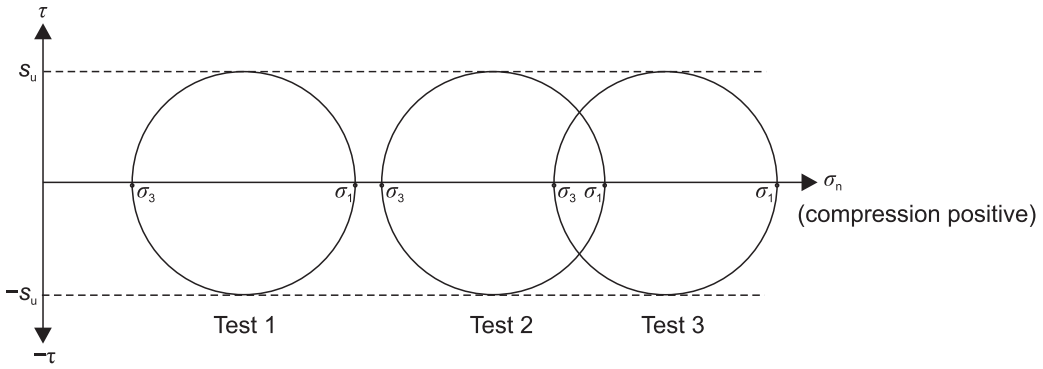

Figure 1.6: Results of unconsolidated, undrained triaxial tests showing Mohr's circles of stress and undrained shear strength, s_u

capacity analysis, such that a total stress analysis is appropriate and the undrained shear strength, s_u, is the governing soil strength parameter.

Interface shear strength and tension capacity need consideration at foundation/soil boundaries. In undrained capacity analysis the available shear strength at an interface is commonly modelled as a roughness factor, α, times s_u. A fully rough foundation can utilise the full shear strength of the adjacent soil ($\alpha = 1$) while a fully smooth foundation has no shear resistance at the interface ($\alpha = 0$). In practice, α can lie anywhere between these bounds. The development of negative excess pore water pressures between a foundation and the soil can prevent contact breaking, allowing for unlimited tension capacity at the interface ($T = \infty$). It is more conservative to assume that a water-filled gap may form between the foundation and the soil; this can be achieved by imposing a tension cutoff ($T = 0$) on the interface.

Undrained triaxial tests can be undertaken on clay samples to determine undrained shear strength. In this test, a confining pressure σ_3 is applied to a cylindrical sample of soil with cross sectional area A. Axial loading P is then applied to the sample until 'failure' occurs. The undrained shear strength is then

$$s_u = \frac{\sigma_1 - \sigma_3}{2} \tag{1.2}$$

where $\sigma_1 = \sigma_3 + P/A$. For an unconsolidated undrained test, the undrained shear strength is not dependent on the confining pressure (as the void ratio remains unchanged) and typically a series of tests at a range of confining pressures are undertaken to estimate s_u (Figure 1.6). In

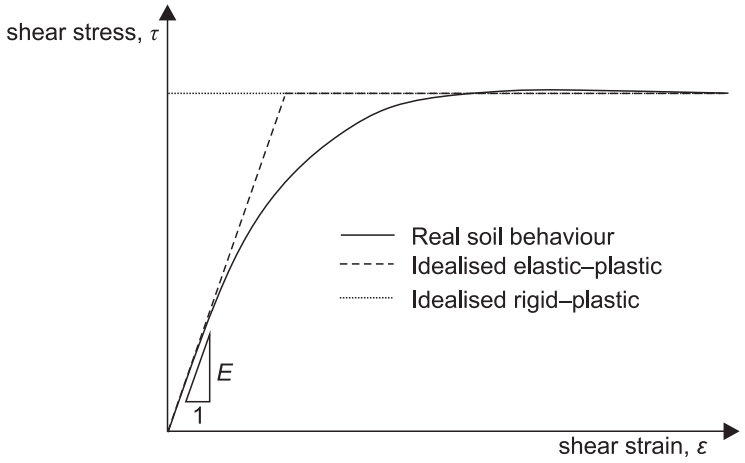

Figure 1.7: Realistic and idealised stress–strain curves for undrained clay

situ tests can also be used to find s_u, such as the shear vane test or, more commonly offshore, the cone penetration test (CPT).

For capacity analysis, the stress–strain behaviour of the soil is commonly simplified as elastic–plastic or rigid–plastic (Figure 1.7). Rigid–plastic behaviour assumes that elastic strain at failure is insignificant when compared to the total plastic strain and has negligible effect on bearing capacity. This common assumption is necessary for plastic limit analysis (PLA), but can be difficult to implement using conventional displacement finite element analysis (FEA). When using FEA to find foundation capacity, it is common to assume that the stress–strain response is elastic–plastic. The elastic response of the soil is governed by its undrained Young's modulus, E_u, and undrained Poisson's ratio, $\nu_u \approx 0.5$. However, it is common when using FEA to assign a value of E_u in excess of $500 s_u$ (Taiebat and Carter, 2000; Gourvenec et al., 2006; Yun and Bransby, 2007; Feng et al., 2014; Vulpe, 2015). In this case, the soil is so stiff that the elastic–plastic soil model is essentially equivalent to rigid–plastic. For both stress–strain simplifications, the soil is assumed to behave perfectly plastic; once plastic yielding (failure) has occurred there is no change in stress with increasing strain.

1.2.1 Yield functions

The two most common failure criteria used to model perfect plasticity of metals and undrained soils are the Tresca criterion (a special case of the Mohr–Coulomb criterion) and the von Mises

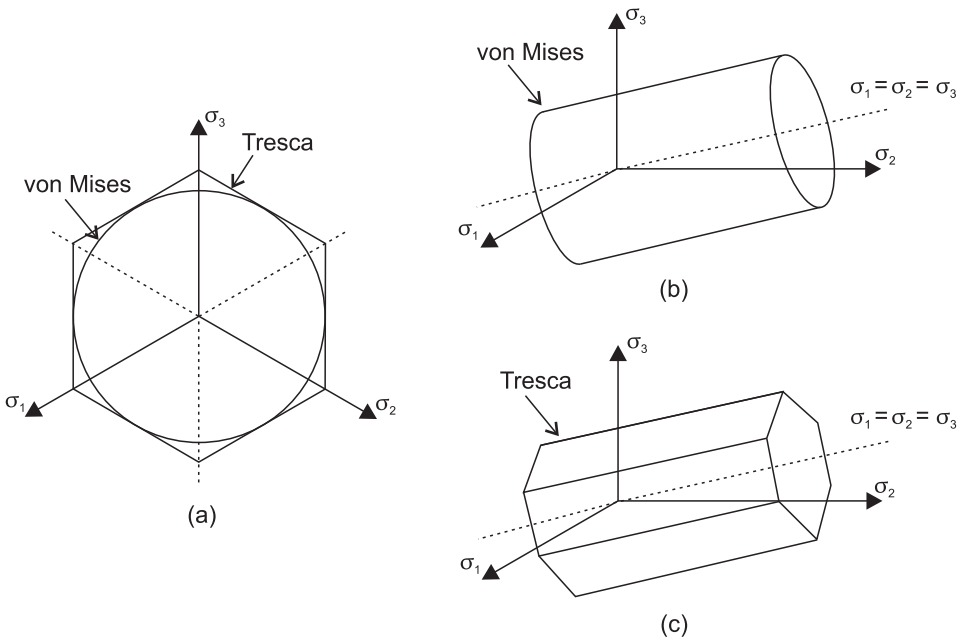

Figure 1.8: Tresca and von Mises failure criteria (when matched for deformation in plane strain): (a) yield surfaces in the deviatoric plane, (b) von Mises criterion in 3D principal stress space; (c) Tresca criterion in 3D principal stress space

criterion. For the Tresca criterion, yield occurs when the maximum shear stress reaches s_u such that the yield function is

$$f = \sigma_1 - \sigma_3 - 2s_u = 0 \tag{1.3}$$

where $\sigma_1 = \sigma_2 = \sigma_3$ along the space diagonal, as shown in Figure 1.8. The von Mises yield function can be expressed as

$$f = (\sigma_1 - \sigma_2)^2 + (\sigma_2 - \sigma_3)^2 + (\sigma_3 - \sigma_1)^2 - 2(\sqrt{3}s_u)^2 = 0 \tag{1.4}$$

when the von Mises criterion and the Tresca criterion are matched for deformation in plane strain (and for shearing of an interface layer). For the analysis of 3D shallow foundation problems this has been found to provide better agreement between the predicted bearing capacities, when compared with matching the strengths of the two criteria under triaxial conditions (Gourvenec et al., 2006).

As a result of assumed associated flow, the plastic potential function matches the yield function. This makes for easy implementation of the von Mises criterion in FEA as there are no singularities in the plastic potential function. When used in lower bound (LB) and upper bound (UB) FELA, analyses with von Mises materials can be cast as standard second-order

cone programming (SOCP) problems. However the Tresca failure criterion is more difficult to implement in FEA due to the singularities in the plastic potential function at the corners of the yield surface (Figure 1.8). When using FELA, 3D analysis of Tresca materials requires semi definite programming, which is a more challenging class of numerical optimisation than SOCP. For these reasons the von Mises criterion is used throughout this thesis, while noting that for plane strain analysis the Tresca and von Mises criteria are equivalent.

1.2.2 Failure envelopes

A failure envelope is defined in load space and describes the ultimate capacity of a foundation under the simultaneous action of two or more load components. This approach is advantageous as it allows for the exploration of foundation capacity under different loading combinations (see Gottardi and Butterfield (1993)). Loading combinations which are located within the envelope are viable and outside are unviable. Numerous failure envelopes have previously been determined by fitting expressions to experimental (Tan, 1990; Martin, 1994; Gottardi et al., 1999) or numerical results (Taiebat and Carter, 2005; Gourvenec, 2008; Feng et al., 2014, and others).

1.3 Motivation

Classical bearing capacity theory for the analysis of shallow foundations, stemming from the methods of Brinch Hansen (1970) and Vesic (1975), has been adopted into design codes such as DNV (1992) and ISO (2003). In this approach, vertical bearing capacity is presumed to be the primary design consideration and semi-empirical reduction factors are used to account for load inclination and eccentricity. It is well known that this can be inaccurate and is often excessively conservative, particularly for clay soils where the undrained shear strength increases with depth or where under-base skirts prevent foundation detachment under short-term moment loading (see Martin, 1994; Ukritchon et al., 1998; Bransby and Randolph, 1998; Gourvenec and Randolph, 2003).

Current oil and gas developments in deep water often comprise a large number of identical mudmat foundations and the current design approach is to optimise the critically

loaded mudmat. Classical bearing capacity theory is used to determine conservative failure envelopes for the critical foundation any load cases which fall outside the envelope are analysed using 3D displacement FEA. As offshore oil and gas developments continue to move into deeper water, pipelines are subjected to increasing levels of temperature and pressure change. This leads to larger mudmats being specified, with mudmat size controlling the vessel requirement for installation, and larger vessels inducing larger costs. Optimisation of the critical foundation can lead to savings that are scaled up considerably.

There exists no consensus on an accepted method for calculating the holding capacity of a suction caisson (Andersen et al., 2005). Two-dimensional (2D) limit equilibrium (LE) methods are commonly used, with 3D effects taken into account using empirical factors (Eltaher et al., 2003). Another common analysis approach employs simplified UB methods (e.g. Aubeny et al., 2001, 2003a). The suitability of these approaches needs confirmation. Results from field tests undertaken by Keaveny et al. (1994) showed that significant additional capacity is gained when caissons are loaded laterally at half the embedment length, compared with lateral loading at the mudline. Since then it has been generally accepted that the optimal load attachment point varies from half to three quarters of the caisson embedment length (Deng et al., 2001; Randolph and House, 2002; Eltaher et al., 2003; Andersen et al., 2005; van Dijk, 2015). When loaded optimally, a caisson translates at failure. This is a result of zero net moment acting on the caisson, when considering the line of action of the load with the caisson centreline, as opposed to the caisson wall.

The use of hybrid mudmat–pile foundations is relatively recent and as such there is limited design guidance. An analytical model for estimating the capacity of hybrid foundations was developed by Dimmock et al. (2013). This study considered the mudmat/pile connection as providing no rotational restraint at the pile head. The interaction of loads between the mudmat and the piles was somewhat simplified, with the piles alone assumed to resist horizontal and torsional loads, and the mat alone assumed to resist vertical loading. Recent publications have offered offered insight into specific hybrid foundation design cases, while recognising the requirement for additional study (Hossain et al., 2015b; Won et al., 2015). As the use of

hybrid foundations offshore is relatively new, and due to the complex nature of the foundation, further analysis is required (Hossain et al., 2015b).

Traditional capacity analysis methods can provide a quick but conservative bearing capacity estimate for simple foundation geometries and loadings. More detailed analysis of offshore foundations is often undertaken using 3D displacement FEA. This can be accurate, but can also be time-consuming, as a mesh refinement study is required to verify the quality of the solution. As such, a major disadvantage of conventional FEA is the lack of a direct error measure associated with the solution. Capacity analyses using FELA differ from those using FEA in that strict LB and UB plasticity solutions are obtained for the collapse load. This allows for a directly quantifiable error measure to be associated with the average bound solution. Furthermore, an adaptive mesh refinement strategy could be used to facilitate bound convergence over successive iterations of the solution. A limitation of FELA is the need to adopt a simple rigid–plastic soil model. However, as previously mentioned, this is essentially equivalent to the elastic–plastic soil models typically used in capacity analyses undertaken using conventional FEA. Ultimately, FELA could provide an attractive alternative to displacement finite element analysis for capacity analysis of offshore foundations on clay.

This research has been funded by Subsea 7, a subsea engineering company serving the offshore energy industry (Subsea 7, 2017), to ascertain if FELA is a viable alternative to conventional FEA for a range of offshore design problems.

1.4 Research objectives

This thesis contributes to research into novel numerical modelling techniques and to research into ultimate limit state analysis of offshore foundations. FELA is performed using the in-house software OxLim, which has recently been extended to solve 3D problems. There is currently limited information available on the implementation of 3D FELA, thus one aim of this research is to provide a description of the method and of its advantages/disadvantages for foundation capacity analysis. In this thesis, 3D OxLim is benchmarked against analytical solutions and against displacement FEA, and the application of 3D FELA to offshore

foundations (shallow foundations, suction anchors and hybrid foundations) is described in detail. This research sets out to demonstrate that 3D FELA with adaptive mesh refinement is a viable preliminary design tool. This will be achieved by considering a number of authentic design case studies, where non-trivial foundation geometries, soil strength profiles, loading conditions, and foundation/soil interface conditions are analysed.

The foremost aim of this thesis is to provide research that is practical for incorporation in current design methods for offshore mudmats, suction caissons, and mudmat–pile hybrid foundations. Three independent studies of mudmat foundations will provide insight into:

- The effect of seabed inclination on planar mudmat capacity.
- Mudmat capacity under realistic 3D load combinations (based on the combined loads generated by a horizontal force applied within the envelope of the mudmat).
- Vertical bearing capacity factors for surface and embedded square foundations with a range of perforation ratios.

This thesis also aims to improve understanding of suction caissons used as anchors for catenary or taut mooring systems, by providing a comprehensive and systematic analysis of their capacity. The influence of design parameters (such as length to diameter aspect ratio, interface conditions, and load angle) on caisson capacity will be quantified and the optimal load location will be found for an extensive range of caissons.

The final aim of this thesis is to obtain, though FELA, the contribution of the constituent foundation parts (mudmat base, mudmat side, pile base, pile side) to the total capacity of a hybrid mudmat–pile foundation under uniaxial loads. The effects of pile length, diameter, and head fixity, on hybrid foundation capacity are quantified.

Throughout this thesis, examining numerically predicted foundation failure mechanisms is given importance. An objective of this research is to take a holistic approach to foundation analysis, linking foundation capacity to the corresponding collapse mechanism in the soil in order to best improve understanding of foundation behaviour.

1.5 Thesis outline

The early chapters provide context to the analysis problems considered later in the thesis. **Chapter 2** provides background information on the undrained analysis of foundations in clay. A state of the art review of numerical techniques and of capacity analysis studies of mudmats, caissons, and hybrid foundations is provided. In **Chapter 3**, the FELA implementation (OxLim) is detailed and discussed. A displacement FEA model, using the commercial software Abaqus (Dassault Systèmes Simulia Corp., 2014), is also described. OxLim is benchmarked against analytical solutions, results obtained using FEA, and results available in the literature.

Analysis of specific foundation types is undertaken in the subsequent chapters. In **Chapter 4**, shallow rectangular foundations are analysed. The chapter begins with plane strain analysis of mudmats, and considers the effect of a possible seabed inclination on mudmat capacity. A case study is presented which is based on a recent mudmat design where seabed inclination was of significant concern. A second design case considers a rectangular mudmat under 3D combined loading. This informs a study in which focus is placed on horizontal loads applied within the plan area of a mudmat which, if applied at an eccentricity from the centre, may transfer a torsional load to the mudmat. Loads applied at a height above the mudmat, inducing overturning moments, are subsequently considered. The effect of a vertical dead load on the combined loading capacity is assessed. This chapter concludes with research into the vertical capacity of square perforated footings. Capacities of surface and embedded perforated footings are compared with a recently developed design formula (Tapper, 2013; Tapper et al., 2015). A modification to this design formula for use with embedded footings is outlined.

Suction caissons are analysed in **Chapter 5**. Capacities under horizontal loading are found for caissons loaded at a range of attachment points along the embedded length of the caisson. An extensive parametric study considering caisson length to diameter aspect ratio, soil strength profile and unit weight, load attachment point and angle, and wall/soil contact breaking is undertaken. Capacity charts showing the variation in caisson capacity with load attachment

location are presented, and tabular results summarise maximum capacities and corresponding load points. Failure mechanisms obtained using plane strain and 3D analyses are presented and discussed. The chapter concludes with a case study, where capacities of a caisson in layered soil are ascertained under two design conditions—ultimate limit state (ULS) and accidental limit state (ALS).

Chapter 6 contains the results of UB analyses of the most complex foundation type considered in the thesis, hybrid mudmat–pile foundations. The contribution of the constituent foundation parts (mudmat base, mudmat side, pile base, pile side) to the total hybrid foundation capacity is quantified, and the influences of pile length, pile diameter, and pile head fixity on the total capacity are examined. A case study is presented which investigates the effect of seabed inclination on hybrid foundation capacity under six degree-of-freedom loading.

Chapter 7 summarises the main findings and suggests areas in which further research would be beneficial.

Chapter 2

Background

2.1 Introduction

This chapter provides background information pertaining to offshore foundation capacity analysis. Analysis methods and software implementations are introduced and described. State of the art research into shallow foundations, caisson foundations, and hybrid foundations is reviewed in detail. Unless stated otherwise, the literature relates to foundations idealised as rigid, founded on undrained clay soil idealised as an elastic–plastic or rigid–plastic material.

2.2 Review of numerical methods

2.2.1 Limit analysis

Limit analysis refers to the use of the lower bound (LB) and upper bound (UB) plasticity theorems, which together place limiting values on the theoretical plastic collapse load of a foundation (or other structure) subject to live loading. The plasticity theorems were developed by Drucker et al. (1952) and Gzodev (1960), amongst others. Assumptions such as perfect plasticity and an associated flow rule are required in order to apply these theorems. It is also assumed that the material's yield function is convex (which is true for Tresca and von Mises yield functions). Once these assumptions have been made, the method is rational and consistent and the bound theorems can be used to obtain foundation collapse loads directly, without intermediate steps.

To satisfy the LB theorem, a stress field must be found which satisfies the equations of

equilibrium, the boundary conditions, and is everywhere below yield. The UB theorem requires an admissible velocity field (mechanism) with compatible plastic deformation (no gaps or overlaps), a rate of external work equal to or exceeding the rate of internal plastic energy dissipation, and for deformations to satisfy the (associated) flow rule. LB limit analysis, by definition, must underestimate or equal the collapse load, while UB limit analysis must overestimate or equal the collapse load.

2.2.2 Finite element limit analysis

Finite element limit analysis (FELA) refers to numerical implementations of the LB and UB theorems through a finite element discretisation of the problem stress and velocity fields. The LB and UB are independent problems but can be formulated using the same element discretisation (although different element types are used). Plasticity bound analyses are undertaken using the following general steps:

1. The problem domain is discretised into elements.

2. The constraints required by the LB or UB theorem are enforced within and between connected elements.

3. The variables and constraints are arranged as an optimisation problem. In general, this problem will involve both linear and nonlinear constraints.

4. A numerical optimisation technique is used to find the optimal LB or UB collapse load multiplier, or load factor.

2.2.2.1 Lower bound FELA

To implement LB FELA, a piecewise continuous stress field is usually introduced in the elements of a discretised domain. An early implementation of LB FELA was undertaken by Belytschko and Hodge (1970). Belytschko and Hodge used quadratic triangle elements, which can cause difficulty in enforcing the yield criterion throughout the element. Analysis undertaken by Lysmer (1970) used linear triangle elements, which have the advantage that

the yield criterion will be satisfied everywhere in the element if it is enforced at the vertices. For this reason, three-noded elements are commonly used in the analysis of 2D problems (e.g. Pastor, 1978; Sloan, 1988; Makrodimopoulos and Martin, 2006). The three-noded triangle used in 2D can be extended to a four noded tetrahedron in 3D without complication (e.g. Pastor et al., 1990; Lyamin and Sloan, 2002a; Yang et al., 2003; Martin and Makrodimopoulos, 2008). Linear extension elements have also been developed which allow for admissible stress fields to be constructed for unbounded domains (Pastor, 1978; Lyamin and Sloan, 2003; Makrodimopoulos and Martin, 2006).

The type of optimisation required is dependent on the yield function. The yield function was linearised in early FELA implementations, allowing for well established linear programming (LP) algorithms to be used (Maier, 1969; Anderheggen and Knöpfel, 1972). Non-linear programming (NLP) was used by Zouain et al. (1993) to model a yield function directly without first linearising it (also Yang et al., 2003; Li and Yu, 2005). Second-order cone programming (SOCP) was used by Ciria and Peraire (2004) and Bisbos et al. (2005), amongst others, to model von Mises materials. The implementation of the Mohr–Coulomb criterion in plane strain using SOCP is described in Makrodimopoulos and Martin (2006) and Krabbenhøft et al. (2007).

A notable algorithm for the analysis of SOCP problems, described in Andersen et al. (2003), is implemented in the commercially available software MOSEK (2014). Other noteworthy algorithms for solving SOCP problems include SeDuMi (Sturm, 1999) and SDPT3 (Tütüncü et al., 2003). The problem constraints must be formulated appropriately before optimisation can be undertaken. Commercially available limit analysis software, OptumG2 (Krabbenhøft et al., 2015), formulates analysis based on the implementation outlined in Krabbenhøft et al. (2007). OptumG2 has recently been used for the LB and UB analysis of plane strain and axisymmetric geotechnical problems (Keawsawasvong and Ukritchon, 2016; Ukritchon and Keawsawasvong, 2016).

OxLim, used in this thesis, is formulated based on the LB implementation described in Makrodimopoulos and Martin (2006). The linear triangle stress elements used by

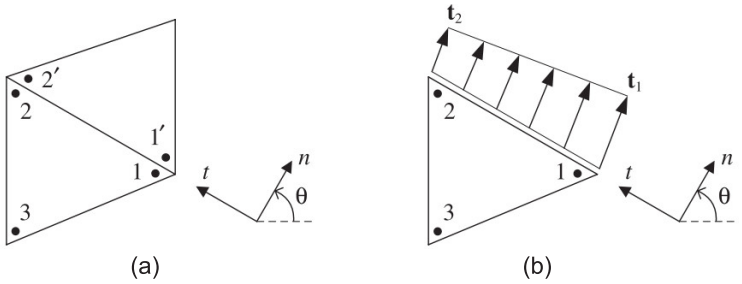

Figure 2.1: Elements in 2D mesh used for LB analysis (Makrodimopoulos and Martin, 2006): (a) interior edge nodes; (b) exterior edge nodes on a traction boundary

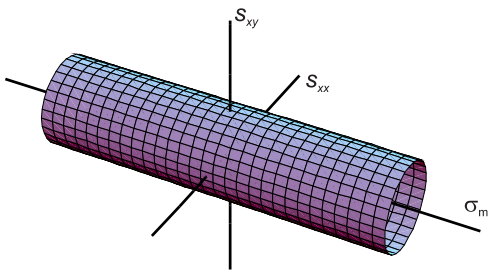

Figure 2.2: Plane strain Tresca yield criterion

Makrodimopoulos and Martin are shown in Figure 2.1. To enforce a rigorous LB it must be ensured that;

- each element is in equilibrium,
- interior edges between elements are in equilibrium (Figure 2.1(a)), and
- exterior edges are in equilibrium (Figure 2.1(b)).

For plane strain conditions, the Mohr–Coulomb yield criterion can be expressed as a linear equality constraint coupled with a second-order cone constraint. The Tresca special case with unlimited tension capacity (see Figure 2.2) can be expressed in the form

$$\begin{gathered} \sqrt{s_{xx}^2 + s_{xy}^2} \leq z \\ z = s_{\mathrm{u}},\ \sigma_{\mathrm{m}} = \text{free} \end{gathered} \tag{2.1}$$

where $\sigma_{\mathrm{m}} = \dfrac{\sigma_{xx} + \sigma_{yy}}{2}$, $s_{xx} = \dfrac{\sigma_{xx} - \sigma_{yy}}{2}$, $s_{xy} = \tau_{xy}$, and z is an auxiliary variable.

The resulting optimisation problem, after applying the equilibrium and material yield constraints, can be solved using MOSEK (2014). Makrodimopoulos and Martin (2006) noted that this approach to LB FELA can be used to handle many popular yield functions, such as Mohr–Coulomb (and Tresca) in plane strain and Drucker–Prager (and von Mises) in 2D or 3D. It was found that SOCP is a powerful technique for non-linear optimisation that allows for accurate LB solutions to difficult classical plasticity problems to be obtained.

2.2.2.2 Upper bound FELA

When implementing UB FELA it is often difficult to ensure that the associated flow rule is satisfied throughout the discretised domain. Constant strain elements (three-noded triangles with a linear variation of velocity) have been used to satisfy this requirement (e.g. Bottero et al., 1980; Abdi et al., 1994; Sloan and Kleeman, 1995; Pastor et al., 2000) and have been combined with discontinuities in the velocity field to help to compensate for poor accuracy when using linear elements. Analysis of incompressible materials (such as undrained clay) can lead to a 'locking' of the failure mechanism (Nagtegaal et al., 1974), but using a constant strain element with discontinuities overcomes this. Just as for LB FELA, early implementations used LP (Bottero et al., 1980; Pastor et al., 2000). More recent implementations have used NLP, the most notable for geomechanics problems has been Lyamin and Sloan (2002b), which is an advancement of an algorithm outlined in Zouain et al. (1993).

An alternative to the constant strain element approach is outlined in Makrodimopoulos and Martin (2007) (first suggested for purely cohesive materials by Yu et al. (1994)). It was found that six-noded triangles could be used to obtain strict UB solutions in plane strain, provided that the sides of the elements were straight. This element is termed a 'simplex strain element' and is shown in Figure 2.3. Because the strains vary linearly, the flow rule need only be enforced at the three triangle vertices to ensure that it is satisfied throughout the triangle. Makrodimopoulos and Martin found that this element type performs better than constant strain elements at similar computational cost. This element, and the method described in Makrodimopoulos and Martin (2007), is implemented in plane strain analyses using OxLim. 3D OxLim analyses use constant strain elements (four-noded tetrahedra) with discontinuities

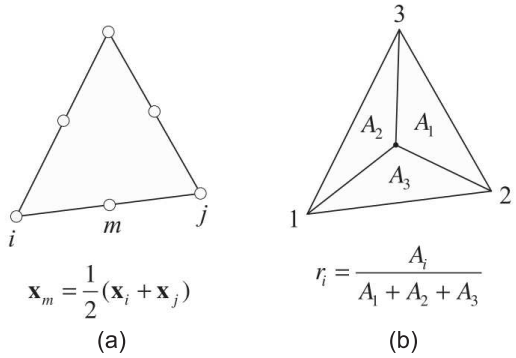

Figure 2.3: 2D UB simplex strain displacement elements used by Makrodimopoulos and Martin (2007): (a) 6-node element with straight sides; (b) notation of area coordinates

in the velocity field between elements, as it has been found that the failure mechanism is prone to locking when 3D simplex strain elements (ten-noded tetrahedra) without discontinuities are used (C.M. Martin, personal communication, 2017).

The optimisation of UB FELA, just as for the LB, can be formulated as a SOCP problem, provided that the yield criterion can be expressed as a quadratic cone constraint. To find an UB solution, a kinematically admissible displacement field (mechanism) must be found that minimises the work done by the applied forces or boundary tractions. To solve this problem using SOCP it is computationally more efficient to solve the dual optimisation problem, as outlined in Makrodimopoulos and Martin (2007). As the dual solution is a maximisation problem where the optimal load multiplier is approached from below over the course of several iterations, it is necessary to check that the optimisation has converged, to ensure that an UB solution has been found. If the optimisation has not converged then the load multiplier obtained may in fact underestimate the exact collapse load.

2.2.3 Previous applications of 3D FELA

Axisymmetric FELA, using SOCP optimisation, has recently been used to find capacities of footings and caissons in clay soil obeying the Tresca criterion (e.g. Kumar and Chakraborty, 2014; Chakraborty and Kumar, 2015; Ukritchon and Keawsawasvong, 2016). 3D FELA has been applied to slope stability problems for a number of years (e.g. Chen et al., 2001a,b; Li et al., 2009; Lim et al., 2015). Other (geotechnical) capacity problems have sporadically been

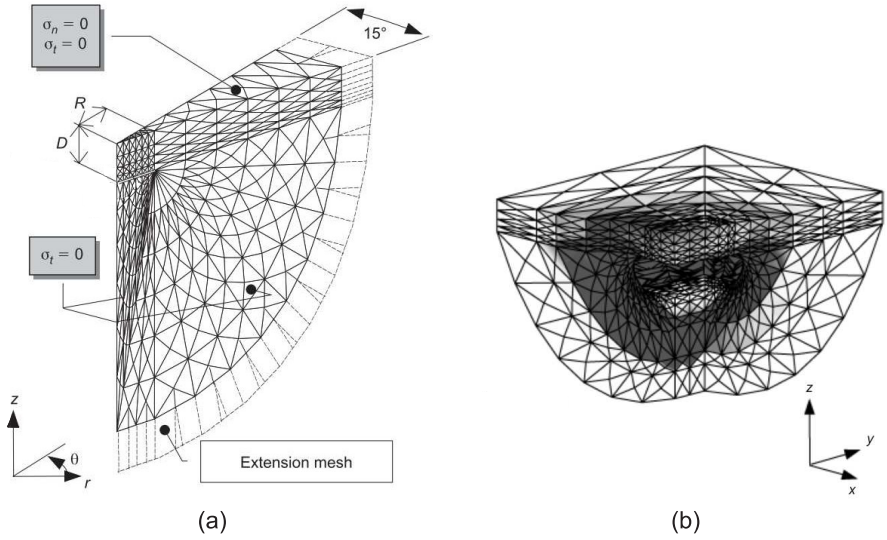

Figure 2.4: 3D FELA undertaken by Salgado et al. (2004): (a) typical LB mesh for circular footing; (b) UB deformation pattern for rectangular footing under vertical loading

examined using 3D FELA.

3D LB FELA was undertaken by Yang et al. (2003). Non-linear programming was used to find the vertical bearing capacity of a smooth rectangular footing resting on the surface of a Drucker–Prager material. Symmetry allowed for one quarter of the soil domain to be modelled; the domain was discretised into a structured mesh comprising 90 elements.

Salgado et al. (2004) used 3D FELA to find the vertical bearing capacity of circular, square, and rectangular footings in clay. The FELA LB and UB implementations followed Lyamin and Sloan (2002a,b). The soil was modelled as a Tresca material, and was discretised into a structured mesh of four-noded tetrahedra. The LB and UB optimisation problems were solved using non-linear programming. Symmetry allowed for 15° of the circular footing problem domain and one quarter of the rectangular footing problem domain to be analysed (see Figure 2.4). Capacity analyses using 3D FELA were subsequently undertaken for circular and rectangular footings on sand (modelled as a Mohr–Coulomb material), as outlined in Lyamin et al. (2007).

Martin and Makrodimopoulos (2008) undertook 3D FELA of Mohr–Coulomb materials by using semidefinite optimisation. Two example problems were considered; the compression of a square block and the expansion of a thick spherical shell. Symmetry allowed for one

eighth of the problem domains to be modelled, and the regular meshes of tetrahedral elements contained up to 3700 elements. The LB analyses employed linear stress elements, while simplex strain elements (without discontinuities) were used in UB analyses.

3D FELA of Mohr–Coulomb materials using semidefinite optimisation was also undertaken by Krabbenhøft et al. (2008). For this study, the vertical bearing capacities of circular and square footings were found using structured meshes comprising approximately 4000 elements. Symmetry allowed for 15° of the circular footing problem domain and one quarter of the rectangular footing domain to be analysed.

2.2.4 Displacement finite element analysis

The finite element method has been used extensively in many fields of engineering for over 40 years. The application of FEA to geotechnical engineering is described in detail by Potts and Zdravković (1999) and Potts and Zdravković (2001). FEA seeks to satisfy equilibrium, compatibility, material constitutive response, and boundary conditions. An elastic–plastic constitutive model is commonly applied in undrained finite element analysis of foundations on clay. As the response of the material is initially elastic, the plastic failure load is only reached after a number of solution increments. This is a significantly different approach to limit analysis.

2.2.5 Discontinuity layout optimisation

Discontinuity layout optimisation (DLO) was developed for plane strain by Smith and Gilbert (2007) to solve for translational failure mechanisms. The formulation was later extended to include rotational mechanisms in cohesive media (Gilbert and Smith, 2013). The stages in the DLO procedure considering translational failure only are outlined in Figure 2.5(a)–(d); rotational slip lines are also considered in Figure 2.5(e)–(f).

When using DLO, UB analysis is formulated in terms of rigid sliding blocks separated by velocity discontinuities. Nodes are spaced across the problem domain with potential lines of discontinuity created to connect each node to every other node. The problem is optimised using LP to find the solution of discontinuities which produces a compatible mechanism with

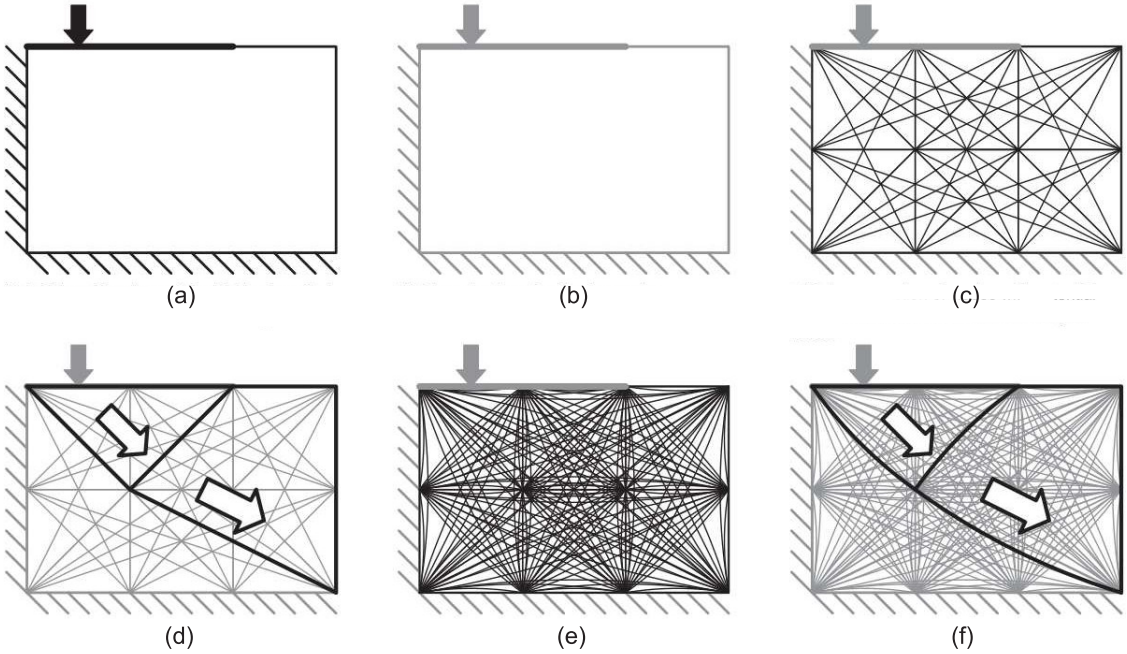

Figure 2.5: Stages in the DLO procedure (Gilbert and Smith, 2013): (a) initial problem (eccentric rigid load applied to block of soil close to a vertical cut); (b) discretisation of soil using nodes; (c) interconnection of nodes with potential straight-line discontinuities interlinking all nodes; (d) identification of critical subset of potential discontinuities using optimisation (giving layout of slip-lines in the critical translational failure mechanism); (e) interconnection of nodes with potential linear and curved discontinuities (for clarity only a small subset of possible curved discontinuities are shown); (f) identification of critical subset of potential discontinuities using optimisation (giving the layout of slip-lines in the critical rotational failure mechanism)

the lowest energy dissipation. The accuracy of the UB solution can be improved by increasing the nodal density. Unlike combined LB and UB FELA, the solution does not have a directly quantifiable error measure, as only an UB solution is found. A nodal refinement study is recommended to check convergence of the collapse load, which is broadly equivalent to a mesh refinement study when using FEA.

The commercial software LimitState:Geo (LimitState Ltd, 2016) implements DLO for the analysis of planar geotechnical problems. Failure mechanisms and corresponding load factors for a strip footing on soil with uniform strength are shown in Figure 2.6(a) using a 'medium' nodal distribution and Figure 2.6(b) using a 'very fine' nodal distribution in LimitState:Geo. As expected, both capacity values ($5.19Bs_u$ and $5.16Bs_u$) lie above the theoretical collapse value of $5.14(2+\pi)Bs_u$ from Prandtl (1920).

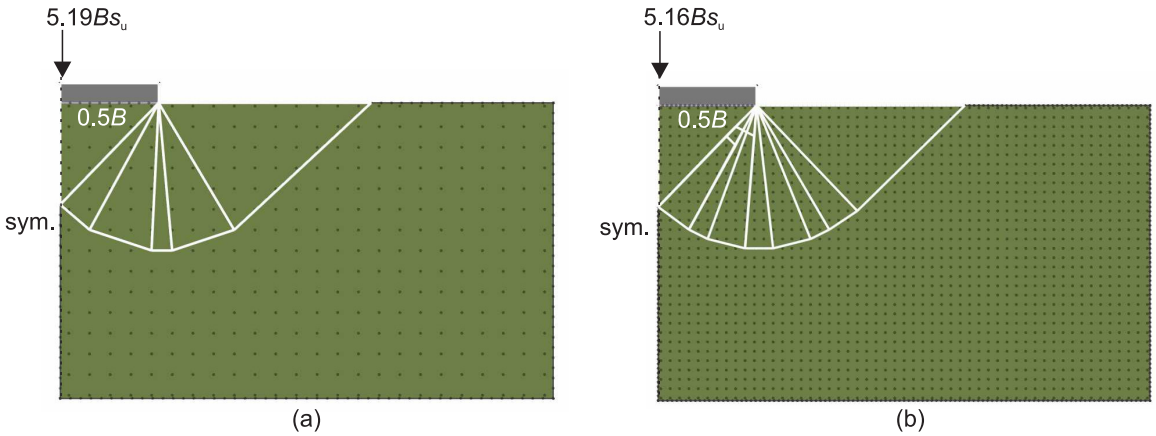

Figure 2.6: Failure mechanisms for a rough ($\alpha = 1$) strip footing under vertical loading on soil with uniform shear strength s_u using LimitState:Geo: (a) 'medium' nodal distribution; (b) 'very fine' nodal distribution

A 3D formulation of DLO has recently been implemented (Hawksbee et al., 2013). A similar solution procedure is followed in 3D. First the problem is discretised into a grid of nodes, nodes are then connected to make edges, these edges are joined to create polygonal discontinuity facets, and the problem is set up in SOCP form and solved using optimisation software. The bearing capacity of a perfectly rough rigid footing resting on the surface of a purely cohesive Tresca material was considered as a benchmarking exercise, amongst other problems, in Hawksbee et al. (2013) and the failure mechanism is shown in Figure 2.7. The authors noted that the failure mechanism extends to the fixed problem bounds, but extending the problem domain further would result in an impractically large problem. This highlights the present numerical inefficiency of 3D DLO, and as such it is possibly limited in its potential applications.

2.2.6 Rigid finite element analysis

Rigid finite element analysis (RFEA) is a discontinuous method where the problem domain comprises rigid elements and interfaces. Deformations are only permitted along interfaces between elements. The method originates from a rigid body and spring method proposed by Kawai (1977). RFEA is often used for slope stability analysis of soils, rocks, or discontinuous media (e.g. Chen et al., 2004; Liu and Zhao, 2013) but more general discrete element slip

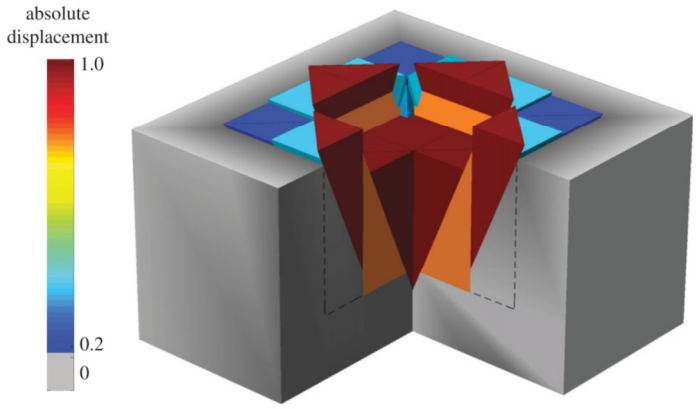

Figure 2.7: Punch indentation using DLO: representative failure mechanism (dashed lines indicate extent of domain modelled) (Hawksbee et al., 2014)

models have also been developed (Alwis, 2000). This method finds collapse mechanisms using defined equilibrium equations and linear programming.

2.2.7 Method of characteristics

The method of characteristics (MoC), also known as the slip line method, can be used to find bearing capacity solutions based on the stress characteristics in the soil. The free computer program ABC for shallow foundation analysis (Martin, 2004) calculates an 'incomplete' LB collapse load (incomplete as only part of the stress field is computed, without extending it throughout the soil). Vertical capacities obtained using ABC have been shown to provide exact bearing capacity calculations for problems in plane strain (Martin, 2005).

2.3 Shallow foundation vertical capacity analysis

Shallow foundation capacity has been extensively researched. Terzaghi (1943) proposed an equation to determine the ultimate vertical bearing capacity, q_u, of a strip footing of width, B, using the superposition of bearing capacities from the soil cohesion, c, surcharge pressure, q, and soil unit weight, γ. The soil is assumed to act as a rigid–plastic Tresca material in undrained conditions ($c = s_u$) and a Mohr–Coulomb material in drained conditions. A modified version of the original equation is still used today and is shown in Equation 2.2:

$$q_u = s_c d_c i_c \cdot cN_c + s_q d_q i_q \cdot qN_q + s_\gamma d_\gamma i_\gamma \cdot \tfrac{1}{2} B\gamma N_\gamma \tag{2.2}$$

Bearing capacity factors N_c and N_q can be derived from analytical equations. There are various numerical approximations for N_γ, most notably from Brinch Hansen (1970) and Vesic (1975). Empirical modification factors accounting for various foundation shapes by using shape factors, s_c, s_q, s_γ, and foundation depths by using depth factors d_c, d_q, d_γ, were found by Skempton (1951). Loads inclined to the vertical can be accounted for by using the factors i_c, i_q, i_γ. Moment loading can be considered by analysing an 'effective width' of the footing, with combined vertical and moment loading transformed into an equivalent eccentric vertical force (from Meyerhof, 1951).

Classical bearing capacity theory, stemming from the Brinch Hansen (1970) method, has been adopted into design codes and is conventionally used for preliminary mudmat design in industry (e.g. DNV (1992), ISO (2003), and API (2011)). The design code API RP 2A-WSD (2000) differs in that it is based on the bearing capacity equation proposed by Vesic (1975).

For a surface strip foundation on weightless soil under purely vertical loading, the bearing capacity equation can be simplified to

$$q_\mathrm{u} = N_c\, s_\mathrm{u} \tag{2.3}$$

N_c for a strip footing resting on the surface of uniform cohesive soil is an exact solution ($N_c = 2+\pi$), first found by Prandtl (1920) (for a large block of metal subjected to a flat rigid punch). N_c can vary for foundations with different shapes and interface conditions. While N_c for a strip footing is a known exact solution, an exact N_c has not been found for square surface foundations. N_c values obtained in the literature for square foundations with rough and smooth foundation/soil interfaces are listed in Table 2.1.

The N_c values in Table 2.1 assume that the foundation is resting on uniform soil. A linear variation of strength with depth is often considered by introducing a dimensionless soil strength heterogeneity factor, $\rho B/s_\mathrm{um}$, where s_um is the soil strength at the mudline and ρ is the strength change per unit depth of soil. Many studies have considered the effect of soil strength heterogeneity on N_c, e.g. Davis and Booker (1973), Tani and Craig (1995), Gourvenec and Mana (2011) and Tapper et al. (2015).

Foundation capacity increases with increasing embedment, d. Gourvenec and Barnett

Table 2.1: Bearing capacity factors (N_c) for square surface foundations on uniform soil

Study	Method	Failure criterion	N_c
Rough interface ($\alpha = 1$)			
Yu et al. (2016)	UB PLA	von Mises	5.78 (UB)*
Tapper (2013)	FEA	Tresca	5.76
Gourvenec et al. (2006)	FEA	Tresca†	5.91
		von Mises	5.74
Salgado et al. (2004)	FELA	Tresca	5.22 (LB)
			6.22 (UB)
Michalowski (2001)	UB PLA	Tresca	6.56 (UB)
Smooth interface ($\alpha = 0$)			
Yu et al. (2016)	UB PLA	von Mises	5.48 (UB)*
Tapper (2013)	FEA	Tresca	5.44
Gourvenec et al. (2006)	FEA	Tresca†	5.56
Puzrin and Randolph (2003)	UB PLA	Tresca	6.13 (UB)
Michałowski and Dawson (2002)	Finite difference	Tresca	5.43

* Not a 'strict' UB solution as flow rule not enforced throughout the domain

† FEA Tresca implemtation uses von Mises flow rule, discussed further in Section 3.5.3.1

(2011) considered foundations with depth to breadth embedment ratios $d/B \leq 1$ and soil strength heterogeneities $0 \leq \rho B/s_{\text{um}} \leq 6$. Algebraic expressions were fitted to capacities of foundations under combined loads obtained using FEA. It was found that foundation capacity is dependent on embedment ratio and degree of soil strength heterogeneity.

2.3.1 Perforated foundations

Early theoretical analysis of perforated foundations on undrained clay showed that beneficial interaction effects are negligible, between vertically loaded foundations spaced closely together in uniform strength clay (Mandel, 1963). For foundations on clay with a linear increase in strength with depth, Hazell and Martin (2005) used MoC and UB analysis to find the vertical bearing capacity of rigidly connected, parallel strip footings. The simplified plane strain geometry of two strip footings of width, B^*, with a gap between them, S, can be used to represent a mudmat with a central perforation, shown in Figure 2.8(a). It was found that the bearing capacity of closely spaced footings can be larger than that for isolated footings, thus

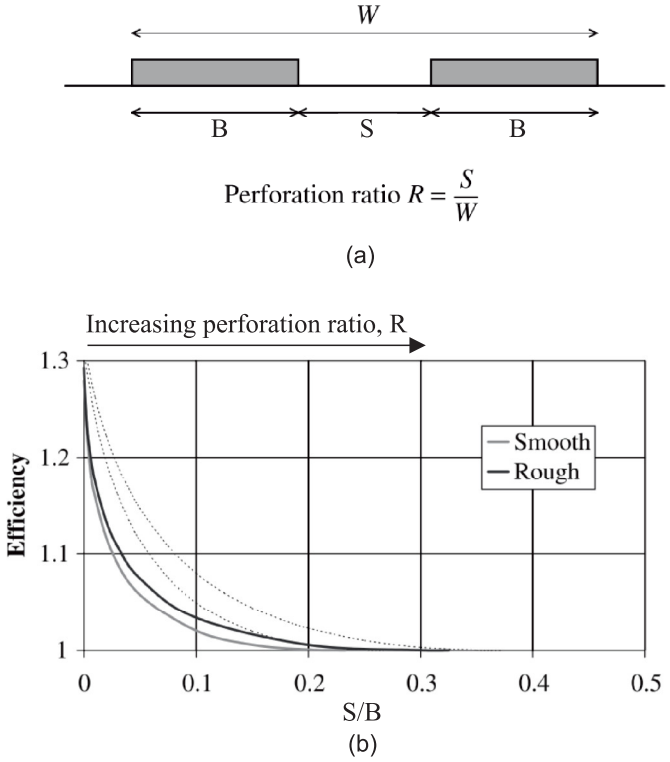

Figure 2.8: A pair of parallel strip footings modelled in plane strain (Hazell and Martin, 2005): (a) notation; (b) variation of efficiency with spacing. Results from MoC shown as solid and simple UB calculations shown as dotted. $\rho B/s_{\mathrm{um}} = 5$

increasing the 'efficiency' of the design (where efficiency is the ratio of the overall capacity to the sum of the individual capacities). Increased efficiency is due to soil arching over the gap which results in no reduction in ultimate capacity but a reduction in the bearing area, leading to a higher capacity per unit foundation area. This beneficial increase in capacity increases with soil strength heterogeneity and is larger for rough footings than smooth footings. Figure 2.8(b) shows efficiency increasing to 1.3 when a perforation is introduced to a foundation on soil with $\rho B/s_{\mathrm{um}} = 5$.

Parallel strip footings on uniform soil under combined loading were analysed using plane strain FEA by Gourvenec and Steinepreis (2007). It was found that under vertical loading there is a small increase in capacity ($\leq 5\%$) when footings are spaced with $S/B < 1$. It was also found that considerable additional moment capacity can be acquired due to the kinematic constraint provided by the rigid connection between the footings.

White et al. (2005) undertook small-scale tests in order to examine the downwards

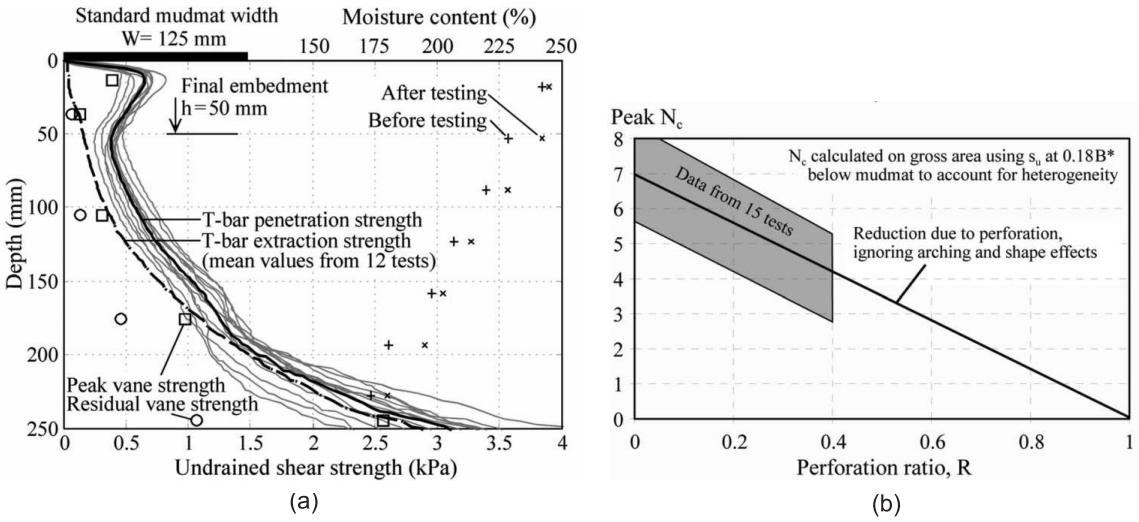

Figure 2.9: Experimental investigation of vertical capacity of perforated foundations (White et al., 2005): (a) results of test bed characterisation showing soil strength profile; (b) peak N_c against perforation ratio, R

vertical and uplift capacities of square foundations with central perforations. The soil used in the experiments had a strong 'crust' and below this the strength was relatively low, before increasing with depth (Figure 2.9(a)). It was found that installation resistance decreased in proportion to perforation area (Figure 2.9(b)) and that there was minimal capacity enhancement at low perforation ratios due to arching.

A comprehensive study of perforated foundations was undertaken by Tapper (2013) and Tapper et al. (2015). Surface and embedded foundations were modelled using FEA and the soil was modelled as an elastic–plastic Tresca material. A range of perforation ratios, R, and soil strength heterogeneity factors were considered, and centrifuge test data was used to verify the numerical results. For surface foundations, it was found that as R increases N_c decreases asymptotically to N_c for a strip footing on uniform soil. In order to derive an expression for estimating the bearing capacity of perforated foundations, a perforation factor, r_c, was introduced where

$$r_c = s_c + \sqrt{R}(1 - s_c)\ . \tag{2.4}$$

Shape factors, s_c, were found for a range of soil strength heterogeneities (using FEA) and are shown in Figure 2.10 for square foundations. A vertical bearing capacity equation was

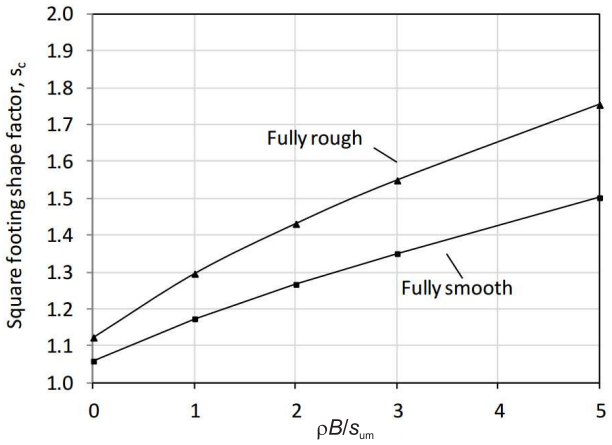

Figure 2.10: Shape factor, s_c, for a square foundation on soil with a range of strength heterogeneity factors (Tapper, 2013)

proposed,

$$q_{\mathrm{u}} = s_{\mathrm{um}} N_c r_{\mathrm{c}} d_c + \gamma' d \tag{2.5}$$

where γ' is the effective unit weight of the soil (rendering $\gamma' d$ the effective overburden stress).

To account for foundation embedment, Tapper (2013) found (using FEA) depth factors, d_c, for perforated foundations in soil with various strength heterogeneities (shown in Figure 2.11). It was suggested, for simplicity, that d_c for a solid foundation could be used for all values of R, although this would become increasingly conservative as R increases.

Tapper (2013) also found that the vertical capacity of a foundation with one central perforation is approximately the same as that for a foundation with multiple equally spaced perforations, provided R is the same. As such, the design expression in Equation 2.5 can be used to give a reasonable prediction for the capacity of foundations with numerous perforations.

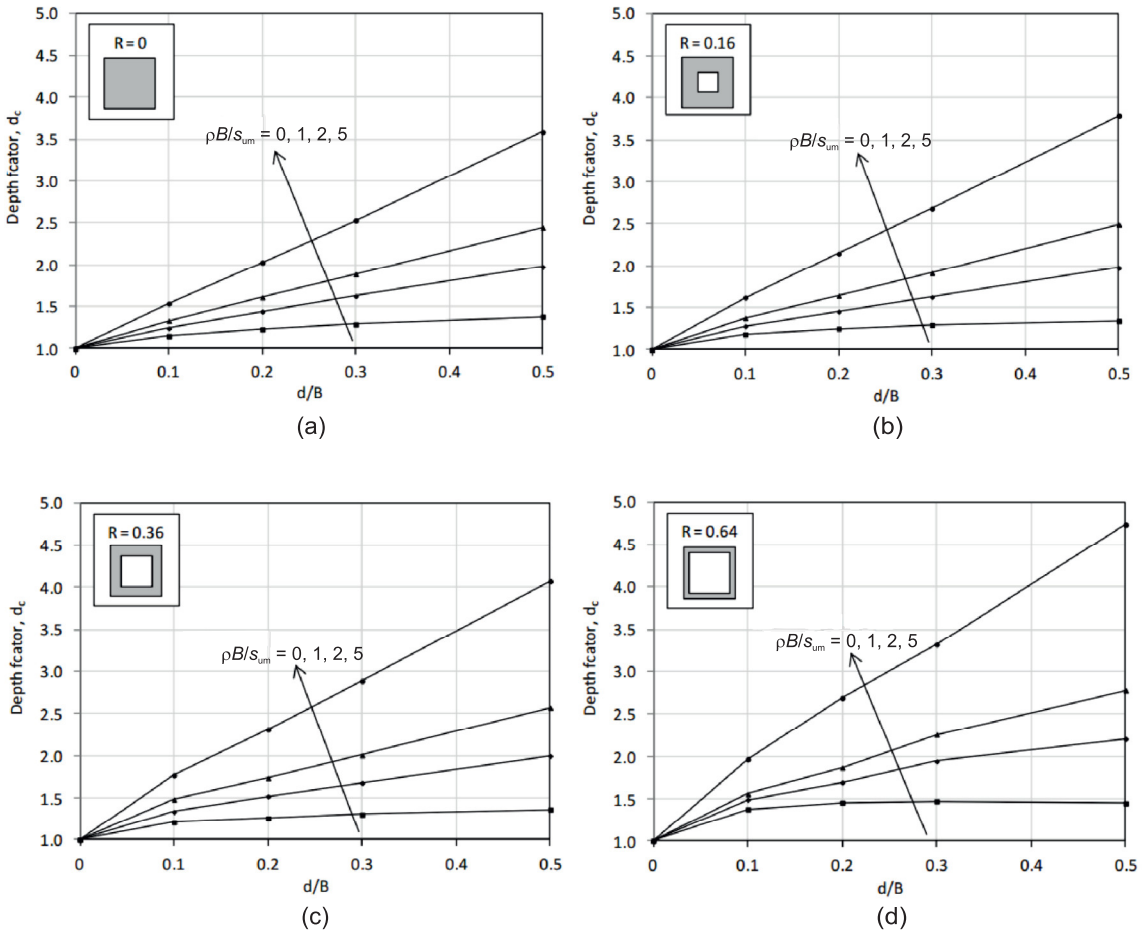

Figure 2.11: Depth factors, d_c, for embedded square foundations (rough base, smooth sides) with a range of embedment to breadth ratios on soil with a range of soil strength heterogeneity factors (Tapper, 2013): (a) $R = 0$; (b) $R = 0.16$; (c) $R = 0.36$; (d) $R = 0.64$

2.4 Rectangular mudmats under combined loading

It is well known that failure of mudmats can be significantly influenced by horizontal and torsional loading (Finnie and Morgan, 2004; Murff et al., 2010; McDonald et al., 2014; Martin et al., 2015; Feng et al., 2017). This has been further highlighted by the development of hybrid mudmat–pile foundations to improve foundation capacity (Dimmock et al., 2013). Vertical loading on mudmats is predominantly due to the self-weight of the supported infrastructure, and is typically small when compared with the ultimate vertical bearing capacity of the mudmat (Feng et al., 2017). However, when a mudmat is located on sloping ground, vertical loading, particularly when applied in combination with other loading, needs additional consideration.

Murff and Miller (1977) used UB limit analysis to study the bearing capacity of offshore structures and found that torsion significantly reduced the sliding resistance of their example. Finnie and Morgan (2004) studied the effect of torsional loads on subsea foundations, including shallow foundations. It was demonstrated that the governing load case for a shallow foundation can be the torsional effect of a horizontal load applied at an eccentricity from the foundation's centre. A limit equilibrium (LE) method was used to determine the factor of safety against torsional failure for a square surface footing.

This analysis was expanded upon by Yun et al. (2009) where it was supplemented by 3D FEA. Failure envelopes for circular, square, and rectangular surface footings subjected to combined vertical, horizontal, and torsional loading were presented. It was found that FEA overestimated the torsional capacity of a square footing by 11% when compared with the analytical solution. This was due to the fully bonded connection between the foundation and the soil in the FEA model. When the foundation and the soil are fully bonded, interface shearing is prevented, forcing failure into the soil domain and artificially increasing the bearing capacity.

Murff et al. (2010) applied UB limit analysis to shallowly embedded square and rectangular footings subjected to combined horizontal and torsional loading. The footing was modelled as a rigid body, displacing wedges of soil along planes at 45° from the base of the

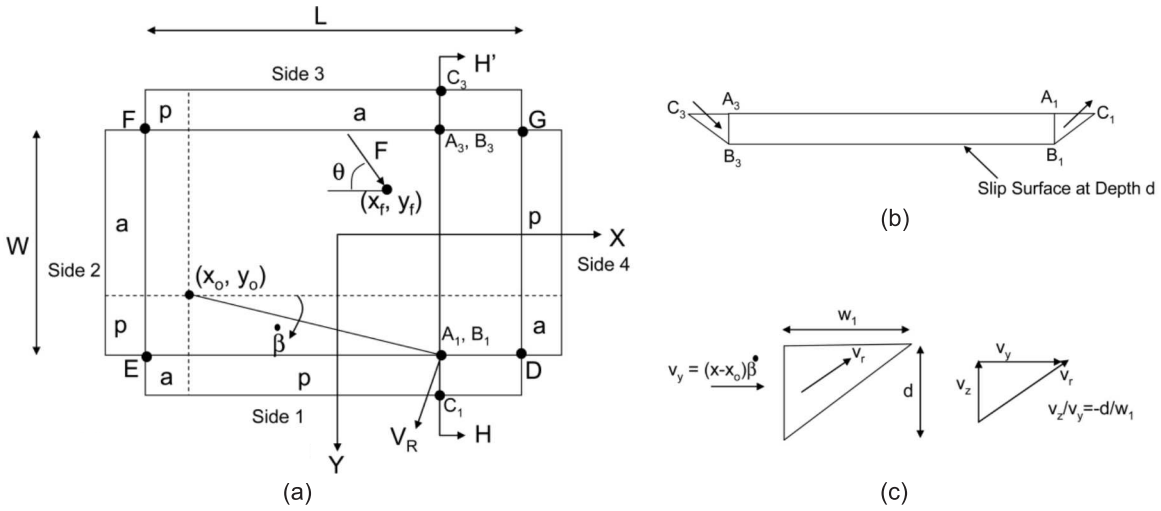

Figure 2.12: Failure mechanism for a rectangular footing under horizontal and torsional loading as described in Murff et al. (2010): (a) plan view of mechanism; (b) elevation view of section H–H′; (c) elevation view of passive wedge $A_1B_1C_1$

foundation to the soil surface. The failure mechanism studied involved an active wedge of soil being pulled behind the footing and a passive wedge of soil being pushed in front (Figure 2.12). The solution presented is capable of considering surface and embedded footings on heterogeneous soil strength profiles when subjected to combined horizontal and torsional loading.

Results from 3D FEA undertaken by Nouri et al. (2014) were found to match the UB PLA equations derived by Murff et al. (2010) reasonably well (Figure 2.13). The FEA was limited to horizontal loads applied parallel to the plan view axes. It was found that although the size of the horizontal–torsional failure envelope increased with embedment depth, its shape remained similar (Figure 2.13(a)). The study found that the eccentricity of lateral loading begins to significantly affect ultimate capacity of square footings at eccentricities greater than approximately 0.1 times the footing breadth. However, increasing the aspect ratio of the footing helps to negate this, particularly when loading is aligned parallel to the short axis.

Feng et al. (2014) used 3D FEA to study six degree-of-freedom loading on shallowly embedded mudmats (Figure 2.14(a)). The focus of this study was on simplifying the failure envelopes for various loading combinations into algebraic expressions (Figure 2.14(b)

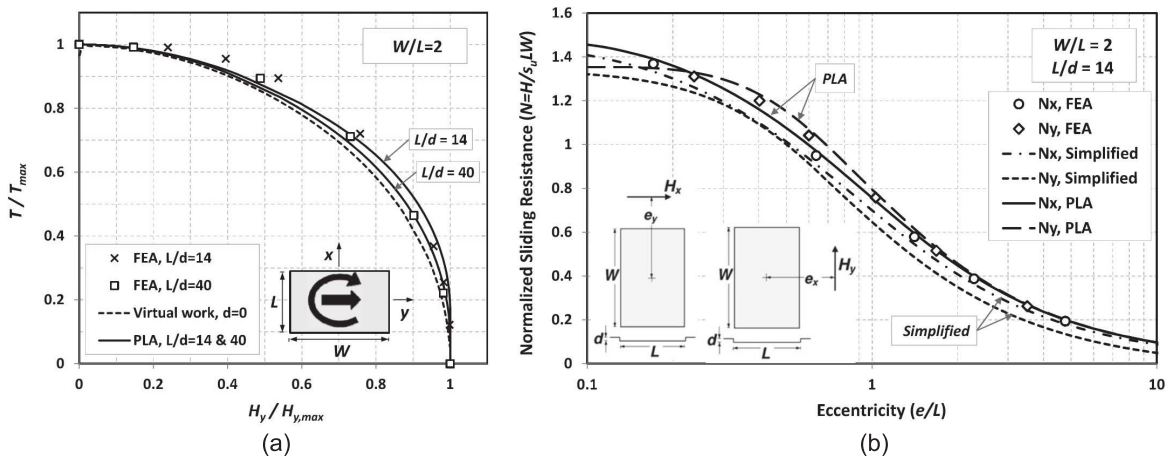

Figure 2.13: Capacities of a rectangular footing under horizontal and torsional loading from Nouri et al. (2014): (a) comparisons of FEA and PLA (from Murff et al. (2010)) horizontal–torsional capacities; (b) capacity reduction versus load eccentricity

and (c)). These expressions can easily be implemented in a spreadsheet, or other software, for use in preliminary design. From the analyses undertaken, a series of design steps for the analysis of rectangular footings was proposed:

1. For a given foundation geometry, evaluate the shear strength at skirt tip level and non-dimensional quantities: breadth to length, embedment depth to breadth, and soil heterogeneity.

2. Evaluate uniaxial capacities for vertical, horizontal, moment, and torsional loading.

3. Reduce ultimate horizontal, moment, and torsional capacities to maximum values available, according to the mobilised (design) proportion of the uniaxial vertical capacity.

4. For a given angle of resultant horizontal load, evaluate corresponding ultimate horizontal capacity, and similarly, ultimate moment capacity.

5. Evaluate reduced ultimate horizontal and moment capacities due to normalised torsional loading.

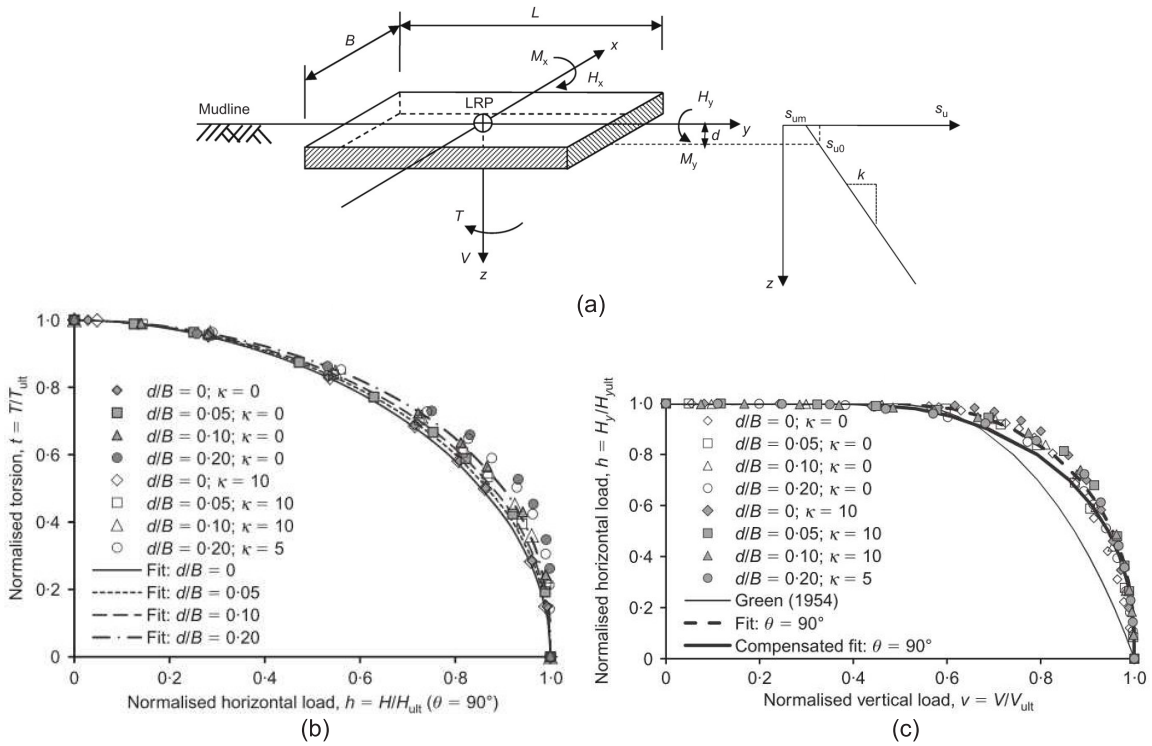

Figure 2.14: Rectangular footing under six degree-of-freedom loading from Feng et al. (2014): (a) notation and sign conventions; (b) FEA results and fit for torsional–horizontal failure envelopes; (c) FEA results and fit for vertical–horizontal failure envelopes

6. Evaluate the extent to which the applied (design) loading falls within the horizontal–moment failure envelope, and thus establish design safety factors.

A realistic design case study of a mudmat subject to six degree-of-freedom loading was also presented in Feng et al. (2014).

Feng et al. (2015) builds on the work of Feng et al. (2014) and considers the effect of a surface crust of strong soil on mudmat capacity. An example shear strength profile for a soil with a crust layer is shown in Figure 2.15(a). The research provides algebraic expressions for mudmat capacity under combined loading once functions of relative crust depth, skirt embedment, and shear strength ratio of the upper crust and underlying soil layer are defined (Figure 2.15(b)). It was found that larger mudmats are required if a strong surface crust is neglected. A no tension interface between the mudmat and the soil was considered by Shen et al. (2017). Reductions in capacity under moment loading, due to detachment of the mudmat from the soil (see Meyerhof (1951)), were quantified. Under combined vertical, horizontal,

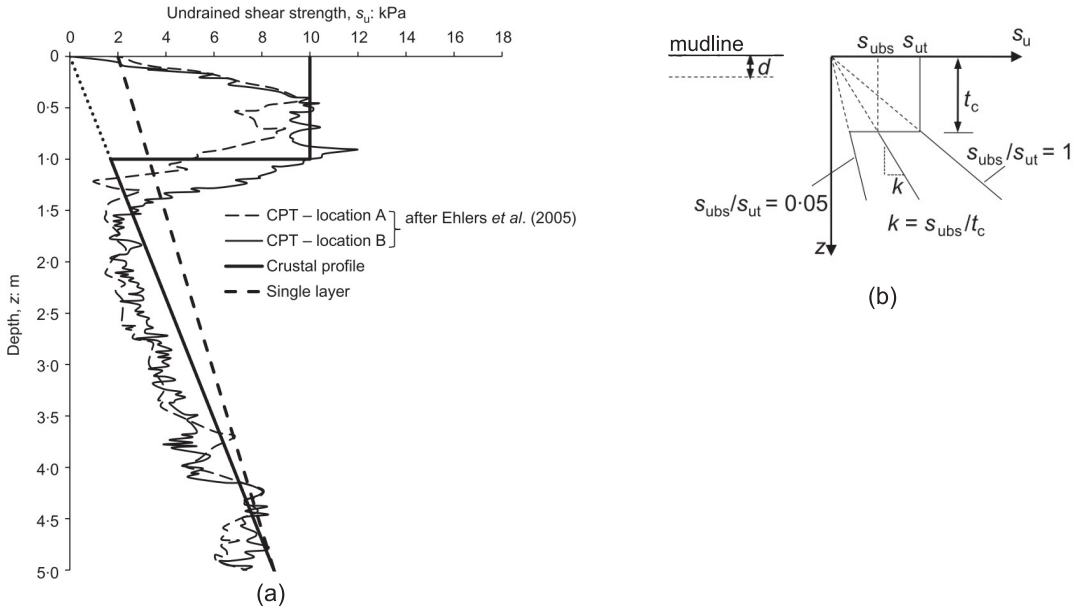

Figure 2.15: Study into capacity of mudmats in soil with a surface crust (Feng et al., 2015): (a) Evidence of surficial crust zone based on in situ investigations in deep water offshore Nigeria; (b) soil strength profile notation

and torsional loading the effect of a no tension interface was found to be negligible. Just as in Feng et al. (2014) and Feng et al. (2015), expressions were proposed for predicting failure envelopes, which can easily be implemented in a spreadsheet.

Research by Feng et al. (2017) focuses on the horizontal–torsional capacity of mudmats. The UB PLA solution presented by Murff et al. (2010) was extended to fully define the failure envelopes for translational and torsional sliding of mudmats. The complex effects of foundation aspect ratio and embedment ratio, skirt roughness, direction of horizontal loading, soil strength heterogeneity, and gapping adjacent to the mudmat skirts were considered. It was found that the shape of the horizontal–torsional failure envelope when normalised by the maximum uniaxial capacities is insensitive to skirt roughness and soil strength heterogeneity, although foundation aspect ratio and the angle of horizontal loading do affect the shape of the failure envelope.

2.4.1 Foundations on sloping ground

There have been several studies of strip footing capacity when located on flat ground at, or near, the crest of a slope, or cut into a slope (e.g. Figure 2.16), but there does not appear to have been any corresponding work for the case of a footing on the slope itself, with inclined ground extending in both directions.

Footings near sloping ground have been considered by Brinch Hansen (1970) and Vesic (1975) through modification factors to the N_c term of Equation 2.2. Kusakabe et al. (1981) and Michalowski (1989) analysed the stability of locally loaded purely cohesive slopes using UB PLA. More recently, Michalowski and Drescher (2009) undertook 3D UB PLA of slope stability problems using a curvilinear cone failure mechanism.

Georgiadis (2010a,b) used FEA to determine the response of undrained slopes to loading by a foundation situated at or near the crest of a slope. It was concluded that the methods of Brinch Hansen (1970) and Vesic (1975) did not consider enough parameters to produce accurate results for many combinations of geometric parameters and soil properties. Georgiadis presented a design proposal for calculating the bearing capacity of strip footings on the crest of or near slopes based on undrained shear strength, bulk unit weight, footing width, the distance of the footing from the slope, the slope angle, the slope height, and load inclination.

Shiau et al. (2011) used plane strain LB and UB FELA (based on procedures described by Lyamin and Sloan (2002a,b) and Krabbenhøft et al. (2005)) to analyse the vertical capacity of foundations at or near the crest of a slope. The effects of slope angle, foundation distance to the slope crest, soil heterogeneity, footing roughness, and surface surcharge were quantified. Results were presented in the form of normalised design charts. It was found that the soil strength to weight ratio is an important parameter when considering the capacity of foundations near slopes as this often defines whether slope failure or local foundation failure occurs.

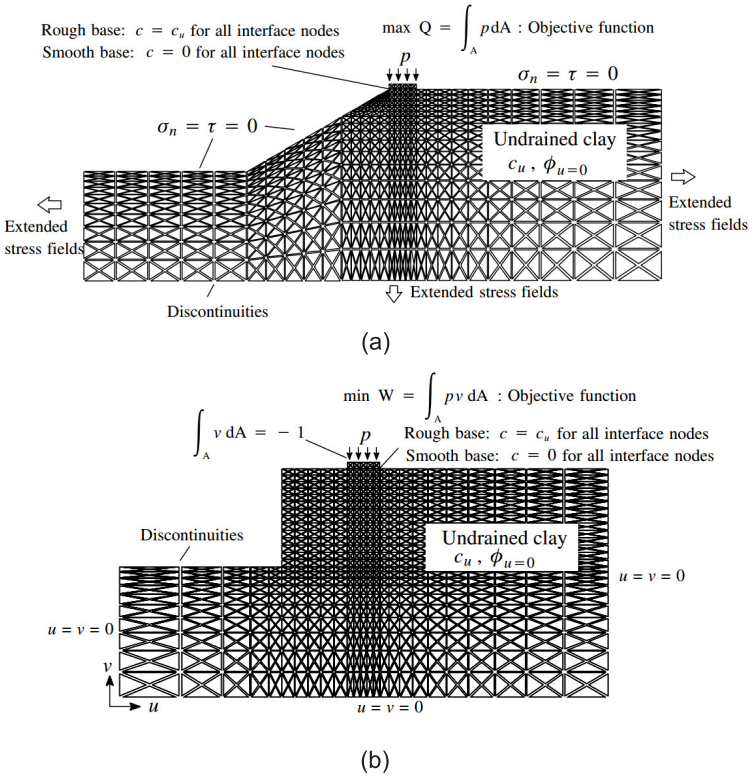

Figure 2.16: Meshes used in Shiau et al. (2011): (a) for LB FELA; (b) for UB FELA

2.5 Caisson capacity analysis

Much research into caisson foundations used as suction anchors offshore stems from the analysis of pile foundations. Murff and Hamilton (1993) describe a 3D collapse mechanism for piles laterally loaded at the mudline, based on UB plasticity theory. The model can incorporate heterogeneous soil strength, a pile plastic hinge failure mechanism, pile/soil adhesion and suction, and tip rotational resistance. A wedge mechanism is proposed near the soil surface, with a gap on the trailing side of the pile (an active soil wedge is also easily included in the model), while a flow around failure mechanism based on Randolph and Houlsby (1984) is modelled at depth (Figure 2.17).

Large scale field model tests of suction caissons were undertaken Keaveny et al. (1994). It was noted that significant additional capacity is gained when caissons are loaded at half the embedment length, when compared to loading at ground level. Andersen and Jostad (1999) also acknowledged that the holding capacity of an anchor is significantly higher if the load is

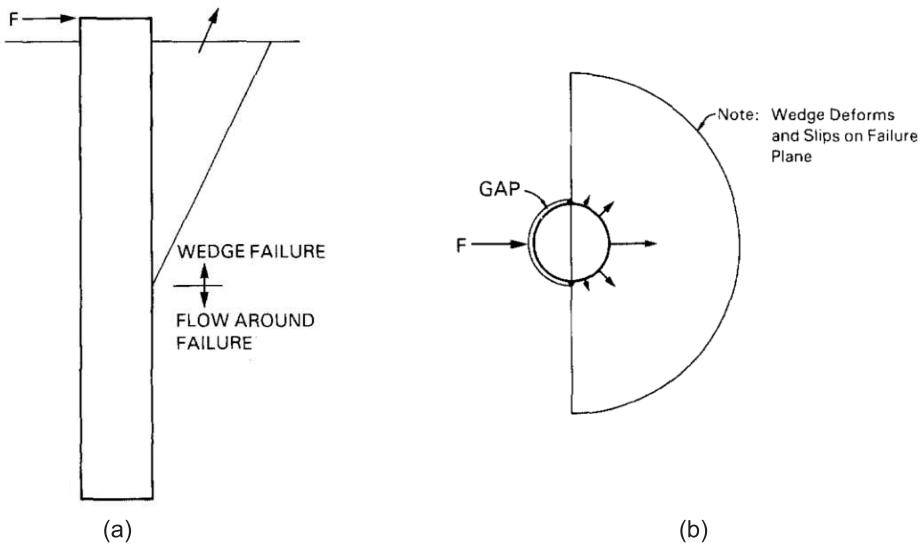

Figure 2.17: Translation mechanism from Murff and Hamilton (1993): (a) elevation view; (b) plan view

applied at an 'optimal' depth below the mudline, when compared with loading at the mudline. It was noted that the location of the optimal load point can depend on the soil profile, the available shear strength along the caisson/soil interface, the load inclination, and the caisson length to diameter aspect ratio.

FEA was used by Sukumaran et al. (1999) to determine the capacity of suction caissons when loaded at various points along the embedded length. Analyses in 2D, 3D, and a pseudo 3D analysis using Fourier conditions to approximate 3D conditions, were undertaken. It was concluded that a pseudo 3D analysis provides accurate results while taking less time than a full 3D analysis. It was found that caisson capacity is maximised when the caisson fails by translating as opposed to rotating (in agreement with Keaveny et al. (1994)). It was also found that the lateral resistance of suction caissons is not affected by installation disturbance of soil near the caisson wall (which reduces the effective interface roughness), as capacity is gained in the soil active and passive failure zones, which are not disturbed. This research focused on a specific case study and the effects of caisson aspect ratio, or a heterogeneous soil strength profile, on caisson capacity were not considered.

Deng et al. (2001) used semi-analytical (Fourier series aided) FEA to investigate the capacity of suction caissons under horizontal loading. A horizontal load was applied at

various points along the embedded length in soil with uniform strength or linearly increasing strength with depth. Fully rough caissons with length to diameter aspect ratios ranging from 1.0 – 2.5 were considered. It was found that the optimum load point was at 0.6 – 0.7 times the caisson length. A simplified method for calculating the maximum capacity, based on an algebraic expression derived from the FEA results, was outlined. Capacity predictions using the simplified equations presented were compared with field tests on caissons in uniform and normally consolidated clay.

Zdravković et al. (2001) investigated the pull-out capacity of caissons loaded at the mudline (along the caisson centreline) using Fourier series aided FEA. The effect of load inclination, caisson/soil interface roughness, and soil strength anisotropy on caisson capacity was quantified. The study considered caissons with length to diameter aspect ratios in the range 0.48 – 1.4. It was found that a roughness factor of 0.5 reduced the capacity by 10 – 15% when compared to a fully rough interface. A more recent study used the same analysis method to consider caissons in normally consolidated clay loaded at four locations along the caisson wall (Zdravković and Potts, 2005). It was found that the optimum load point is at mid caisson length, and for this attachment point a mooring line inclination of 45° to the horizontal is optimal. This study considered length to diameter aspect ratios in the range 2 – 5.

Aubeny et al. (2001) proposed a simplified UB method to determine caisson horizontal capacity, based on the Murff and Hamilton (1993) method. The caisson was assumed to be fully rough and embedded in uniform soil or soil with a linear strength profile. The mechanism was divided into two parts: side resistance and end resistance (Figure 2.18). The energy dissipation at the side of the caisson due to translational and rotational caisson rigid body motion, $\dot{D}_s$, is

$$\dot{D}_s = v_0 D \int_0^{L_f} \left[\left(N_1 - N_2 e^{\left(-\frac{\xi z}{D}\right)} \right) (s_{u0} + s_{u1} z) \left| 1 - \frac{z}{L_0} \right| \right] dz \tag{2.6}$$

where v_0, D, L_f, L_0, and z are as shown in Figure 2.18. N_1 is the limiting lateral pile resistance (from Randolph and Houlsby (1984)) and $N_1 - N_2$ is the lateral pile resistance at the free

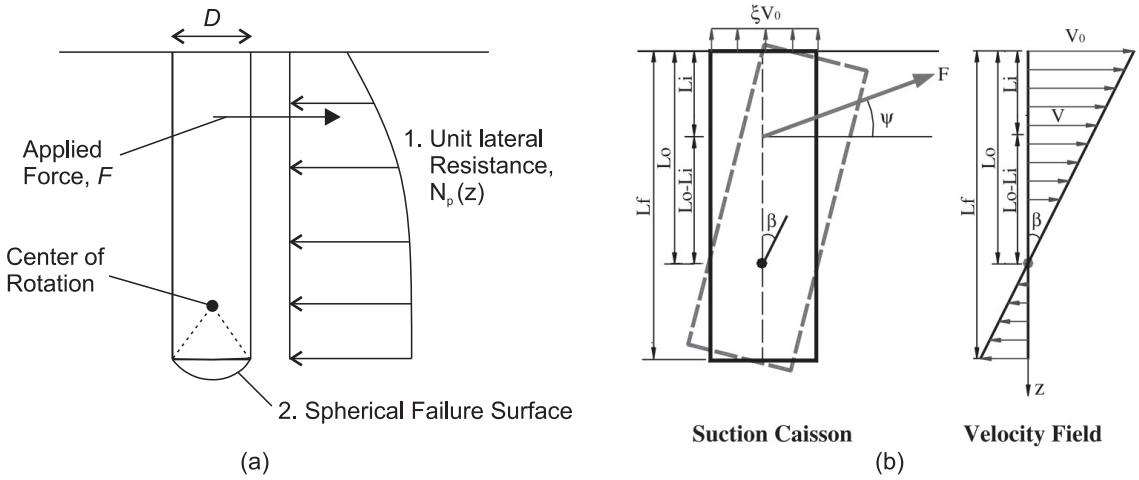

Figure 2.18: UB solution for caisson capacity from Aubeny et al. (2001), extended in Aubeny et al. (2003a): (a) simplified two-part mechanism; (b) caisson rigid body motions

surface. ξ is a curve fitting factor described in Murff and Hamilton (1993), and s_{u0} and s_{ul} are the soil strengths at the mudline and the caisson base respectively.

The energy dissipation at the end of the caisson, $\dot{D}_e$, is

$$\dot{D}_e = \frac{R_2^3 v_0}{L_0} \int_{\phi=0}^{2\pi} \int_{\omega=0}^{\sin^{-1}\left(\frac{1}{\sqrt{(R_1/R_2)^2+1}}\right)} [s_{u0} + (L_0 + R_2 \sin\omega) s_{u1}] \sqrt{(\sin\omega \sin\phi)^2 + (\cos\omega)^2} \sin\omega \, d\omega d\phi \quad (2.7)$$

where R is the radius of the caisson, $R_1 = L_f - L_0$ (distance from rotation point to caisson base) and $R_2 = \sqrt{R^2 + R_1^2}$ (distance from rotation point to corner of caisson). ω is the angular coordinate from the caisson rotation point in the vertical plane (varying from 0 to $\sin^{-1}(R/R_2)$) and ϕ is the angular coordinate from the caisson centreline in the horizontal plane (varying from 0 to 2π).

For the case of a translational failure mechanism (corresponding to maximum caisson capacity), $L_0 = \infty$, and the term $|1 - z/L_0|$ in Equation 2.6 becomes unity. The dissipation at the end of a caisson failing through translation, $\dot{D}_{et}$, is therefore

$$\dot{D}_{et} = v_0 (s_{u0} + s_{u1} L_f) \frac{\pi D^2}{4} \, . \quad (2.8)$$

The total caisson capacity can be found by equating the external work rate to the internal

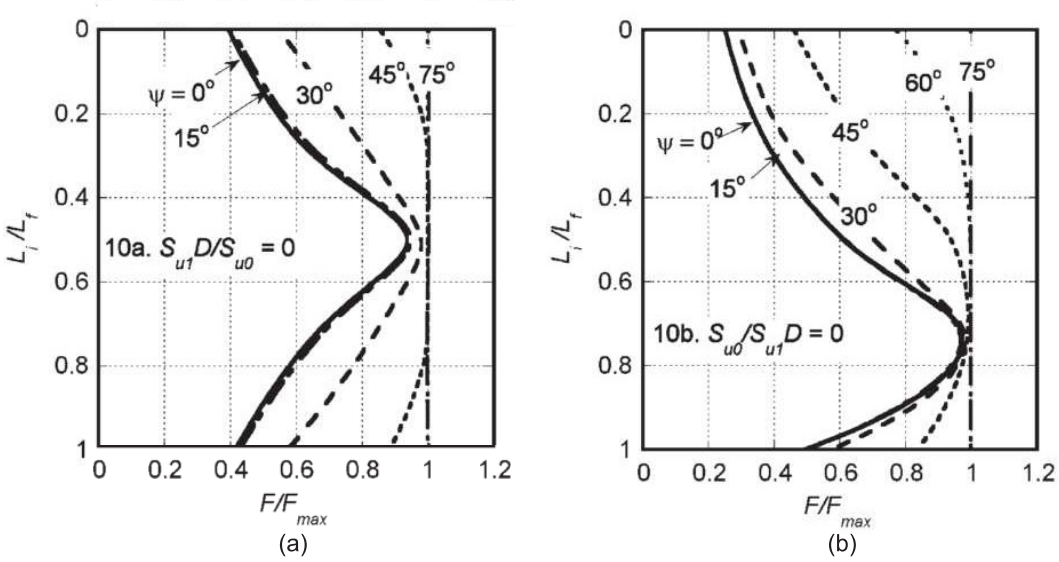

Figure 2.19: Effect of load attachment point on caisson capacity for a range of load inclinations, ψ (Aubeny et al., 2003a): (a) uniform soil; (b) normally consolidated soil

dissipation rate, giving an upper bound capacity, F, where

$$F = \frac{D_s + D_e}{|1 - L_i/L_0|} \,. \tag{2.9}$$

The only parameter needed to describe the mechanism is L_0, which can be varied to find the lowest UB solution for F. This simplified approach was found to compare favourably with capacities obtained using 2D and 3D FEA for caissons with length to diameter aspect ratios in the range 1 – 10 (Aubeny et al., 2001). A parametric study was undertaken to identify the effect of caisson base resistance, tensile gapping behind the caisson, caisson/soil roughness, and load attachment point, on caisson capacity. A further study considered the effects of soil strength anisotropy (Aubeny et al., 2003b). Inclined loading was examined in Aubeny et al. (2003a), and normalised caisson capacities for various load points are shown in Figure 2.19(a) and (b) for uniform and normally consolidated soil respectively. It was found that horizontal load capacity was largely unaffected by vertical load components for load inclinations up to 15° from horizontal.

Caisson capacities obtained using FEA and centrifuge model tests undertaken by Clukey et al. (2004) suggest that the UB PLA approach in Aubeny et al. (2003a) overpredicts holding capacity by up to 9% (Figure 2.20). The PLA model was more accurate under horizontal

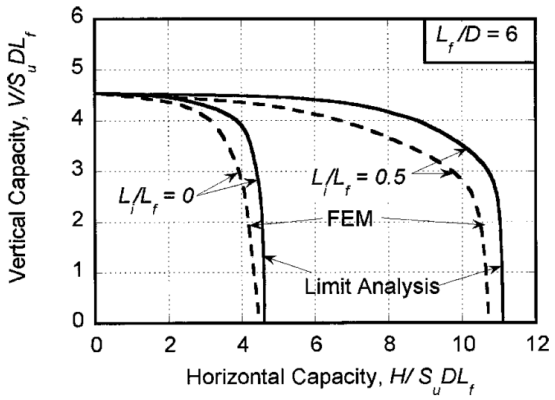

Figure 2.20: A comparison of caisson capacities obtained using FEA and using the limit analysis method described in Aubeny et al. (2003a) (Clukey et al., 2004)

loading (3% error) when compared with inclined loading.

Software for UB capacity analysis of suction anchors, AGSPANC (Advanced Geomechanics, 2001), is described in Randolph and House (2002). The mechanism for a caisson under inclined loading was idealised into three main regions. At shallow depths the mechanism comprises a conical wedge (as suggested by Murff and Hamilton (1993)). Below this, lateral soil flow around the caisson is assumed and at the base of the caisson an internal soil plug shears along a spherical surface centred on the centre of rotation (Figure 2.21). This solution is not a strict UB as there is incompatibility at the upper and lower surfaces of the flow region. Figure 2.21 shows double sided mechanisms but cases where a gap extends to the base of the conical wedge were also considered. Caisson capacities were computed for caisson length to diameter aspect ratios $0.5-4$ and the effects of wall/soil interface roughness and shear strength anisotropy were considered. It was concluded that the non-rigorous AGSPANC capacities were a good match to capacities obtained using FEA, but that further 3D analyses of suction caissons with aspect ratios $4-6$ are needed. It was also concluded that the roughness factor is likely to be $0.5-0.6$ after full consolidation.

The effect of torsional loading on vertical and lateral caisson capacity was considered by Taiebat and Carter (2004, 2005) and Carter and Taiebat (2005). These studies used Fourier series aided FEA to find caisson capacity under vertical, horizontal, and torsional loading. 3D failure envelopes for foundations under combined vertical, horizontal, and torsional loads

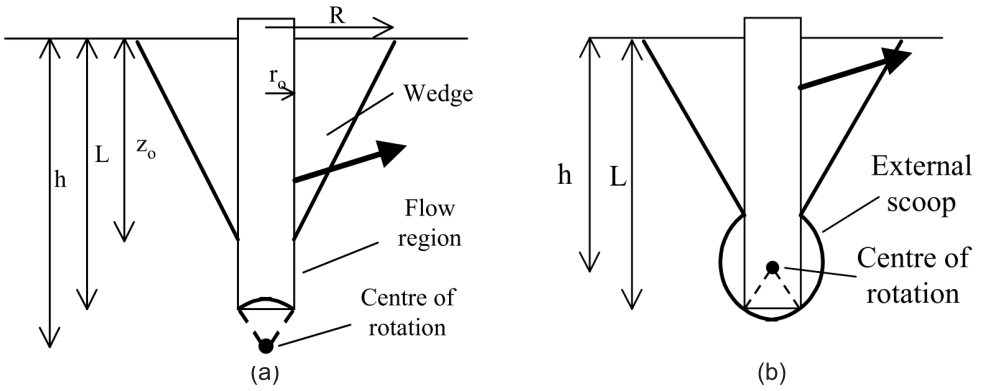

Figure 2.21: Simplified mechanisms from Randolph and House (2002): (a) distinct regions of soil failure mechanism; (b) mechanism with high centre of rotation

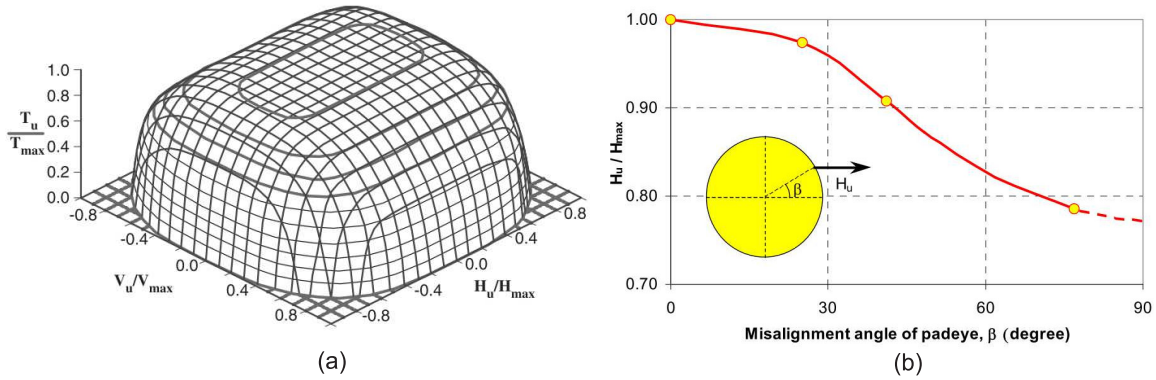

Figure 2.22: Effect of torsional loads on caisson capacity: (a) 3D vertical–horizontal–torsional failure envelope in non-dimensional load space (Carter and Taiebat, 2005); (b) effects of the misalignment of padeye on caisson lateral capacity (Taiebat and Carter, 2004)

were presented (Figure 2.22(a)). It was found that the effects of torsional loads on the lateral capacity of caissons can be ignored if the torsional loads are applied to the caisson at a misalignment angle, β, of 25° or less (Figure 2.22(b)).

An extensive industry-sponsored study on suction anchors for deepwater applications is summarised in Andersen et al. (2005). Detailed reference data for installed caissons were compiled and prediction methods related to installation performance and holding capacity of suction caissons were identified and summarised. For caisson capacity analysis, three general methods were categorised as FEA, LE or PLA methods, and semi-empirical methods. It was found that plane strain LE and plane strain FEA generally agreed well with 3D FEA capacities when 3D effects were accounted for by use of a "side shear factor" calibrated using 3D FEA.

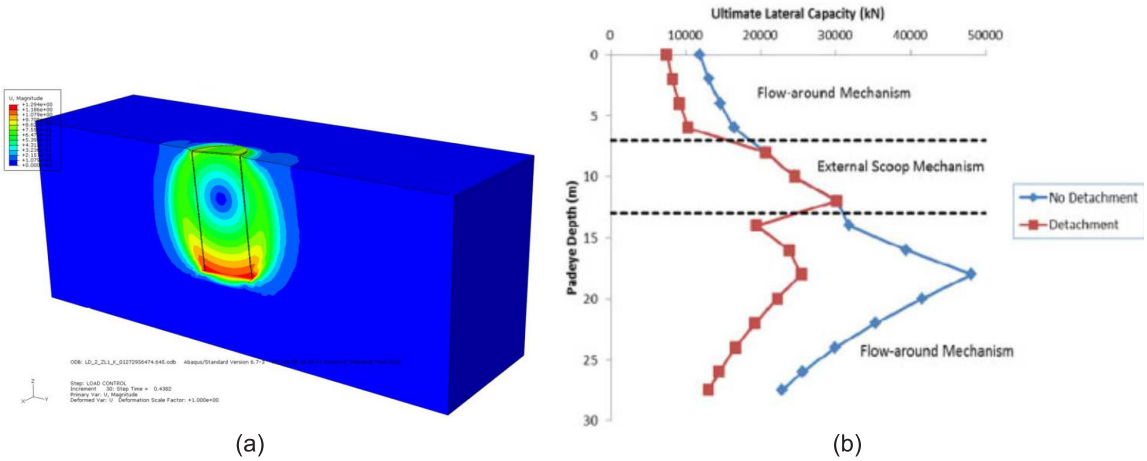

Figure 2.23: LE design software CAISSON: (a) side shear components calibrated using 3D FEA (Kennedy et al., 2013); (b) variation in lateral capacity with load point (padeye depth), length to diameter aspect ratio = 4 (Kennedy et al., 2015)

It was found that LE methods based on mechanisms described in Murff and Hamilton (1993) gave good agreement with 3D FEA capacities for longer caissons, but overestimated capacity for shallow caissons.

The methods used in LE based suction caisson design software, CAISSON, are outlined in Kennedy et al. (2013, 2015). 2D FEA was first used to identify failure mechanisms before LE equations were developed based on these mechanisms. The mechanisms identified included a short caisson mechanism, a translation mechanism, a flow around mechanism, an external scoop mechanism, and a counterclockwise mechanism. A side shear component, calibrated using caisson capacities from 3D FEA (Figure 2.23(a)), was added to the LE equations to account for 3D effects. Identified mechanisms for various load points, along with caisson capacities, are shown in Figure 2.23(b).

Keawsawasvong and Ukritchon (2016) used LB and UB FELA to find vertical pull-out capacities of planar caissons in clay. This was later extended to axisymmetric caissons (Ukritchon and Keawsawasvong, 2016). Soil with a linear increase in strength with depth was modelled, and the caisson was modelled as a rigid plate element with full tension capacity assumed between the caisson and the soil. The focus of the study was on quantifying the effects of caisson/soil interface roughness and caisson length to diameter

aspect ratio on caisson capacity. The results were compared to a conventional method used to find pullout capacity, where the general bearing capacity equation (Equation 2.2) is used with appropriate depth and shape factors to find the base uplift capacity and this is summed with the external wall friction capacity. It was found that the conventional method was unconservative when the length to diameter aspect ratio was less than 1.7. An algebraic expression for reverse end bearing capacity was presented.

Zhang et al. (2010) used 3D UB limit analysis to find the capacity of a caisson with a length to diameter aspect ratio of 1.2, loaded horizontally above the mudline. Capacities were found for an assumed failure mechanism and were compared with capacities obtained in centrifuge model tests. It was found that UB FELA provides a relatively simple basis for finding caisson capacity. However, it was noted that further investigation is needed to identify critical failure mechanisms.

2.6 Hybrid mudmat–pile capacity analysis

Hybrid subsea foundations are a novel type of offshore foundation used to support PLETs and PLEMs. However, piled raft foundations have been used extensively onshore and there has been much research into their design (e.g. Poulos, 1994; Clancy and Randolph, 1996; Poulos, 2001). These studies focus on the vertical stiffness and capacity of a piled raft group. In many of these applications, the piles are slender and can be approximated as one-dimensional spring elements (Clancy and Randolph, 1996).

For piled raft foundations used onshore it has been found that the pile head can provide some restraint, but restraint which falls short of complete fixity (Gerber and Rollins, 2009). The influence of pile head fixity on foundation response under lateral loading was studied by Mokwa and Duncan (2003). Full scale lateral load tests of pile groups in partially saturated sandy clay soil were undertaken. It was found that assuming a fixed head can underestimate the deflection at the pile head, while assuming a free head can result in excessive deflections (Figure 2.24).

An analytical model for estimating the capacity of offshore hybrid mudmat–pile

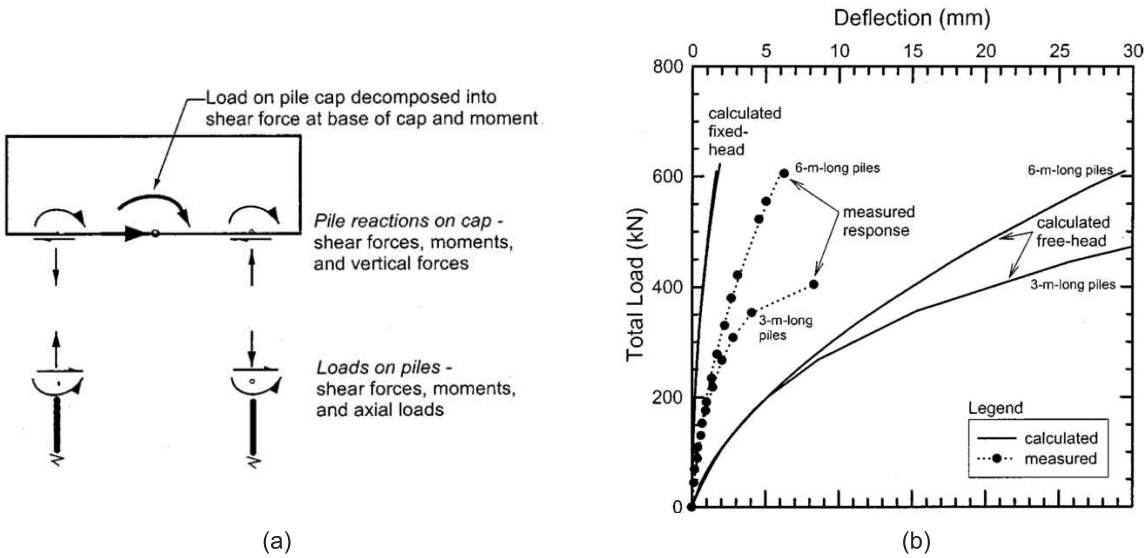

Figure 2.24: Load–displacement response of a laterally loaded pile group (Mokwa and Duncan, 2003): (a) forces and moments induced by lateral loading; (b) load–displacement response of a four-pile group

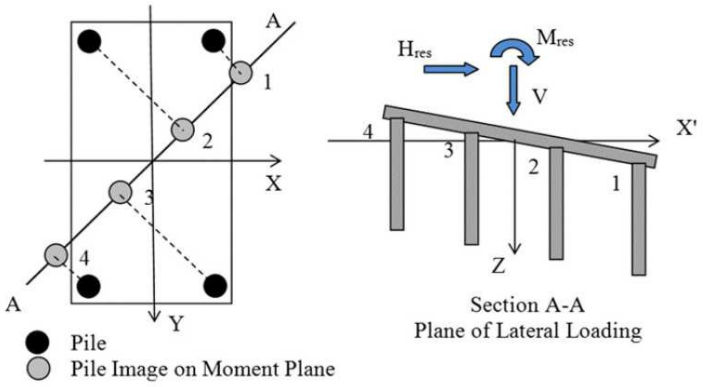

Figure 2.25: Hybrid foundation moment resistance model from Dimmock et al. (2013)

foundations under combined loading was developed by Dimmock et al. (2013). This study considered the mudmat/pile connection as providing no rotational restraint at the pile head. A design guideline was outlined where the interaction of loads between the mudmat and the pile was somewhat simplified, depending on the loading condition. It was assumed that the mudmat alone resists vertical loads, the piles alone resist horizontal and torsional loads, and overturning moments are resisted by both the mudmat and piles. Pile capacity under horizontal loading was calculated according to the Murff and Hamilton (1993) method, extended by Aubeny et al. (2003a), as described in Section 2.5. Under torsional loading capacity was estimated by summing, for each pile, the lateral resistance times the distance to the rotation centre. Overturning moment capacity was found by summing the moment capacity of the mudmat, augmented by the axial 'push pull' capacity of the piles (both calculated using the design code API (2000)) times the distance to the rotation centre. A schematic of the pile moment resistance model is shown in Figure 2.25. Tension capacity at the base of the mudmat is conservatively neglected. The vertical capacity, which considers the mudmat only, was obtained using the solution presented in Davis and Booker (1973) for soils with increasing strength with depth, along with appropriate shape and depth factors found using API (2011). The design method proposed gives a conservative 'lower bound' estimation of capacity when compared with 3D FEA also undertaken. The foundation geometry and soil strength profile used by Dimmock et al. (2013) were representative of current designs in the Gulf of Mexico.

The effect of pile head restraint on the response of hybrid mudmat–pile foundations used offshore was considered by Won et al. (2015). A specific hybrid foundation design used for the Julia Field development project in the Gulf of Mexico was presented (Figure 2.26(a)). It was found that pile head fixity can strongly influence the lateral response of hybrid foundations (Figure 2.26(b)). It was concluded that employing a pile head locking system to allow full transfer of moment loads from the mudmat to the piles can significantly improve the vertical and moment capacity of hybrid foundations. Also, the pile dimensions can be governed by the vertical capacity requirements of the foundation.

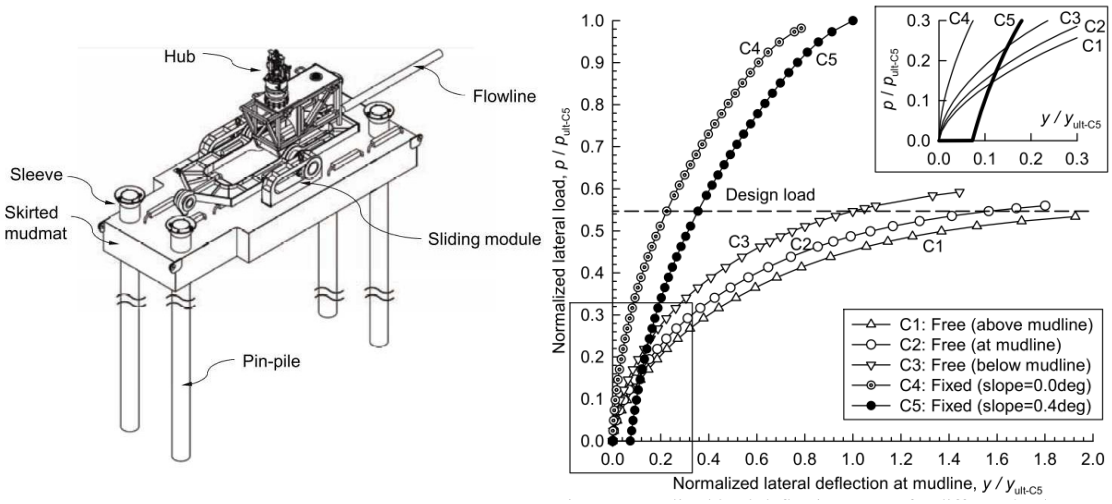

(a) (b)

Figure 2.26: Study into the effect of pile head restraint on foundation response (Won et al., 2015); (a) schematic drawing of the Julia Field hybrid foundation; (b) normalised load–displacement curves for foundations under lateral loading

Hossain et al. (2015a,b) considered the pile head both as fully fixed and as a sliding connection (no restraint in the vertical direction) in FEA of the Julia Field hybrid foundation. The authors noted that fully fixed and sliding connections have been used in actual hybrid foundation design. A fixed connection is achieved by using a "pile to mudmat locking mechanism" which enforces load sharing between the mudmat and the piles. This study considered the effect of pile length on foundation capacity. A linear elastic material was used to model slender piles, with length to diameter aspect ratios in the range 14 – 30. The study offered insight into the specific design case considered, while recognising the requirement for additional research into general hybrid foundation behaviour.

2.7 Summary

In the past, 3D FELA has been used to solve slope stability and vertical bearing capacity problems, but analyses considering complex loading of foundations (which may require a large number of elements) have not been undertaken.

Until recently, there has been little consideration of the effect of perforations on the capacity of shallow foundations. A design formula proposed by Tapper et al. (2015) has not

been verified for embedded foundations with perforation ratios exceeding 0.36.

Generally speaking, previous research focusing on mudmat capacity under combined horizontal and torsional loading has not considered the additional effect of biaxial overturning moments. Research on combined six degree-of-freedom loading has not been performed with a focus on practically relevant levels of torsion and overturning moment. There has been little interpretation of failure mechanisms for foundations under complex loading (e.g. combined horizontal, torsional, and moment loading).

There have been several capacity studies of foundations located on flat ground at or near the crest of a slope, but there has not been any corresponding work for the case of a foundation located on the slope itself, with inclined ground extending in both directions.

UB limit analysis methods are commonly used in the analysis of suction anchors. To use these methods, a failure mechanism is first assumed. 3D FEA has been used to identify caisson failure mechanisms, however, one disadvantage of the use of FEA is the lack of a direct error measure associated with the solution. This makes it difficult to determine if the critical failure mechanism has been identified. Another common design method is to use plane strain analysis coupled with a suitable correction factor applied to the calculated capacity. The suitability of this approach is still uncertain. Bounded 3D FELA capacities have not previously been obtained for caissons used as suction anchors.

In the literature, a simplified analysis approach has been recommended for the design of hybrid mudmat–pile foundations. Studies have shown that pile length and the fixity of the mudmat/pile connection can have a significant effect on mudmat capacity. These studies have considered specific design cases. A parametric study which considers various idealised soil strength profiles, foundation geometries, and mudmat/pile connections has not been undertaken.

Chapter 3

Methodology

3.1 Introduction

This chapter describes the numerical methods used in this thesis. In the first section, features of the FELA software OxLim are described and its implementation in this thesis is detailed. Displacement FEA using the commercial software Abaqus (2014) is also described, including a user subroutine capable of modelling undrained foundation/soil interfaces. The differences between FEA and FELA are highlighted.

The subsequent sections verify the OxLim FELA and Abaqus FEA implementations used as part of this research. Three verification exercises are undertaken:

- Strip footings under vertical loading are modelled using 3D FEA and using two FELA meshes. The capacities obtained are compared with known exact solutions.
- Polygonal approximations of circular piles are modelled using plane strain and 3D FELA. Lateral pile capacities are compared with UB capacities available in the literature.
- Uniaxial and combined vertical, horizontal, and moment capacities of circular surface footings are found using FELA and FEA. Capacities and failure mechanisms are compared with results available in the literature.

3.2 OxLim FELA software

Plane strain and 3D limit analysis is undertaken using the software OxLim. This program has been developed at the University of Oxford since 2009. It has previously been used extensively for the analysis of plane strain problems (e.g. Martin, 2011; Martin and White, 2012; Mana et al., 2013; Dunne et al., 2015) and recently for 3D problems (e.g. Martin et al., 2015; Dunne and Martin, 2017b,a; Dunne et al., 2017). While the steps involved in undertaking plane strain and 3D OxLim analyses are similar, there are differences in how these steps are implemented. For both analysis types:

1. Open source code is used to generate a mesh.
2. The LB and UB variables and constraints (Section 2.2.1) are arranged as separate optimisation problems.
3. MOSEK optimisation software is called to perform the optimisations.
4. UB element dissipation rates are used to determine target element sizes for a refined mesh.
5. Steps $1-4$ are repeated until a predefined condition is met.

OxLim models foundations as rigid bodies, and loading is applied to a foundation according to the sign conventions shown in Figure 3.1. Undrained clay is modelled as a rigid–plastic von Mises material.

The best estimate OxLim solution (the load factor) is taken as the average of the lower and upper bounds,

$$\mathrm{LF} = \frac{\mathrm{LB} + \mathrm{UB}}{2} \tag{3.1}$$

and the associated bracketing error is quantified as

$$\mathrm{ERROR}\ \% = \frac{\mathrm{UB} - \mathrm{LB}}{\mathrm{UB} + \mathrm{LB}} \times 100 \tag{3.2}$$

OxLim uses adaptive mesh refinement (if required) to improve the bracketing of the exact collapse load multiplier. The adaptivity strategy used is based on the spatial variation of the

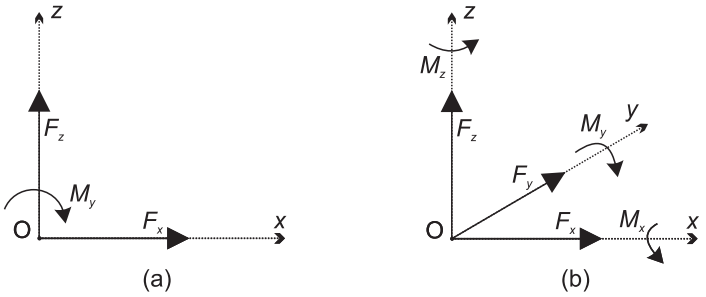

Figure 3.1: Sign conventions for loads applied to foundation: (a) 2D; (b) 3D

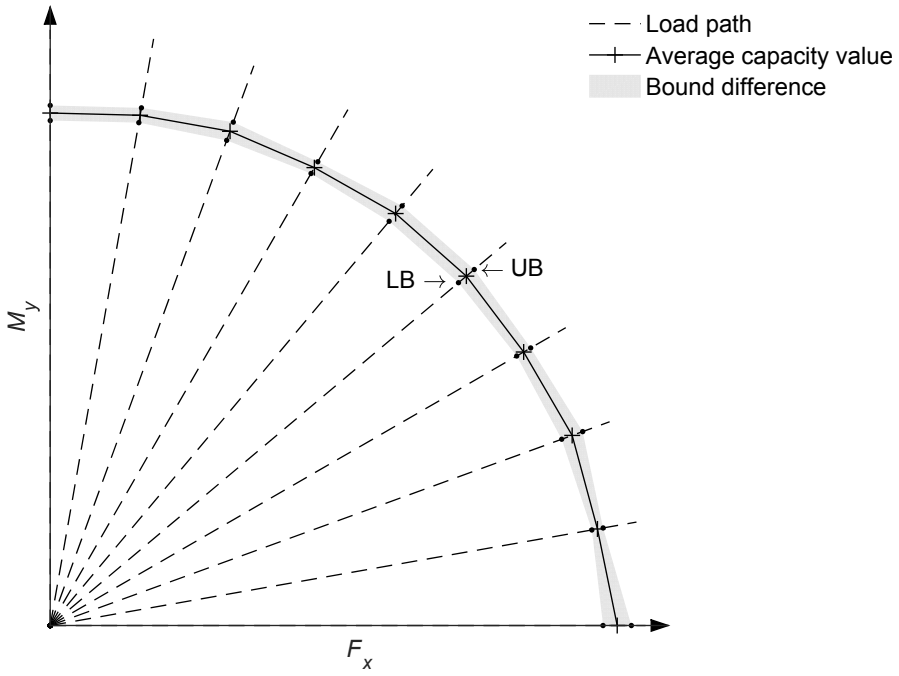

Figure 3.2: Quadrant of a failure envelope found using FELA load-controlled probes

maximum shear strain rate in the UB velocity field. This results in an output mesh refined along mechanism slip-lines, aiding visualisation of the failure mechanism. This strategy has been used in several previous studies of plane strain problems (e.g. Martin, 2011; Martin and White, 2012; Mana et al., 2013), and a similar technique has been implemented for 3D analysis (Martin et al., 2015; Dunne and Martin, 2017a,b; Dunne et al., 2017).

Failure envelopes for foundations under combined loading are found using OxLim by probing outwards in load space. A series of combined loading ratios are applied to the foundation and load factors are determined for each probe to make up the full failure envelope. Figure 3.2 shows a quadrant of a failure envelope found using 10 load-controlled probes. Once a loading ratio is defined, the load path travels directly from the origin in the

direction of the load until the failure envelope is reached. The bracketing range associated with the failure envelope is shown as the shaded band in Figure 3.2.

A script written in the general-purpose programming language Python (2016) facilitates OxLim analyses by generating the required input files and processing the output files. The implementation of plane strain and 3D analyses is outlined schematically in Figure 3.3, which should be consulted for Sections 3.2.1 – 3.2.2.

3.2.1 Plane strain analysis

A script is not required for a plane strain OxLim analysis, but it can be useful in reducing the time between multiple analyses by allowing batches of analyses to be undertaken consecutively. Input parameters required by OxLim include the dimensions of the problem domain, boundary and interface conditions, dead and live traction loading, soil properties (e.g. strength, dead and live unit weight), the target bracketing error, and the maximum number of elements. These parameters are input to the script which creates an OxLim input file (or multiple files for a batch analysis). The script then calls OxLim to undertake the analysis.

OxLim uses the open-source mesh generation code Triangle (Shewchuk, 1996) to generate an unstructured mesh of triangles. OxLim arranges the limit analysis constraints in SOCP form before calling the optimisation solver MOSEK to find the optimal LB and UB. The LB and UB are solved for in parallel, speeding up analysis time (typical analysis times to $\pm 1\%$ error are in the range 10 – 45 s). If the bracketing error obtained with the initial mesh is larger than that required, OxLim provides Triangle with target element areas for a refined mesh. The process of problem analysis and mesh refinement is repeated until the target bracketing error is reached or until a predefined maximum number of elements is exceeded. The maximum number of elements prevents excessively long analysis times if the bounds do not converge to the required level of accuracy for a reasonably sized mesh. In this work the maximum number of elements was set at 20 000, although in all cases the target bracketing error (in all cases at most $\pm 1\%$) was achieved before this number of elements was exceeded.

The control script generates a summary file at the end of each analysis, which is

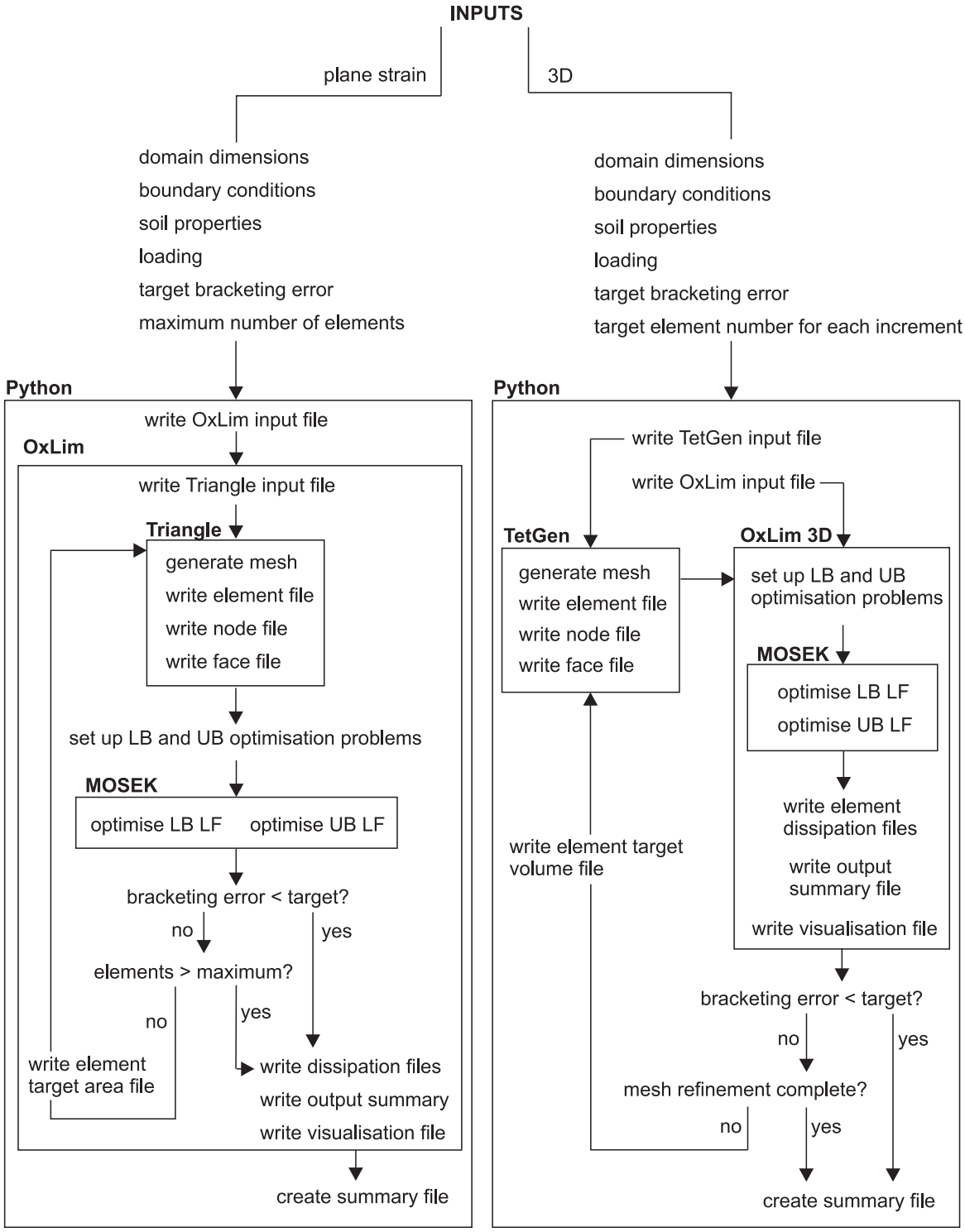

Figure 3.3: Flow chart describing the steps involved in plane strain and 3D OxLim analyses

particularly useful for batch analyses. OxLim outputs LB stress field and UB velocity field data which can be visualised using the post-processing code GiD (CIMNE, 2006).

3.2.2 Three-dimensional analysis

Unlike for plane strain analyses, for 3D analyses the number of mesh refinement iterations and the approximate number of elements in each iteration are predefined in the control script (see Figure 3.3). The control script is more intrinsic to 3D analysis as the 3D OxLim code does not conduct mesh generation or refinement. The decision to remove the task of mesh generation from 3D OxLim was made deliberately (C.M. Martin, personal communication, 2017). While finesse is not needed for plane strain mesh generation (a brute force unstructured mesh refinement approach proves to be adequate), for 3D analysis run times are far higher (analysis time for a 40 000 element mesh is $\sim$600 s). The script can readily be altered, giving the user flexibility to customise the mesh refinement strategy for specific problems. For a similar reason, a wholly unstructured initial mesh is not always used for a 3D OxLim analysis. It has been found that if certain prescribed facets are added to an otherwise unstructured mesh, then the bounds converge more rapidly when compared with a completely unstructured mesh. This is described in more detail in Section 3.5.1.

The control script is used to generate OxLim input mesh generation files. In this thesis, all 3D mesh generation is performed using the open-source code TetGen (Si, 2013). The mesh input file contains the coordinates of vertices, and their connectivity to make facets, which define the problem domain. Boundary labels are assigned to facets and region labels are assigned to volumes enclosed within facets. Attributes are assigned to these labels in the OxLim input file. For example, boundary labels can be specified as rigid bodies (with interface strength properties), free/fixed surfaces, or planes of symmetry/antisymmetry. Material properties are assigned to region labels. Just as for plane strain analysis, OxLim sets up the optimisation problem, and calls MOSEK to find the optimal LB and UB solutions. OxLim outputs an element dissipation file, and a summary of the current analysis.

If the bracketing error is lower than that required, then a summary file is generated by the script. If the error is higher than required, then the script checks if the analysis has completed

all of the predefined mesh refinement cycles. If it has not then a mesh refinement function generates a TetGen input file. The process of analysis and mesh refinement is repeated until either the target bracketing error has been reached, or the predefined sequence of mesh refinement iterations has been exhausted. OxLim outputs UB velocity field data which can be visualised using the open-source code ParaView (Ayachit, 2015).

3.2.2.1 Mesh refinement

The 3D mesh refinement process used in this study generally follows that used for OxLim plane strain analyses (e.g. Martin (2011)). However, 3D mesh refinement is undertaken through the control script and the mesh refinement process is subsequently described.

At the end of a solution iteration (for a mesh comprising n elements), for each element, i, 3D OxLim outputs the element volume, V_i, and the element dissipation, D_i:

$$D_i = \bar{\varepsilon}^p V_i \tag{3.3}$$

where $\bar{\varepsilon}^p$ is the von Mises equivalent plastic strain rate, $\bar{\varepsilon}^p = \sqrt{\frac{2}{3}\varepsilon^p_{ij} \cdot \varepsilon^p_{ij}}$). The target number of elements for a refined mesh, n_{ref}, is input from the control script at the start of each solution iteration (Figure 3.3). The average element dissipation across a mesh is $\bar{D}$. Target element volumes for the new mesh are generated by comparing the dissipation in each element of the old mesh to the average dissipation across all elements of the old mesh:

$$V_{\text{new}_i} = V_i \times \frac{\bar{D}}{D_i} \times \beta_j \tag{3.4}$$

where β is a scaling factor initially set to $\beta_j = 1$. Excessive refinement is prevented by imposing a limit on the refinement ratio such that $\bar{D}/D_i \geq 0.1$.

TetGen generates a refined mesh accounting for the target element volumes found using Equation 3.4. This mesh is deemed acceptable if the number of elements in the mesh, n_{trial}, is within $\pm 5\%$ of the target number of elements, n_{ref}. Otherwise, β is updated, such that

$$\beta_{j+1} = \beta_j \times \frac{n_{\text{trial}}}{n_{\text{ref}}} \tag{3.5}$$

and new target volumes are found using Equation 3.4. A trial-and-error process of mesh generation is followed until the mesh generated contains the required number of elements, to within the allowable range of $\pm 5\%$.

A coarse mesh is analysed initially, but after several iterations of adaptivity the concentration of elements in the refined mesh reflects the intensity of $\bar{\varepsilon}^p$. This can aid identification of the failure mechanism, as plastically yielding regions in the soil can be identified as regions of dense refinement.

3.2.3 Contact modelling

Foundation/soil interface properties are specified in the OxLim input file. Limiting values of shear stress, αs_u, and tensile stress in the normal direction, T, can be enforced on an interface. An interesting consequence of enforcing a tension cutoff with associated flow is that when $\alpha > 0$, non-zero shear stresses may continue to act even when separation is occurring at the foundation/soil interface (Houlsby and Puzrin, 1999). These so-called 'phantom' shear stresses were encountered by Martin and White (2012) when analysing the bearing capacity of offshore pipelines.

Rigid bodies can be connected in OxLim 3D by specifying relative translational and rotational degrees of freedom as free or fixed. This feature is only available for UB analysis and is only used to model connections between piles and mudmats in Chapter 6. Where multiple rigid bodies are defined, OxLim outputs the resultant forces acting on each rigid body. This allows for the contributions of constituent foundation parts to the total foundation capacity to be easily identified.

3.3 Displacement FEA using Abaqus software

As discussed in Chapter 2, elastic–plastic FEA is used extensively for the analysis of offshore foundations. In this thesis, FEA is undertaken using the commercial software Abaqus (version 6.14–1). In keeping with previous studies (e.g. Gourvenec, 2008; Feng et al., 2014; Nouri et al., 2014; Vulpe, 2015), undrained clay is modelled as a linearly elastic–perfectly plastic material. Poisson's ratio, ν_u, is set to 0.49 in order to approximate the elastic incompressibility of soil in undrained conditions without encountering the numerical difficulties associated with $\nu_u = 0.5$. Young's modulus, E_u, is set to a relatively high value ($E_u = 1000 s_u$) to ensure that

negligible strains and displacements occur before plastic failure (E_u/s_u values of 500, 1000, and 2000 are considered in Section 3.5.1). A von Mises failure criterion is adopted.

For 3D analysis a structured mesh of fully integrated, hybrid, eight-noded brick elements are used to model the soil (Abaqus element type C3D8H). Hybrid elements are recommended for modelling (near) incompressible materials (such as undrained clay). Foundations are modelled as rigid surfaces with associated reference nodes that can be assigned displacements and queried for reactions. Manual mesh refinement is undertaken until foundation capacity is unaffected by further refinement.

Failure envelopes for combined loading are found by probing in displacement space. Displacement-controlled probes are more popular than load-controlled probes for FEA because of their good convergence properties. When an FEA load probe reaches the failure envelope, the analysis will fail to converge as the perfectly plastic soil is unable to support additional load. As such, it must be ensured that very small load increments are used in order to accurately find the point on the failure envelope. When displacements are applied to a foundation, the soil initially responds elastically before reaching plastic yielding. In all analyses with displacement probes it was ensured that the prescribed displacements were sufficiently large to create a state of fully developed soil failure. The final load state at the end of a displacement-controlled probe is located on the failure envelope at a point where the direction of the displacement probe is normal to the failure envelope.

A number of displacement-controlled probes can be used to define a failure envelope (Figure 3.4). A disadvantage to using displacement controlled probes is that the resulting load path cannot be specified, and is hard to predict. This is particularly apparent when comparing Figure 3.2 with Figure 3.4. However, FEA is very popular for the analysis of offshore foundations and displacement-controlled probes are the most common method for determining failure envelopes (e.g. Bransby and Randolph, 1999; Gourvenec and Barnett, 2011; Feng et al., 2014).

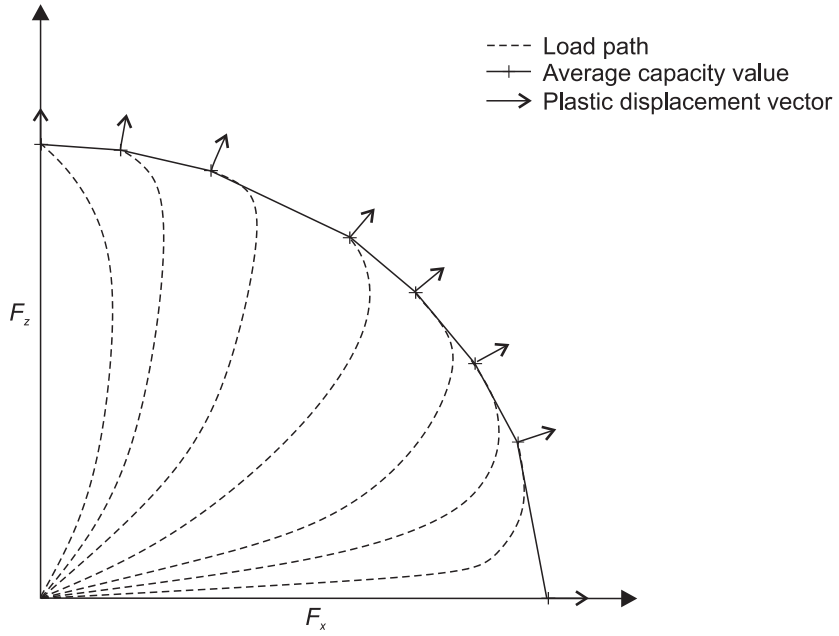

Figure 3.4: Quadrant of a failure envelope found using FEA displacement controlled probes

3.3.1 Contact modelling

There are various methods for approximating foundation/soil interface conditions in FEA simulations. A rough foundation ($\alpha = 1$) with unlimited tension capacity ($T = \infty$) is often modelled by tying the foundation to the adjacent soil (e.g. Gourvenec and Barnett, 2011; Feng et al., 2014). A smooth ($\alpha = 0$) or partially rough ($\alpha < 1$) foundation/soil interface with $T = \infty$ can be approximated by assigning soil strength αs_u to a thin layer of elements next to the interface (e.g. Kay and Palix, 2010, 2011). These techniques can lead to overestimation of foundation capacity because the failure mechanism is forced into the soil domain if the critical failure mechanism involves shearing at the interface.

A Coulomb friction model is available in the standard Abaqus library. Coulomb friction relates contact pressure to the maximum allowable shear stress, τ_{max}, such that

$$\tau_{max} = \mu p \tag{3.6}$$

where μ is the coefficient of friction and p is the contact pressure. A limiting, critical shear stress, τ_{crit}, can also be set. If $\tau_{crit} = \alpha s_u$ and μ is set to a high value, this model can be used to approximate an αs_u interface with $T = 0$ (Figure 3.5). This approach was found to work well in a recent study of the capacity of strip footings under planar loading (Shen et al.,

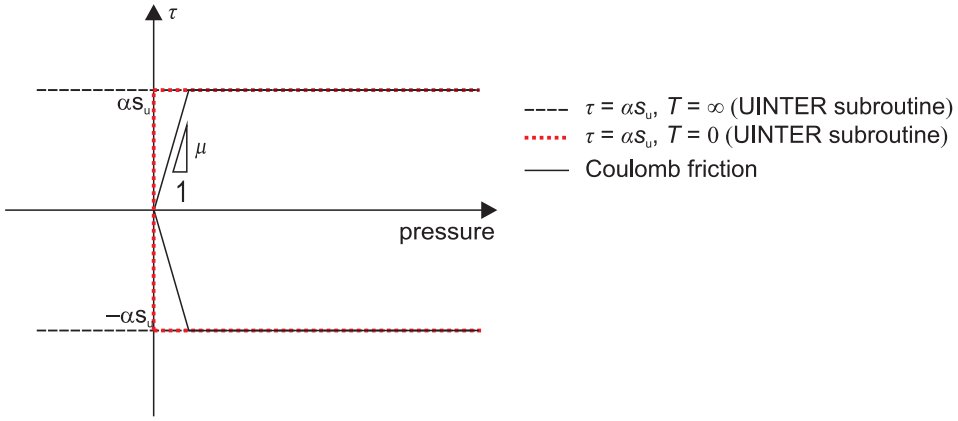

Figure 3.5: Coulomb friction model with critical shear stress, $\tau_{\text{crit}} = \alpha s_{\text{u}}$ and UINTER user defined interface with $\tau = \alpha s_{\text{u}}$ and unlimited tension capacity $T = \infty$ or tension cutoff $T = 0$

2016). However Figure 3.5 shows that this contact method does not match the theoretically correct αs_{u} interface at low contact pressures. It is also not possible to model an interface with unlimited tension capacity, $T = \infty$.

A foundation/soil interface with shear strength αs_{u} and tensile capacity $T = 0$ or ∞ can be implemented in Abaqus by supplying the interface constitutive behaviour in a user subroutine, UINTER. UINTER is written in the FORTRAN language and can interface with the Abaqus model. A UINTER subroutine for a plane strain zero-tension interface is presented in Shen et al. (2016). A UINTER subroutine has also been written as part of this research. It models the αs_{u} and $T = 0$ or ∞ interfaces shown in Figure 3.5. To use the subroutine the user must specify four interface parameters in the Abaqus input file;

- the soil normal stiffness, k_{n},
- the soil shear stiffness, k_{s},
- the interface shear strength, αs_{u}, and
- a 'switch', t, identifying if $T = 0$ or $T = \infty$ is required.

The increments in relative positions between the two surfaces are retrieved from Abaqus. With this information the interface stiffness matrix and the stress vector can be defined, and these values returned to Abaqus. The subroutine is described in further detail in Appendix A.

3.4 Differences between the FELA and FEA models

The FEA parameters selected for this study result in a model that closely resembles the FELA model. However, there are still differences between the models and the most noteworthy of these are:

- The soil model. A rigid–plastic soil model is implemented in FELA and elastic–plastic in FEA. In FELA the soil is incompressible while in FEA it is near incompressible.
- The mesh. An unstructured mesh that undergoes automated refinement over successive iterations of the solution is implemented in the FELA model. A regular mesh is manually refined in the FEA model.
- The application of loads. Loads are applied directly to foundations in the FELA model while displacements are applied to foundations in the FEA model (the load state is obtained at the end of the displacement step).
- The analysis timestep. There is no time step in FELA (and there is no stress history) while the governing equations of FEA are solved at a number of time step increments.

3.5 Verification of 3D OxLim

3D OxLim has been verified by analysing three separate problems with known solutions or benchmark solutions available in the literature; vertical capacity of a strip footing, lateral capacity of a pile section, and capacity of a circular surface footing under general loading.

3.5.1 Strip footing

The vertical capacity of a rigid surface strip footing on uniform cohesive soil is an exact plasticity solution ($2+\pi$, Prandtl (1920)). A section of strip footing with breadth, B, and arbitrary thickness, also chosen as B, was modelled using 3D FELA (two different initial meshes considered) and FEA, and is shown in Figure 3.6(a). Symmetry boundary conditions were applied on the plane $x = 0$, $y = 0$, and $y = B$, the sides of the soil block at $z = -2.5B$

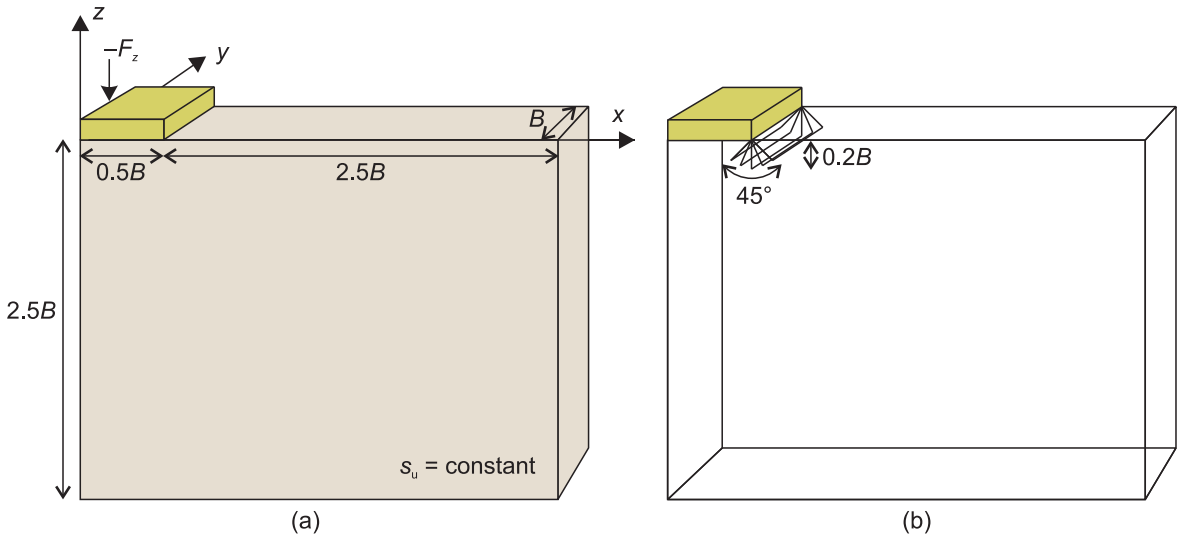

Figure 3.6: Strip footing under vertical loading: (a) notation and sign conventions; (b) singularity facets added to FELA model

and $x = 3B$ were modelled as rigid boundaries, and a free surface was modelled adjacent to the footing. The footing was constrained against all movement other than vertical translation. The footing/soil interface was modelled as either fully rough ($\alpha = 1$) or fully smooth ($\alpha = 0$). The soil was weightless ($\gamma' = 0$) and had constant undrained shear strength ($s_u = \text{constant}$).

FELA: A downwards unit vertical live load was applied to the footing. An initial wholly unstructured mesh (termed U mesh) comprising ~50 tetrahedral elements was generated and automated adaptive mesh refinement was used to refine the mesh to ~10 000, ~20 000, and ~40 000 elements on successive iterations of the solution. Separately, an initial mesh was generated which contained a fan of five prescribed 'singularity planes' stemming from the footing edge (termed SP mesh). Prescribed facets are shown in Figure 3.6(b)). This initial mesh comprised ~550 elements and, again, automated mesh refinement was used to refine the mesh to ~10 000, ~20 000, and ~40 000 elements over successive solution iterations.

FEA: A downwards vertical displacement was imposed on the footing. The initial coarse, regular mesh comprised ~500 elements and three stages of mesh refinement were manually undertaken (to refine the mesh to ~10 000, ~20 000, and ~40 000 elements). The reaction force from the soil was checked to have reached a steady state at the end of the displacement

history of the foundation. The elastic stiffness of the soil was varied in order to quantify any effect on the foundation capacity. E/s_u values of 500, 1000, and 2000 were considered. The foundation/soil interface was modelled using the UINTER subroutine described in Section 3.3.1.

3.5.1.1 Results

Capacities obtained for each mesh discretisation of the FEA and FELA analyses are shown in Figure 3.7(a) and (b) for rough and smooth footings respectively. E/s_u values of 500, 1000, and 2000 used in the FEA model were found to have no effect on foundation capacity.

It is clear from Figure 3.7 that the FELA bracketing error reduces as the number of elements increases. The Prandtl (1920) failure mechanism for a rough footing is shown in Figure 3.8(a). Figure 3.8(b)–(e) shows the FELA SP mesh after each iteration of mesh refinement. The mesh refinement strategy is evidently working; the mesh is refining in areas where high shear strain rates are expected. The FELA SP mesh analyses achieve lower bracketing errors than the FELA U mesh analyses, particularly for the smooth footing. The analysis time is mostly dependent on the number of elements in the mesh, which makes the SP mesh advantageous when compared to the U mesh due to its greater accuracy. Tighter FELA bounds are achieved for the smooth footing when compared with the rough footing, with 1.9% and 2.6% bracketing errors respectively (for the SP mesh).

Table 3.1 compares capacities obtained using FELA (SP mesh) and FEA. FELA average capacities are close to the exact solution, even with coarse mesh discretisations. In contrast, the capacities obtained using coarse FEA meshes (6.30 and $6.36B^2 s_u$ for rough and smooth footings respectively) considerably overestimate the theoretical capacity ($5.14B^2 s_u$). As mesh refinement is undertaken the FEA capacities reduce. The difference between capacities obtained using FELA (SP mesh) and FEA models with 40 000 elements is small ($< 1\%$) for both rough and smooth footings. FELA and FEA failure mechanisms for rough footings are shown in Figure 3.9(a) and (b) respectively. The mechanisms compare favourably with the Prandtl failure mechanism (shown in Figure 3.8(a)).

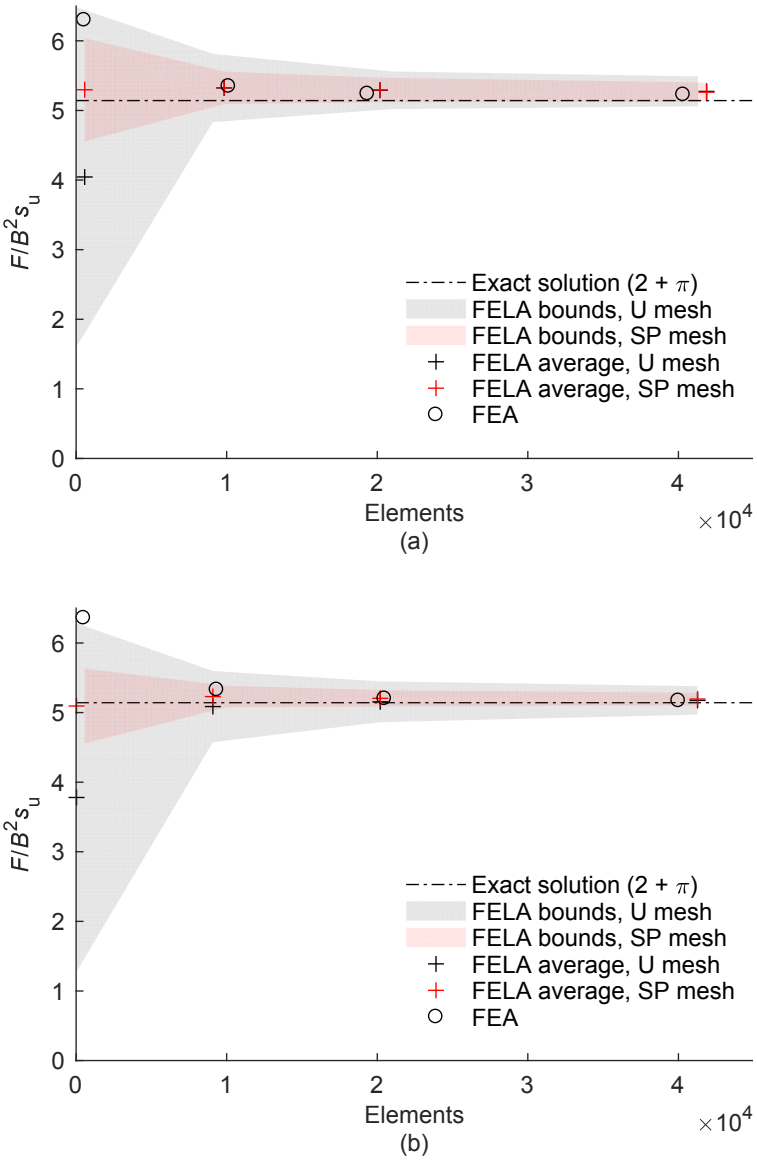

Figure 3.7: Vertical capacities of surface strip footings on uniform soil modelled in 3D FELA and FEA; (a) rough footing ($\alpha = 1$); (b) smooth footing ($\alpha = 0$)

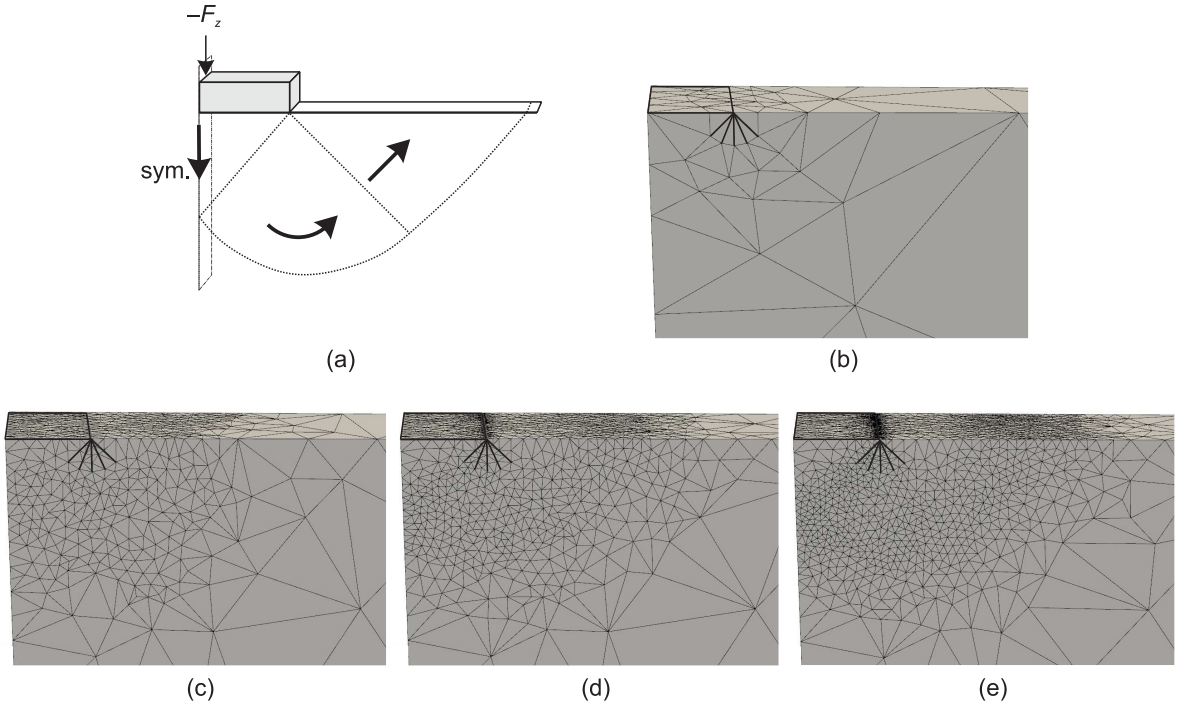

Figure 3.8: FELA SP mesh refinement, rough footing ($\alpha = 1$): (a) Prandtl (1920) failure mechanism; (b) ∼550 elements; (c) ∼10 000 elements; (d) ∼20 000 elements; (e) ∼40 000 elements

The FELA LB performs very well and LB capacities for a mesh comprising 10 000 elements are only marginally lower than the exact solution (Figure 3.7). The relatively inaccurate UB solution leaves an average capacity value that is marginally higher than the theoretical value for both interface conditions.

3.5.2 Pile section

The plastic capacity of a rough circular pile section of diameter, D, translating laterally in cohesive soil was found by Randolph and Houlsby (1984) using the method of characteristics. The UB solution presented by Randolph and Houlsby for a pile with $\alpha < 1$ was originally believed to be exact, but was subsequently improved by Martin and Randolph (2006). This problem was modelled using plane strain FELA and using 3D FELA, where an arbitrary thickness of the pile, chosen as D, was modelled. A curved pile wall is approximated in OxLim as a series of planar facets. As an additional verification exercise, the number of facets required to accurately represent a circular pile section was calibrated against

Table 3.1: Comparison of 3D FELA (SP mesh) and FEA solutions for a vertically loaded surface strip footing on uniform soil

	Elements (approx.)	FELA LB ($B^2 s_u$)	FELA UB ($B^2 s_u$)	Error ($\pm\%$)	FELA average ($B^2 s_u$)	FEA ($B^2 s_u$)
$\alpha = 1$	550	4.59	6.01	14.0	5.30	6.30
	10 000	5.09	5.57	4.4	5.33	5.35
	20 000	5.11	5.47	3.4	5.29	5.24
	40 000	5.12	5.40	2.6	5.26	5.23
$\alpha = 0$	550	4.55	5.62	10.6	5.09	6.36
	10 000	5.39	5.07	3.0	5.23	5.32
	20 000	5.09	5.31	2.2	5.20	5.20
	40 000	5.10	5.29	1.9	5.20	5.17

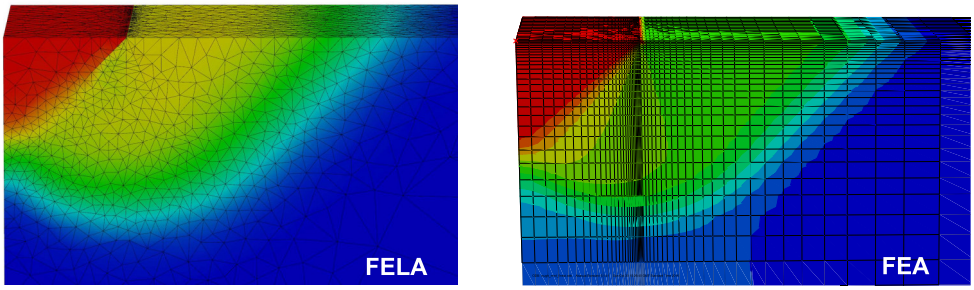

(a) (b)

Figure 3.9: Failure mechanisms of a rough ($\alpha = 1$) surface strip footing: (a) FELA refined mesh (~40 000 elements). Shaded by UB velocity magnitude; (b) FEA final mesh (~40 000 elements). Shaded by displacement magnitude

the Randolph and Houlsby (1984) and Martin and Randolph (2006) plasticity solutions.

The pile cross sections were modelled as regular N-sided polygons that inscribe the 'true' circular pile. The number of facets was varied from $N = 4$ (a square pile) to $N = 240$ and the facets were oriented such that the pile is loaded 'point on' rather than 'flat on' (Figure 3.10(a)). For plane strain analysis, planes of symmetry along $x = 0$ and antisymmetry along $z = 0$ were exploited and for 3D analysis planes of symmetry along $y = 0$ and $y = D$ were also exploited (Figure 3.10(b)). Automated adaptive mesh refinement was undertaken in the plane strain analysis until the bracketing error was $\leq 1\%$. In the 3D analysis, three iterations of mesh refinement were undertaken and the final mesh comprised ~40 000 elements. Three pile/soil roughness factors were considered: $\alpha = 0$, 0.5, and 1. An unlimited tension interface was

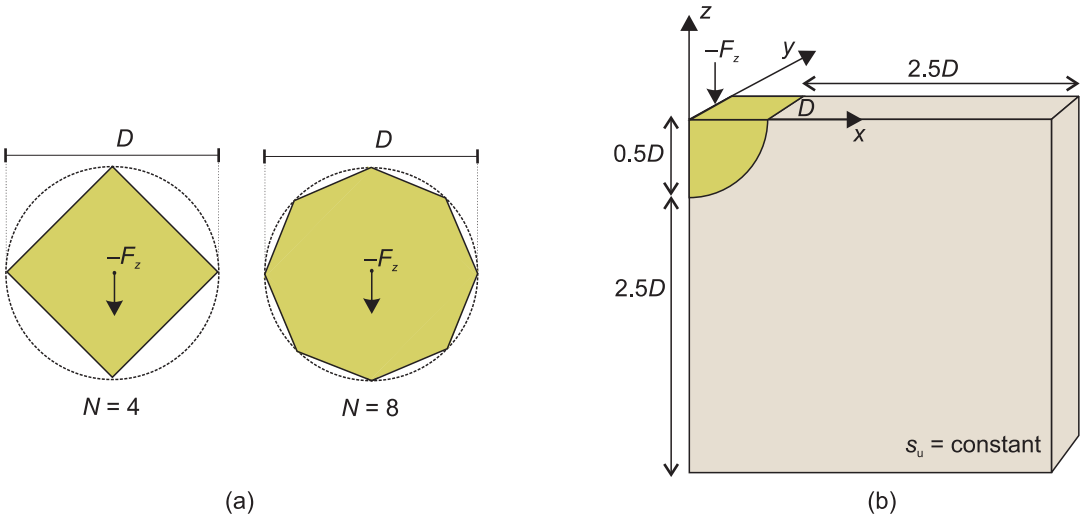

Figure 3.10: Pile section loaded laterally: (a) two pile polygonal approximations; (b) notation and sign conventions

modelled between the pile and the soil, in keeping with the solutions outlined in Randolph and Houlsby (1984) and Martin and Randolph (2006).

3.5.2.1 Results

The capacities of the pile polygonal approximations when loaded laterally are shown in Figure 3.11. The capacity of a square pile is lower than the true circular pile capacity. However once $N \geq 8$ the capacity obtained using plane strain FELA overestimates the capacity when $\alpha = 0$ and 0.5, but matches the UB solution in Randolph and Houlsby (1984) when $\alpha = 1$. For piles with $\alpha = 0.5$ and 1, as N increases the accuracy of the polygonal approximation increases and the capacity approaches that of the true piles. When $N = 90$ the capacity obtained by the polygonal approximation closely matches the capacities for circular piles available in the literature for all values of α. These capacities are summarised in Table 3.2.

The bracketing errors associated with the 3D analyses range from $\pm 2.9\%$ for $\alpha = 1$ to $\pm 4.4\%$ for $\alpha = 0$. Unlike the strip footing problem, tighter bounds are achieved for a rough interface when compared with a smooth interface (comparing Table 3.2 with Table 3.1). The LB solution again proves to be very accurate while the UB solution is relatively inaccurate, causing the average of the bounds to marginally overestimate the true capacity. The failure

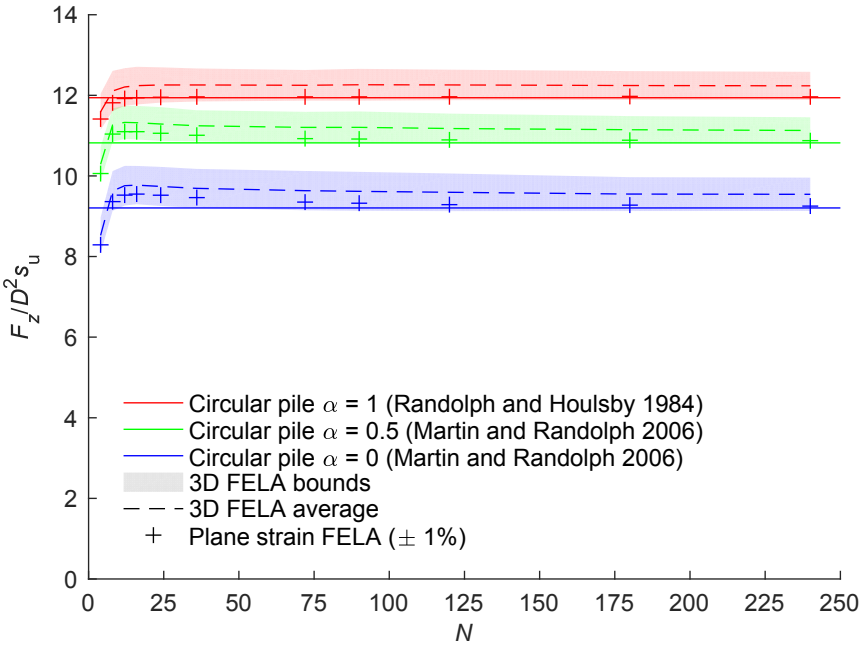

Figure 3.11: Lateral capacities of N-sided polygonal pile sections

Table 3.2: Comparison of 3D FELA solutions with known plasticity solutions for laterally loaded circular pile sections ($N = 90$)

α	FELA LB ($D^2 s_u$)	FELA UB ($D^2 s_u$)	Bracketing error (%)	FELA average ($D^2 s_u$)	Exact solution ($D^2 s_u$)	FELA error (±%)
1.0	11.88	12.60	2.9	12.24	11.94 [a]	+ 2.5
0.5	10.80	11.46	2.9	11.13	10.82 [b]	+ 2.8
0.0	9.13	9.97	4.4	9.55	9.20 [b]	+ 3.7

[a] Houlsby and Randolph (1994)
[b] Martin and Randolph (2006)

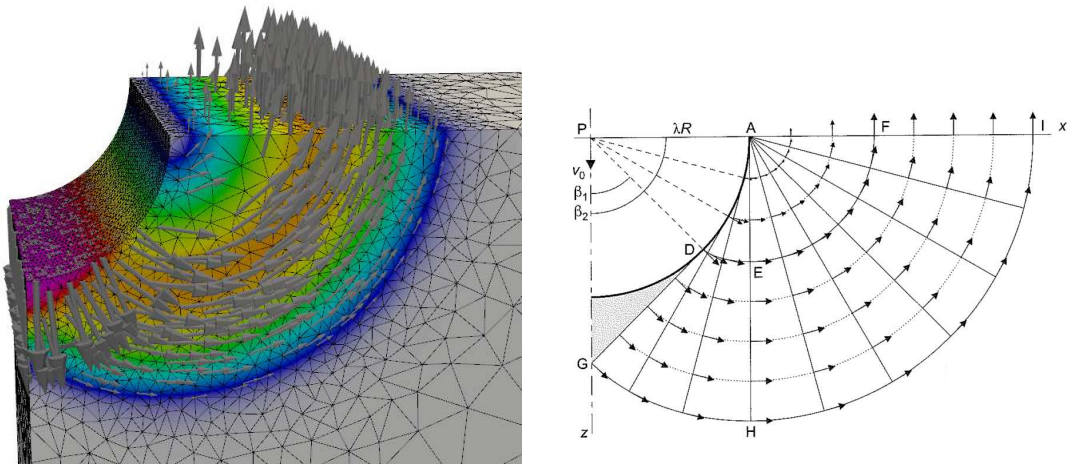

(a) (b)

Figure 3.12: Failure mechanisms of half-rough ($\alpha = 0.5$) pile sections: (a) FELA refined mesh (∼40 000 elements). Vectors and shading show UB velocity magnitudes; (b) mechanism described in Martin and Randolph (2006)

mechanism for a 3D pile section with $\alpha = 0.5$ and $N = 90$ is shown in Figure 3.12(a) (only one quarter of the doubly symmetric mechanism shown). Strong similarities are visible between this mechanism and that described in Martin and Randolph (2006), shown in Figure 3.12(b).

3.5.3 Circular surface footing

Many previous studies have analysed capacities of circular surface footings on cohesive soil under vertical (F_z), horizontal (F_x), and moment (M_y) loading (e.g. Shield, 1955; Eason and Shield, 1960; Gourvenec and Randolph, 2003; Gourvenec, 2007; Gourvenec and Mana, 2011; Shen et al., 2016; Fu et al., 2017). A circular surface footing of diameter, D, resting on weightless soil with uniform strength was modelled using 3D FELA and FEA. Uniaxial capacities F_{z0}, F_{x0}, and M_{y0} are compared with capacities available in the literature. The sign conventions follow Figure 3.1 and the load reference point was at the centre of the foundation at the mudline.

Combined $F_z - F_x$, $F_z - M_y$ and $F_x - M_y$ loading was also considered with the results presented in the form of normalised failure envelopes. Finally, failure envelopes for footings under combined $F_z - F_x - M_y$ loading were found and are compared with failure envelopes presented in Gourvenec (2007).

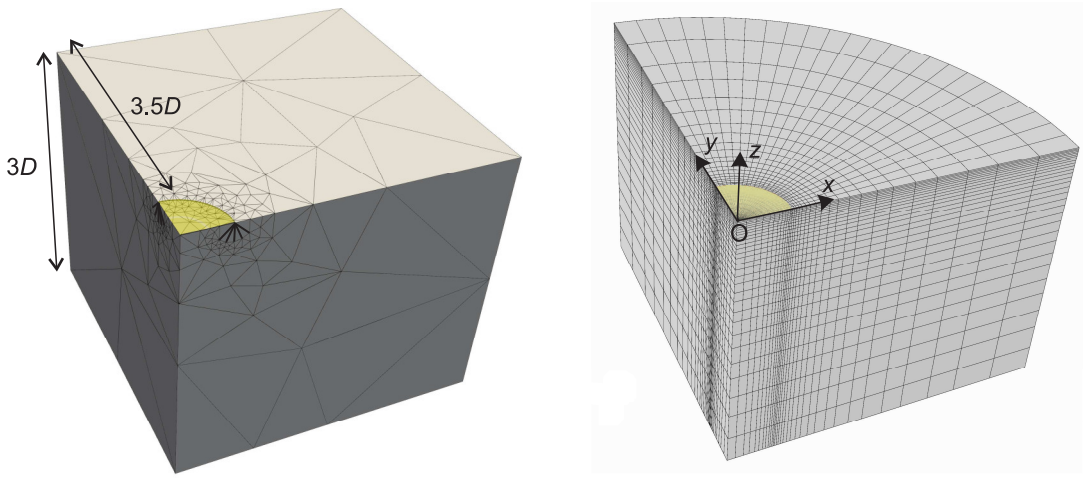

Figure 3.13: Quarter model mesh: (a) initial FELA mesh (singularity facets shown as bold lines); (b) FEA mesh

The footing/soil interface was modelled as either rough or smooth ($\alpha = 1$ or 0). The tensile capacity at the footing/soil interface was modelled using two extreme values; unlimited tensile capacity ($T = \infty$) and no tension capacity ($T = 0$). The curved footing edge is approximated as an N-sided polygon that inscribes the true circular footing. A polygonal refinement study was undertaken to ensure that sufficient planar facets were used. It was found that a 96-sided polygon is sufficient, the area of a 96-sided polygon is only $< 0.08\%$ smaller than the circle that it inscribes. For the analysis of uniaxial capacity when $T = \infty$, two planes of symmetry/antisymmetry (depending on the loading) were exploited (Figure 3.13). In all other cases, half of the soil domain was modelled and symmetry was only exploited along $y = 0$. A soil domain of depth $3D$ and radius $4D$ was found to be sufficiently large. An initial FELA mesh and a refined FEA mesh of a quarter model soil domain exploiting two planes of symmetry are shown in Figure 3.13.

FELA: Uniaxial capacities were found by applying unit loads to the footing and determining the corresponding load factors. Failure envelopes were analysed by applying numerous load-controlled probes. The directions of the probes were chosen to give an accurate definition of the full failure envelope, with particular attention given to extremities and sharp apex points — at least 36 load-controlled probes were used to obtain each failure envelope. Initial meshes

comprised ∼5000 elements and were unstructured except for a fan of prescribed singularity planes which stem from the edge of the foundation (shown as bold lines in Figure 3.13(a)). Just as for the analysis of strip footings in Section 3.5.1, it was found that when these planes are present the bounds converge much more rapidly than when a completely unstructured mesh is used. For half models, automated mesh refinement was used on successive iterations of the solution to generate meshes of ∼10 000, ∼20 000, and ∼40 000 elements. Meshes of half this size were generated for quarter models. Mesh refinement was not undertaken if the bracketing error was $< \pm 1\%$.

FEA: Uniaxial capacities were found by applying displacements to the footing and obtaining the load states at the end of the displacement steps. Failure envelopes were determined by applying numerous displacement-controlled probes. When using this method, higher resolution of the failure envelope is naturally obtained around any apexes in a failure envelope as the final load state reached is dependent on the plastic potential gradient, which is prescribed in the analysis (and is normal to the failure envelope). Structured FEA meshes comprising ∼40 000 elements for half models and ∼20 000 elements for quarter models were used. A process of manual mesh refinement was undertaken to ensure that the solution had converged. The foundation/soil interface was modelled using the UINTER subroutine described in Section 3.3.1.

3.5.3.1 Results: uniaxial loading

Table 3.3 compares uniaxial capacities obtained using FELA and FEA with capacities available in the literature. Capacities are normalised using the foundation area, $A = \pi D^2/4$. First, considering the ultimate vertical capacity of a rough footing ($\alpha = 1$) with unlimited tension capacity ($T = \infty$), it is shown that the FELA average capacity and the FEA capacity compare well, only differing by $< 0.5\%$. The exact solution for a rough circular footing on Tresca soil ($6.05 A s_u$) was first found by Eason and Shield (1960). The capacities obtained using FELA and FEA are lower than this (even the FELA UB) but this is simply due to the von Mises failure criterion used in the simulations. It may at first seem surprising that FEA

Table 3.3: Uniaxial capacities of circular surface footings. F_x and F_y normalised by undrained shear strength and footing area (As_u), M_y normalised by ADs_u

			FELA			FEA	From the literature
			LB	UB	Ave		
$T=\infty$	$\alpha=1$	F_{z0}	5.45	5.76	5.61	5.66	6.05[1], 5.94[2,3], 5.87[4]
		F_{x0}	1.00	1.00	1.00	1.00	1.0[5], 1.02[2,4]
		M_{y0}	0.66	0.70	0.68	0.71	0.67[6], 0.71[2]
	$\alpha=0$	F_{z0}	5.17	5.41	5.29	5.35	5.69[7], 5.54[3]
		F_{x0}	0.00	0.00	0.00	0.00	0.0[5]
		M_{y0}	0.67	0.70	0.68	0.70	—
$T=0$	$\alpha=1$	M_{y0}	0.58	0.63	0.60	0.60	0.61[4]
	$\alpha=0$	M_{y0}	0.54	0.58	0.56	0.57	—

[1] Exact solution (Tresca criterion) - Eason and Shield (1960)
[2] FEA (Abaqus Tresca implementation) - Fu et al. (2017)
[3] FEA (Abaqus Tresca implementation) - Gourvenec and Mana (2011)
[4] FEA (Abaqus Tresca implementation) - Shen et al. (2016)
[5] Exact solution = $\alpha A s_u$
[6] UB solution (Tresca criterion) - Randolph and Puzrin (2003)
[7] Exact solution (Tresca criterion) - Shield (1955)

results obtained in the literature using a Tresca criterion underestimate the true capacity (by 2.8%), but this is likely to be due to the implementation of the Tresca criterion in the Abaqus FEA software. Abaqus uses a Tresca/von Mises hybrid whereby the Tresca yield function is implemented with a von Mises surface used for the plastic potential, resulting in lower capacities than for a foundation on a 'true' Tresca soil (Tapper et al., 2014).

The failure mechanisms observed in the FELA and FEA models compare favourably and are shown in Figure 3.14(a) and (b) respectively. These mechanisms can be compared with the axisymmetric failure mechanism obtained using the MoC software ABC (Martin, 2003) which is shown in Figure 3.15(a). The FELA adaptive mesh refinement captures the failure mechanism and the FELA and FEA mechanisms both closely resemble the mechanism in Figure 3.15(a). A 'false head' of soil directly under the footing (shown as red shading in Figure 3.14(a) and (b)) is also visible in Figure 3.15(a).

The exact vertical capacity of a circular smooth foundation on Tresca soil ($5.69A s_u$) was

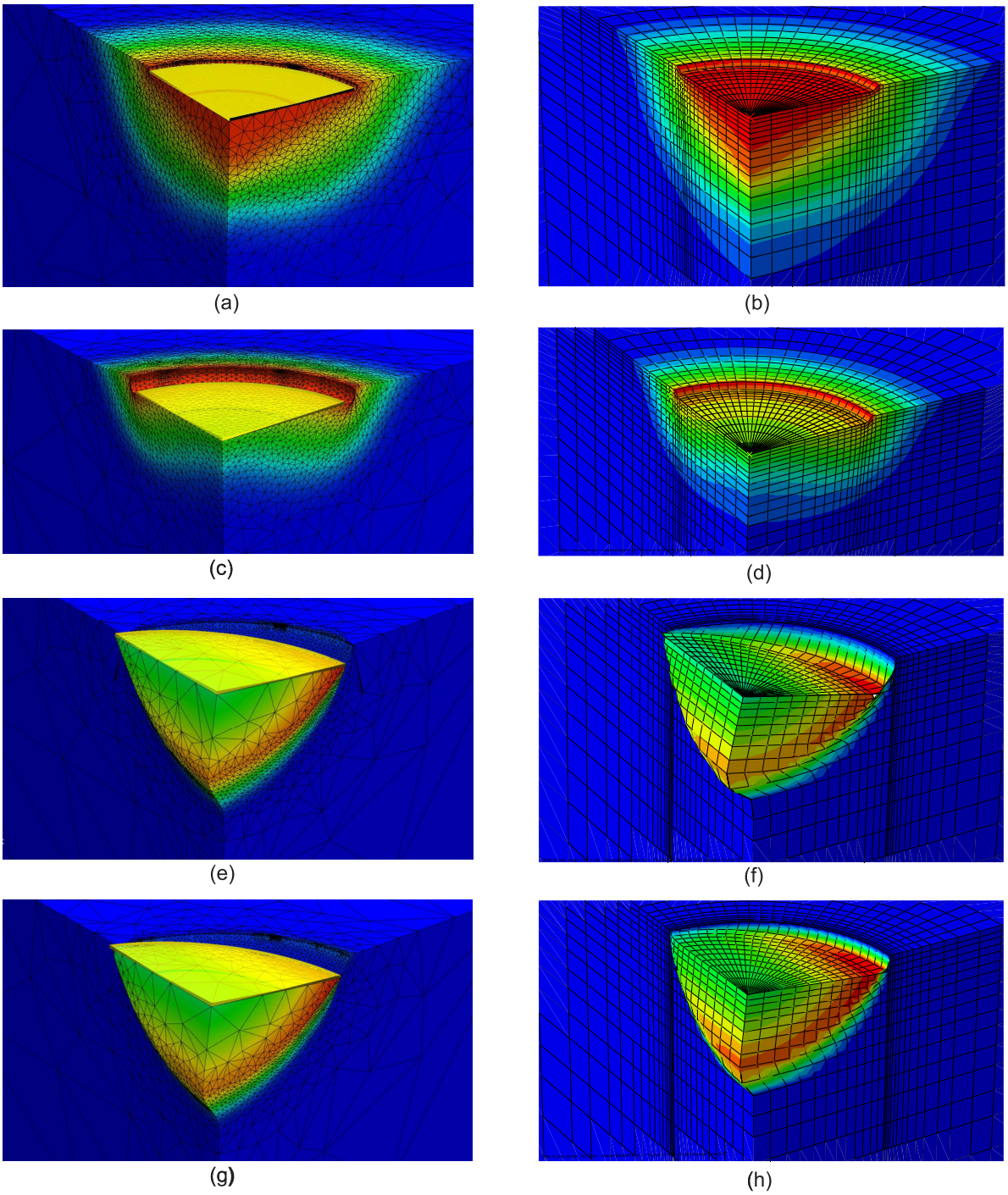

Figure 3.14: Circular footing failure mechanisms under uniaxial loading. Quarter model shown. $T = \infty$. FELA mesh shaded by UB velocity magnitudes, FEA mesh shaded by deformation magnitudes: (a) FELA, $-F_{z0}$, $\alpha = 1$; (b) FEA, $-F_{z0}$, $\alpha = 1$; (c) FELA, $-F_{z0}$, $\alpha = 0$; (d) FEA, $-F_{z0}$, $\alpha = 0$; (e) FELA, M_{y0}, $\alpha = 1$; (f) FEA, M_{y0}, $\alpha = 1$ (g) FELA, M_{y0}, $\alpha = 0$; (h) FEA, M_{y0}, $\alpha = 0$

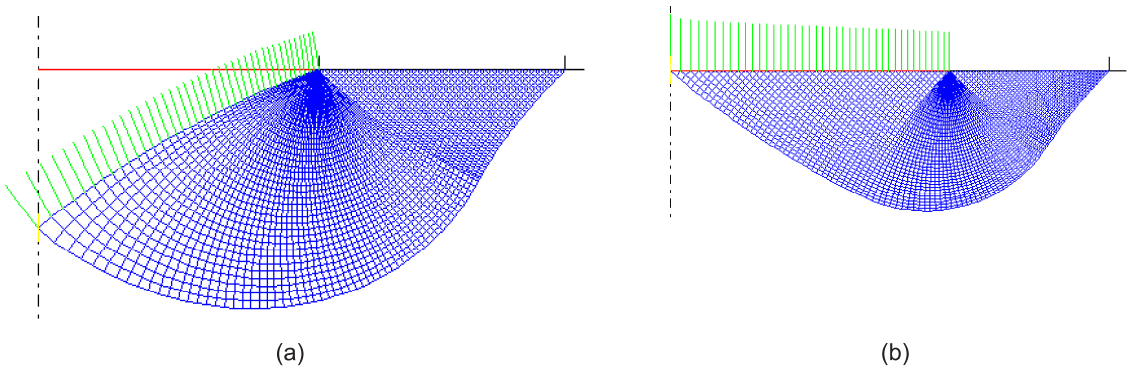

Figure 3.15: Circular footing $-F_{z0}$ failure mechanisms using the method of characteristics (Martin, 2003): (a) rough footing ($\alpha = 1$); (b) smooth footing $\alpha = 0$

found by Shield (1955). Again, the FELA (average) and FEA capacities, obtained with the von Mises criterion, underestimate this value by 7% and 6% respectively ($5.29As_u$ and $5.35As_u$). An FEA study undertaken by Gourvenec and Mana (2011) (which used the Abaqus Tresca implementation) obtained a capacity that lies between the values obtained here and that from Shield, at $5.54As_u$ (Table 3.3). Failure mechanisms from the FELA and FEA simulations are shown in Figure 3.14(c) and (d). These compare favourably with the MoC mechanism obtained using ABC and shown in Figure 3.15(b).

Exact horizontal foundation capacities are easily found, as the capacity is simply the roughness factor times the foundation area times the soil shear strength at the mudline (αAs_u). A rough footing therefore has capacity $F_{x0} = As_u$ and a smooth footing has no capacity. The exact solution obtained using FEA highlights the effectiveness of the UINTER subroutine (described in Section 3.3.1). Capacities obtained for rough and smooth footings using FELA also match the exact solutions (Table 3.3). Some previous FEA studies of rough footings have tied the footing base to the soil surface, which prevents relative movement at the interface and results in a slight overestimation of capacity (e.g. Gourvenec and Mana, 2011; Fu et al., 2017).

Under moment loading with $T = \infty$ the capacities obtained using FELA and FEA are 1.4% and 5.8% higher than the UB solution found by Gourvenec and Randolph (2003). The FEA value is slightly higher than the FELA UB at $0.71Ds_u$ compared with $0.70Ds_u$. FEA and FELA failure mechanisms are shown in Figure 3.14(e) and (f). The FELA mesh

refinement highlights the slip line of the simple scoop failure mechanism described by Murff and Hamilton (1993) and implemented by Gourvenec and Randolph (2003). There is no relative slip at the footing/soil interface (Figure 3.14(g) and (h)) and as a result the capacity is independent of interface roughness.

When tension is not permitted at the interface ($T = 0$) the footing has no capacity when loaded with $+F_z$ as a gap forms over the full footing area. The $-F_{z0}$ capacity is equal to that when $T = \infty$, and F_{x0} is unaffected by interface tension capacity. These cases were analysed but are omitted from Table 3.3 for the sake of brevity.

Footing capacity under moment loading is affected by interface tension capacity. If the footing is free to move vertically then under moment loading it can pivot about its edge, thus avoiding failure in the soil or at the footing/soil interface (the foundation then has no capacity). If the foundation is free to rotate but prevented from displacing in the vertical direction then it is forced to penetrate the soil at failure, and this is the case considered here. The M_{y0} capacity of a rough footing with $T = 0$ reduces by approximately 15% compared with the unlimited tension case. Figure 3.16(a) and (b) show FELA and FEA mechanisms for a rough footing. The failure mechanisms are virtually identical and both show a gap forming where the footing lifts from the soil. The matching mechanisms highlight the ability of the Abaqus UINTER subroutine to model $T = 0$ interfaces.

The M_{y0} capacity when $T = 0$ is no longer independent of interface roughness, and the failure mechanisms for rough and smooth footings are quite different. Comparing Figure 3.16(a) and (b) with (c) and (d) shows that the failure mechanism is much shallower for the smooth footing. Table 3.3 shows that the capacities obtained using FEA and FELA are marginally lower for a smooth footing than for a rough footing, although results were not found in the literature to compare with the results obtained here.

3.5.3.2 Results: combined loading

As this is a verification exercise, known symmetrical planes of some failure envelopes were not exploited. Figure 3.17(a) shows the $F_z - F_x$ failure envelope for a rough footing with unlimited tension capacity in black and with no tension capacity in red. The FELA bounds

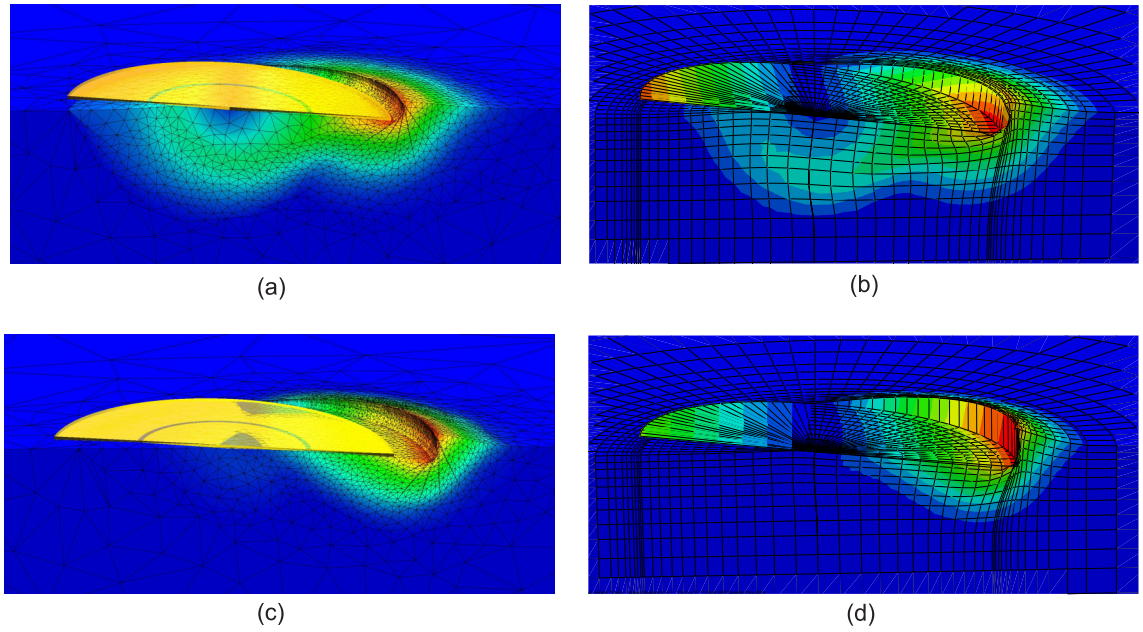

Figure 3.16: Circular footing M_{y0} failure mechanisms. Half model shown. $T = 0$. FELA mesh shaded by UB velocity magnitudes, FEA mesh shaded by deformation magnitudes: (a) FELA, $\alpha = 1$; (b) FEA, $\alpha = 1$; (c) FELA, $\alpha = 0$; (d) FEA, $\alpha = 0$

agree well with the capacities obtained using FEA. When $F_z \leq 0$ (downwards vertical loading) the interface tension capacity does not effect the failure envelope. Also, as expected, when $F_z > 0$ (upwards vertical loading) there is no capacity when $T = 0$ because a gap forms at the footing/soil interface. A smooth footing has no capacity when $F_x \neq 0$. The resulting $F_z - F_x$ failure envelope degenerates to a line that extends from $+F_{z0}$ to $-F_{z0}$ when $T = \infty$ and from 0 to $-F_{z0}$ when $T = 0$ (Figure 3.17(b)).

$F_z - M_y$ failure envelopes for rough and smooth footings are shown in Figure 3.17(c) and (d) respectively; FELA and FEA capacities show good agreement. The $T = \infty$ envelopes are a similar shape but the vertical capacity is lower when $\alpha = 0$. The failure envelopes when $T = 0$ have an apex at $F_z = M_y = 0$. For these analyses the footing is free to move vertically and, as already mentioned, the footing can pivot about its edge avoiding failure in the soil or at the footing/soil interface. In order to probe outwards and reach the failure envelope, it was first necessary to apply a downward vertical dead load to the foundation. Probes then began from the dead load point instead of from the origin. Figure 3.17(c) and (d) show that the maximum moment capacity is achieved when the downward vertical load is approximately

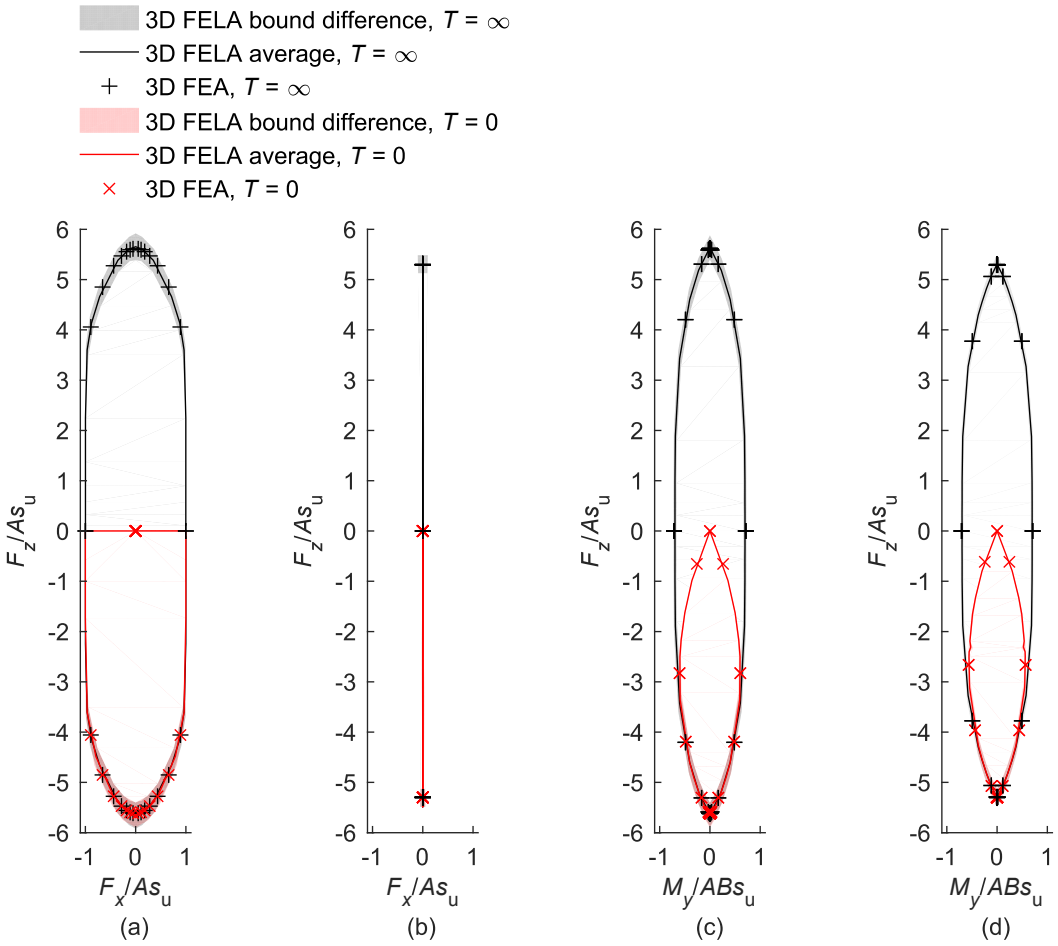

Figure 3.17: Normalised failure envelopes for circular footings with $T = \infty$ and $T = 0$: (a) $F_z - F_x$, $\alpha = 1$; (b) $F_z - F_x$, $\alpha = 0$; (c) $F_z - M_y$, $\alpha = 1$; (d) $F_z - M_y$, $\alpha = 0$

half of the vertical capacity ($F_z = -2.8A\,s_u$ for a rough footing and $F_z = -2.65A\,s_u$ for a smooth footing).

Figure 3.18(a) and (b) show $F_x - M_y$ failure envelopes for rough and smooth footings respectively. For a rough footing with $T = \infty$, the failure envelope is not symmetric about $F_x = 0$. This well established failure envelope (e.g. Gourvenec, 2007) shows that combining horizontal and moment loading can be beneficial as it can provide additional capacity when compared with pure moment loading. For a rough footing with $T = 0$ the failure envelope is not quite symmetric about $F_x = 0$. Under the sign conventions adopted here, the combined load capacity is slightly higher when two positive, or two negative, loads are (F_x, M_y or $-F_x$, $-M_y$) applied when compared with one positive and one negative ($-F_x$, M_y or F_x, $-M_y$) (Figure 3.18(a)). Just as for $F_z - F_x$ loading, the failure envelope for a smooth footing is

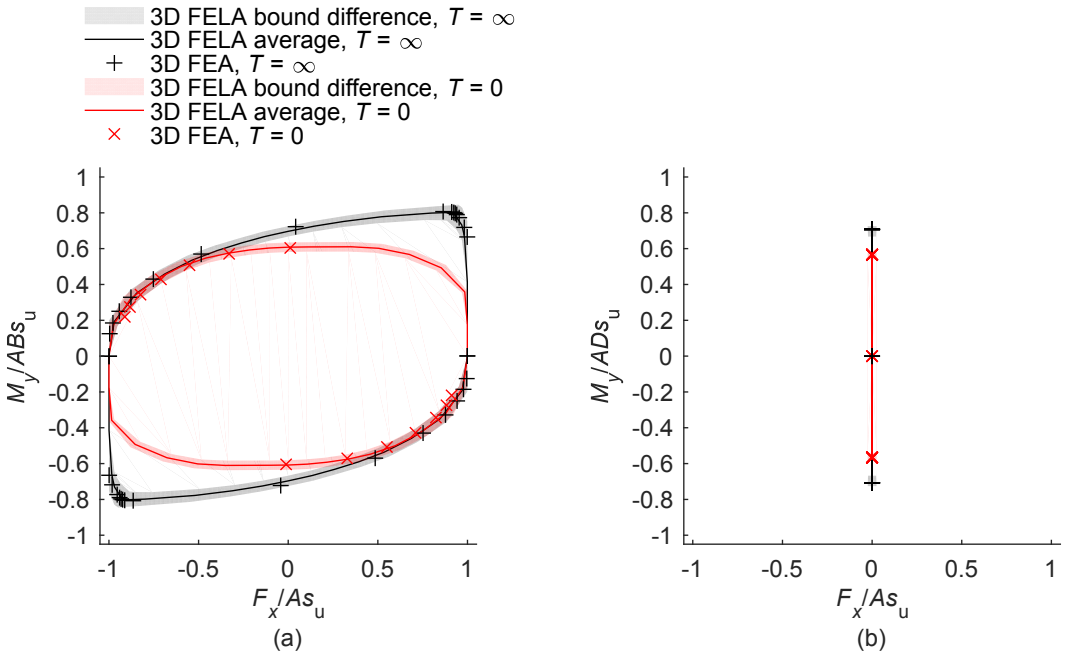

Figure 3.18: Normalised $F_x - M_y$ failure envelopes for footings with $T = \infty$ and $T = 0$: (a) $\alpha = 1$; (b) $\alpha = 0$

simply a line extending from $+M_{y0}$ to $-M_{y0}$ for both cases $T = \infty$ and $T = 0$ (Figure3.18(b)).

Finally, the 3D $F_z - F_x - M_y$ failure surface was obtained for a circular footing with $\alpha = 1$ and $T = \infty$. The full failure surface was found by taking $F_x - M_y$ 'slices' at fixed F_z values. Dead F_z loads were applied to the footing in ratios of the ultimate vertical capacity $F_z/F_{z0} = 0$, 0.25, 0.5, 0.75, and 0.875 (F_{z0} values obtained using FELA and FEA can be found in Table 3.3). At each dead load level, load-controlled (FELA) or displacement-controlled (FEA) probes were used to define the $F_x - M_y$ failure envelope. Figure 3.19(a) shows that looser FELA bounds are achieved as the vertical dead load increases. However, the FELA average still compares favourably with the capacity obtained using FEA. FELA average capacities are compared with FEA capacities from Gourvenec (2007) (where the Abaqus Tresca implementation was used) in Figure 3.19(b). The failure surfaces are a very close match despite the differing yield criterion (von Mises in this work and (Abaqus) Tresca in Gourvenec (2007)).

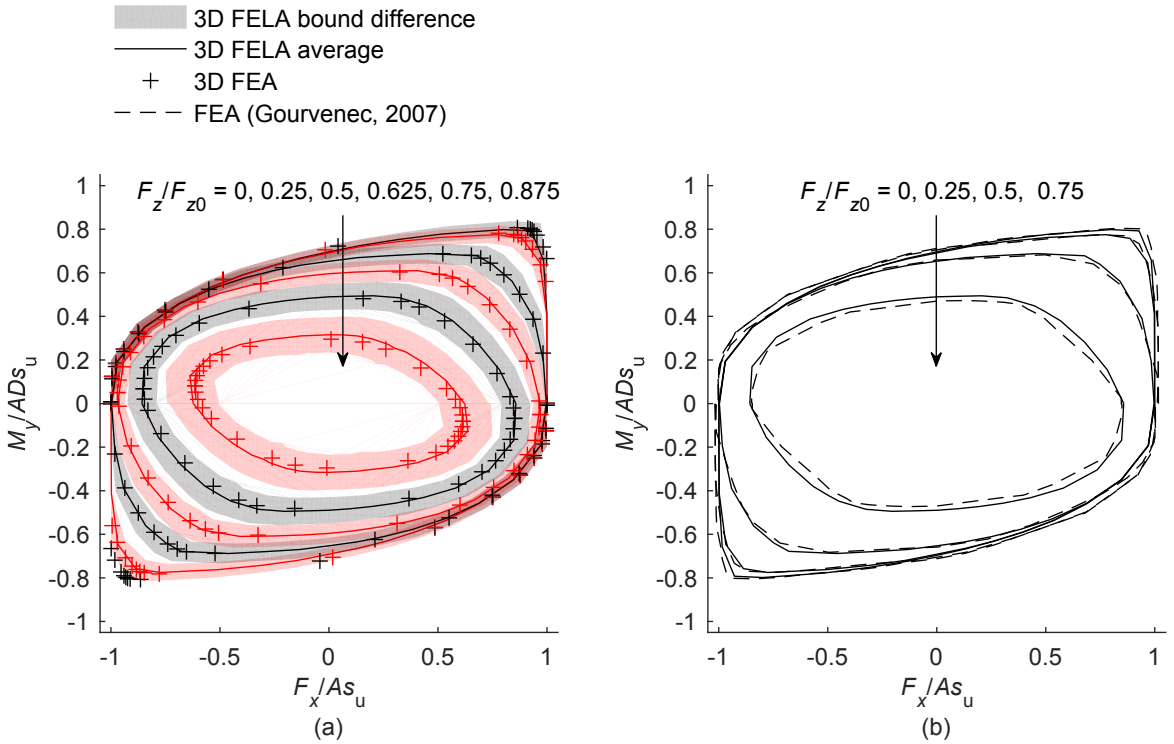

Figure 3.19: Normalised $F_z - F_x - M_y$ failure surface for circular footing with $T = \infty$ and $\alpha = 1$: (a) FELA and FEA capacities. Red and black colours are alternated to increase clarity; (b) surface obtained using FELA averages compared with surface obtained using FEA from Gourvenec (2007)

3.6 Summary

In this chapter the implementation of FELA used in the thesis was outlined, the FEA features used in this thesis were described in detail, and the main differences between FELA and FEA were highlighted. Three verification exercises have shown that the FELA and FEA implementations are working as desired.

Analysis of a 3D model of a strip footing under vertical loading using 3D FELA and 3D FEA gave capacities that compared well with exact theoretical solutions. The introduction of singularity planes in the FELA mesh was shown to assist convergence of the bounds. For the second exercise a circular pile section under lateral loading was modelled. Capacities obtained using plane strain FELA and 3D FELA showed a good match to solutions available in the literature. The number of planar facets required to represent a circular pile section under lateral loading was investigated for three pile/soil roughness conditions. Finally, 3D FELA and

3D FEA models of a circular strip footing under a range of uniaxial and combined load cases were shown to provide similar results to each other, and to results in the literature.

For each verification exercise, failure mechanisms obtained using FELA and FEA have matched those available in the literature. Inspection of FELA mechanisms has shown that adaptive refinement of the mesh is occurring in areas where high shear strain rates are expected.

Chapter 4

Shallow rectangular foundations

4.1 Introduction

This chapter considers the capacity of shallow rectangular foundations under a range of loading conditions. In the first section, plane strain FEA and FELA are used to investigate how the ultimate bearing capacity of a skirted shallow foundation (mudmat) is affected by seabed inclination. Sometimes it is necessary for mudmat foundations to be sited in areas where the seabed has a gradient, perhaps up to 10°. Failure envelopes are found for a range of seabed inclinations, soil unit weights, and interface behaviours. This section concludes with a case study based on a real design scenario, which involves a skirted mudmat on an inclined seabed with a linear increase in strength with depth.

The next section opens with a typical design example of a rectangular mudmat under complex 3D loading. Observations made in the analysis of this design case lead to a comprehensive study involving complex loading of rectangular mudmats resting on the surface of, or embedded in, homogeneous undrained clay. Realistic 3D load combinations are applied, based on the combined horizontal, moment, and torsional loading generated by a horizontal force applied within the envelope of the mudmat and the equipment that it supports. The study begins by considering combined horizontal and torsional loading. As it is deemed improbable that a mudmat would be loaded from outside its plan area, emphasis is given to horizontal loads applied at points within the plan area of the mudmat, which generate what are referred to here as 'feasible' levels of torsion. Next, horizontal forces applied at an eccentricity from, and a height above, the load reference point are considered.

This results in five degree-of-freedom loading. The capacity of surface and embedded mudmats under pure vertical loading is then closely bracketed using 3D FELA. A prescribed fraction of the ultimate vertical capacity is applied to the mudmat as a vertical dead load, and horizontal forces are again applied at a range of eccentricities from, and heights above, the load reference point.

The final section considers capacity analysis of square foundations with a central perforation. The vertical bearing capacity factor for surface and embedded footings with a range of perforation ratios is found. Results obtained using FELA are compared with FEA and experimental results available in the literature. The efficacy of a design formula outlined in Tapper (2013) and Tapper et al. (2015) is assessed, and a modification to the design formula is proposed for the analysis of embedded perforated foundations.

4.2 Mudmat capacity on sloping ground

4.2.1 Problem overview

The bearing capacity of skirted mudmats on sloping ground under combined loading was investigated using FELA. Analysis of surface (unskirted) foundations was also undertaken using displacement FEA for comparison and verification. A mudmat of breadth, B, and skirt embedment depth, d, was modelled in plane strain and is shown in Figure 4.1. The analyses mainly focused on combined $F_z - F_x$ loading, with some analyses considering M_y loading also undertaken.

Referring to Figure 4.1, analyses were performed for the reference case of level ground ($\xi = 0$) and for two ground inclinations ($\xi = 5^\circ$ and 10°). Two mudmat geometries were considered; an unskirted mudmat ($d = 0$), and a mudmat with perimeter skirts of embedment $d = 0.2B$ and thickness $t = 0.005B$. The skirted mudmat geometry is representative of typical mudmat designs (Subsea 7, personal communication, 2014). The mudmat was modelled as rigid. For analyses where the soil was modelled as weightless, a soil domain of width $7B$ and depth $3.5B$ was found to be sufficiently large (Figure 4.2). The base and the sides of the soil block were modelled as rigid boundaries. In cases where soil submerged unit-weight,

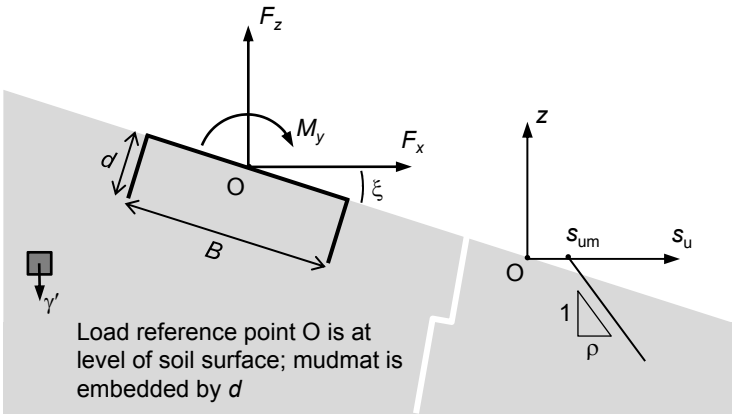

Figure 4.1: Mudmat on sloping ground notation and sign conventions

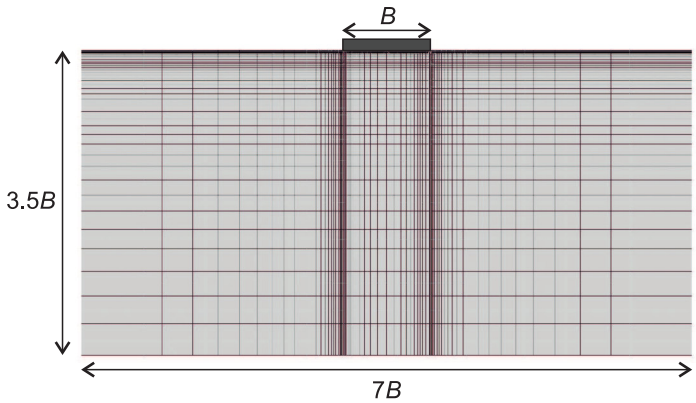

Figure 4.2: FEA mesh for a surface mudmat on flat ground

γ', was modelled, the soil domain was made as large as possible without inducing problems with global slope stability of the model. The FEA structured mesh comprising ~3 600 second-order quadrilateral hybrid elements (Abaqus element type CPE8H) is shown in Figure 4.2. The FELA mesh, initially coarse and unstructured, underwent automated adaptive mesh refinement until the bracketing error reached $< \pm 1\%$.

In the main parametric study, soil of uniform strength was assumed. However, in the design case study, soil with linearly increasing strength with depth was modelled. The submerged unit weight was initially taken as zero and was then increased to give normalised weight to strength ratios $\gamma' B / s_u$ as large as 10. Once soil weight was incorporated in the model, it was necessary to check for global slope stability before attempting to analyse the bearing capacity of the mudmat.

Various values of mudmat/soil interface roughness and interface tensile capacity were

considered. The main parametric study used the extreme conditions of fully rough ($\alpha = 1$) and smooth ($\alpha = 0$), with an intermediate value ($\alpha = 0.5$) added for the case study. The tensile capacity at the interface was also predominantly modelled using two extreme values; unlimited tensile capacity ($T = \infty$), and no tension capacity ($T = 0$). A third case, with $T = 0$ on the outside of the skirts and $T = \infty$ elsewhere, was considered in the case study. The interface conditions were incorporated in the FEA model using the UINTER subroutine described in Section 3.3.1.

In the main study using FELA, failure envelopes for combined loading were generated using load-controlled probes and the directions of these load-controlled probes were chosen to give an accurate definition of the full failure envelope. Displacement-controlled probes were used in the FEA modelling.

4.2.2 Combined vertical and horizontal loading

4.2.2.1 Surface mudmat

Initially, surface (unskirted) mudmats were analysed and the effect of soil weight was excluded. Figure 4.3 shows the normalised $F_z - F_x$ failure envelope for a fully rough ($\alpha = 1$) surface mudmat with full tension capacity ($T = \infty$) on weightless soil ($\gamma' = 0$). On flat ground ($\xi = 0$), this envelope is the well known solution of Green (1954), with vertical and horizontal capacities of $(2+\pi)Bs_u$ and Bs_u respectively.

When a ground inclination, ξ, is introduced and the soil remains weightless, the failure envelope retains the same shape, but rotates through an angle ξ. When ξ is small ($\leq 10^\circ$, say) the horizontal capacity increases very slightly but the vertical capacity can decrease significantly. To highlight this effect, Figure 4.3(b) shows a zoomed view of the failure envelopes for ground inclinations of 0 and 10°. The capacity normal to the ground surface is the same in both cases ($5.14Bs_u$) but the vertical capacity when $\xi = 10^\circ$ is 20% smaller ($4.12Bs_u$). Furthermore, it is clear from Figure 4.3 that $F_z - F_x$ loading of a mudmat on inclined (but weightless) ground can readily be analysed by considering the same foundation on flat ground, with loads applied in a suitably rotated axis system. Figure 4.3 also shows that the results of the FELA load-controlled probe and the FEA displacement-controlled

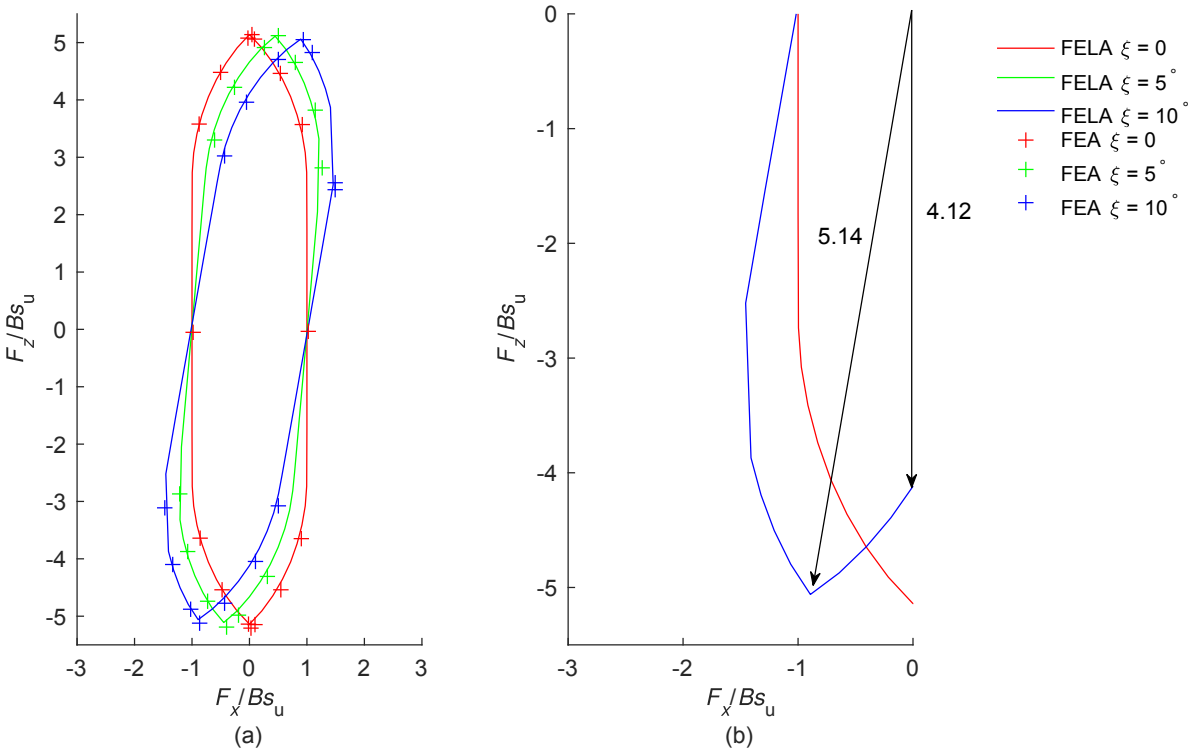

Figure 4.3: Normalised $F_z - F_x$ failure envelopes for weightless soil ($\gamma' B/s_u = 0$). $d/B = 0$, $\alpha = 1$, $T = \infty$

probe match very closely. The exact horizontal capacities achieved using FEA highlight the effectiveness of the UINTER subroutine.

Soil weight was then added to the analysis. It was first necessary to check that undrained slope failure of the modelled soil domain would not interfere with the failure envelope calculations for the foundation. A uniform vertical body force was applied (as a live load) to 5° and 10° slopes with no foundation present, thus determining the critical submerged unit weight (γ'_{crit}) that would cause global slope failure. The aspect ratio of the soil domain was fixed at $2W$ wide and W high along the centreline (Figure 4.4). The value of W was then varied from B to $15B$ and for each case the ratio $\gamma'_{crit}B/s_u$ was found using FELA. In the subsequent analyses with mudmats on inclined ground, the soil weight γ' was always set some way below γ'_{crit} and it was checked that the local failure mechanisms formed by bearing capacity failure of the mudmat were comfortably contained within the boundaries of the soil domain. The limiting ratios of γ'_{crit} for a range of W/B ratios are shown in Figure 4.4.

For a mudmat on inclined ground with soil weight present, the simple analytical approach

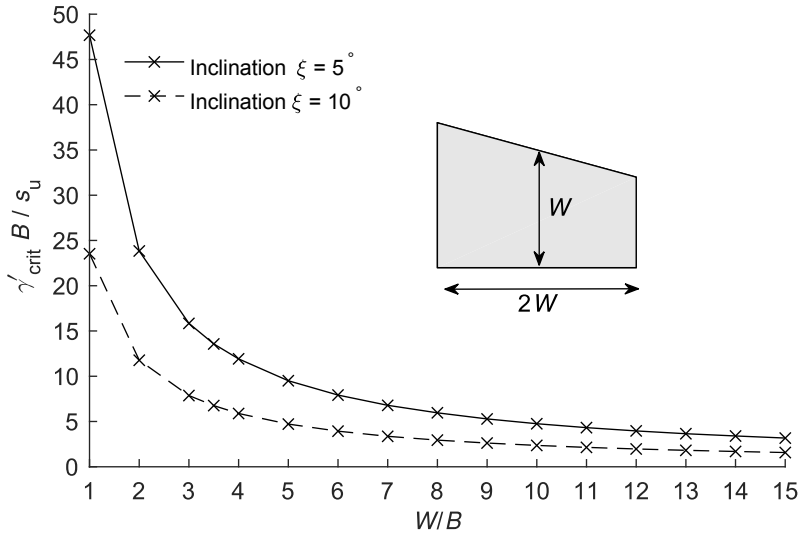

Figure 4.4: Limiting values of $\gamma' B/s_u$ as a function of soil domain size for two ground inclinations

outlined above (rotated Green's envelope) is no longer valid as the body force vector from the soil weight does not act perpendicular to the ground surface. Instead the problem must be analysed directly, ensuring that the global slope stability precautions in the previous paragraph are observed. Figure 4.5 shows the $F_z - F_x$ failure envelopes obtained for various ground inclinations and a normalised soil weight of $\gamma' B/s_u = 5$. The capacities obtained using FEA again show good agreement with with the FELA capacities. Comparing these capacities with those in Figure 4.3, it can be seen that the larger the ground inclination, the greater the deviation of the failure envelope from the rotated Green's envelope that is obtained when soil weight is neglected.

The failure mechanisms for a foundation under vertical loading on flat ground with weightless soil ($\gamma' = 0$) and soil with normalised weight $\gamma' B/s_u = 5$ are shown in Figure 4.6(a) and (c) respectively. These asymmetric mechanisms highlight that at the cusps of the $F_z - F_x$ failure envelope, a range of asymmetric mechanisms, not just the iconic Prandtl (1920) mechanism, gives the same collapse load. Figure 4.6(b) and (d) show the corresponding failure mechanisms for mudmats on ground with $\xi = 10°$. In this case the two mechanisms are different; a larger section of soil is mobilised in the soil with weight (Figure 4.6(d)). For a ground inclination of 10°, the capacity normal to the slope is reduced from $5.14Bs_u$ in weightless soil to $3.79Bs_u$ in soil with weight $\gamma' B/s_u = 5$. Figure 4.5(b)

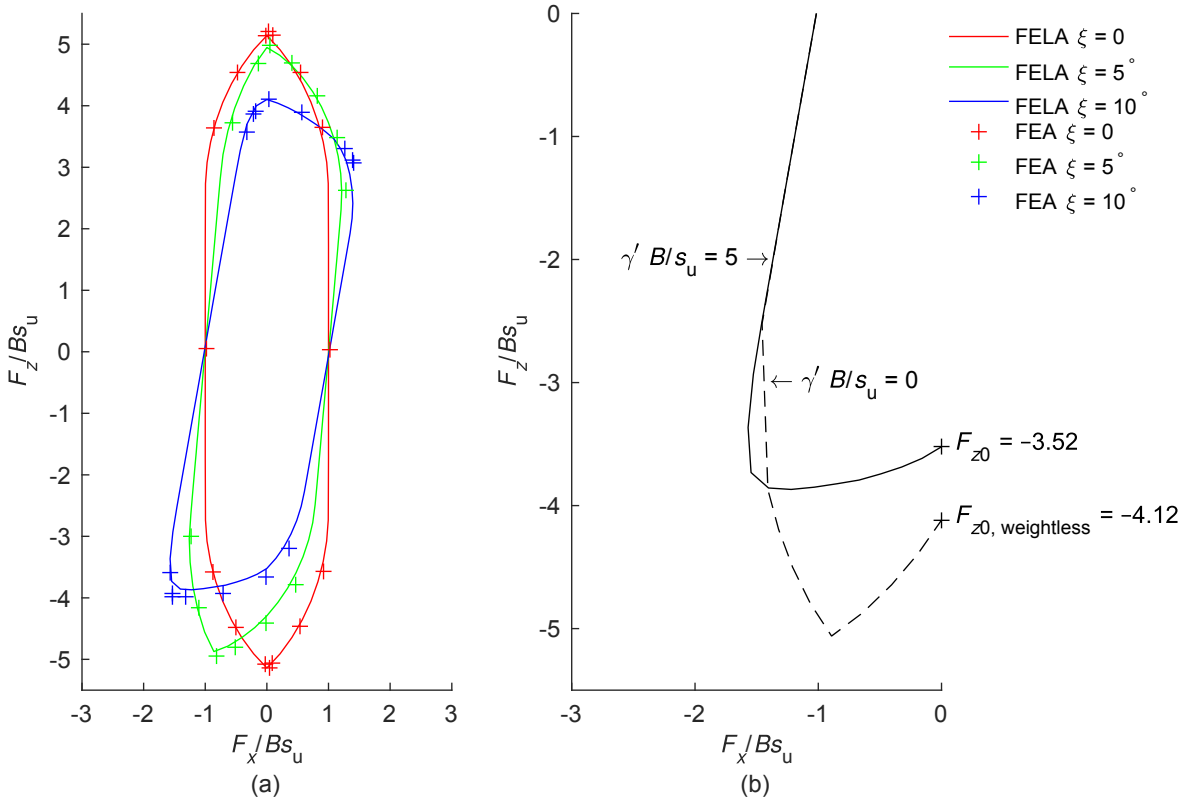

Figure 4.5: Normalised $F_z - F_x$ failure envelopes for soil with weight ($\gamma' B/s_u = 5$). $d/B = 0$, $\alpha = 1$, $T = \infty$: (a) full envelopes (b) zoomed view comparing failure envelopes for weightless soil and soil with $\gamma' B/s_u = 5$

shows that the uniaxial downwards vertical capacity (F_{z0}) reduces from $4.12Bs_u$ in weightless soil to $3.52Bs_u$ in soil with weight $\gamma' B/s_u = 5$, giving $F_{z0}/F_{z0,\text{ weightless}} = 0.854$. The variation of the $F_{z0}/F_{z0,\text{ weightless}}$ ratio was explored further using FELA. The results are shown in Figure 4.7 for a range of inclinations and normalised soil weight values. On flat ground, $F_{z0}/F_{z0,\text{ weightless}}$ is equal to 1; the capacity is independent of the soil weight. For low values of $\gamma' B/s_u$ the $F_{z0}/F_{z0,\text{ weightless}}$ ratio drops very gradually as the ground inclination increases from 0 to 10°. For higher values of $\gamma' B/s_u$, $F_{z0}/F_{z0,\text{ weightless}}$ decreases more rapidly with increasing inclination.

4.2.2.2 Skirted mudmat

The above analyses were repeated with perimeter skirts of embedment $d = 0.2B$ added to the mudmat. A normalised soil weight of $\gamma' B/s_u = 5$ was adopted for these analyses. Figure 4.8 shows that when skirts are introduced, the increase in horizontal capacity is greater for loading

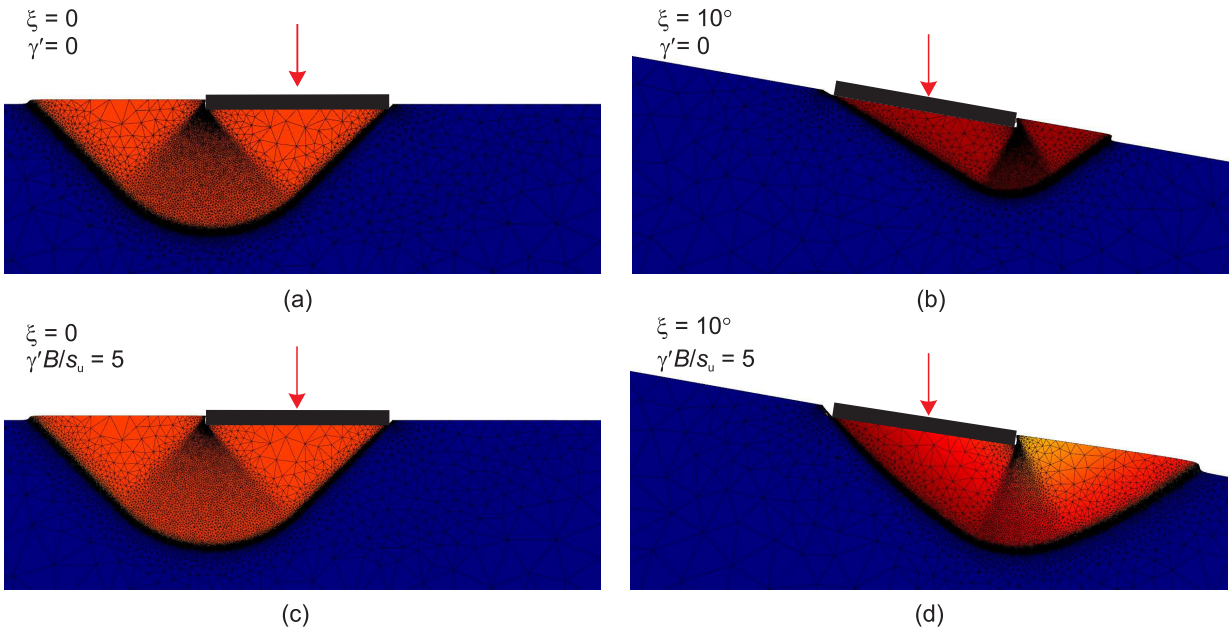

Figure 4.6: Failure mechanisms for surface mudmat under vertical loading: (a) $\xi = 0$, $\gamma' = 0$, (b) $\xi = 10°$, $\gamma' = 0$; (c) $\xi = 0$, $\gamma' B/s_u = 5$, (d) $\xi = 10°$, $\gamma' B/s_u = 5$. $d/B = 0$, $\alpha = 1$, $T = \infty$

into the slope than loading away from the slope. The addition of skirts also increases the mudmat's capacity under vertical loading, though this effect is more pronounced on flat ground than on inclined ground.

Thus far, the perimeter skirts and the underside of the mudmat have been treated as fully rough ($\alpha = 1$), with unlimited tension capacity ($T = \infty$). Figure 4.9 shows the effect of a smooth interface between the skirts and the adjacent soil ($\alpha = 0$ on all interfaces) for a skirted mudmat ($d/B = 0.2$) on soil with $\gamma' B/s_u = 5$. Note that a smooth foundation without any skirts only provides bearing capacity normal to the slope. Comparing the two sets of failure envelopes in Figure 4.9, it is apparent that smooth interface behaviour decreases the horizontal capacity by a greater amount for loading into the slope than loading away from the slope.

If it is assumed that no tension can be sustained ($T = 0$), the only source of uplift capacity is interface shearing on the skirts and on the underside of the mudmat. Figure 4.10 shows that even with fully rough behaviour ($\alpha = 1$) assumed on all interfaces, the change from $T = \infty$ to $T = 0$ causes an almost complete loss of uplift capacity, as well as a decrease in horizontal capacity.

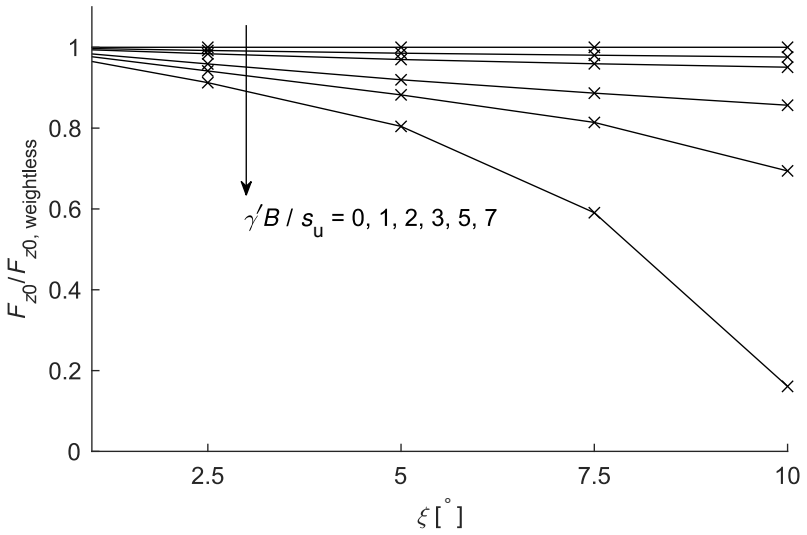

Figure 4.7: Reduction of capacity under purely vertical loading. $d/B = 0$, $\alpha = 1$, $T = \infty$

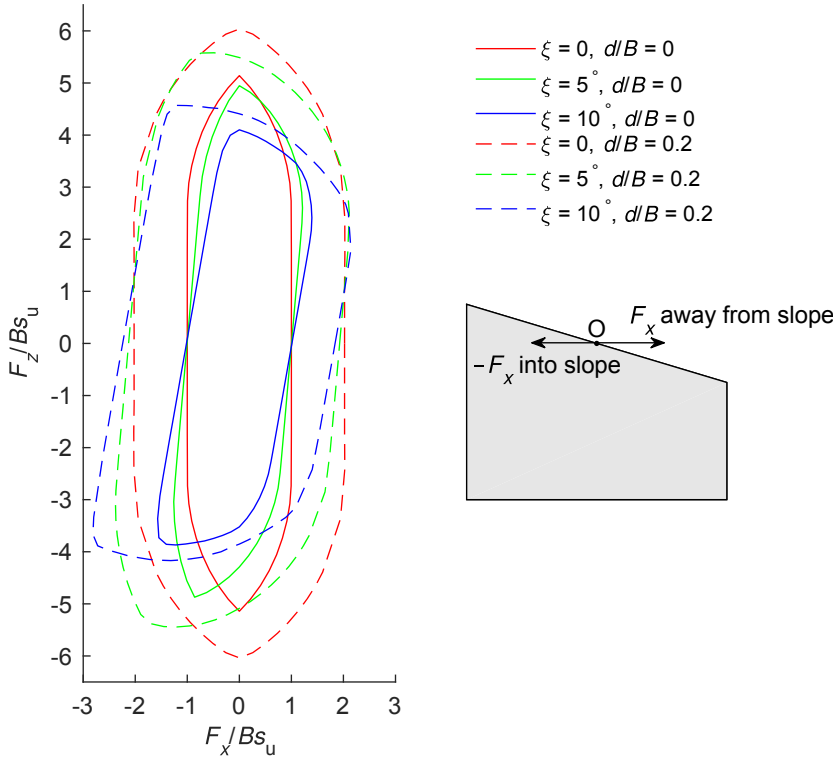

Figure 4.8: Effect of skirts on normalised $F_z - F_x$ failure envelopes. $\alpha = 1$, $T = \infty$, $\gamma' B/s_u = 5$

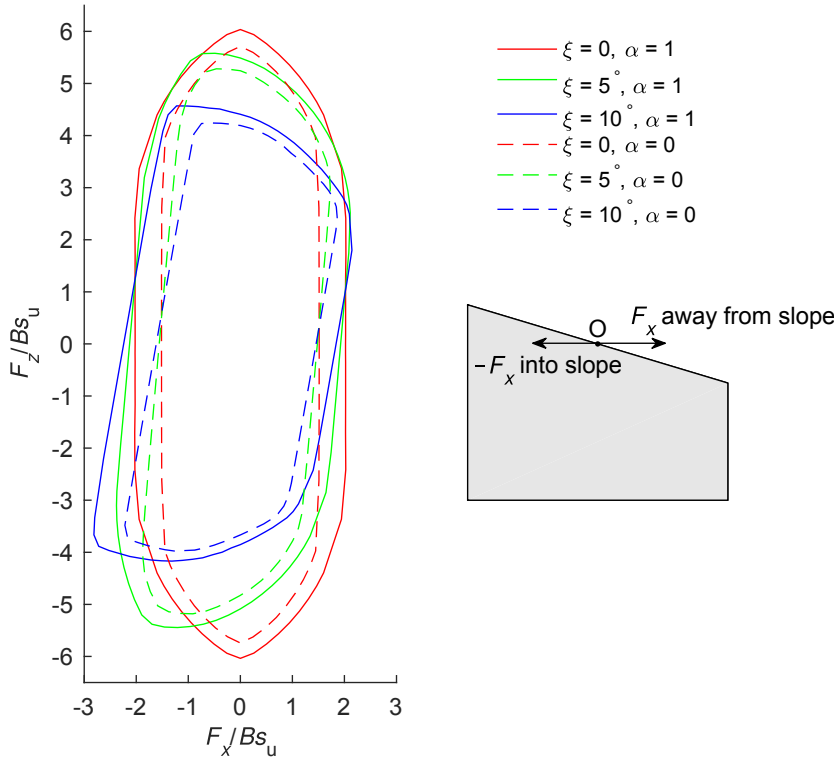

Figure 4.9: Effect of interface roughness on normalised $F_z - F_x$ failure envelopes. $d/B = 0.2$, $T = \infty$, $\gamma' B/s_u = 5$

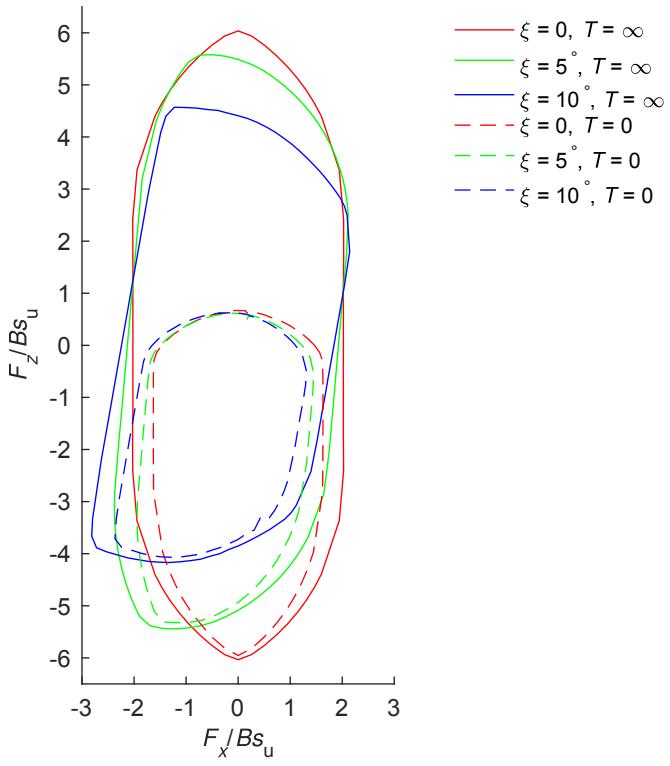

Figure 4.10: Effect of interface tensile capacity on normalised $F_z - F_x$ failure envelopes. $d/B = 0.2$, $\alpha = 1$, $\gamma' B/s_u = 5$

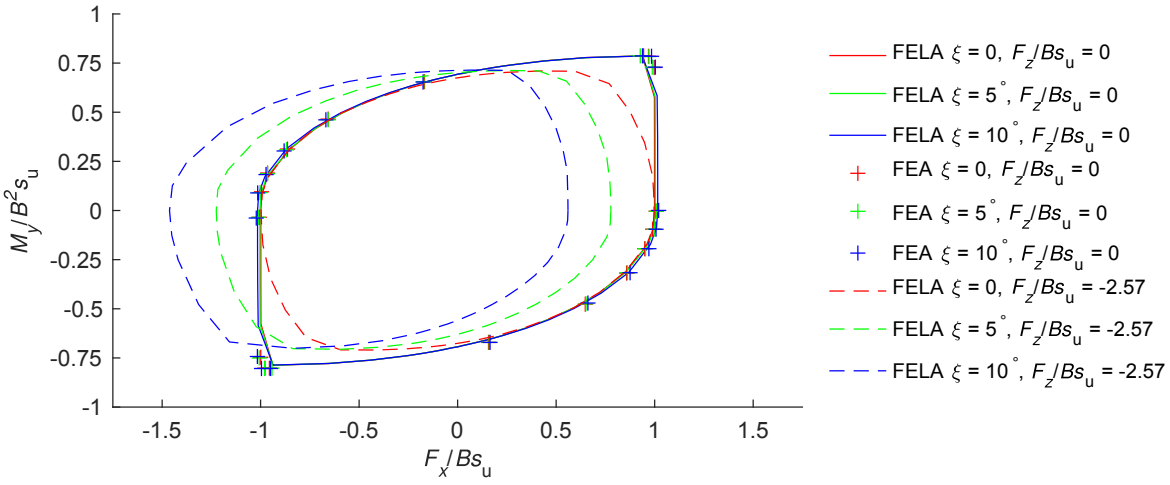

Figure 4.11: Normalised $F_x - M_y$ failure envelopes for two levels of vertical loading. $d/B = 0$, $\alpha = 1$, $T = \infty$, $\gamma' B/s_u = 0$

4.2.3 Combined horizontal and moment loading

Combined $F_x - M_y$ loading with $F_z = 0$ was analysed for an unskirted mudmat resting on weightless soil. All interfaces were modelled as fully rough with unlimited tensile capacity. Figure 4.11 shows that there is good agreement between capacities obtained using FELA and FEA. The solid lines in Figure 4.11 show that the $F_x - M_y$ failure envelope is only very marginally affected by ground inclination; this is because the moment M_y is unchanged by a rotation of axes, and for a small inclination the component of F_x acting tangential to the slope ($F_x \cos\xi$) is virtually identical to F_x. The well-known analytical 'scoop' mechanism predicts $M_y = 0.69B^2 s_u$ for the case of pure moment loading with $F_x = 0$. This result (which formally is only an upper bound plasticity solution) was confirmed by OxLim to within $\pm 1\%$ for all three values of ground inclination, and would appear to be exact.

4.2.4 Combined vertical, horizontal, and moment loading

A vertical dead load equal to half of the ultimate bearing capacity on flat ground (i.e. $F_{z0} = 2.57Bs_u$) was then applied, and the $F_x - M_y$ failure envelope calculations were repeated. As the ground inclination increases, the component of F_z acting tangential to the slope ($F_z \sin\xi$) increases. From the dashed lines in Figure 4.11, it can be seen that this causes translation of the $F_x - M_y$ failure envelope to the left. The horizontal capacity for loading away from the

Table 4.1: Input parameters for case study of a mudmat on sloping ground

Breadth of mudmat (B)	5 m
Length of foundation (out of plane) (L)	10 m
Embedment depth of skirts (d)	1.3 m
Thickness of skirts (t)	0.025 m
Soil submerged unit weight (γ')	3 kN/m^3
Mudline strength (s_{um})	0.77 kPa
Vertical strength gradient (ρ)	1.05 kPa/m
Seabed inclination (ξ)	0, 5°

slope is reduced by ∼55% and there is a similar increase in horizontal capacity for loading into the slope. These results are consistent with the $F_z - F_x$ failure envelopes in Figure 4.3 where at the same level of vertical load ($F_z/Bs_{\text{u}} = -2.57$) the horizontal capacity ranges from $+0.45Bs_{\text{u}}$ to $-1.47Bs_{\text{u}}$.

4.2.5 Case study

Plane strain FELA was applied to a recently completed mudmat design undertaken by Subsea 7 (a subsea engineering company serving the offshore energy industry) where seabed inclination was a concern (Subsea 7, 2013). The design parameters are summarised in Table 4.1. Roughness factors of $\alpha = 0$, 0.5, and 1 were considered in the analysis. Three different assumptions about interface tension were considered; $T = \infty$ on all interfaces: $T = 0$ on all interfaces, and $T = 0$ on the outside faces of the skirts only (with $T = \infty$ elsewhere).

The vertical and horizontal capacities obtained with the various combinations of α and T are summarised in Table 4.2. Upper bound failure mechanisms for the case of full roughness ($\alpha = 1$) are presented in Figure 4.12 (vertical loading) and Figure 4.13 (horizontal loading). $F_z - F_x$ failure envelopes for $T = \infty$ are shown in Figure 4.14.

Figure 4.12 shows failure mechanisms for vertical loading, assuming $T = \infty$. On flat ground the mechanism shows similarities to the Prandtl (1920) mechanism as it comprises a rigid wedge of soil directly under the foundation with fan zones of diffuse shearing next to this. On sloping ground the mechanism is more one-sided and corresponds to an 18% reduction in vertical capacity (Table 4.2). A similar reduction in vertical capacity is observed for the other

Table 4.2: Effect of seabed inclination on case study vertical and horizontal capacities

	α	$F_{z\,\text{slope}}/F_{z\,\text{flat}}$ [kN / kN]	$F_{x\,\text{slope}}/F_{x\,\text{flat}}$ [kN / kN]
$T=\infty$	0	771 / 971 = 0.79	114.5 / 121.6 = 0.94
	0.5	823 / 1014 = 0.81	149.9 / 157.5 = 0.95
	1	848 / 1031 = 0.82	168.9 / 181.5 = 0.93
$T=0$	0	748 / 964 = 0.78	0.0 / 41.6 = 0.00
	0.5	789 / 1012 = 0.78	115.1 / 135.4 = 0.85
	1	817 / 1031 = 0.79	148.8 / 160.0 = 0.93
$T=0, T=\infty^*$	0	749 / 964 = 0.78	104.4 / 110.0 = 0.95
	0.5	790 / 1011 = 0.78	134.3 / 140.2 = 0.97
	1	817 / 1031 = 0.79	149.5 / 160.4 = 0.93

* $T=0$ on outside of skirts, $T=\infty$ elsewhere

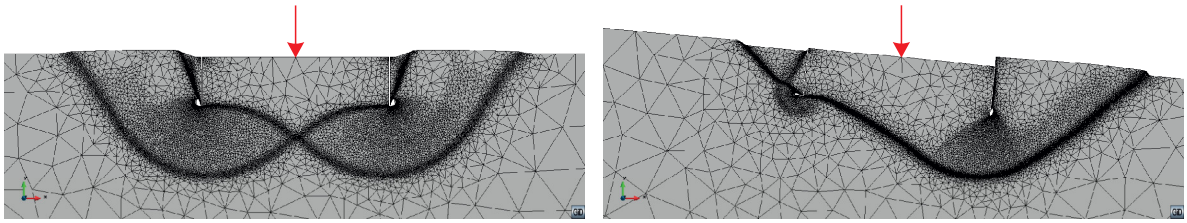

(a) (b)

Figure 4.12: Failure mechanisms under pure vertical loading: (a) $\xi=0$, $\alpha=1$, $T=\infty$; (b) $\xi=5^\circ$, $\alpha=1$, $T=\infty$

combinations of α and T.

Figure 4.13(a) and (b) and Figure 4.13(c) and (d) confirm the expectation that under horizontal loading, the elimination of interface tension causes a gap to form on the trailing side of the mudmat. Table 4.2 shows that the associated loss of capacity is around 12%: $160.0/181.5 = 0.88$ on flat ground and $148.8/168.9 = 0.88$ on sloping ground. Figure 4.13(e) and (f) are very similar to (c) and (d) and Table 4.2 shows that the corresponding capacities are virtually unchanged, but this only holds for the illustrated case of full roughness ($\alpha = 1$). If it is pessimistically assumed that the whole of the foundation/soil interface is both smooth ($\alpha = 0$) and unable to sustain tension ($T = 0$) then very low capacities are calculated. This includes a predicted capacity of zero for pure

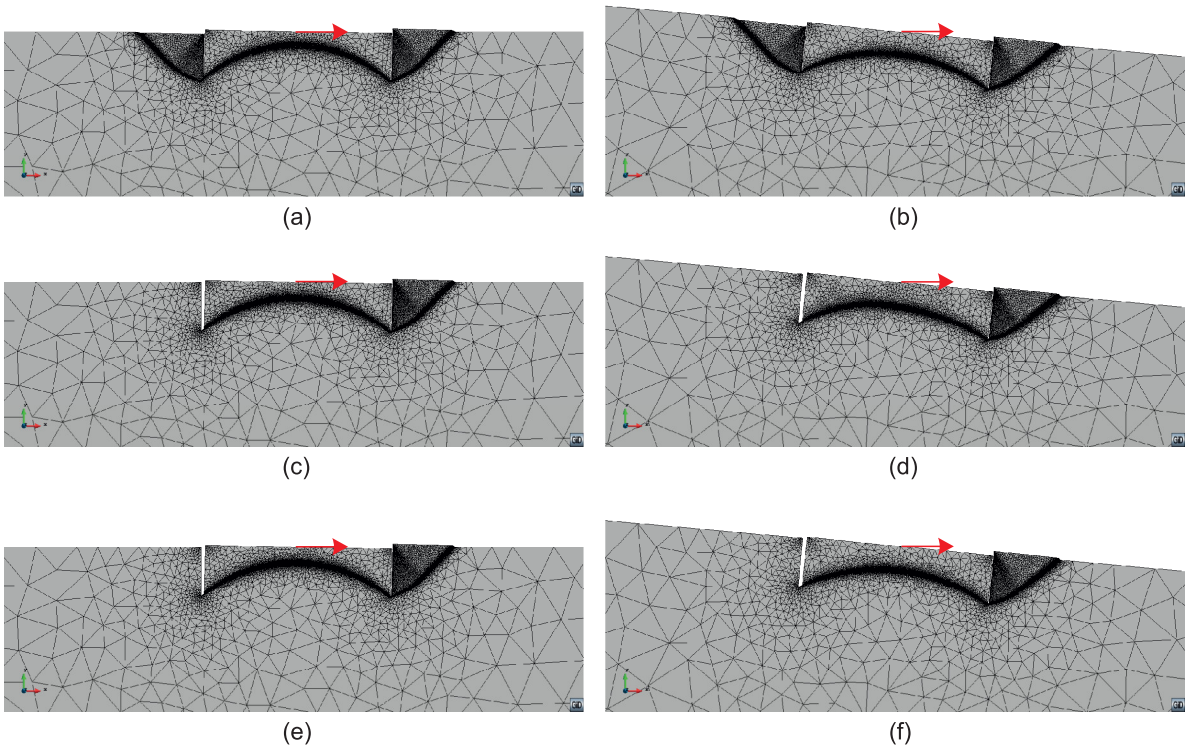

Figure 4.13: Failure mechanisms under pure horizontal loading: (a) $\xi = 0$, $\alpha = 1$, $T = \infty$; (b) $\xi = 5°$, $\alpha = 1$, $T = \infty$; (c) $\xi = 0$, $\alpha = 1$, $T = 0$; (d) $\xi = 5$, $\alpha = 1$, $T = 0$; (e) $\xi = 0$, $\alpha = 1$, $T = 0$ on outside of skirts, $T = \infty$ elsewhere; (f) $\xi = 5°$, $\alpha = 1$, $T = 0$ on outside of skirts, $T = \infty$ elsewhere

horizontal loading on sloping ground in which case the mudmat slips out of the ground, normal to the slope, with no resistance encountered.

The failure envelopes in Figure 4.14 (for $T = \infty$) show that the roughness factor can significantly influence capacity, particularly when the mudmat is on sloping ground and is loaded horizontally.

This case study highlights that it is not straightforward to predict the capacity of a mudmat on sloping ground under combined vertical and horizontal loading. FELA can provide a quick capacity estimate, and adaptive mesh refinement has been shown to be a useful aid in identification of the failure mechanism.

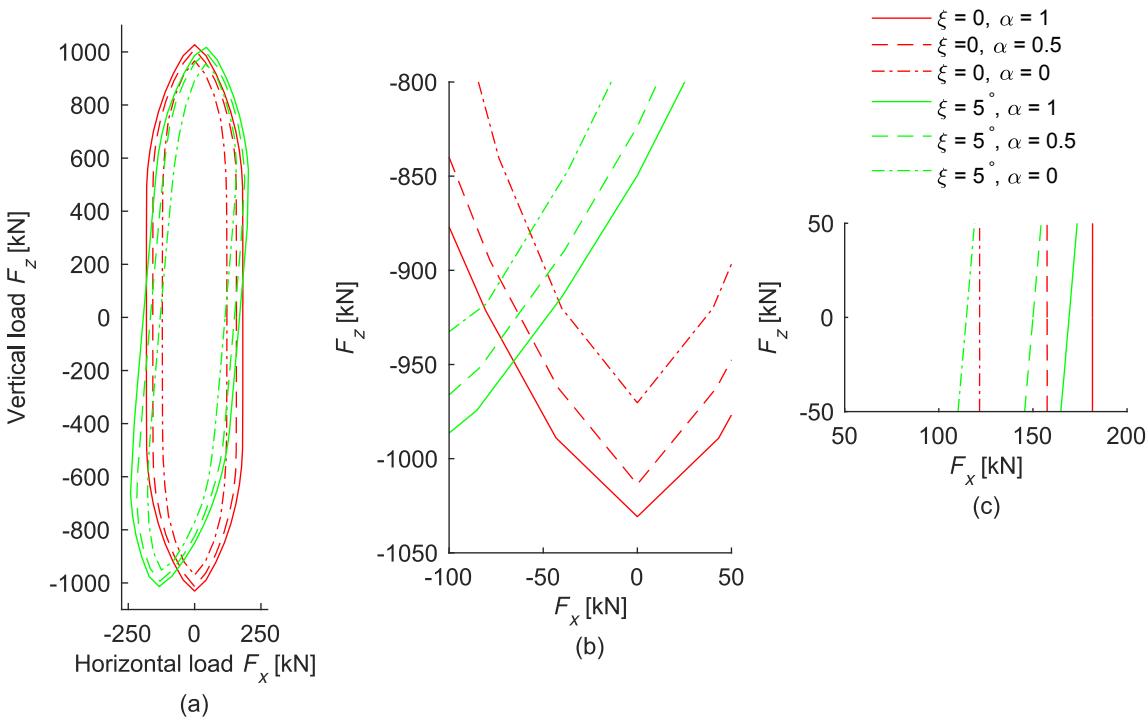

Figure 4.14: $F_z - F_x$ failure envelopes for case study ($T = \infty$ on all interfaces): (a) full failure envelopes; (b) zoomed view of failure envelope for predominantly vertical loading; (c) zoomed view of failure envelope for predominantly horizontal loading

4.3 Rectangular mudmat capacity under combined loading

4.3.1 Design case

An example design case of a rectangular mudmat, previously analysed by Feng et al. (2014), is the starting point for this section. The mudmat notation, geometry, loading, and soil parameters are shown in Figure 4.15. It is assumed that the mudmat skirts and the confined soil plug act as a rigid body, and that the mudmat base is fully rough with unlimited tension capacity ($\alpha_{\text{base}} = 1$ and $T_{\text{base}} = \infty$). The skirt walls are modelled as half-rough with no tension capacity ($\alpha_{\text{skirt}} = 0.5$ and $T_{\text{skirt}} = 0$). The design input parameters match those in Feng et al. (2014) and are listed in Table 4.3.

Analysis was undertaken using 3D FELA. An initial unrefined mesh is shown in Figure 4.16(a) and Figure 4.16(b) shows additional prescribed planes in the mesh. As well as 'fans' of planes at the mudmat base, planes were added from the mudmat base rising at 45° to the soil surface. The bracketing error obtained using the initial unrefined mesh was sufficiently small ($\pm 2.4\%$), and resulted in a very quick analysis time (< 20 seconds, when

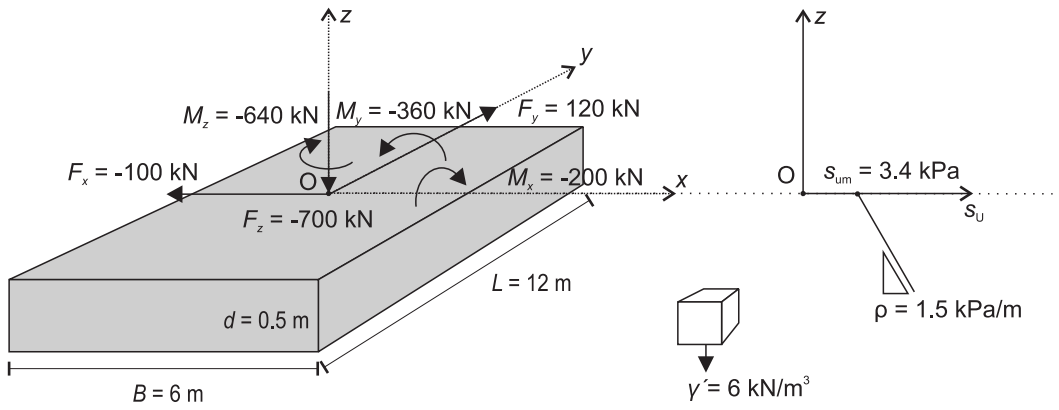

Figure 4.15: Rectangular mudmat design case notation, geometry, loading, and soil parameters

Table 4.3: Design case input data (from Feng et al. (2014))

Mudmat geometry		Soil and interface properties		Loading	
B	6 m	s_{um}	3.4 kPa	F_x (live)	-100 kN
L	12 m	ρ	1.5 kPa/m	F_y (live)	$+120$ kN
d	0.5 m	α_{skirt}	0.5	F_z (dead)	-700 kN
		γ'	6 kPa/m	M_x (live)	-200 kNm
		α_{base}	1	M_y (live)	-360 kNm
		T_{skirt}	0	M_z (live)	-640 kNm
		T_{base}	∞		

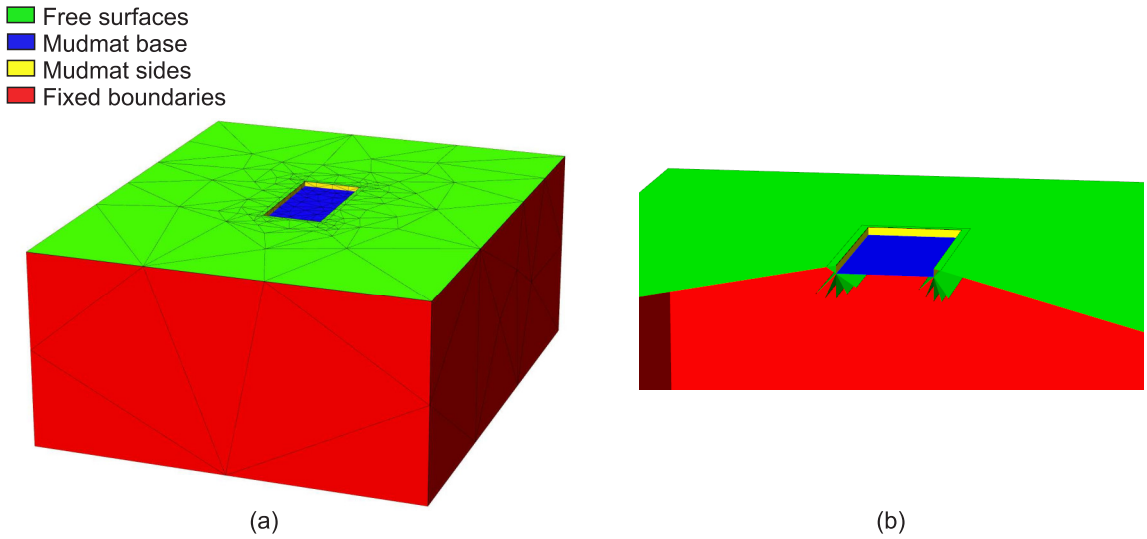

Figure 4.16: Rectangular mudmat soil domain and boundary conditions: (a) initial unrefined FELA mesh; (b) a cutaway view of the soil domain showing prescribed planes in the mesh

LB and UB analyses were solved in series on a 3.1 GHz machine with 32 GB RAM). The tight bracketing obtained is somewhat explained by visualising the failure mechanism (Figure 4.17). The mechanism involves interface shearing at the foundation base and the displacement of wedges of soil next to the foundation skirts. The prescribed planes in the mesh rising from the base of the foundation at 45° help to capture this component of the mechanism. Figure 4.17 shows that the foundation is rotating about a vertical axis axis through a point near its back right corner. The FELA calculated load factor is 1.53, which is almost identical to the load factor of 1.54 obtained using by Feng et al. (2014). Feng et al. followed a design methodology based on a series of expressions for foundation capacity derived using FEA (the methodology is outlined in Section 2.4). Both FELA and the Feng et al. design approach provide very quick capacity estimates.

The loads on the mudmat were varied from the base case (Table 4.3) in order to quantify any effect on the load factor. The results are summarised in Table 4.4. The load factor is very sensitive to doubling or removing the torsional load on the mudmat (0.974 when M_z is doubled and 2.413 when M_z is removed). However, there is little, or no, change to the load factor when the overturning moments are doubled or removed. This highlights the significance of torsional loads on mudmat capacity. These results informed a study that focuses on the combined horizontal and torsional capacity of mudmats, and is subsequently described.

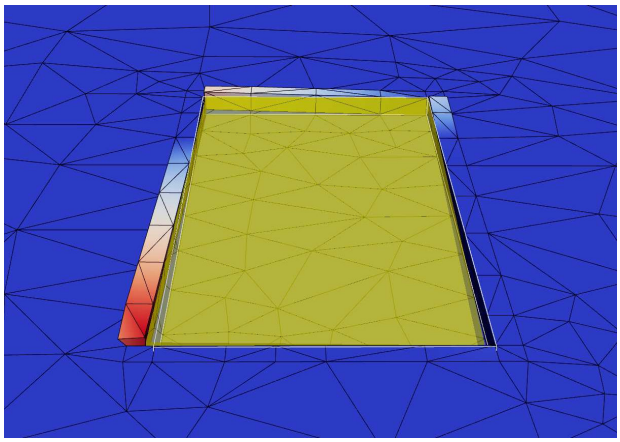

Figure 4.17: Failure mechanism for the design case. Shaded by UB velocity magnitude

Table 4.4: Design case load factors

Load case	Load factor
Design case	1.535
M_z doubled	0.974
M_z removed	2.413
M_x doubled	1.535
M_x removed	1.535
M_y doubled	1.513
M_y removed	1.535
M_x and M_y doubled	1.513

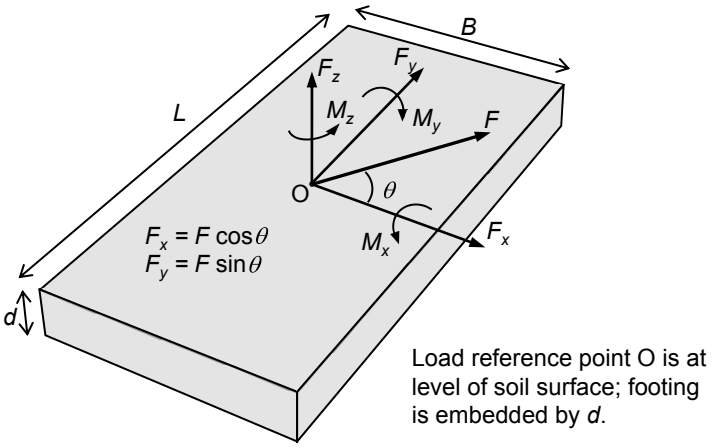

Figure 4.18: Mudmat notation and sign conventions

4.3.2 Problem overview

As shown in Figure 4.18, a skirted mudmat is modelled as an embedded rigid body of breadth, B, along the x-axis, length, L, along the y-axis, and depth, d, along the z-axis. The length to breadth aspect ratio was fixed at $L/B = 2$ as this is a typical value adopted in practice (Subsea 7, personal communication, 2014). In treating the embedded mudmat as a rigid body it was tacitly assumed that sufficient interior skirts are present to fully confine the soil plug (Mana et al., 2013). The base of the rigid body was modelled as fully rough, with unlimited interface tension capacity. The soil was modelled as having homogeneous undrained shear strength. Along the mudmat sides, both unlimited-tension and zero-tension interfaces with the adjacent soil were considered.

Previous research has shown that the inclusion of soil weight in the model does not affect the calculated capacity of an embedded mudmat on flat ground if an unlimited-tension interface is assumed along the sides, while it does when a zero-tension interface is assumed. If a zero-tension interface is assumed and the soil is modelled as weightless, a gap forms behind the mudmat if it displaces horizontally. Consequently, there is no active soil mobilisation. If a zero-tension interface is assumed and soil weight is included in the model then the soil may remain attached on the active side, which leads to enhanced capacity, but this is dependent on the dimensionless soil weight to strength ratio $\gamma' B/s_u$. It is shown here that if a mudmat is modelled in weightless soil with unlimited-tension and zero-tension

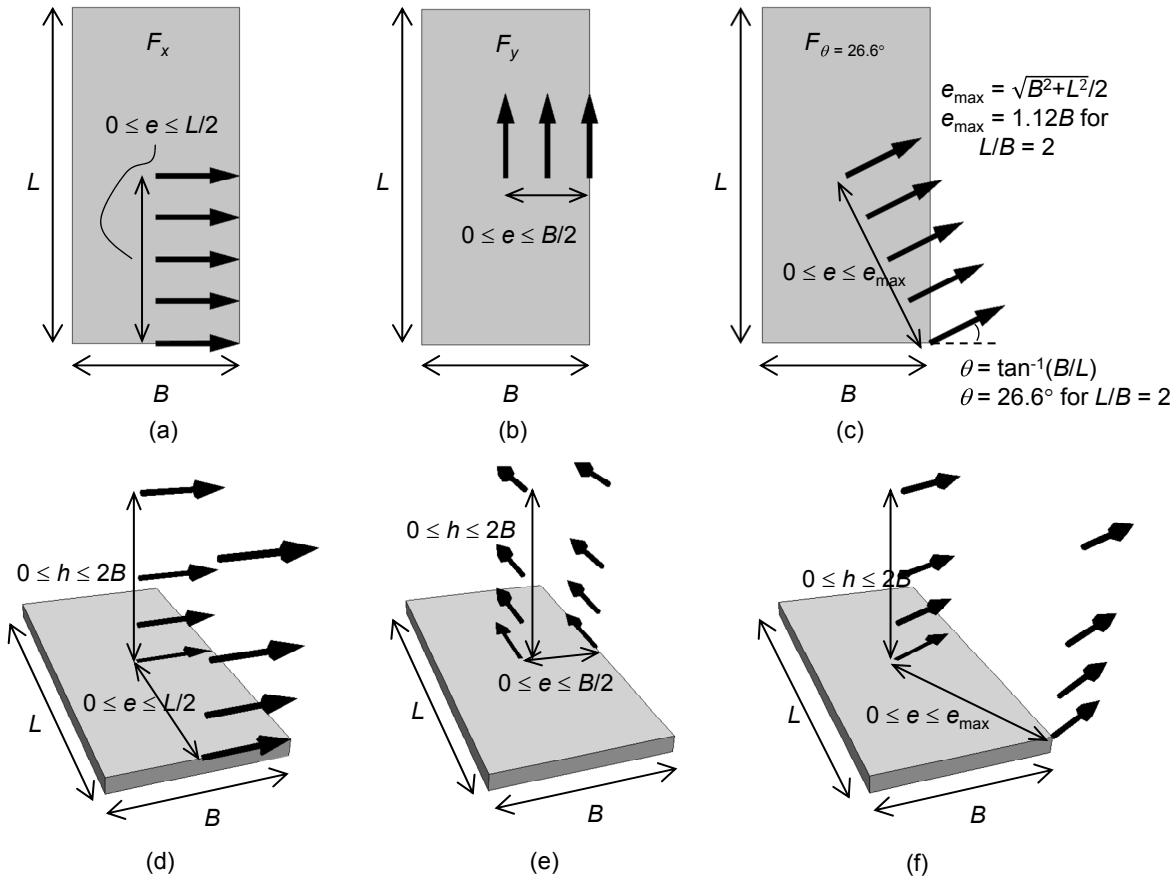

Figure 4.19: Mudmat loading arrangement: (a)–(c) feasible eccentricity e of horizontal loading; (d)–(f) horizontal loading applied at height h

interfaces along the sides, the resulting capacities bracket the corresponding capacity of a mudmat in soil with weight, irrespective of the assumed interface tension capacity on the sides.

Complexity is added to the analysis in three stages.

Stage 1. Horizontal and torsional loading: When considering combined horizontal and torsional loading (F_x, F_y, M_z), emphasis was given to horizontal loads generating 'feasible' levels of torsion as defined in Figure 4.19(a)–(c). The largest feasible eccentricity $e_{\max}$ occurs when a force is applied at the mudmat corner at an angle $\theta = \tan^{-1}(B/L)$, which is 26.6° due to the 2:1 aspect ratio considered.

Stage 2. Horizontal, torsional, and moment loading: Horizontal forces were applied at a height, h, above the mudmat, resulting in combined horizontal and moment loading

on the foundation (Figure 4.19(d)–(f)). Forces applied at both an eccentricity, e, and a height, h, with respect to the mudmat centre result in five degree-of-freedom loading (F_x, F_y, M_x, M_y, M_z).

Stage 3. Horizontal, torsional, moment, and vertical loading: The ultimate vertical capacity (F_{z0}) was calculated using a refined FELA mesh to closely bracket the solution. A vertical dead load equal to $0.5F_{z0}$ was then applied while the mudmat was again subjected to five degree-of-freedom live loading (F_x, F_y, M_x, M_y, M_z) as outlined in Stage 2.

The soil domain was sized such that it comfortably contained the soil failure mechanism for all of the load combinations considered. For a surface foundation ($d = 0$), a soil domain $7B \times 7B$ in plan and $3.5B$ deep was sufficient, with larger domains used for embedded foundations ($d > 0$). As in the design case, additional prescribed planes were attached to the edges of the mudmat base and for embedded mudmats, planes rising at 45° from the mudmat base to the soil surface were also included. Initial unrefined FELA meshes for surface and embedded foundations are shown in Figure 4.20.

The interface at the base of the embedded rigid foundation was modelled as fully rough, with unlimited tensile capacity. The mudmat sides were conservatively modelled as fully smooth with either unlimited tensile capacity, $T = \infty$, or zero tensile capacity, $T = 0$.

4.3.3 Surface mudmats (d = 0)

4.3.3.1 Horizontal and torsional loading

A surface mudmat under combined horizontal and torsional loading was analysed using two independent approaches: by applying the LB and UB plasticity theorems to the interface, and using 3D FELA.

Analytical LB values for F_x, F_y and M_z were found by numerically integrating the shear stress components τ_x and τ_y that would be induced by foundation rotation about a prescribed point (x_0, y_0), as shown in Figure 4.21(a):

$$F_x = \int_{-L/2}^{L/2} \int_{-B/2}^{B/2} \tau_x \, \mathrm{d}x\mathrm{d}y \tag{4.1}$$

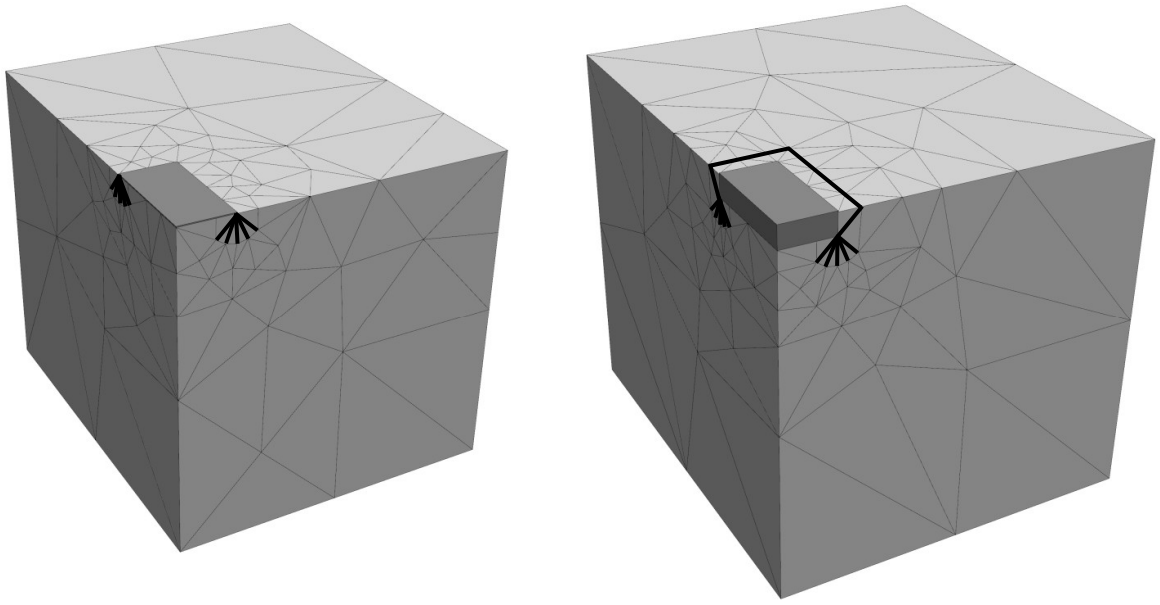

Figure 4.20: Initial FELA mesh of quarter model showing prescribed planes in the mesh as bold lines: (a) surface mudmat; (b) embedded mudmat

$$F_y = \int_{-L/2}^{L/2} \int_{-B/2}^{B/2} \tau_y \, \mathrm{d}x\mathrm{d}y \tag{4.2}$$

$$M_z = \int_{-L/2}^{L/2} \int_{-B/2}^{B/2} (x\tau_y - y\tau_x) \, \mathrm{d}x\mathrm{d}y \tag{4.3}$$

where $\tau_x = s_\mathrm{u} \cos\alpha$ and $\tau_y = s_\mathrm{u} \sin\alpha$, with $\cos\alpha$ and $\sin\alpha$ calculated as shown in Figure 4.21.

The analytical UB solution was formulated by equating the internal and external work rates when the mudmat rotates with a virtual angular velocity ω about (x_0, y_0), as shown in Figure 4.21(b):

$$\dot{W}_\mathrm{int} = s_\mathrm{u} \, \omega \int_{-L/2}^{L/2} \int_{-B/2}^{B/2} r \, \mathrm{d}x\mathrm{d}y \tag{4.4}$$

$$\dot{W}_\mathrm{ext} = F_x \omega y_0 - F_y \omega x_0 + M_z \omega \tag{4.5}$$

with r calculated as shown in Figure 4.21. The 3D failure surface obtained by evaluating these equations numerically for a range of rotation centres is shown in Figure 4.22(a). It should be noted that the complete failure surface is symmetrical about the $F_x - F_y$, $F_x - M_z$, and $F_y - M_z$ planes. The LB equations produced results which matched precisely with the UB equations, indicating an exact theoretical solution. The circular contour in the plane $M_z = 0$ confirms that the horizontal capacity of the mudmat in this case is always equal to the interface shear

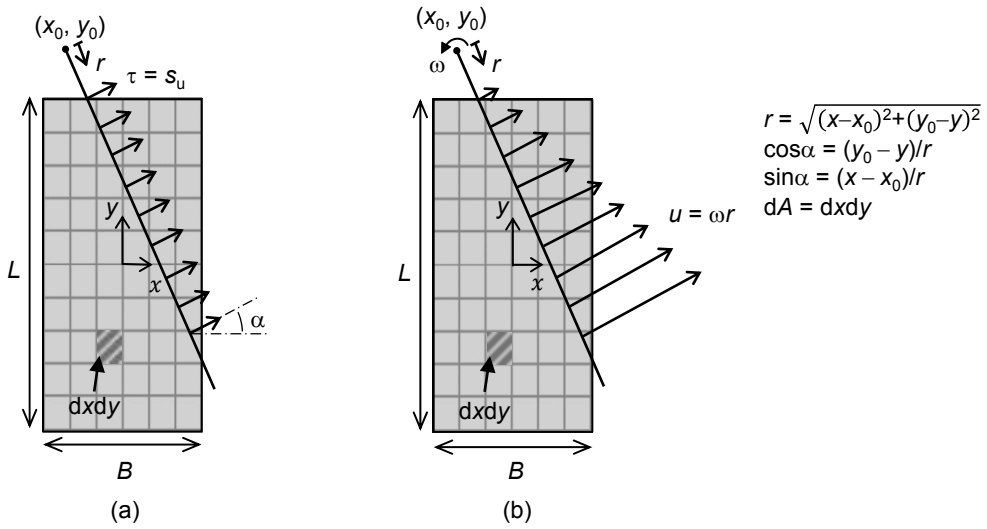

Figure 4.21: Analytical solution for combined horizontal and torsional loading of a surface mudmat: (a) lower bound shear stresses; (b) upper bound velocities

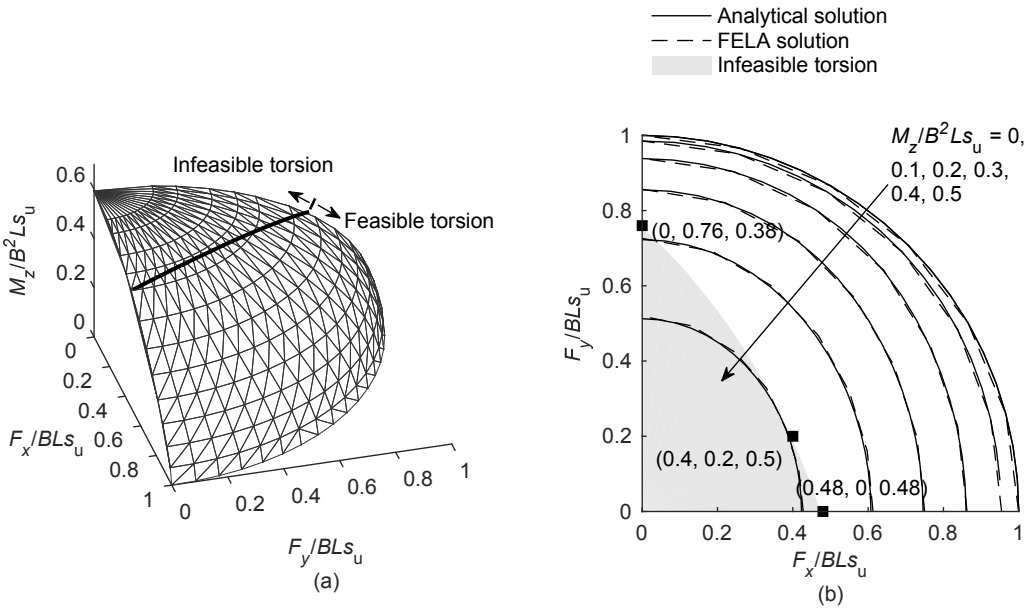

Figure 4.22: Failure envelope for a surface mudmat under combined horizontal and torsional loading, showing region of feasible torsion: (a) 3D failure surface from analytical solution; (b) 2D contour plot comparing analytical solution with FELA solution

capacity, BLs_u, irrespective of the relative magnitudes of F_x and F_y.

Figure 4.22(b) shows that excellent agreement was found between the analytical solution and the results obtained using 3D FELA. The FELA results for combined horizontal loading (F_x, F_y) with $M_z = 0$ solved to $\pm 0.01\%$ error without any mesh refinement, while in pure torsion (M_z with $F_x = F_y = 0$) an unrefined mesh solved to $\pm 2\%$ error. Each analysis completed in less than 10 seconds and the failure mechanism was always confined to interface shearing between the mudmat and the soil. The feasible torsion limit increases as the loading direction θ is varied (Figure 4.18); from $M_z = 0.48B^2Ls_u$ when $\theta = 0$ (pure F_x loading), to a maximum of $M_z = 0.5B^2Ls_u$ when $\theta = 26.6^\circ$, before reducing to $M_z = 0.38B^2Ls_u$ when $\theta = 90^\circ$ (pure F_y loading).

4.3.3.2 Combined horizontal, torsional, and moment loading

Figure 4.23 shows the capacity of a surface mudmat subjected to horizontal forces applied at a range of eccentricities from, and heights above, the load reference point (O in Figure 4.18). When $e/B = 0$ and $h/B = 0$ the capacity of a surface mudmat is the same whether the mudmat is loaded by F_x, F_y, or $F_{\theta=26.6^\circ}$ (corresponding to the circular failure locus when $M_z = 0$ in Figure 4.22). When these forces are applied at a normalised height $h/B = 0.5$ there is no reduction in capacity compared with $h/B = 0$ and failure still occurs though interface shearing between the mudmat and the soil. When F_x and $F_{\theta=26.6^\circ}$ are applied at a height $h/B = 1$ there is a small reduction in capacity compared with the same forces applied at $h/B = 0$, but no reduction for F_y. When $h/B = 2$ the reduction in capacity is substantial for F_x and $F_{\theta=26.6^\circ}$, but there is still only a minor reduction in capacity for a mudmat subjected to F_y at this height.

The reduction in capacity when the mudmat is subjected to F_x or $F_{\theta=26.6^\circ}$ at $h/B > 0.5$ can be attributed to the increased overturning moment acting on the mudmat, and the effect can be seen in the failure mechanism. Figure 4.24 shows failure mechanisms for a mudmat subjected to forces in various directions at a height $h/B = 2$. F_x and $F_{\theta=26.6^\circ}$ cause failure by 'rolling' about the y-axis (Figure 4.24(a) and (c)), whereas F_y predominantly causes failure through translation in the y-direction with very little rotation (Figure 4.24(b)). This is consistent with the increased moment capacity associated with 'pitching' rotation about the x-axis.

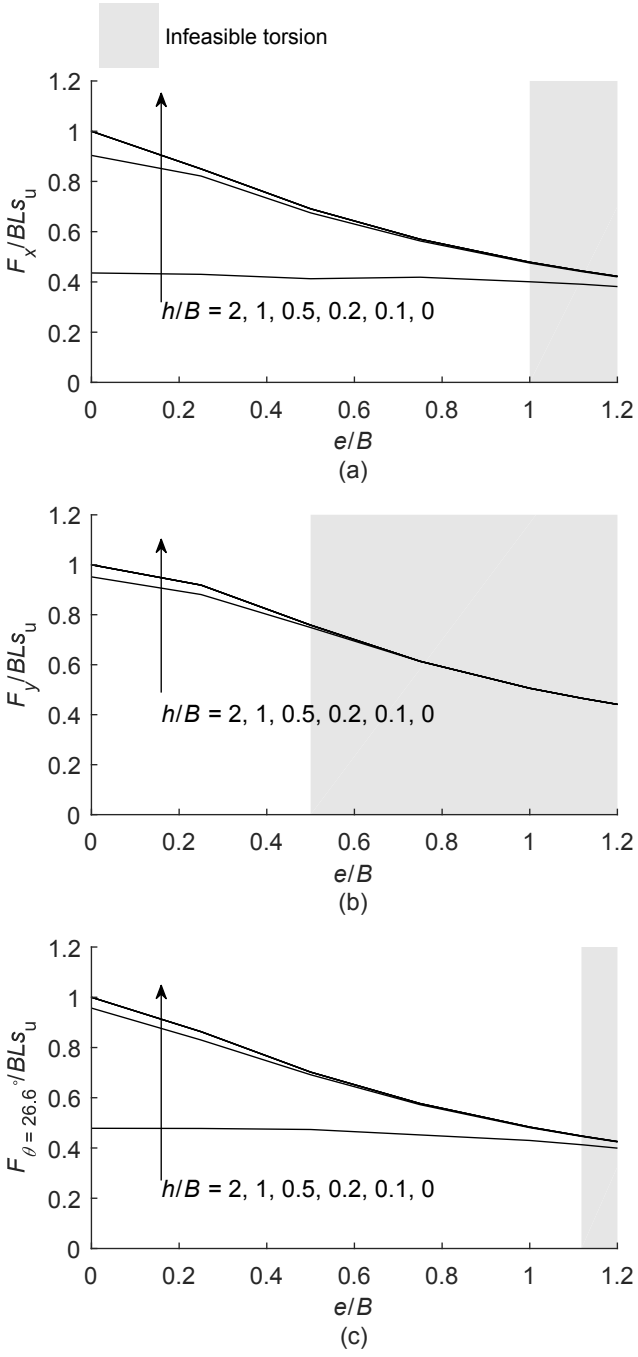

Figure 4.23: Capacity charts for surface mudmats under horizontal loading in various directions, applied at a range of normalised eccentricities (e/B) and heights (h/B): (a) F_x; (b) F_y; (c) $F_{\theta=26.6^\circ}$. Lines representing the lower values of h/B may overlap

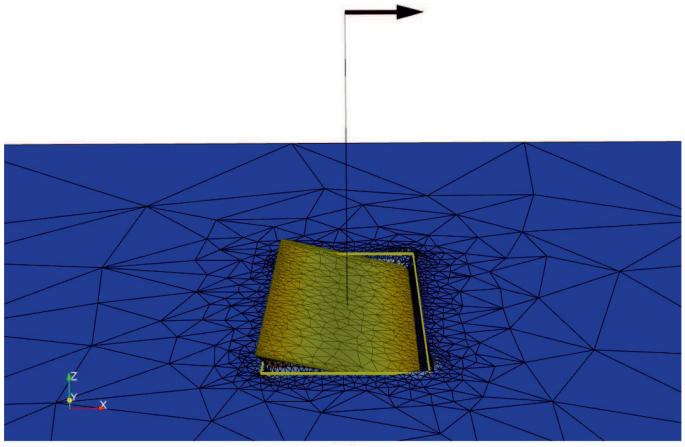

(a)

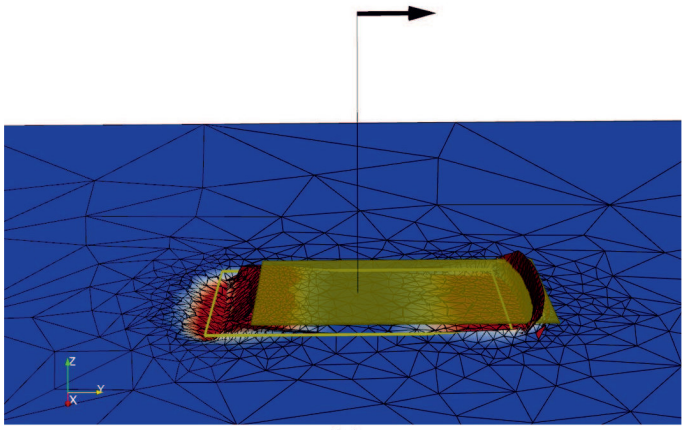

(b)

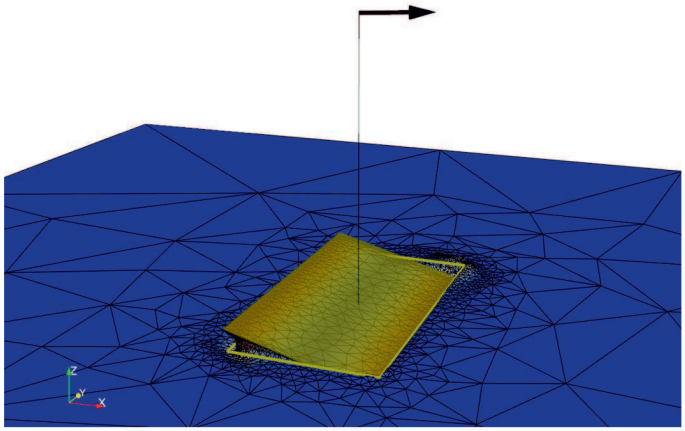

(c)

Figure 4.24: Failure mechanisms for a surface mudmat subjected to horizontal loading in various directions, applied at a normalised height $h/B = 2$: (a) F_x; (b) F_y; (c) $F_{\theta=26.6^\circ}$. $T = \infty$ on sides. Shaded by UB velocity magnitude

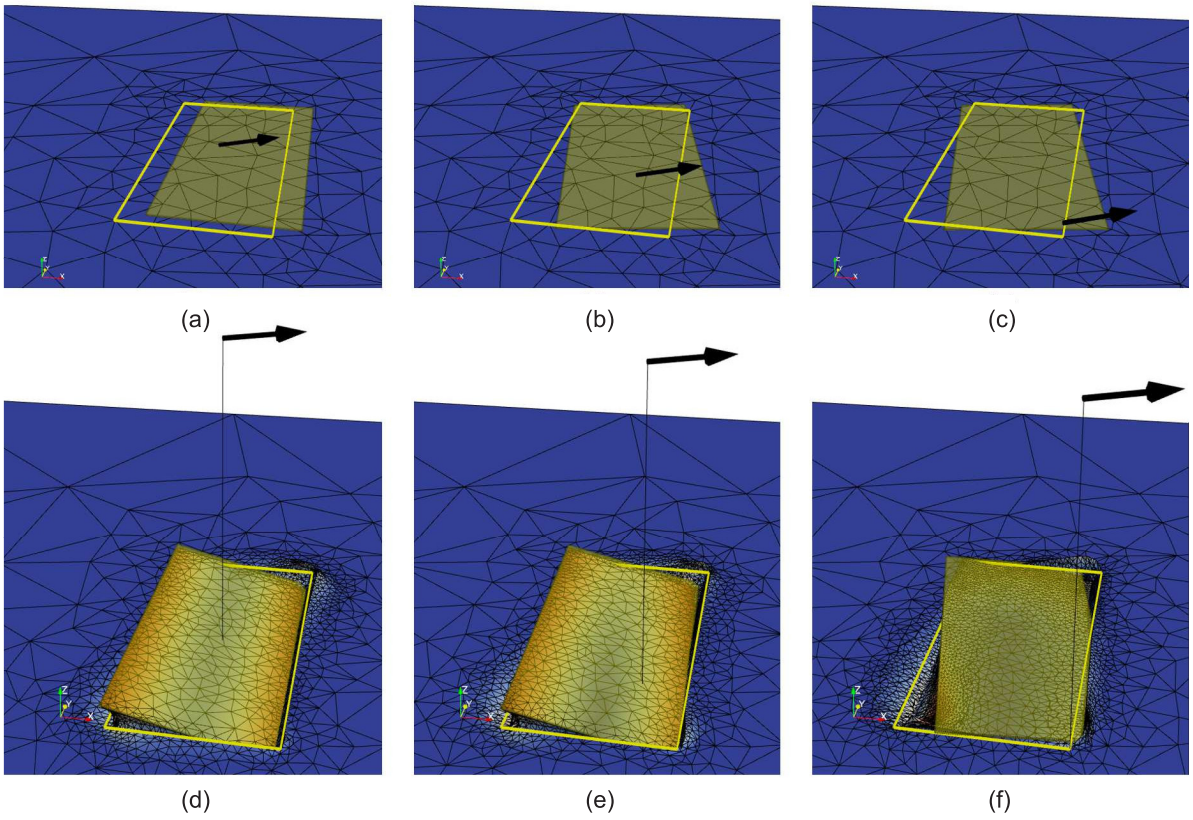

Figure 4.25: Failure mechanisms for a surface mudmat subjected to horizontal loading $F_{\theta=26.6^\circ}$, showing effect of eccentricity and height of application: (a) $e/B = 0$, $h/B = 0$; (b) $e/B = 0.5$, $h/B = 0$; (c) $e/B = 1.12$, $h/B = 0$; (d) $e/B = 0$, $h/B = 2$; (e) $e/B = 0.5$, $h/B = 2$; (f) $e/B = 1.12$, $h/B = 2$. Shaded by UB velocity magnitude

For a given height of load application, the capacity reduces as the normalised eccentricity e/B increases due to the additional torsional moment acting on the mudmat. This reduction is less apparent when the mudmat is loaded at a height $h/B = 2$ by F_x or $F_{\theta=26.6^\circ}$, as failure is still dominated by rolling about the y-axis and not twisting about the z-axis. Failure mechanisms are presented in Figure 4.25 for a mudmat subjected to loading by $F_{\theta=26.6^\circ}$. When $F_{\theta=26.6^\circ}$ loading is applied at $h/B = 0$ and $e/B = 0$ failure occurs through translation with no rotation or twist (Figure 4.25(a)). When $F_{\theta=26.6^\circ}$ is applied with increasing eccentricity the mudmat fails through translation as well as increasing amounts of twist (Figure 4.25(b) and (c)). This corresponds to the steep reduction in capacity when $h/B = 0$ and $0 \leq e/B \leq 1.12$ in Figure 4.23(c). A mudmat under to $F_{\theta=26.6^\circ}$ loading at $h/B = 2$ and $e/B = 0$ fails through rotation about the y-axis (Figure 4.25(d)). The failure mechanism does not change significantly as e/B increases to 0.5 (Figure 4.25(e)) which corresponds to the

constant capacity when $h/B = 2$ and $0 \leq e/B \leq 0.5$ in Figure 4.23(c). When $e/B = 1.12$ twisting is visible in the failure mechanism (Figure 4.25(f)) and the capacity reduces slightly (Figure 4.23(c)).

4.3.4 Embedded mudmats ($d > 0$)

4.3.4.1 Combined horizontal and torsional loading

Embedded mudmats under combined horizontal and torsional loading mobilise wedges of soil adjacent to the mudmat at failure, and this significantly increases their capacity when compared with surface mudmats. Because of the 2:1 aspect ratio considered, embedded mudmats have a larger capacity under pure F_x loading than under pure F_y loading. This is shown in Figure 4.26(a), where the failure envelopes for combined $F_x - F_y$ loading (with $M_z = 0$) are no longer circular when the mudmat is embedded. Failure envelopes for surface and embedded mudmats subjected to three cases of combined horizontal loading (F_x, F_y, and $F_{\theta=26.6^\circ}$) and torsional loading are shown in Figure 4.26(b) – (d), with zones of infeasible torsion shaded.

Comparing the solid and dotted lines in Figure 4.26, it can be seen that imposition of a tension cutoff on the sides of the mudmat reduces the resistance to combined horizontal and torsional loading, but the shape of the failure envelope does not change appreciably. The failure mechanism for an embedded mudmat with $T = \infty$ on the sides, subjected to F_y loading, is shown in Figure 4.27(a). Wedges of soil are displaced on either side of the mudmat in the direction of the horizontal load. Figure 4.27(b) shows the failure mechanism when $T = 0$ on the sides. In this case, a wedge of soil is only displaced in front of the mudmat and a gap forms behind. The mudmat in Figure 4.27(a) mobilises more soil at failure than the mudmat in Figure 4.27(b), which results in a higher capacity.

Plastic displacement vectors which are inclined at angle, ζ, to the F_x axis are plotted in Figure 4.26(a) for a mudmat subjected to horizontal loading in the direction $\theta = 45^\circ$ (equal components of F_x and F_y). As expected, a surface mudmat ($d/B = 0$) has a plastic displacement direction $\zeta = \theta$ and the failure mechanism shows the mudmat translating in the direction of the load (Figure 4.28(a)). As the embedment ratio increases, however, the mudmat translates more

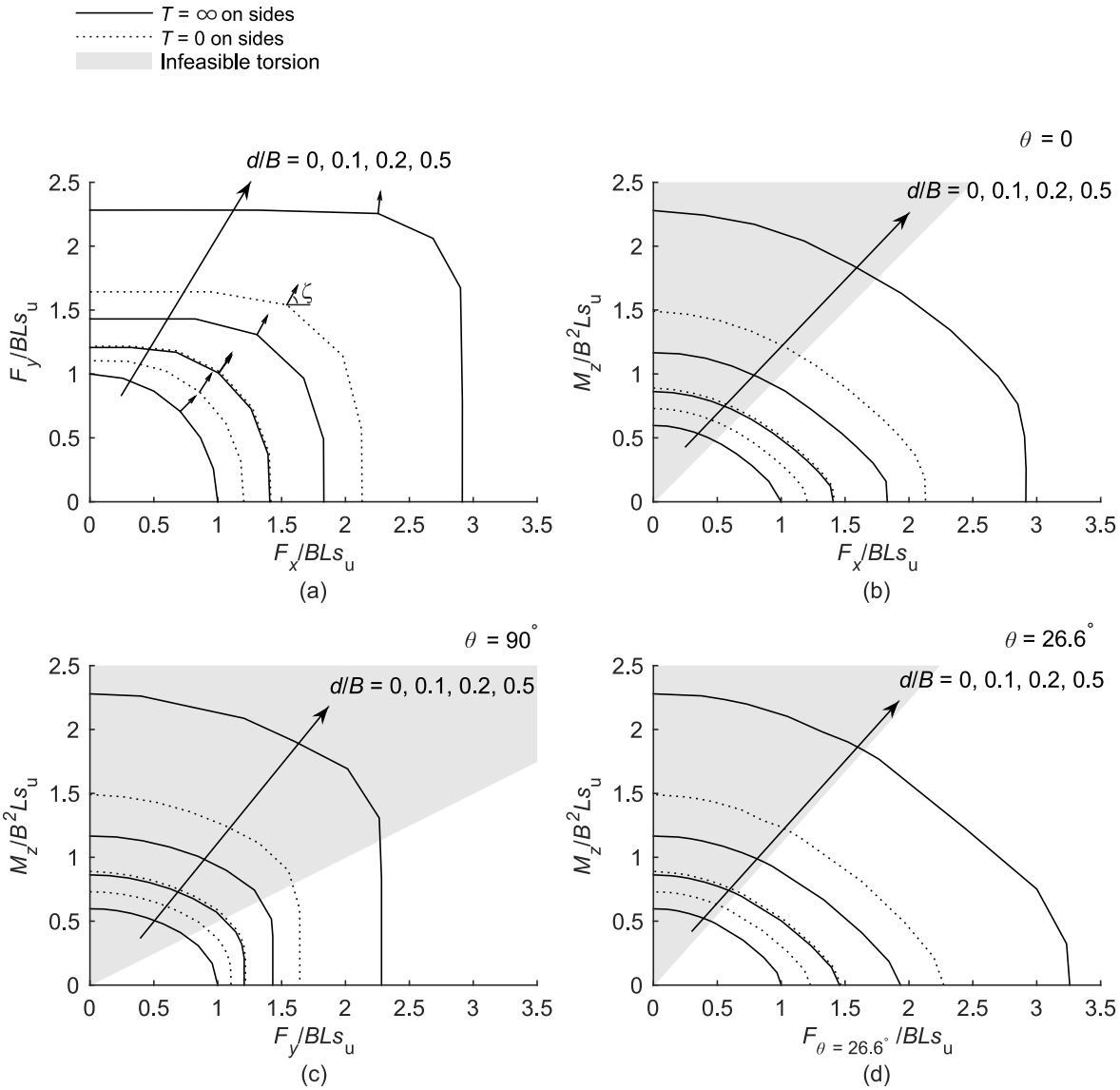

Figure 4.26: Failure envelopes for surface and embedded mudmats subjected to combined horizontal and torsional loads: (a) $F_x - F_y$ ($M_z = 0$); (b) $F_x - M_z$; (c) $F_y - M_z$; (d) $F_{\theta=26.6^\circ} - M_z$

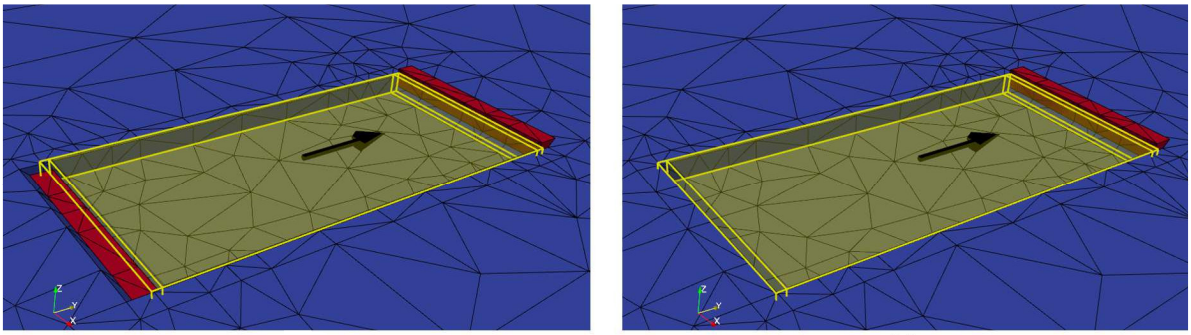

Figure 4.27: Failure mechanisms for an embedded mudmat ($d/B = 0.1$) loaded horizontally (F_y), showing the effect of interface tension capacity on the mudmat sides: (a) $T = \infty$; (b) $T = 0$. Shaded by UB velocity magnitude

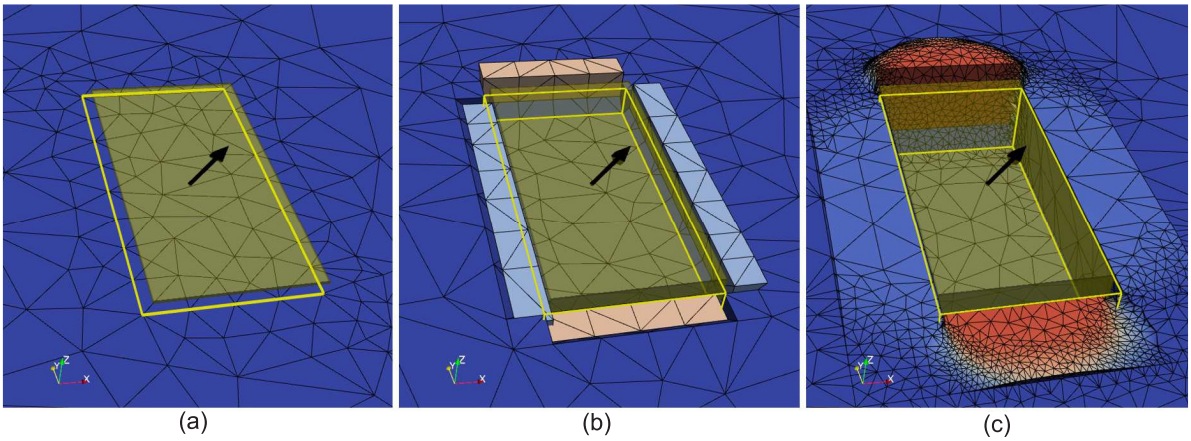

Figure 4.28: Failure mechanisms for mudmats loaded horizontally ($F_{\theta=45^\circ}$) showing effect of embedment: (a) $d/B = 0$; (b) $d/B = 0.2$; (c) $d/B = 0.5$. $T = \infty$ on sides. Shaded by UB velocity magnitude

in the y-direction than the x-direction even though the direction of loading remains the same. A mudmat embedded with $d/B = 0.5$ has a displacement vector at $\zeta = 84^\circ$ when subjected to loading at $\theta = 45^\circ$. This corresponds to translation that is predominantly in the y-direction, as is clear from the failure mechanism (Figure 4.28(c)). The failure envelope for a mudmat embedded with $d/B = 0.5$ and $T = \infty$ on the sides comprises linear sections parallel to the axes when $F_x < 2.3BLs_u$ and also when $F_y < 1.7BLs_u$ (Figure 4.26(a)). In general, the failure mechanism for a mudmat under combined $F_x - F_y$ loading changes from oblique translation at lower embedments towards axis-aligned translation as the embedment ratio increases.

Figure 4.29 shows capacity charts for an embedded mudmat with $d/B = 0.2$ subjected to horizontal forces applied at a range of eccentricities from the mudmat centre. The capacity of a

foundation embedded in weightless soil is considerably larger with $T = \infty$ along the sides than with $T = 0$ along the sides. When the submerged unit weight of the soil, γ', is included in the analysis, the capacity with $T = \infty$ remains unchanged but the capacity with $T = 0$ increases. The capacity when $T = 0$ increases with increasing normalised soil weight, $\gamma' B/s_u$, but it never exceeds the capacity when $T = \infty$ (which is independent of γ').

This can be explained by considering the corresponding failure mechanisms. In weightless soil, when $T = 0$ a gap forms behind the mudmat when it is loaded horizontally (as in Figure 4.27(b)), while when $T = \infty$ a gap cannot form (as in Figure 4.27(a)) and an active region of soil is mobilised behind the mudmat. When soil weight is included in the analysis, the failure mechanism when $T = \infty$ is unchanged, while when $T = 0$ soil may mobilise behind the mudmat. Whether soil mobilises behind the mudmat is dependent on the normalised soil weight $\gamma' B/s_u$, with heavier soil more inclined to mobilise. As more soil cannot be mobilised than when $T = \infty$, this provides an upper limit for the capacity of a mudmat in soil with weight. Less soil cannot be mobilised than when $T = 0$ in weightless soil, and as such this provides a lower limit for the capacity of a mudmat in soil with weight. For this reason, in all subsequent analyses the soil is modelled as weightless with either $T = \infty$ or $T = 0$ on the mudmat sides.

Failure mechanisms for an embedded mudmat with $d/B = 0.2$, loaded both concentrically and at the maximum feasible eccentricity, are shown in Figure 4.30. Comparing Figure 4.30(a) and (c), a mudmat subjected to F_x loading mobilises larger wedges of soil than a mudmat subjected to F_y loading and this results in greater capacity (compare Figure 4.29(a) and (b)). A mudmat subjected to F_x loading at the maximum feasible eccentricity has significant twisting visible in the failure mechanism, and the capacity reduces by nearly 50% (Figures 4.30(b) and 4.29(a)). A mudmat subjected to F_y loading has a smaller maximum feasible eccentricity and torsion causes only a 12% reduction in capacity (Figures 4.30(d) and 4.29(b)). The largest reduction in capacity due to eccentric horizontal loading occurs for a mudmat subjected to $F_{\theta=26.6^\circ}$ loading, with significant twisting visible in the failure mechanism and a 55% reduction in capacity (Figures 4.30(f) and 4.29(c)).

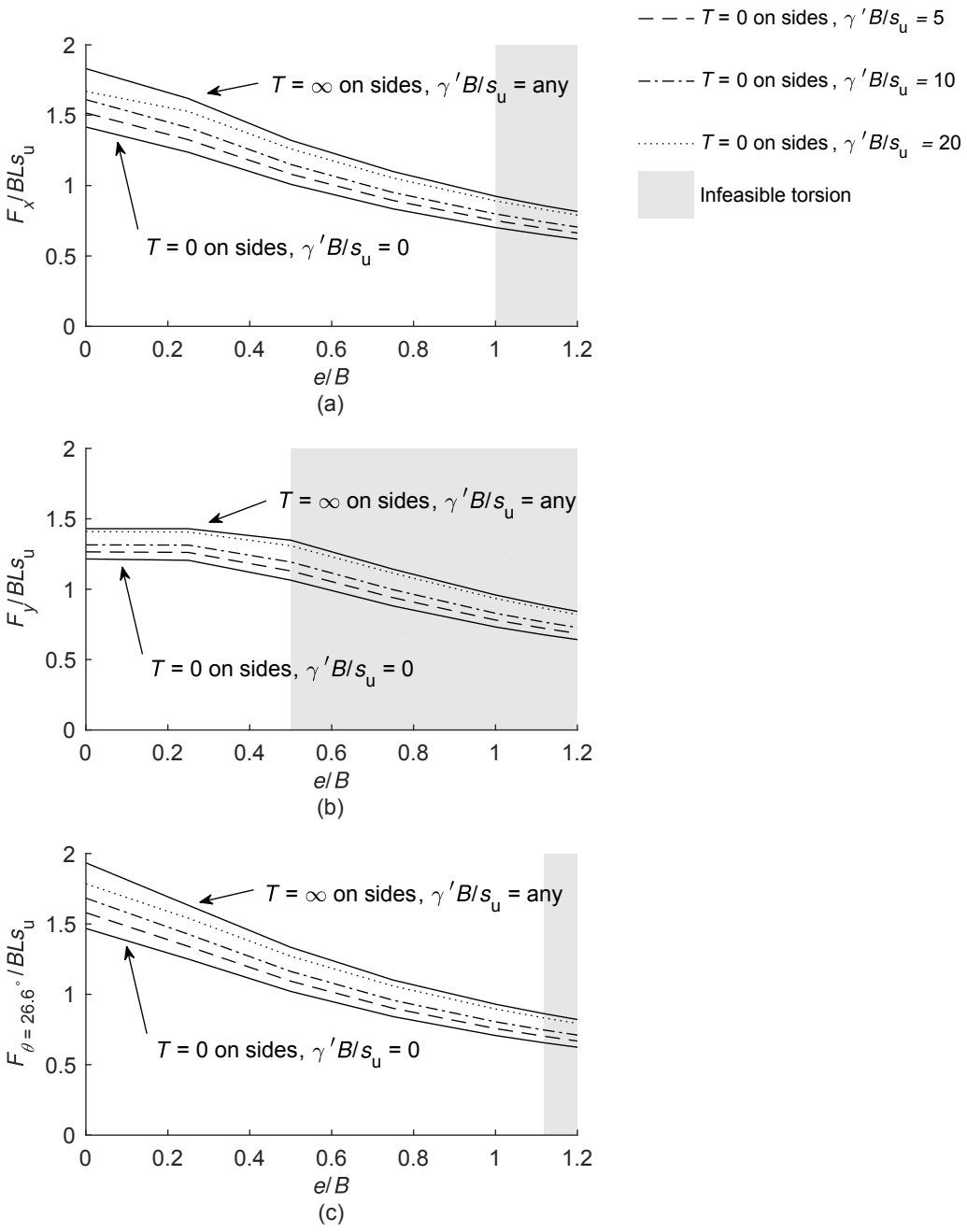

Figure 4.29: Capacity of an embedded mudmat ($d/B = 0.2$) subjected to horizontal loading at a range of eccentricities, showing effect of normalised soil weight $\gamma' B/s_u$: (a) F_x; (b) F_y; (c) $F_{\theta=26.6^\circ}$

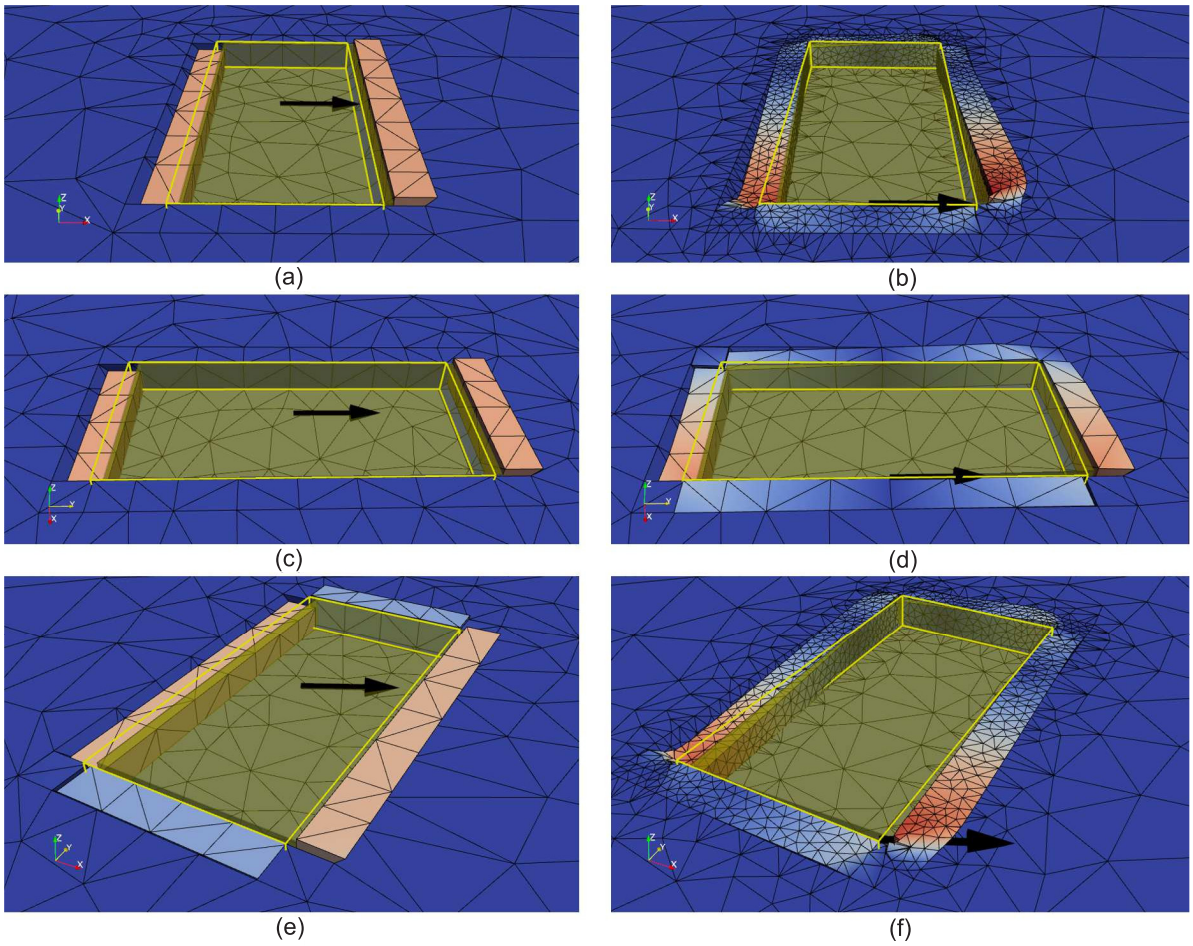

Figure 4.30: Capacity of an embedded mudmat ($d/B = 0.2$) subjected to horizontal loading at a range of eccentricities showing effect of normalised soil weight $\gamma' B/s_u$: (a) F_x; (b) F_y; (c) $F_{\theta=26.6^\circ}$

4.3.4.2 Combined horizontal, torsional, and moment loading

Figure 4.31 shows capacity charts for surface and embedded mudmats when subjected to horizontal loads F_x, F_y, and $F_{\theta=26.6^\circ}$ at a range of normalised eccentricities and heights. When a mudmat is loaded by F_x or $F_{\theta=26.6^\circ}$ at $h/B = 0$, mudmat embedment does not significantly influence the rate of reduction in capacity as the eccentricity of the horizontal load increases. For example, a surface mudmat subjected to $F_{\theta=26.6^\circ}$ loading undergoes a 55% reduction in capacity as e/B increases from 0 to 1.12 (Figure 4.31(i)) and a mudmat embedded with $d/B = 0.5$ undergoes a 53% reduction in capacity (Figure 4.31(l)). However, an embedded mudmat subjected to F_y loading shows better performance under torsional loading. In this instance, a surface mudmat subjected to F_y loading undergoes a 26% reduction in capacity as

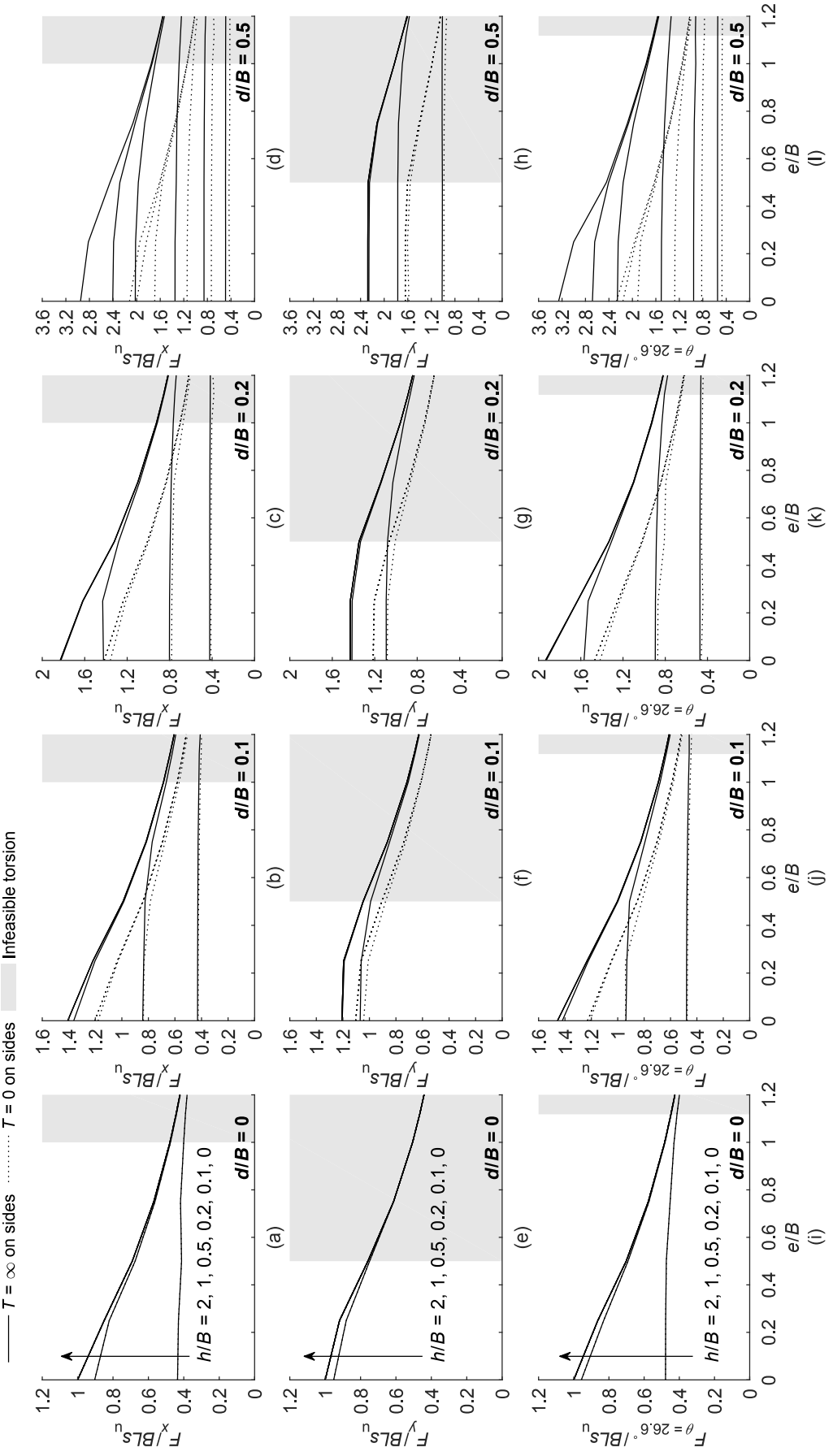

Figure 4.31: Capacity charts for surface and embedded mudmats subjected to horizontal loading in various directions, applied at a range of normalised eccentricities (e/B) and heights (h/B): (a)–(d) F_x, $d/B = 0$ to 0.5; (e)–(h) F_y, $d/B = 0$ to 0.5; $F_{\theta=26.6°}$, $d/B = 0$ to 0.5. Lines representing the lower values of h/B may overlap

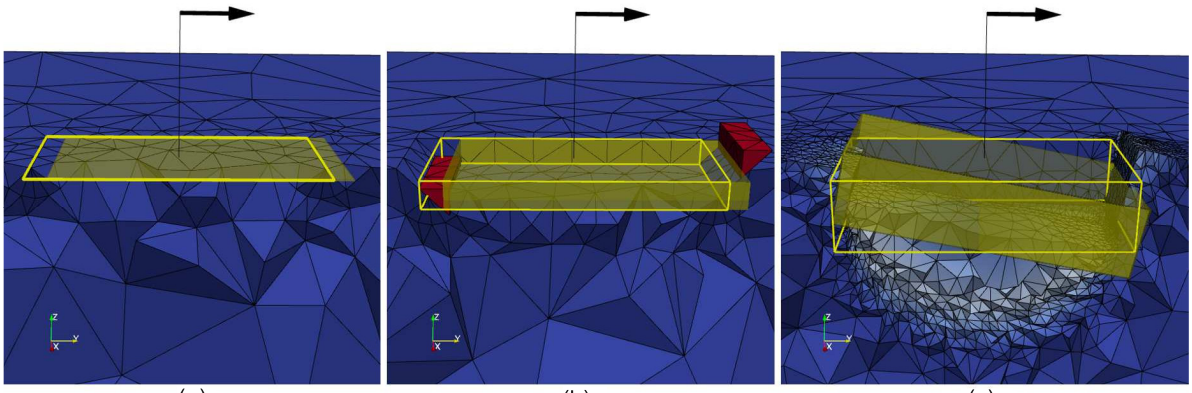

Figure 4.32: Failure mechanisms for mudmats subjected to horizontal loading F_y applied at a normalised height $h/B = 1$, showing effect of embedment: (a) $d/B = 0$; (b) $d/B = 0.2$; (c) $d/B = 0.5$. $T = \infty$ on sides. Shaded by UB velocity magnitude

e/B increases from 0 to 0.5 (Figure 4.31(e)), but if the mudmat is embedded with $d/B = 0.5$, the capacity does not change over the same range of e/B (Figure 4.31(h)).

As was the case with a surface mudmat, when an embedded mudmat is subjected to a horizontal force applied at a height above the load reference point there is generally no reduction in capacity until a critical height is reached, whereupon the capacity reduces rapidly. However, the critical height reduces with increasing mudmat embedment. This can be attributed to the increased lever arm from the load to the base of the mudmat. Figure 4.32 shows failure mechanisms for mudmats with various embedment ratios, subjected to F_y loading applied at $h/B = 1$. A surface mudmat fails through interface shearing between the mudmat and the soil, and the foundation translates horizontally (Figure 4.32(a)). A mudmat embedded with $d/B = 0.2$ also translates horizontally at failure, but displaces wedges of soil (Figure 4.32(b)). However, the failure mechanism for a mudmat embedded with $d/B = 0.5$ changes to 'pitching' about the x-axis.

4.3.4.3 Combined horizontal, torsional, moment, and vertical loading

The ultimate vertical bearing capacities, F_{z0}, of surface and embedded mudmats (assuming unlimited tension capacity on the sides) were closely bracketed using FELA and the results are presented in Table 4.5. A vertical dead load of magnitude $0.5F_{z0}$ was applied to the mudmat while it was again subjected to live horizontal loads applied at a range of

Table 4.5: Normalised vertical bearing capacities (F_{z0}/BLs_u) for surface and embedded mudmats obtained using FELA. $T = \infty$ on sides

Embedment ratio (d/B)	0	0.1	0.2	0.5
LB	5.33	5.77	6.13	6.78
UB	5.73	6.34	6.70	7.38
Average	5.53	6.06	6.42	7.08
Bracketing error $\pm\%$	3.6	4.7	4.5	4.3

eccentricities from, and heights above, the load reference point. Capacities for mudmats with and without a vertical dead load are presented in Figure 4.33 for the two extreme cases of embedment considered here ($d/B = 0$ and 0.5). It is apparent that the addition of a substantial vertical dead load has no significant effect on the capacity under horizontal loading in conjunction with feasible levels of torsional and moment loading. Note that because the base and sides of the mudmat have been assumed to have unlimited tension capacity, the results in Figure 4.33 are unaffected by the direction of the vertical dead load (upward or downward).

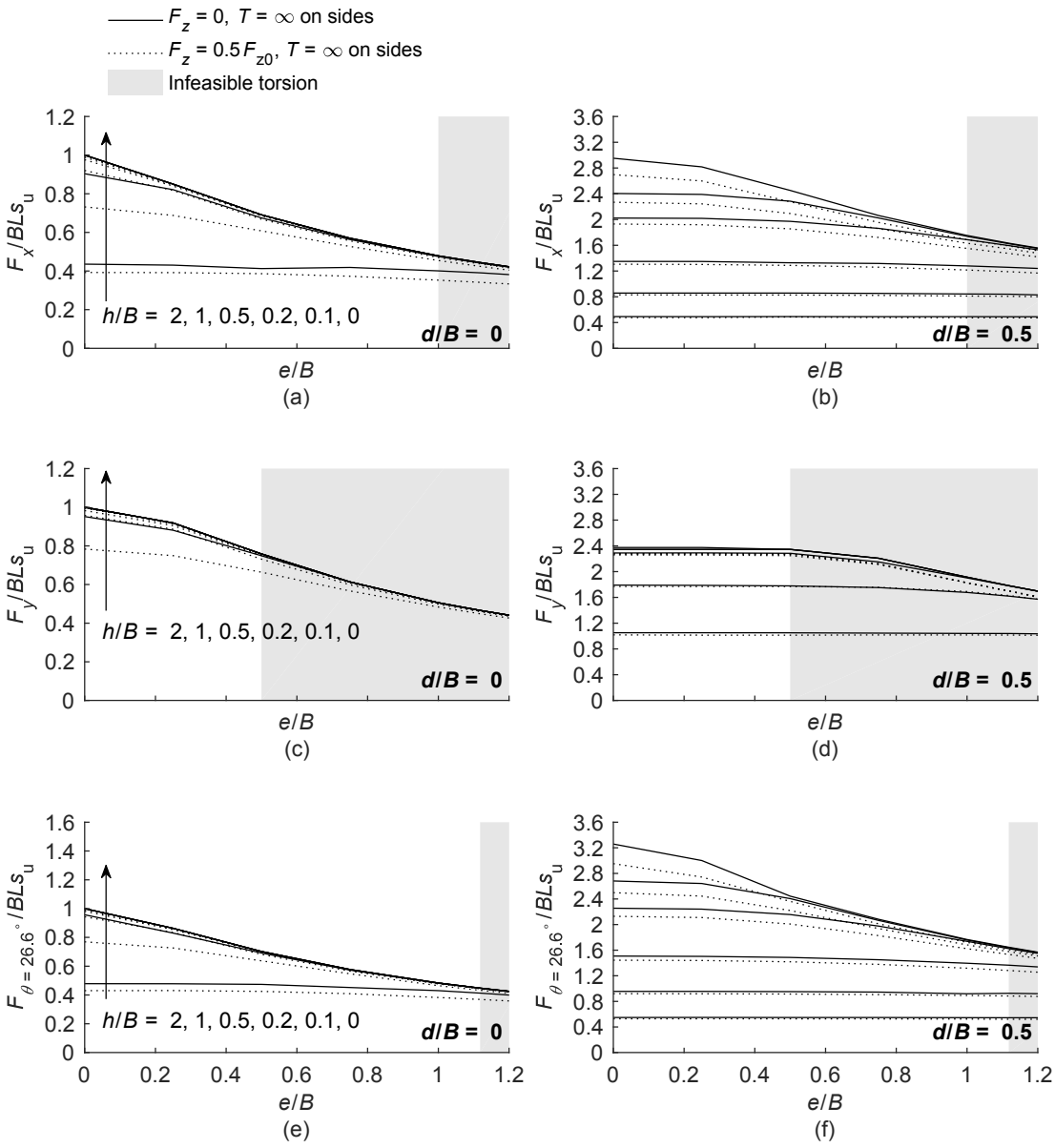

Figure 4.33: Capacity charts for surface and embedded mudmats subjected to horizontal loading in various directions, applied at a range of normalised eccentricities (e/B) and heights (h/B), in conjunction with a vertical dead load $F_z = 0$ or $F_z = 0.5F_{z0}$: (a) F_x, $d/B = 0$; (b) F_x, $d/B = 0.5$; (c) F_y, $d/B = 0$; (d) F_y, $d/B = 0.5$; (e) $F_{\theta=26.6^\circ}$, $d/B = 0$; (f) $F_{\theta=26.6^\circ}$, $d/B = 0.5$. Lines representing the lower values of h/B may overlap

4.4 Capacity analysis of square perforated foundations

4.4.1 Problem overview

The problem geometry and notation for the analysis of square perforated foundations is shown in Figure 4.34. The foundation is modelled as a rigid body of overall breadth, B, and depth, d. Perforated foundations can be categorised by their perforation ratio, R, which is the ratio of the perforated area to the gross foundation area ($R = A_i/A_o$, see Figure 4.34). This study uses 3D FELA to consider the vertical capacity of surface and embedded square footings with a range of perforation ratios ($R = 0-0.95$). Uniform soil and soil with increasing strength with depth are modelled, in accordance with

$$s_u = s_{um} - \rho z \tag{4.6}$$

where s_{um} is the mudline strength and ρ is rate of strength increase with depth (Figure 4.34). To allow comparison with previous studies available in the literature (Tapper, 2013; Tapper et al., 2015), the strength profile is characterised by a dimensionless strength heterogeneity factor $\rho B/s_{um}$ which was modelled at $\rho B/s_{um} = 0$ (uniform soil), 1, 2, and 5.

Surface footings were considered first, before analysing footings embedded at ratios $d/B = 0.1$, 0.2, 0.3, and 0.5. Surface footings were modelled as fully rough ($\alpha = 1$) or smooth ($\alpha = 0$). Embedded footings were modelled as having a fully rough base and smooth sides. Interface tension capacity and soil weight were excluded from the analysis, as for the load cases considered (vertical loading only) their inclusion does not affect foundation

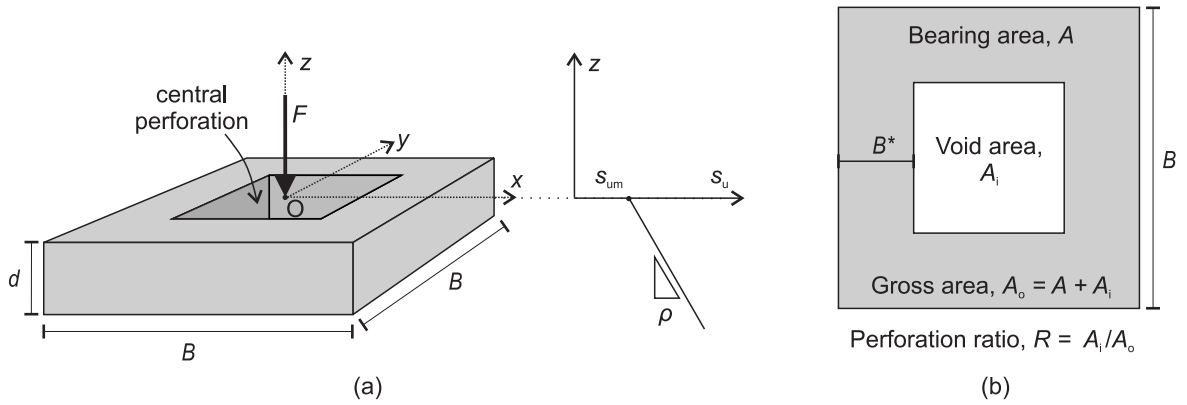

Figure 4.34: Perforated square mudmat notation: (a) foundation geometry. Load reference point O level with the soil mudline; (b) plan view of perforated foundation

capacity. Bracketed FELA capacities are compared with capacities derived from FEA presented in Tapper et al. (2015), although it should be noted that this study idealises the soil as a rigid–plastic von Mises material whereas Tapper et al. assumed an elastic–plastic Tresca material.

A design formula for estimating the vertical bearing capacity of foundations with perforations is presented in detail in Tapper (2013) (also published in Tapper et al. (2015)) and is summarised in Section 2.3.1. The design formula uses analytical expressions derived from an extensive FEA study, and was verified using centrifuge test data.

The efficacy of this design formula was examined for surface and embedded footings with a large range of perforation ratios. A modification to this design formula is proposed for capacity analysis of embedded perforated footings.

This study considers vertical capacity (capacity under F in Figure 4.34) of square footings, which allows for planes of symmetry to be exploited such that only one eighth of the problem needs to be modelled. An unrefined mesh for an embedded perforated footing is shown in Figure 4.35. As with previous analyses, additional prescribed planes were added to an otherwise unstructured mesh as it was found that this was beneficial for convergence of the FELA bounds. These planes are shown as bold lines in Figure 4.35. Three iterations of automated adaptive mesh refinement were undertaken for each analysis and the final refined mesh comprised ∼40 000 elements.

4.4.2 Surface perforated footings

The results are presented in the form of the dimensionless bearing capacity factor N_c, where $N_c = F/As_{\text{um}}$ (see Figure 4.34). FELA bounds for N_c are shown in Figure 4.36 for surface foundations with a range of perforation ratios. First, considering rough foundations (Figure 4.36(a)), it is shown that the average of the FELA bounds is in good agreement with the FEA results and the centrifuge test data obtained by Tapper et al. (2015). The bearing capacity factors found using FEA remain within the FELA bounds. The bearing capacity factors found using centrifuge tests are marginally higher than the FELA UB when $R = 0.36$ but are within the FELA bounds when $R = 0.64$. Bearing capacity factors obtained using the

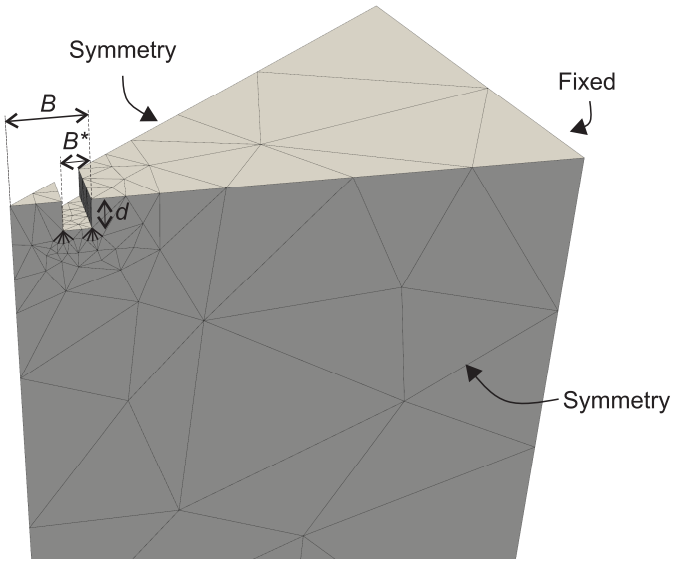

Figure 4.35: Initial FELA mesh of one eigth of the soil domain (symmetry exploited) showing prescribed planes in the mesh as bold lines

design formula proposed by Tapper (2013) are within the FELA bounds.

The bearing capacity factor for a strip footing, from Prandtl (1920), is also shown in Figure 4.36(a). As the perforation ratio R increases, N_c approaches that for a strip footing on uniform soil ($N_c = 2 + \pi$) regardless of the soil strength gradient. This trend can be easily explained by considering the relevant foundation failure mechanisms. The UB mechanism for a rough surface footing with $R = 0.3$ is shown in Figure 4.37(a). Similarities to the Prandtl (1920) failure mechanism are visible in that a central wedge of soil is displacing vertically downwards under the effective foundation bearing width, B^*. At this perforation ratio, there is interaction between the mechanisms formed under the bearing areas on either side of the perforation. When $R = 0.4$ there is less interaction between the mechanisms on either side of the perforation (Figure 4.37(b)).

A footing with a large perforation ($R = 0.95$) is shown in Figure 4.37(c). The failure mechanism is very shallow when compared with Figure 4.37(a) and (b). The zoomed view in Figure 4.38(a) shows that the mechanism closely resembles the Prandtl (1920) failure mechanism for a strip footing. The plan view highlights that at this perforation ratio, the mechanism is that of a strip foundation of width B^* and length roughly equal to the perimeter of the footing (Figure 4.38(c)). This very shallow mechanism at high R demonstrates why,

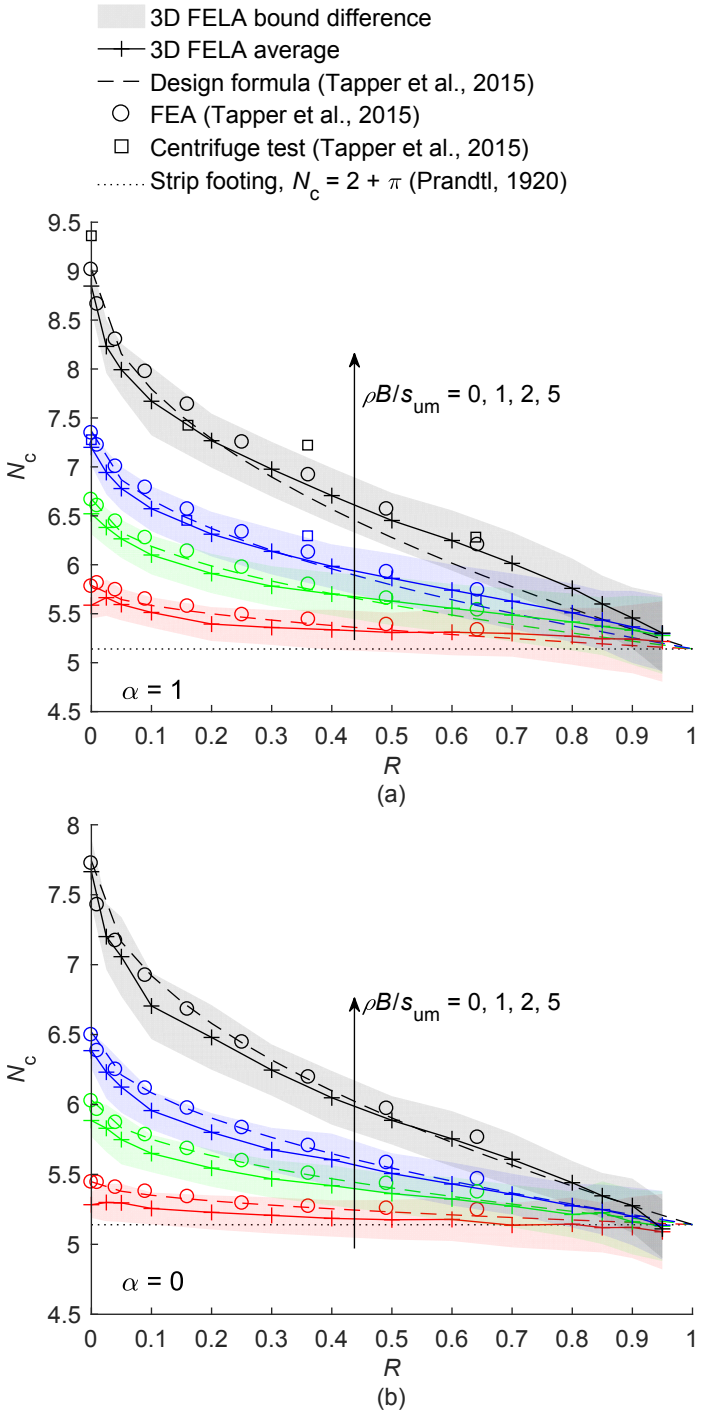

Figure 4.36: Bearing capacity factors N_c for surface footings ($d = 0$) with a range of perforation ratios (R) on soil with a range of strength heterogeneity factors ($\rho B/s_{\mathrm{um}}$): (a) rough footings ($\alpha = 1$); (b) smooth footings ($\alpha = 0$)

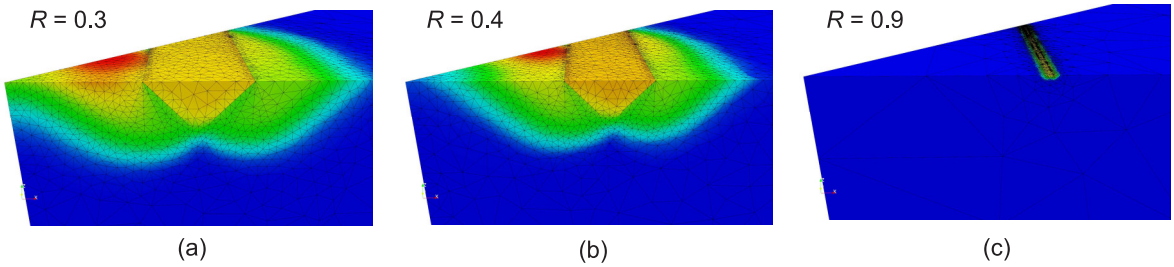

Figure 4.37: Failure mechanisms for rough ($\alpha = 1$) perforated surface footings on uniform soil ($\rho B/s_{\mathrm{um}} = 0$) under vertical loading showing effect of perforation ratio (R): (a) $R = 0.3$; (b) $R = 0.4$; (c) $R = 0.95$. One eighth of the soil domain shown. Shaded by UB velocity magnitude

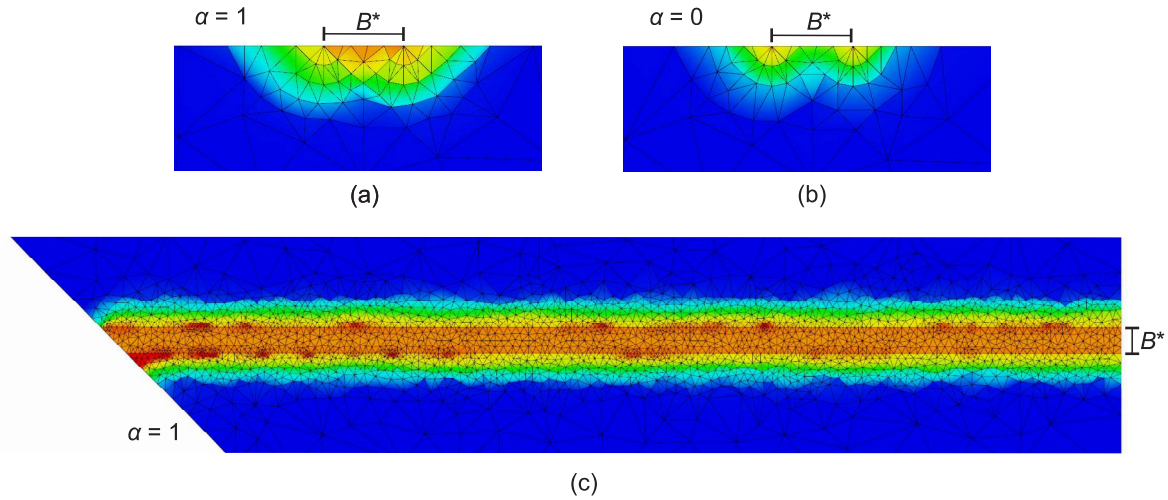

Figure 4.38: Zoomed view of failure mechanisms for perforated ($R = 0.95$) surface footings on uniform soil ($\rho B/s_{\mathrm{um}} = 0$) under vertical loading: (a) rough foundation ($\alpha = 1$), elevation view ; (b) smooth foundation ($\alpha = 0$), elevation view; (c) rough foundation ($\alpha = 1$), plan view. Shaded by UB velocity magnitude

for all soil strength profiles, N_c converges to that for a footing on uniform soil.

Figure 4.36(b) shows N_c for smooth footings ($\alpha = 0$). When comparing Figure 4.36(b) to (a), it is apparent that smooth square footings have lower capacities than rough square footings. The same overall trend as Figure 4.36(a) can be seen in Figure 4.36(b), in that, as the perforation ratio increases the bearing capacity factor decreases, although the factors seem to converge more rapidly to the Prandtl (1920) capacity. Failure mechanisms for smooth perforated footings are shown in Figure 4.39. Comparing Figure 4.39(b) to Figure 4.37(a) (both $R = 0.3$), the smooth footing has a more shallow mechanism. It is for this reason that there is less interaction between the mechanisms formed on either side of the perforation for a smooth footing. Figure 4.38(b) and Figure 4.39(c) show that the mechanism for a smooth

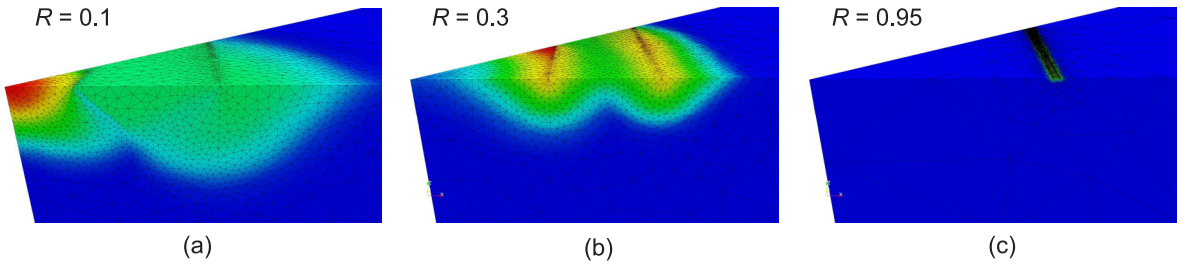

Figure 4.39: Failure mechanisms for smooth ($\alpha = 0$) perforated surface footings on uniform soil ($\rho B/s_{\text{um}} = 0$) subject to vertical loading, showing effect of perforation ratio (R): (a) $R = 0.1$; (b) $R = 0.3$; (c) $R = 0.95$. One eighth of the soil domain shown. Shaded by UB velocity magnitude

footing with a high perforation ratio resembles the Hill-type mechanism of a smooth strip footing of width B^* (Hill et al., 1947).

The very shallow failure mechanisms at high R gives rise to an increase in FELA bracketing error when $R \geq 0.8$ (see the shaded bands in Figure 4.37). A large adaptively refined mesh with many elements directly under the footing bearing area would be needed to improve the FELA bounds. However, the large bracketing error associated with the results for $R \geq 0.8$ demonstrates a significant advantage of LB and UB FELA over FEA. When using displacement FEA, N_c may not appear to approach the (Prandtl, 1920) solution at high perforation ratios, due to inaccuracies associated with an overly coarse mesh. When using FELA, inaccuracies due to an inadequate mesh are highlighted by a large bracketing error, but from the coverage of the bounds it can still be seen that N_c approaches Prandtl's solution as R increases.

4.4.3 Embedded perforated footings

FELA bounds for N_c are shown in Figure 4.40 for embedded perforated footings with depth to breadth embedment ratios $d/B = 0.1$, 0.2, 0.3, and 0.5. Consider the bearing capacity factors obtained using FELA for a footing with $d/B = 0.1$ in soil with $\rho B/s_{\text{um}} = 5$ (Figure 4.40(a), black line). Initially as R increases, N_c reduces, as expected from the behaviour seen in Figure 4.36. However, N_c then remains approximately the same until $R = 0.7$. When $R > 0.7$, N_c increases. The same general trend can be seen for all footing embedments and soil strength heterogeneities, although the trend is more pronounced in soil

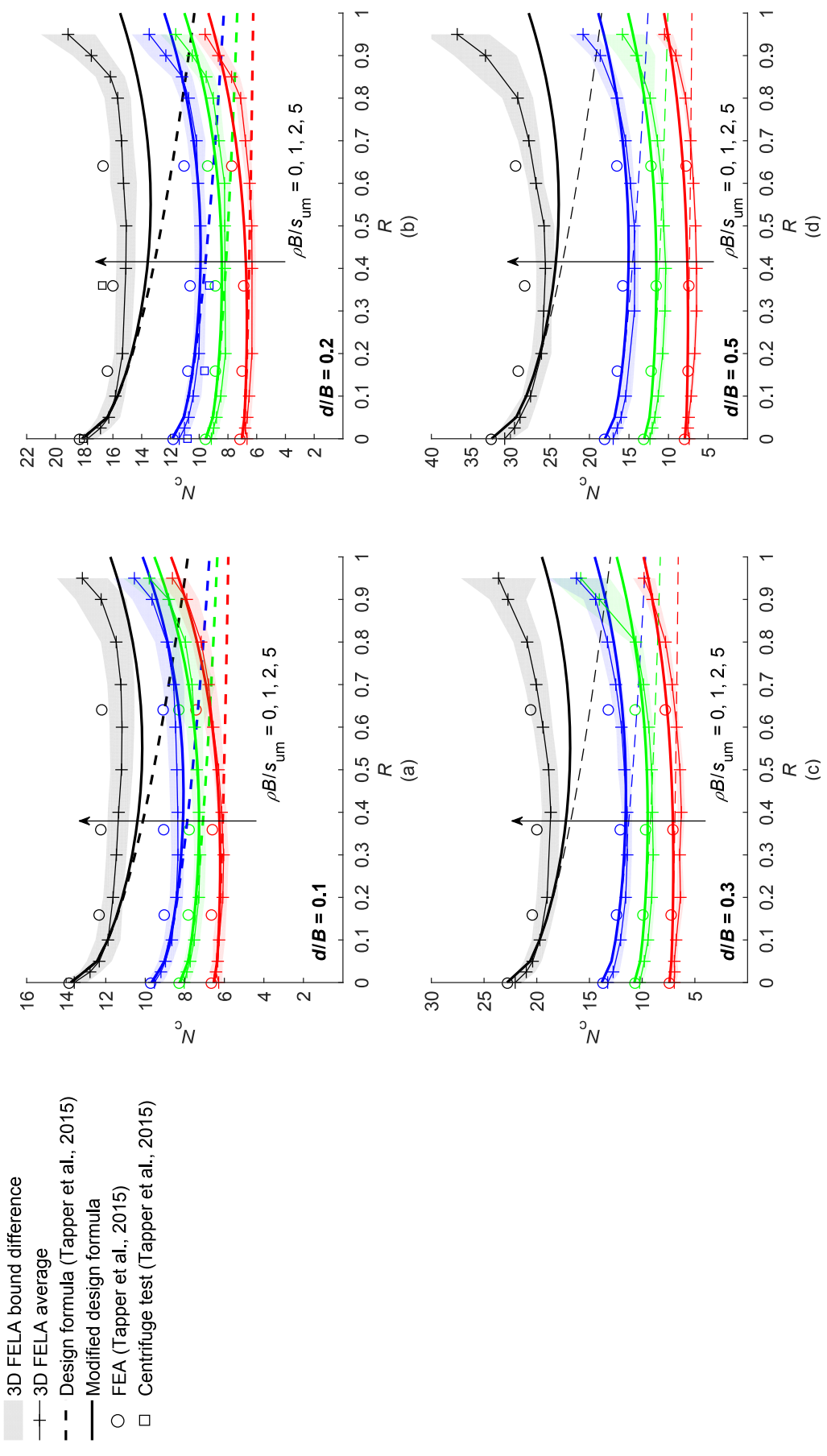

Figure 4.40: Bearing capacity factors N_c for embedded footings (smooth sides and rough base) with a range of perforation ratios (R) in soil with a range of strength heterogeneity factors ($\rho B/s_{um}$): (a) $d/B = 0.1$; (b) $d/B = 0.2$; (c) $d/B = 0.3$; (d) $d/B = 0.5$

Table 4.6: Depth factors, d_c, for embedded square footings in soil with various strength gradients (data from Tapper (2013))

$\rho B/s_{\text{um}}$	$d/B = 0.1$	$d/B = 0.2$	$d/B = 0.3$	$d/B = 0.5$
0	1.13	1.21	1.28	1.37
1	1.24	1.43	1.61	1.96
2	1.31	1.61	1.88	2.45
5	1.53	2.01	2.53	3.59

with high strength heterogeneity when compared with uniform soil.

It might initially seem surprising that N_c increases at high R as the opposite was shown to happen for surface footings (Figure 4.36). Tapper et al. (2015) considered footings with $R \leq 0.64$ (Figure 4.40). At $R < 0.64$ the upwards trend in N_c is not obvious and the slight rise in N_c when $R = 0.64$ could have been attributed to numerical errors at high perforation ratios. It is shown in Figure 4.40 that the design formula proposed by Tapper et al. (2015) follows the same trend in N_c as was the case for surface perforated footings although (Figure 4.36) this is not a good fit for N_c values found using FELA for embedded footings with $R > 0.6$.

An important input into the Tapper et al. (2015) design formula is the depth factor, d_c (defined in Section 2.3.1), which is associated with the footing depth to embedment ratio (d/B). For surface footings $d_c = 1$ and embedded footings have $d_c > 1$. As already covered in Section 2.3.1, Tapper et al. (2015) used FEA to determine d_c factors for solid square footings in soil with $\rho B/s_{\text{um}} = 0$, 1, 2, and 5 (also, see Figure 2.11). Table 4.6 shows that d_c increases as d/B increases. It is also shown that d_c increases more rapidly with d/B in soil with high strength heterogeneity. The design formula proposed by Tapper conservatively uses d_c for foundations without perforations, as given in Table 4.6. However for a given embedment ratio and strength profile d_c increases with increasing R, as shown in Figure 4.41.

To help understand the reason for the increase in d_c (and consequently N_c) with increasing R, it is useful to consider foundation failure mechanisms. Figure 4.42 shows failure mechanisms for footings with $R = 0.025$, 0.3, 0.6, and 0.9 at a constant embedment ratio $d/B = 0.5$. These diagrams show that the failure mechanism for an embedded perforated footing is dependent on the embedment ratio d/B^*, not d/B. As the perforation

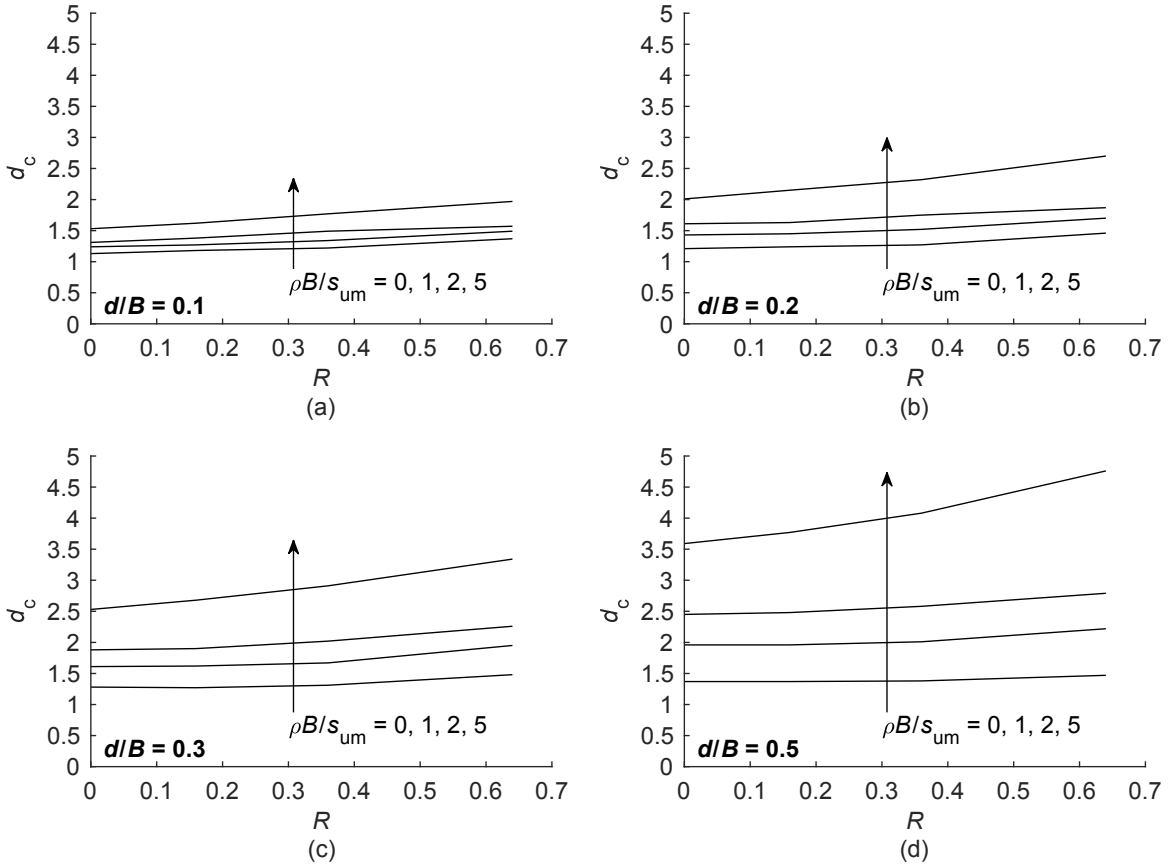

Figure 4.41: Depth factors (d_c) for embedded footings with a range of perforation ratios (R) in soil with a range of strength heterogeneity factors ($\rho B/s_{\mathrm{um}}$): (a) $d/B = 0.1$; (b) $d/B = 0.2$; (c) $d/B = 0.3$; (d) $d/B = 0.5$. Data from Tapper (2013)

ratio increases B^* becomes smaller, and as such d/B^* is different for every perforation ratio. For surface footings at high R the failure mechanism (and bearing capacity factor) becomes similar to that for a strip footing (Figure 4.37 and Figure 4.39). For an embedded footing the failure mechanism becomes equivalent to that for a strip footing embedded d/B^*, not d/B. For this reason, d_c formulated based on d/B becomes increasingly inaccurate as the perforation ratio increases.

Figure 4.40 shows that for all values of d/B and $\rho B/s_{\mathrm{um}}$ the formula proposed by Tapper et al. (2015) underestimates N_c when $R > 0.6$. It is proposed here that a simple empirical modification is made to d_c to account for its change with increasing R:

$$d_{cR} = d_c + 0.5R^2 d_c. \tag{4.7}$$

The bold line in Figure 4.40 shows the 'modified design formula', which is the Tapper et al.

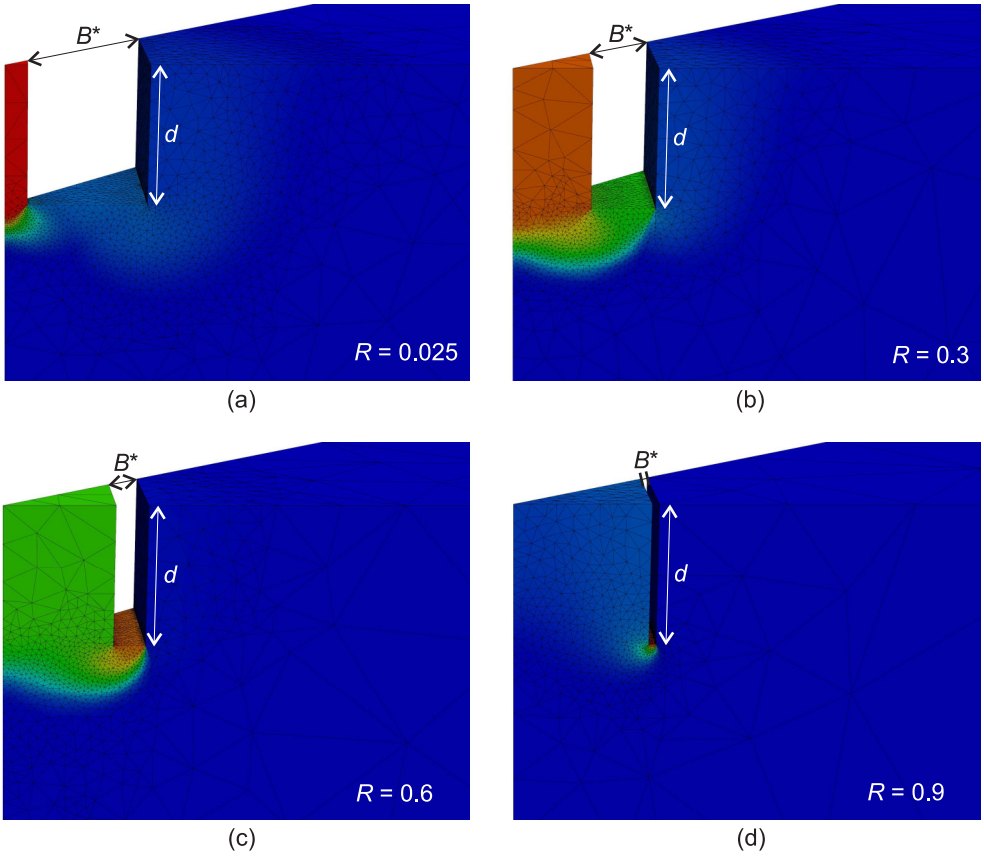

Figure 4.42: Failure mechanisms of embedded ($d/B = 0.5$) perforated foundations on uniform soil ($\rho B/s_{\text{um}} = 0$) subject to vertical loading, showing effect of perforation ratio (R): (a) $R = 0.3$; (b) $R = 0.4$; (c) $R = 0.95$. One eighth of soil domain shown. Shaded by UB velocity magnitude

(2015) design formula used with d_{cR} replacing d_c. The modified formula does not provide a perfect match to the FELA data, but it does offer a closer fit than the original design formula, particularly in soils with high strength heterogeneity.

4.5 Summary

In this chapter rectangular foundations were analysed using displacement FEA, analytical limit analysis solutions, and FELA. The chapter was divided into three sections which considered; mudmat capacity on sloping ground, rectangular mudmat capacity under combined loading, and bearing capacity analysis of square perforated footings.

For the study into mudmat capacity on sloping ground emphasis was placed on combined $F_z - F_x$ loading. It was found that if soil self-weight is neglected then the problem can be

analysed as an equivalent foundation on flat ground, with the applied loads suitably rotated. When soil weight is included then a direct analysis is required. The parametric study conducted here revealed some potentially significant reductions in the vertical capacity of a mudmat on sloping ground. The addition of perimeter skirts can offset this effect to some degree while also providing much improved horizontal capacity. Various values of interface roughness and interface tensile capacity have also been studied in detail. In the analysis of a case study based on a recent project it was found that a small ground inclination (5°) caused a $\sim$20% reduction in vertical capacity and a $\sim$6% reduction in horizontal capacity.

The second section opened with a typical design case of a rectangular mudmat, where it was demonstrated that torsional loading can significantly affect mudmat capacity. This led to a study where rigorous 3D limit load analyses were carried out using both analytical calculations and FELA. Horizontal forces were applied to a mudmat at a range of eccentricities from, and heights above, the load reference point (encompassing five degree-of-freedom loading). Particular attention was given to identifying the levels of torsion and overturning moment that may realistically arise from horizontal loading applied within the envelope of a mudmat and the equipment that it supports. The final stage of the study considered the effect of a concurrent vertical dead load. A range of parameters were considered, including the embedment ratio, the interface tension capacity on the sides of a mudmat, and soil unit weight.

The results quantify the gradual reduction in capacity as the eccentricity of a horizontal force increases. Depending on the degree of embedment, the failure mechanism in this case can change from pure translation to combined translation and twisting. Mudmat embedment helps to negate the reduction in capacity due to eccentric loading, particularly when the load is aligned with the longer side of the mudmat. A horizontal load applied at a height above the mudmat causes no reduction in capacity until a critical height is reached, whereupon the capacity reduces rapidly. This threshold was found to be higher when the horizontal force is aligned parallel to the longer side of the mudmat. The failure mechanism changes from pure translation to combined translation and rotation once the threshold has been reached. Mudmat embedment causes a reduction in the threshold height, since the effective lever arm

from the load to the mudmat base is larger. A vertical dead load equal to (or less than) half of the ultimate vertical capacity has minimal effect on the resistance to horizontal loading in conjunction with practically feasible levels of torsional and moment loading.

The final section studied the bearing capacity of square perforated footings. The bearing capacity factor N_c (based on the actual bearing area, A) was tightly bracketed using FELA for foundations with a range of perforation ratios, in soil with a range of strength heterogeneity factors. It was found that for surface foundations, bearing capacity factors found using FELA correspond well with values obtained using a design formula proposed by Tapper et al. (2015). For embedded foundations, it was found that the design formula proposed by Tapper et al. is conservative for foundations with large perforation ratios, particularly in soil with high strength heterogeneity. A modification to this design formula was proposed which provides a better approximation to the bearing capacity factors obtained using FELA.

Chapter 5

Suction caissons

5.1 Introduction

In this chapter analysis is undertaken on caisson foundations used offshore as suction anchors (also known as suction caissons or suction piles). A range of parameters that may affect caisson capacity are considered, such as: caisson length to diameter aspect ratio, load attachment point, and load angle. Attention is given to identifying the load attachment point that results in maximum caisson capacity, termed the optimal load point. The main parametric study considers two soil strength profiles; uniform soil and soil with a linear increase in strength with depth. A case study considers a caisson in layered soil.

The first section describes and validates assumptions made in the FELA models specific to caisson analysis. The subsequent section considers suction caissons under horizontal loading. The effect of contact breaking between the caisson and the soil on the holding capacity and optimal load point is quantified for a range of soil weight to strength ratios. In the final section, suction caissons under inclined loading are analysed. Again the effect of contact breaking on caisson capacity and optimal load point is quantified.

Capacity charts showing the variation in caisson capacity with load attachment point are presented, and maximum caisson capacities with corresponding optimal load points are summarised in tabular form. The efficacy of a plane strain analysis, approximating a full 3D analysis, is explored. Caisson failure mechanisms are presented and discussed.

This chapter concludes with a case study of a suction anchor in layered soil. FELA is used to find the caisson's capacity under two design conditions; ultimate limit state (ULS) and

accidental limit state (ALS). The ULS capacity is confirmed using the derived capacity charts.

5.2 Problem overview

Caissons of length, L, and diameter, D, are modelled using plane strain and 3D FELA according to the notation and sign conventions shown in Figure 5.1(a) and (b) for plane strain and 3D analyses respectively. This study considers six caisson length to diameter aspect ratios, $L/D = 1$, 2, 3, 4, 5, and 6. It is assumed that the caisson caps are sealed such that negative excess pore water pressures can develop along the internal caisson wall, which prevents contact breaking. Along the external wall it is either assumed that negative excess pore pressures can develop, preventing contact breaking ($T = \infty$), or that they cannot develop and a gap can form between the caisson and the soil ($T = 0$). The wall/soil interface roughness factor (α) can range from $0.5-0.7$ in practice (Randolph and House, 2002), but Kennedy et al. (2013) found that caisson capacity was insensitive to a $\pm 25\%$ change in the roughness factor. As such an interface roughness factor $\alpha = 0.5$ is adopted for all analyses.

As shown in Figure 5.1 the two strength profiles considered are uniform soil ($s_u =$ constant) and soil with no strength at the mudline and a linear increase in strength with depth, which represents a normally consolidated (NC) soil ($s_u = -\rho z$, where $\rho = D$). In the latter case it is convenient to normalise the holding capacity with respect to the average shear strength, $s_{u,av}$, at $z = -L/2$. Capacities of caissons modelled in plane strain are extrapolated for a slice of thickness D in the y-direction, as shown in Figure 5.1(b)). The 3D FELA models exploit symmetry about the plane $y = 0$.

Horizontal live loading ($\beta = 0$, Figure 5.1) is applied to the caisson at intervals of $0.1L$ along the caisson length. Capacity charts are produced to show the effect of load location on the holding capacity. Soil weight does not affect caisson capacity when contact breaking is prevented, but it does when contact breaking can occur. For this case, three normalised soil weight to strength ratios are considered; in uniform soil $\gamma' D/s_u = 0$ (weightless), 1, and 5 and in NC soil $\gamma'/\rho = 0$ (weightless), 1, and 5. The analysis is then repeated for caissons under inclined loading at $\beta = 15^\circ$, 30°, and 45° (see Figure 5.1).

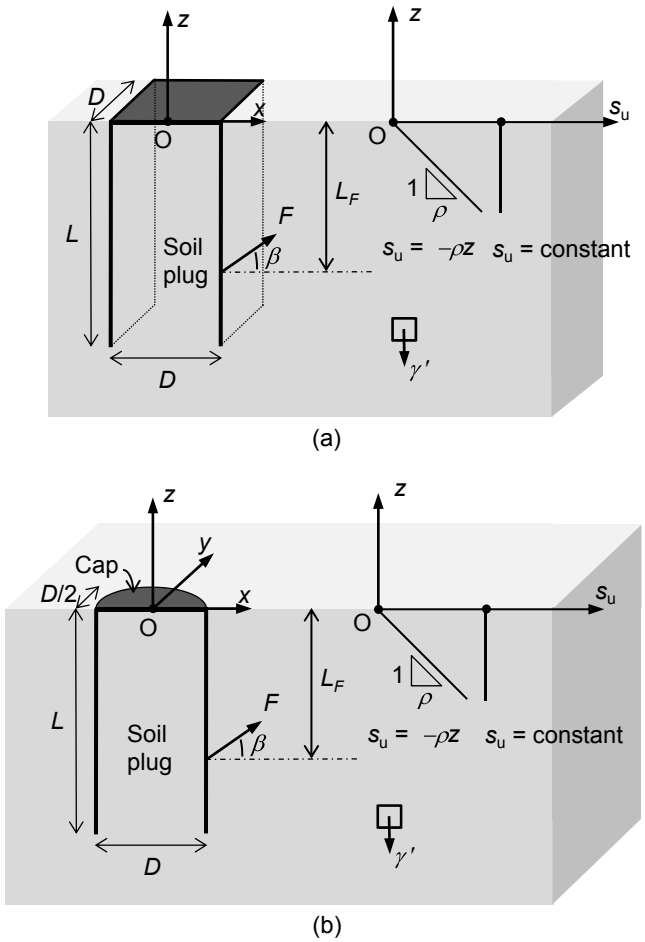

Figure 5.1: Notation and sign conventions: (a) for plane strain analysis; (b) for 3D analysis

5.3 Model assumptions and validation

The curved caisson wall is approximated in the 3D FELA model as a series of planar facets that inscribe the circular caisson. The number of facets required to accurately represent the caisson was calibrated against known plasticity solutions for a laterally loaded circular pile in Section 3.5.2. For a half-rough caisson a discetisation of 90 facets for a full circular caisson is sufficient (from Figure 3.11). Capacities obtained using 3D FELA for a pile comprising 90 facets are summarised in Table 3.2. This discretisation is used to model caissons for the rest of this study.

It was ensured that the plan dimensions of the modelled soil domain were sufficiently large as to comfortably contain the failure mechanism, and the depth of the soil domain was varied depending on the caisson aspect ratio. Analysis of the mooring line was not undertaken; a unit

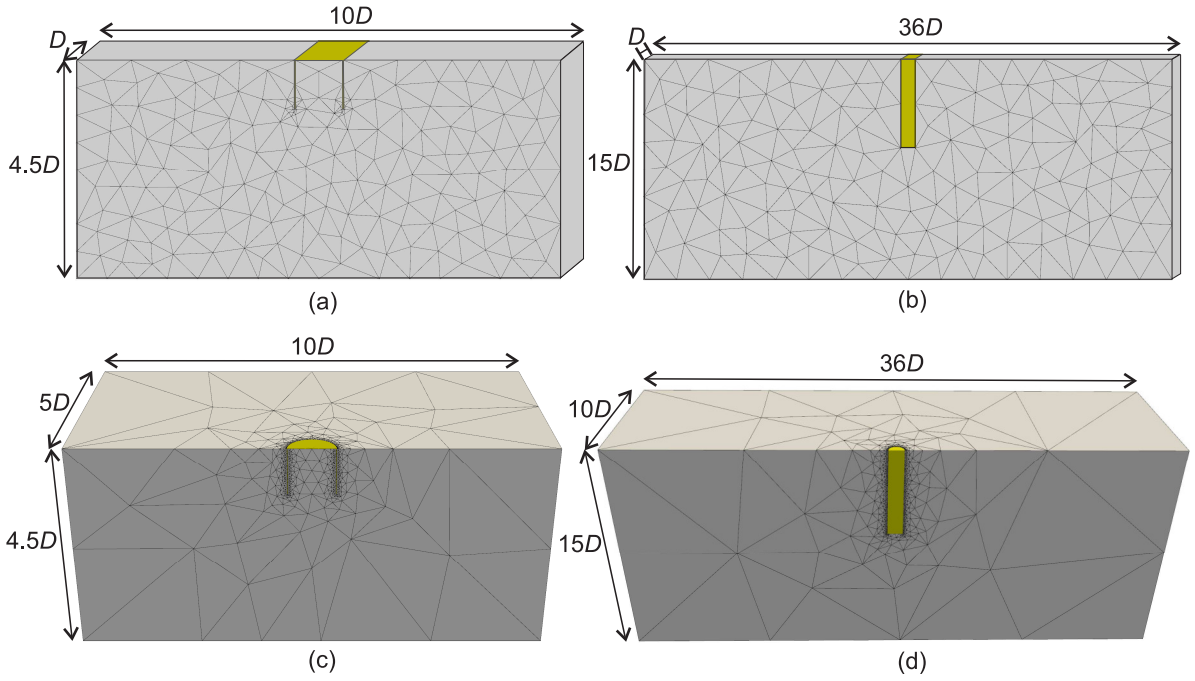

Figure 5.2: Initial FELA mesh domains: (a) plane strain FELA, $L/D = 1$ and $t = 0.01B$ (deformable soil plug); (b) plane strain FELA, $L/D = 6$ (rigid soil plug); (c) 3D FELA with $L/D = 1$ and $t = 0.01B$ (deformable soil plug); (d) 3D FELA with $L/D = 6$ (rigid soil plug)

live load in the appropriate direction was applied at the attachment point. Initial (unrefined) meshes of planar caissons and 3D caissons with $L/D = 1$ and $L/D = 6$ are shown in Figure 5.2. Automated mesh refinement was undertaken in plane strain analyses until the bracketing error was $< \pm 1\%$. For 3D analyses, three iterations of adaptive mesh refinement were undertaken with the final mesh comprising $\sim$55 000 elements.

Previous studies have idealised caissons with $L/D > 1.5$ as rigid bodies comprising the soil plug, such that the soil plug is not explicitly modelled (e.g. Kay and Palix, 2010; Palix et al., 2010). Kennedy et al. (2015) found that the failure mechanism of a caisson with $L/D < 2$ could contain a shear zone within the soil plug, and as such a deformable soil plug should be modelled in this case. The suitability of modelling a caisson as a rigid body comprising the soil plug, in contrast to modelling the caisson as rigid and the soil plug as deformable, is briefly investigated here as a precursor to the main study. The base of the soil plug was modelled as fully rough ($\alpha = 1$) with infinite tension capacity ($T = \infty$) (to replicate a soil/soil interface).

The full range of caissons in the parametric study was modelled using plane strain FELA

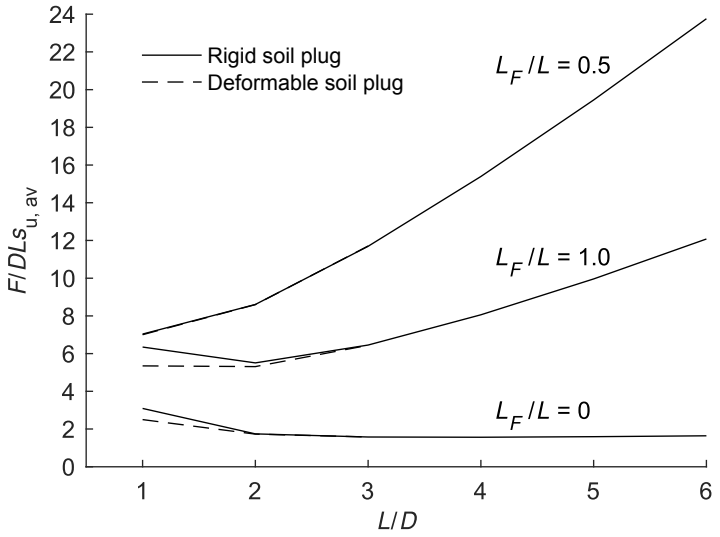

Figure 5.3: Normalised capacities of 3D caissons modelled with a deformable soil plug and $t = 0.01D$, and with a rigid soil plug. $\beta = 0$, $s_u = -\rho z$, $T = 0$, $\gamma'/\rho = 0$

as (a) plates of thickness $0.01D$ with a deformable soil plug (Figure 5.2(a)) and (b) rigid bodies comprising the soil plug (Figure 5.2(b)). It was found that the largest discrepancy between capacities of caissons modelled with a rigid soil plug and with a deformable soil plug occurs when $T = 0$, $s_u = -\rho z$, $\gamma'/\rho = 0$, and $\beta = 0$. This case was modelled using 3D FELA. Caissons of all aspect ratios were modelled as (a) plates of thickness $0.01D$ with a deformable soil plug (Figure 5.2(c)) and (b) rigid bodies comprising the soil plug (Figure 5.2(d)). Capacities for both models are shown in Figure 5.3 when the caissons are loaded at $L_F/L = 0$, 0.5, and 1. When $L/D = 1$ there is a significant difference between the capacities of caissons modelled with a rigid soil plug and those modelled with a deformable soil plug. When a caisson with a deformable soil plug is loaded at the mudline ($L_F/L = 0$) failure is as described in Kennedy et al. (2015) and involves a shear zone within the soil plug (Figure 5.4(a)). This shear zone cannot be present when the soil plug is modelled as rigid, which results in a substantially different mechanism involving a shear zone below the caisson (Figure 5.4(b)) and leading to an artificially increased capacity (Figure 5.3).

As L/D increases, the difference between the capacities of caissons modelled with a rigid soil plug and with a deformable soil plug decreases; there is no difference when $L/D \geq 3$ (Figure 5.3). Caissons with $L/D = 4$ that are modelled with deformable and rigid soil plugs and loaded at the mudline ($L_F/L = 0$) fail as shown in Figures 5.4(c) and (d). The failure

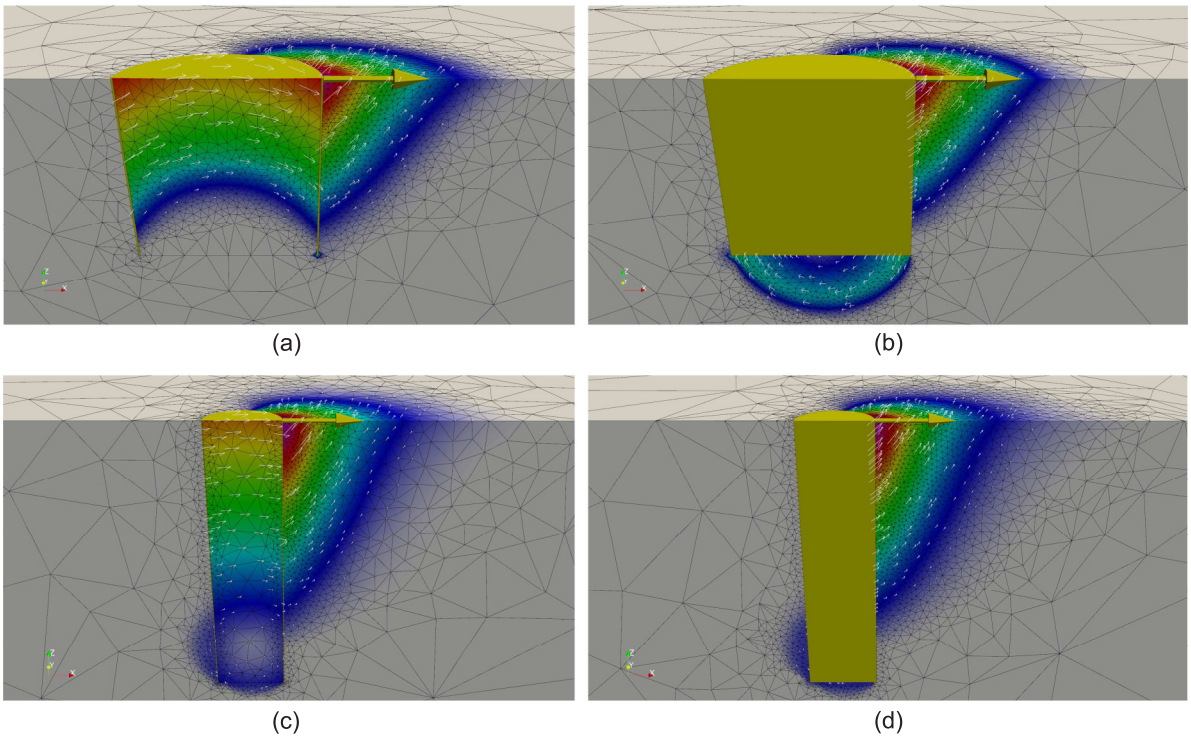

Figure 5.4: Failure mechanisms of 3D caissons when loaded horizontally ($\beta = 0$) at the mudline ($L_F/L = 0$). $s_u = -\rho z$, $T = 0$, $\gamma'/\rho = 0$. Shading and vectors show UB velocity magnitudes and directions: (a) $L/D = 1$ and $t = 0.01D$ (deformable soil plug); (b) $L/D = 1$ (rigid soil plug); (c) $L/D = 4$ and $t = 0.01D$ (deformable soil plug); (d) $L/D = 4$ (rigid soil plug)

mechanisms are essentially identical, showing the suitability of modelling the soil plug as rigid for this case. For the rest of this study caissons with $L/D = 1$, 2, and 3 are modelled as rigid plates of thickness $0.01D$ with a deformable soil plug, and caissons with $L/D = 4$, 5, and 6 are modelled as rigid bodies comprising the soil plug (with $\alpha = 1$ and $T = 0$ modelled at the soil plug base/soil interface). If an analysis includes soil weight then a vertical dead load equivalent to the weight of the soil plug is applied to caissons modelled as a rigid body.

5.4 Horizontal loading

5.4.1 Contact breaking prevented between caisson and soil

Normalised capacities of caissons when loaded horizontally at various points along the caisson length, obtained using 3D FELA, are shown in Figure 5.5(a) and (b) for uniform soil and NC soil respectively. It is shown that 3D FELA with adaptive mesh refinement can produce quite

close bounds on caisson capacities. The optimal depth of the attachment point (to the nearest $0.1L$) obtained using 3D FELA is referred to as L_{opt}. The solid black lines in Figure 5.5 indicate that caissons in uniform soil have $L_{\text{opt}} = 0.6L$ when $L/D \leq 5$ and a slightly higher $L_{\text{opt}} = 0.5L$ when $L/D = 6$. For caissons in NC soil the optimal load location is deeper, at $L_{\text{opt}} = 0.7L$, and is independent of caisson aspect ratio. The optimal load point can also be found using moment equilibrium, by assuming that the caisson translates at failure when loaded optimally.

Also shown (in blue) are capacities obtained using the approximate UB method described in Aubeny et al. (2003a) (see Equations 2.6 – 2.9). The UB capacities compare favourably with the FELA capacities. In uniform soil the optimal load point is slightly higher than that found using FELA, at $0.5L$ for all aspect ratios. Surprisingly, the Aubeny et al. capacities marginally underestimate FELA estimated capacities when $L_F/L > 0.6$ (Figure 5.5(a)). In NC soil the Aubeny et al. capacities also marginally underestimate FELA capacities when $L/D = 5$ and 6, but FELA capacities are overestimated at lower caisson aspect ratios ($L/D = 2$ and 3, Figure 5.5(b)). Capacities obtained in field model tests undertaken by Keaveny et al. (1994) are also shown in Figure 5.5(a) and these also compare favourably with the capacities obtained using FELA.

From Figure 5.5 it is apparent that when $L/D = 1$ the trend in capacity for different values of L_F is quite different to that when $L/D \geq 2$. When $L/D \geq 2$ the normalised caisson capacities are very similar and follow the same trend as L_F is varied. The solid lines in Figure 5.6 show the average normalised capacities of caissons with $L/D = 1$, 2, and 3 ($L/D = 4$, 5, and 6 removed to increase clarity). It is shown that the capacity of a caisson reduces rapidly when it is loaded away from L_{opt}. The rate of reduction in capacity is more severe in NC soil than in uniform soil. The maximum capacity of a caisson with $L/D = 3$ embedded in soil with $s_u = -\rho z$ is $10.1DLs_{u,av}$. When the same caisson is loaded just $0.1L$ above the optimal load location L_{opt}, the capacity reduces by 24% to $7.7DLs_{u,av}$ (see Figure 5.6(b)).

Capacities obtained using plane strain FELA for caissons with $L/D = 1$, 2, and 3 are shown as dashed lines in Figure 5.6. A caisson with $L/D = 1$ loaded at the mudline ($L_F/L = 0$) has

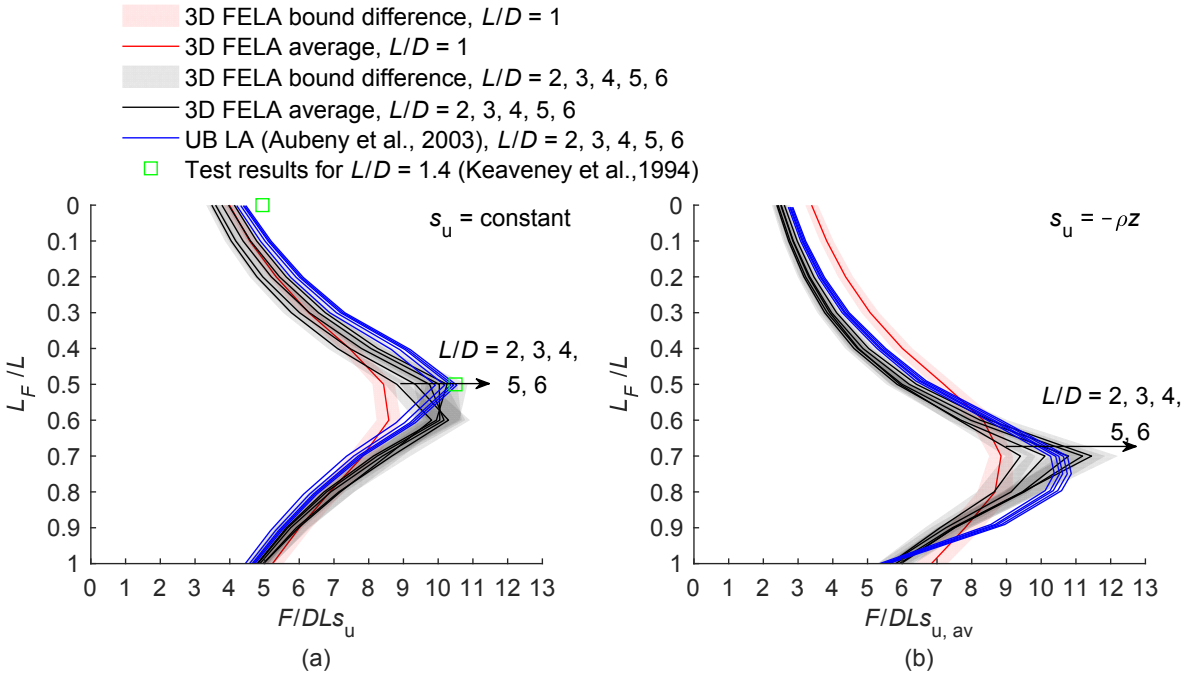

Figure 5.5: Normalised capacities of caissons when loaded horizontally ($\beta = 0$) at intervals of $0.1L$ along the caisson length. $T = \infty$, $\gamma' =$ any: (a) $s_u =$ constant; (b) $s_u = -\rho z$

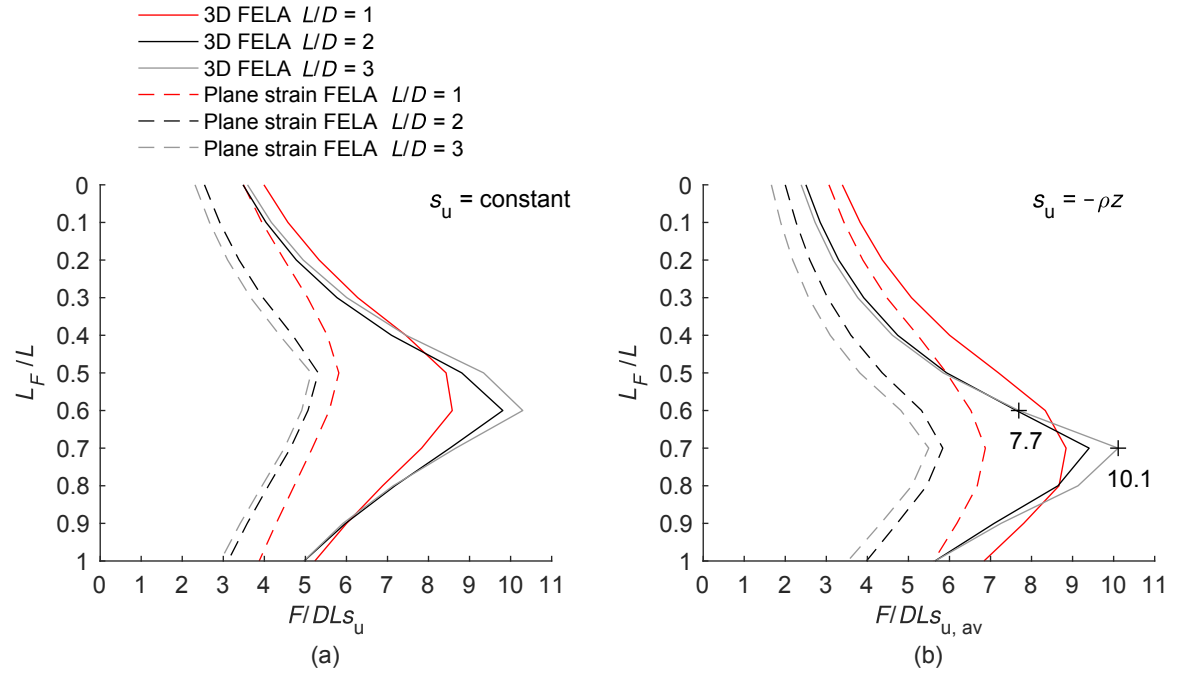

Figure 5.6: Normalised capacities of caissons modelled in 3D and plane strain when loaded horizontally ($\beta = 0$) at intervals of $0.1L$ along the caisson length. $T = \infty$, $\gamma' =$ any: (a) $s_u =$ constant; (b) $s_u = -\rho z$

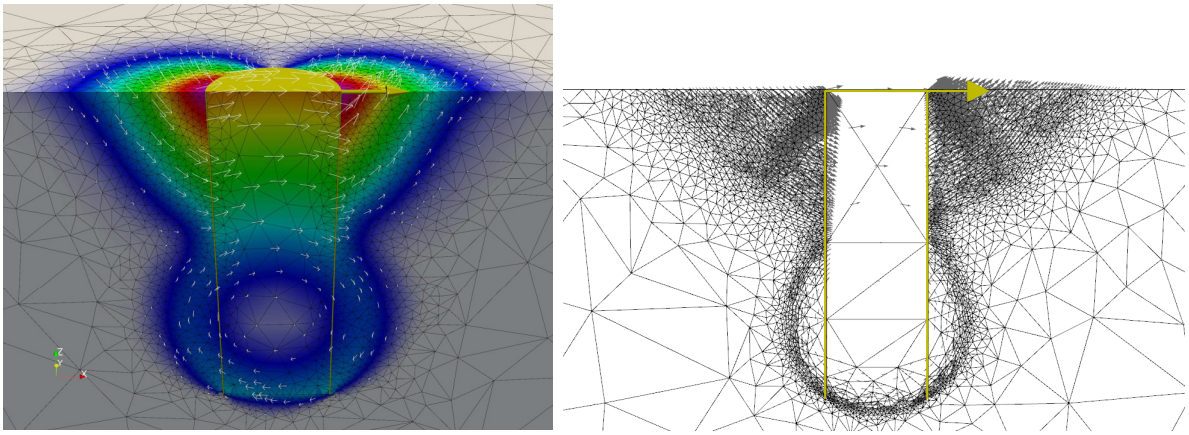

(a) (b)

Figure 5.7: Failure mechanism of a caisson with $L/D = 3$ when loaded horizontally ($\beta = 0$) at the mudline ($L_F/L = 0$). s_u = constant, $T = \infty$, $\gamma' =$ any. Shading and vectors show UB velocity magnitudes and directions: (a) 3D FELA; (b) plane strain FELA

a plane strain capacity that is only 13% lower than the corresponding 3D capacity in uniform soil and 10% lower in NC soil. However as L_F increases from zero to L_{opt} the difference between the plane strain and 3D capacities increases. In NC soil (Figure 5.6(b)) the trend of the plane strain capacities matches the trend of the 3D capacities reasonably well, while in uniform soil (Figure 5.6(a)) the plane strain analysis predicts an optimal load location that is marginally higher (by $0.1L$) than that found using 3D analysis. For both soil strength profiles, particularly when $L/D > 1$, there are large differences between the simplified plane strain and 3D capacities. For example, a caisson with $L/D = 3$ in uniform soil has a maximum plane strain capacity that is less than half of the maximum 3D capacity.

The plane strain and 3D capacities compare most favourably when the caisson is loaded at the mudline and least favourably when it is loaded at L_{opt}. The 3D failure mechanism for a caisson with $L/D = 3$ in uniform soil loaded at the mudline is shown in Figure 5.7(a). The caisson rotates clockwise at failure, with active and passive wedges of soil developing near the mudline. Below these a circular flow pattern is visible. The 3D mechanism involves minimal lateral soil flow around the caisson, and consequently the plane strain mechanism in Figure 5.7(b) closely resembles the 3D mechanism in the plane $y = 0$.

A caisson loaded below L_{opt} rotates counter-clockwise at failure, though the failure mechanism in the soil depends on the caisson aspect ratio. The 3D mechanism for a caisson

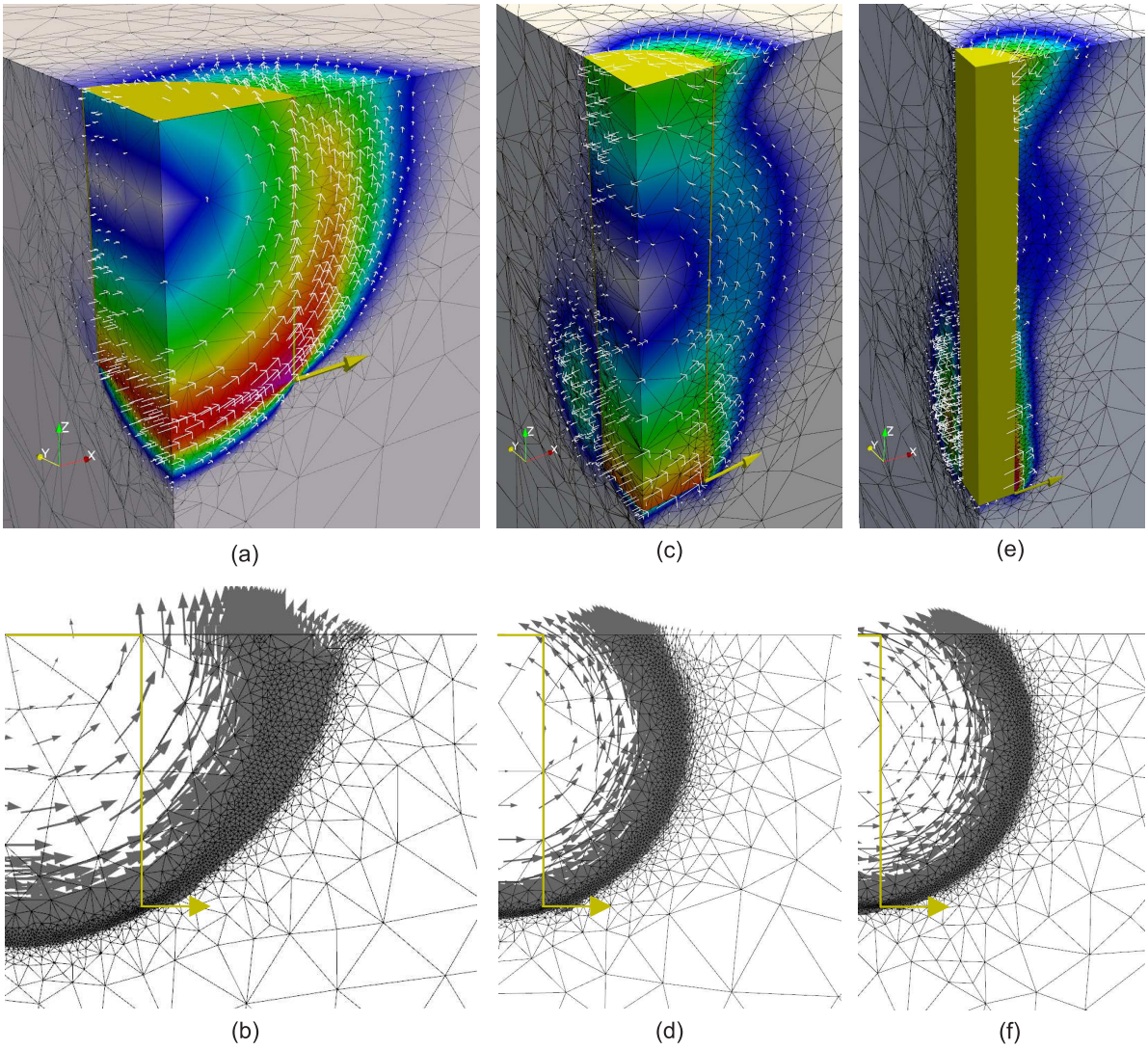

Figure 5.8: Failure mechanisms of caissons (antisymmetrical about $x = 0$ and symmetrical about $y = 0$) when loaded horizontally ($\beta = 0$) at the caisson base ($L_F/L = 1$). s_u = constant, $T = \infty$, $\gamma' =$ any. Shading and vectors show UB velocity magnitudes and directions: (a) $L/D = 1$, 3D FELA; (b) $L/D = 1$, plane strain FELA; (c) $L/D = 3$, 3D FELA; (d) $L/D = 3$, plane strain FELA; (e) $L/D = 6$, 3D FELA; (f) $L/D = 6$, plane strain FELA

with $L/D = 1$ in uniform soil loaded at its base is shown in Figure 5.8(a). In the plane $y = 0$, a circular flow pattern is visible and there is negligible lateral soil flow around the caisson. The corresponding plane strain mechanism (Figure 5.8(b)) is similar to the 3D mechanism in the plane $y = 0$. The 3D mechanism when $L/D = 3$ is shown in Figure 5.8(c). This mechanism is more complex than the one in Figure 5.8(a) as it involves additional deforming regions near the mudline and towards the base of the caisson. At the mudline, active and passive wedges of soil are mobilised, and below the centre of rotation the predominant mechanism is lateral soil flow around the caisson. These features are not identifiable in the failure mechanism from the corresponding plane strain analysis (Figure 5.8(d)). When $L/D = 6$, the wedges of soil displaced at the mudline and the lateral soil flow around the lower part of the caisson are more prominent in the 3D mechanism (Figure 5.8(e)). The plane strain mechanism has not changed substantially with increasing L/D (Figures 5.8(b), (d), and (f)) and as such the plane strain mechanism when $L/D = 6$ (Figure 5.8(f)) is a poor representation of the 3D failure mechanism (Figure 5.8(e)).

When a caisson is loaded at the optimal location L_{opt} the failure mechanism is again dependent on the aspect ratio. When $L/D = 1$ there is negligible lateral soil flow around the caisson, and the caisson translates at failure (Figure 5.9(a) and (b)). When $L/D > 1$ the 3D mechanism is dominated by lateral soil flow around the caisson at depths below $z = -L/2$ (Figure 5.9(c)). Clearly this behaviour cannot be captured by the corresponding plane strain analysis (Figure 5.9(d)).

The failure mechanism changes considerably when a caisson is loaded just above or just below L_{opt}. In Figure 5.10(a) a caisson in uniform soil with $L/D = 6$ is loaded at $0.1L$ above L_{opt}. The caisson rotates clockwise at failure, pivoting about a point near its base, and shows similarities to a caisson loaded at the mudline (Figure 5.7(a)). The mechanism of a caisson with $L/D = 6$ loaded at L_{opt} is similar to that for a caisson with $L/D = 4$ (comparing Figure 5.10(b) and Figure 5.9(c)). When the load is applied just $0.1L$ below L_{opt} the mechanism changes and is now similar to that for a caisson loaded at its base (comparing Figure 5.10(c) and Figure 5.8(e)).

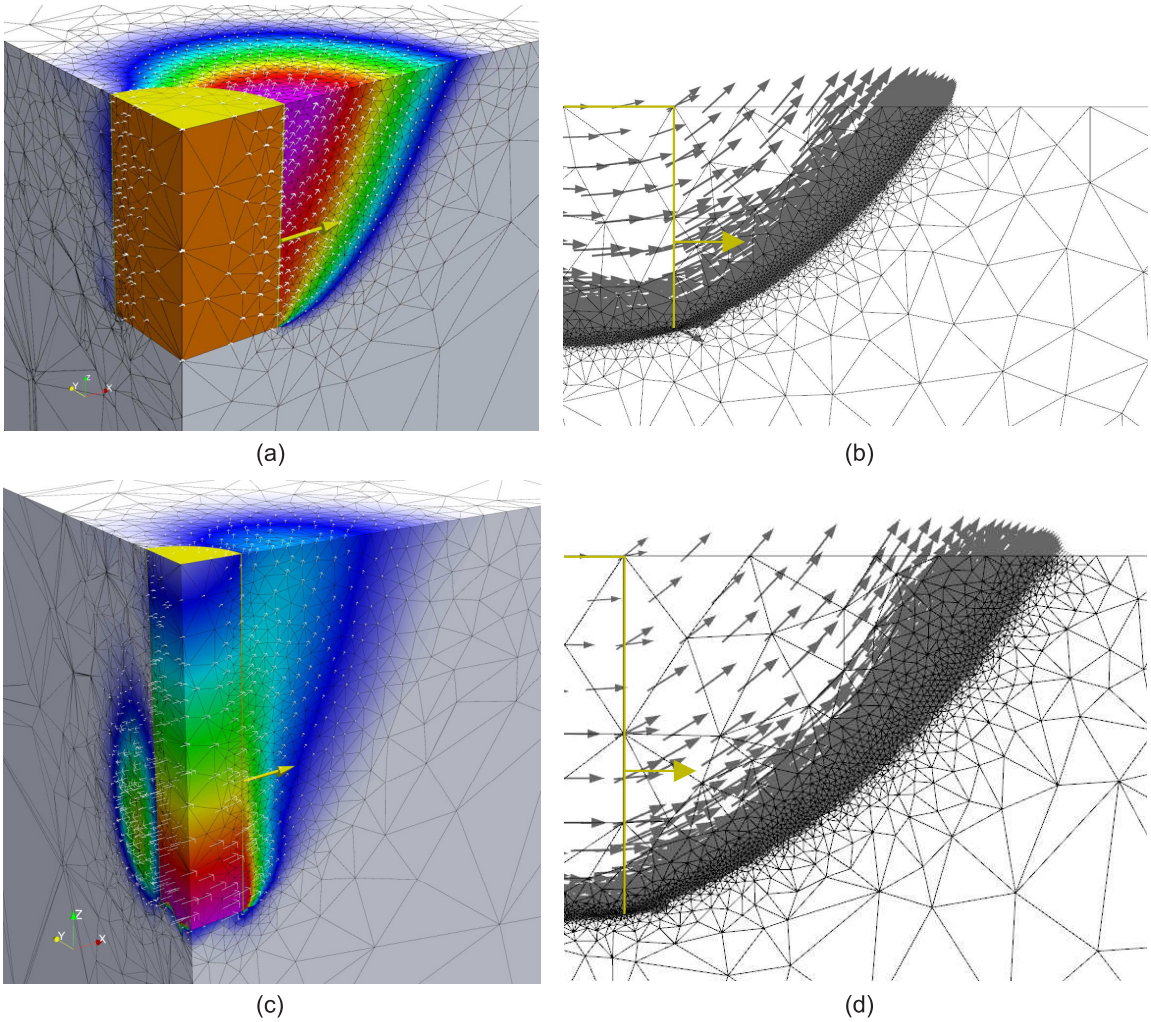

Figure 5.9: Failure mechanisms of caissons (antisymmetrical about $x = 0$ and symmetrical about $y = 0$) when loaded horizontally ($\beta = 0$) at the optimal point ($L_F = L_{\text{opt}} = 0.6L$). s_u = constant, $T = \infty$, $\gamma' =$ any. Shading and vectors show UB velocity magnitudes and directions: (a) $L/D = 1$, 3D FELA; (b) $L/D = 1$, plane strain FELA; (c) $L/D = 3$, 3D FELA; (d) $L/D = 3$, plane strain FELA

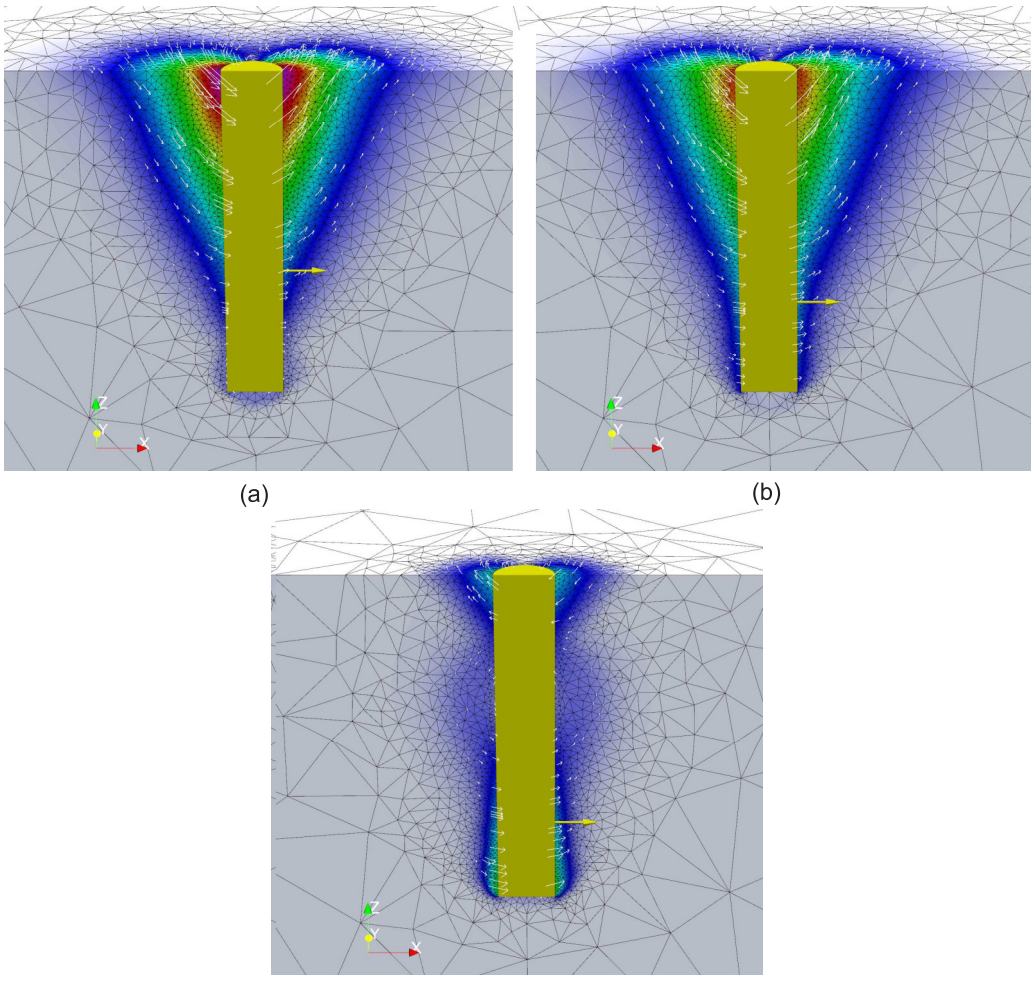

Figure 5.10: Failure mechanism of a caisson with $L/D = 6$ when loaded horizontally ($\beta = 0$). s_u = constant, $T = \infty$, $\gamma' =$ any. Shading and vectors show UB velocity magnitudes and directions: (a) $L_F/L = 0.6$; (b) $L_F = L_{opt} = 0.7L$; (c) $L_F/L = 0.8$

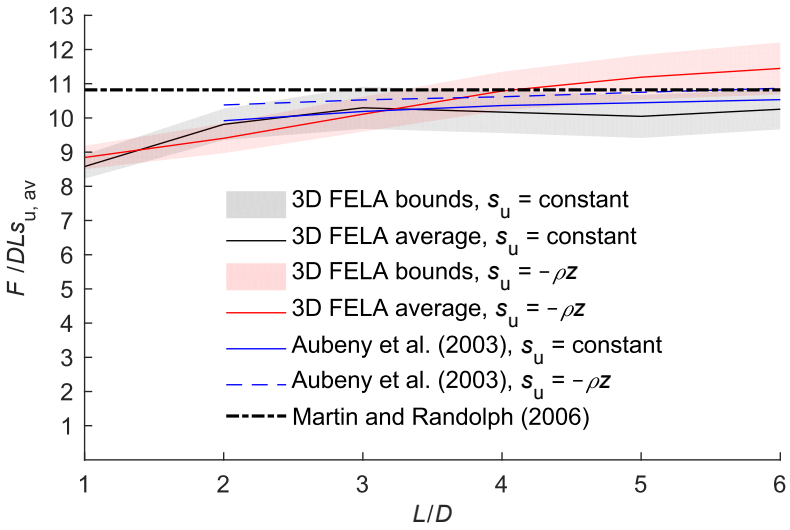

Figure 5.11: Maximum normalised capacities of caissons with roughness factor $\alpha = 0.5$. $\beta = 0$, $T = \infty$, $\gamma' =$ any

As the caisson aspect ratio L/D increases, the maximum normalised 3D capacity increases, but the maximum normalised plane strain capacity decreases (Figure 5.6). Upon consideration of the corresponding failure mechanisms, the increase in normalised capacity with increasing aspect ratio in a 3D analysis can be attributed to increased lateral soil flow around the caisson. In a plane strain analysis lateral soil flow around the caisson is not possible. For this case increasing the caisson aspect ratio results in a lower normalised capacity as the relative contribution of base shear to the overall capacity is reduced.

The capacity of horizontally loaded caissons is highest when, at failure, the caisson undergoes translation without any rotation. As previously discussed in Section 3.5.2, UB solutions for the plastic capacity of a circular pile section with $\alpha = 0.5$ translating in cohesive soil can be found in Martin and Randolph (2006). Figure 5.11 shows the maximum normalised capacities of horizontally loaded caissons obtained using 3D FELA, UB capacities using the Aubeny et al. (2003a) method, and the capacity of a translating pile section with $\alpha = 0.5$ from Martin and Randolph (2006). As the aspect ratio L/D increases, the maximum normalised capacity of a caisson in uniform soil (obtained for loading applied at L_{opt}) approaches the theoretical limit. This increase in capacity as L/D increases corresponds to a failure mechanism that becomes increasingly dominated by lateral soil flow

around the caisson. The normalised capacity of a caisson in NC soil shows similar behaviour, although the average FELA maximum capacity is slightly higher than the theoretical UB capacity from Martin and Randolph (2006) when $L/D \geq 4$, when the capacity is normalised by the average shear strength along the caisson length $s_{u,av}$. Capacities obtained using the Aubeny et al. (2003a) method do not exceed the capacity of a pile translating from Martin and Randolph (2006).

5.4.2 Contact breaking allowed between caisson and soil

This section introduces the possibility of contact breaking between the external caisson wall and the soil ($T = 0$). This allows a gap to form between the caisson and the soil if it is optimal to do so and results in a reduction in capacity. Whether a gap forms or not is dependent on the weight to strength ratio of the soil. A caisson loaded horizontally at L_{opt} translates horizontally at failure. Irrespective of caisson aspect ratio, when contact breaking is prevented ($T = \infty$), an active wedge of soil is pulled behind the caisson (Figure 5.10(b)). When contact breaking is allowed, a gap forms along the full caisson length on its active side if the soil is weightless ($\gamma' = 0$) (Figure 5.12). The soil weight to strength ratio determines whether soil fails actively or not, as gravity encourages active failure of a relatively heavy soil, which prevents a gap from opening (also discussed in Section 4.3.4.1). This study considers three soil weight to strength ratios, $\gamma' D/s_u = 0$, 1, and 5 in uniform soil and $\gamma'/\rho = 0$, 1, and 5 in NC soil.

The capacities of caissons with $L/D = 1$, 2, and 3 loaded horizontally at various points along the caisson length are shown in Figure 5.13(a), (c), and (e) for uniform soil and Figure 5.13(b), (d), and (f) for NC soil. Inspection shows that for all load locations, the capacity of a caisson with $T = 0$ in weightless soil is lower than that for a caisson with $T = \infty$. It is also apparent that when $L/D = 1$ the shape of the normalised caisson capacity curve is quite different to those when $L/D = 2$ and 3. Accordingly, when $L/D = 2$ and 3, the capacity curves are similar. As might be expected, when $4 \leq L/D \leq 6$ the shapes of the curves match those for $L/D = 2$ and 3, and for the sake of brevity these results are not shown as capacity charts. However, maximum capacities with corresponding optimal attachment points for all caisson aspect ratios, soil strength profiles, wall/soil interface conditions, and

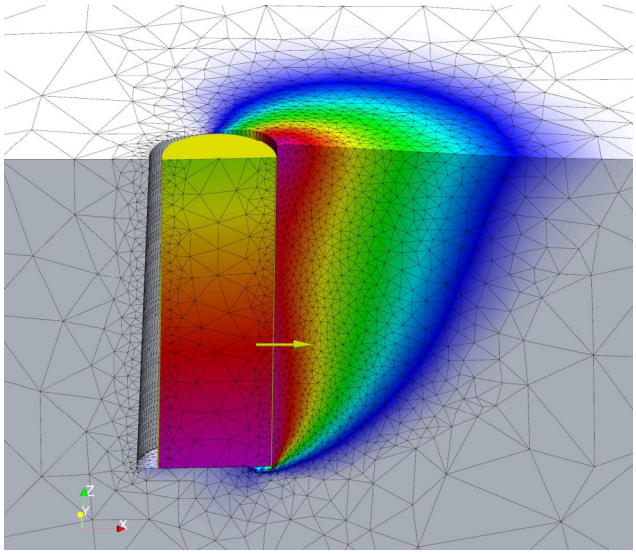

Figure 5.12: Failure mechanism of a caisson with $L/D = 3$ loaded horizontally ($\beta = 0$) at $L_F = L_{opt} = 0.6L$. s_u = constant, $T = 0$, $\gamma' = 0$. Deformation and shading show UB velocity magnitudes and directions

soil weights are listed in Table 5.1.

The maximum capacities of caissons with $L/D = 1$, 2, and 3 in weightless soil of uniform strength with $T = 0$ are 5.2, 5.7, and $6.2DLs_u$ respectively, about 40% lower than the corresponding capacities with $T = \infty$ (8.6, 9.8, and $10.3DLs_u$, see Figure 5.13(a), (c), and (e)). The capacity of caissons with $T = 0$ increases with increasing soil weight to strength ratio.

A caisson with $L/D = 1$ and $T = 0$ in uniform soil with normalised weight $\gamma' D/s_u = 5$ has a maximum capacity that is lower than that of a caisson with $T = \infty$ (Figure 5.13(a)). However, when $L/D = 3$, the maximum capacities are the same for caissons with $T = \infty$ and $T = 0$, $\gamma' D/s_u = 5$ (Figure 5.13(e)). The mechanisms in Figure 5.14(a)–(c) show that a gap forms on the trailing side of the caisson with $L/D = 1$, $T = 0$, and $\gamma' D/s_u = 5$ whether it is loaded above, below, or at L_{opt}. Soil is consequently not mobilised on the active side of the caisson and the capacity is lower than that for a caisson with $T = \infty$.

When $L/D \geq 2$, caissons in soil with $\gamma' D/s_u = 5$ have the same maximum capacity as a caisson with $T = \infty$ (Figure 5.13(c) and (e)). But careful inspection of Figure 5.13(c) and (e) shows that there is a slight reduction in the capacity of a caisson with $T = 0$ and $\gamma' D/s_u = 5$ when compared to a caisson with $T = \infty$ when it is loaded away from L_{opt}. This reduction in

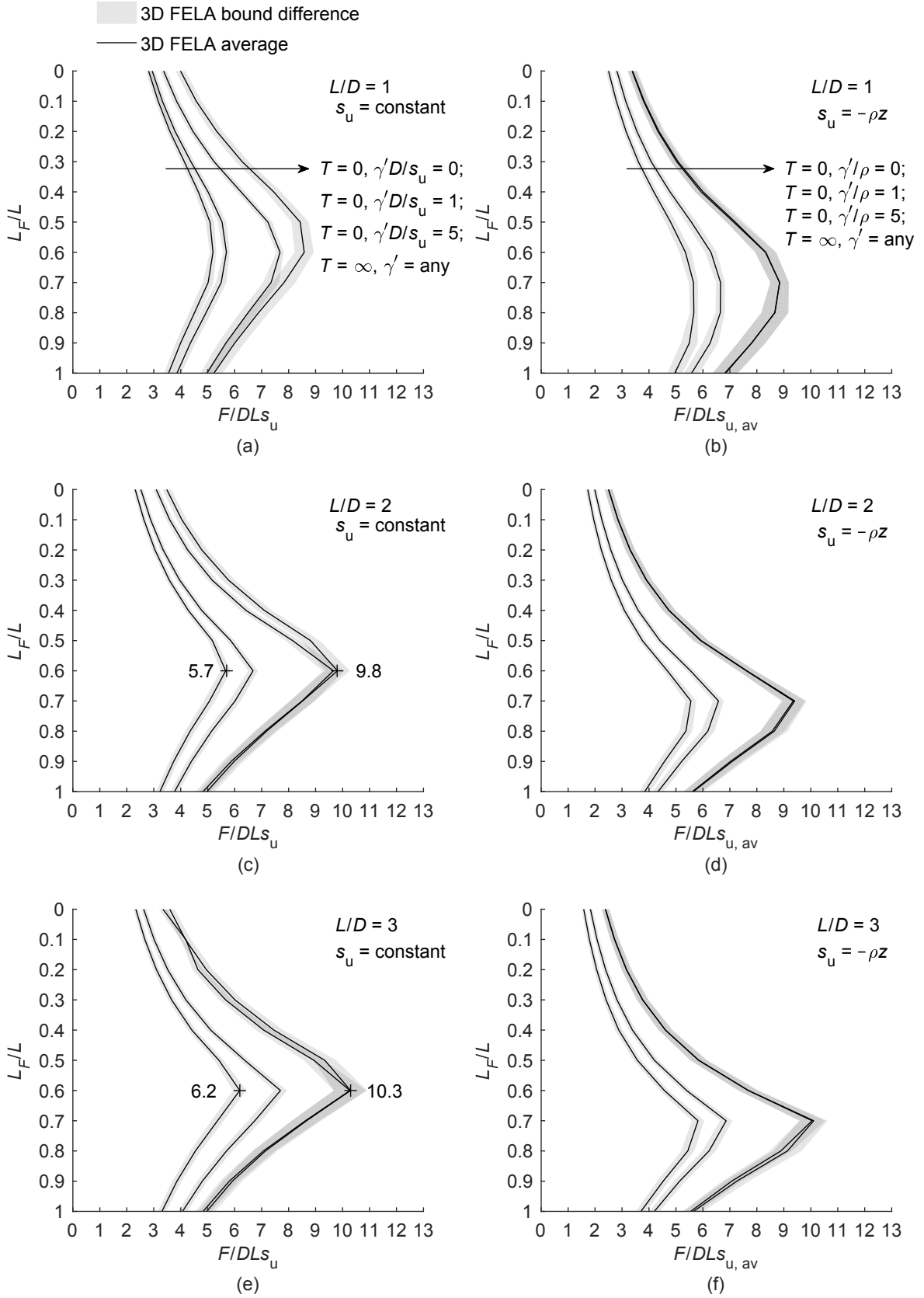

Figure 5.13: Normalised capacities of caissons when loaded horizontally ($\beta = 0$) at various points along the caisson length showing the effect of contact breaking: (a) $L/D = 1$, $s_u =$ constant; (b) $L/D = 1$, $s_u = -\rho z$; (c) $L/D = 2$, $s_u =$ constant; (d) $L/D = 2$, $s_u = -\rho z$; (e) $L/D = 3$, $s_u =$ constant; (f) $L/D = 3$, $s_u = -\rho z$

Table 5.1: Maximum capacities (F in table = $F/DLs_{u,av}$) and corresponding optimal load points to the nearest $0.1L$ (L_{opt} in table $= L_{opt}/L$) for caissons loaded horizontally ($\beta = 0$)

s_u = constant	$T = 0$						$T = \infty$	
	$\gamma'/s_u = 0$		$\gamma'/s_u = 1$		$\gamma'/s_u = 5$		$\gamma' =$ any	
L/D	F	L_{opt}	F	L_{opt}	F	L_{opt}	F	L_{opt}
1	5.20	0.6	5.69	0.6	7.68	0.6	8.59	0.6
2	5.67	0.6	6.68	0.6	9.66	0.6	9.81	0.6
3	6.18	0.6	7.70	0.6	10.27	0.6	10.30	0.6
4	6.60	0.6	8.57	0.6	10.16	0.6	10.17	0.6
5	6.96	0.6	9.18	0.6	10.03	0.6	10.05	0.6
6	7.28	0.6	9.46	0.6	10.05	0.5	10.26	0.5
$s_u = -\rho z$	$T = 0$						$T = \infty$	
	$\gamma'/\rho = 0$		$\gamma'/\rho = 1$		$\gamma'/\rho = 5$		$\gamma' =$ any	
L/D	F	L_{opt}	F	L_{opt}	F	L_{opt}	F	L_{opt}
1	5.66	0.8	6.65	0.7	8.84	0.7	8.84	0.7
2	5.55	0.7	6.58	0.7	9.35	0.7	9.40	0.7
3	5.81	0.7	6.86	0.7	10.05	0.7	10.11	0.7
4	6.21	0.7	7.24	0.7	10.59	0.7	10.79	0.7
5	6.48	0.7	7.52	0.7	10.90	0.7	11.19	0.7
6	6.75	0.7	7.81	0.7	11.11	0.7	11.45	0.7

capacity can be attributed to the opening of gaps between the caisson and the soil at failure. A caisson loaded above L_{opt} rotates clockwise at failure and a deep gap opens up at the mudline behind the caisson (Figure 5.14(d)). When the caisson is loaded at L_{opt} it tilts counter-clockwise at failure and this prevents a gap from forming; the mechanism is very similar to that of a caisson with $T = \infty$ (comparing Figure 5.14(e) to Figure 5.10(b)). When the caisson is loaded below L_{opt} a shallow gap opens at the mudline in front of the caisson (Figure 5.14(f)).

Comparing Figure 5.14(a) to (d) it is apparent that as caisson length increases, the size of any gap relative to the overall caisson length decreases for any given normalised soil weight. This leads to capacities of caissons (with $T = 0$) in soil with weight that tend towards the capacity of a caisson with $T = \infty$ as L/D increases. This can be demonstrated by considering the capacities of a caisson in uniform soil with $T = 0$ and $\gamma' D/s_u = 1$ in Figure 5.13. As L/D

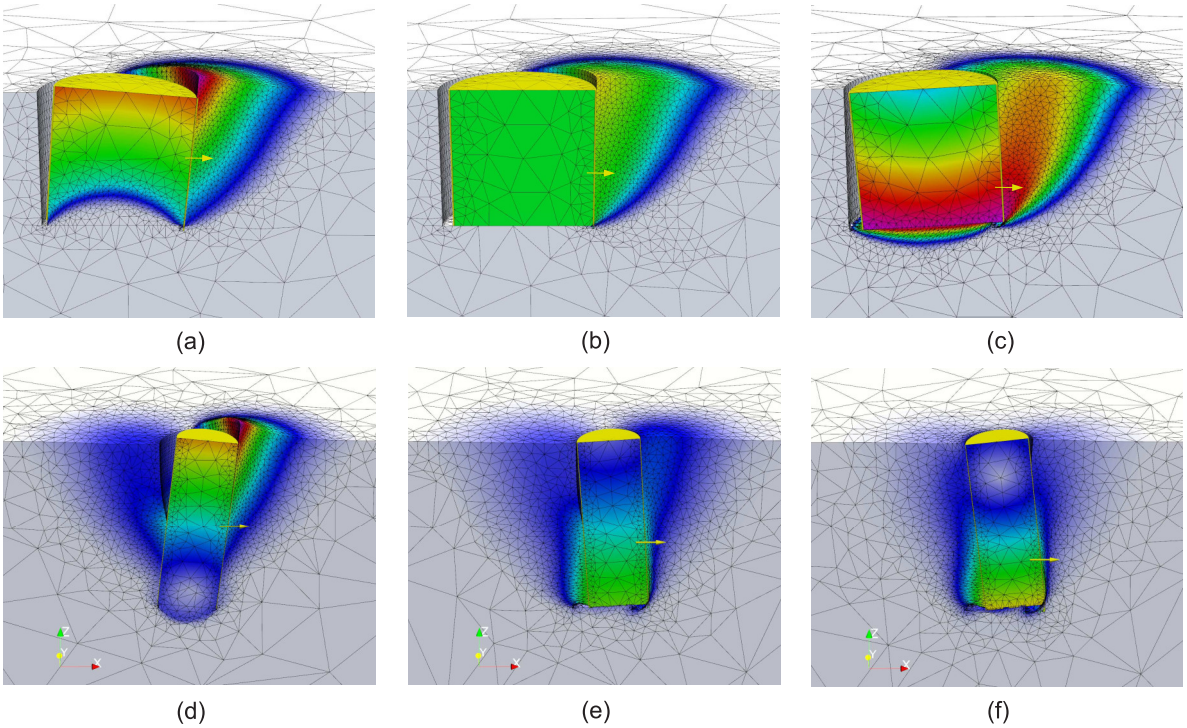

Figure 5.14: Failure mechanisms of caissons loaded horizontally. s_u = constant, $T = 0$, $\gamma' D/s_u = 5$. Deformation and shading show UB velocity magnitudes and directions: (a) $L/D = 1$, $L_F/L = 0.5$; (b) $L/D = 1$, $L_F = L_{opt} = 0.6L$ (c) $L/D = 1$, $L_F/L = 0.7$; (d) $L/D = 3$, $L_F/L = 0.5$; (e) $L/D = 3$, $L_F = L_{opt} = 0.6L$ (f) $L/D = 3$, $L_F/L = 0.7$

increases (moving from Figure 5.13(a), to (c), to (e)), these curves are further from the curve for $T = 0$, $\gamma' = 0$ and closer to the curve for $T = \infty$.

In NC soil, for all L/D and L_F, capacities when $T = 0$ and $\gamma'/\rho = 5$ are the same as when $T = \infty$. The effect of tension breaking on the capacities as L_F is varied, for a given normalised soil weight, is very similar for all caisson aspect ratios (Figure 5.13(b), (d), and (f) and Table 5.1).

5.5 Inclined loading

5.5.1 Contact breaking prevented between caisson and soil

In this section loading is applied to caissons at angles $\beta = 15°$, $30°$, and $45°$. Capacities of caissons subjected to an inclined load applied at various points along the caisson length are shown in Figure 5.15(a), (c), and (e) for uniform soil, and (b), (d), and (f) for NC soil. Maximum caisson capacities and corresponding load locations are also summarised in

Table 5.2: Maximum capacities (F in table = $F/DLs_{u,av}$) and corresponding optimal load points to the nearest $0.1L$ (L_{opt} in table = L_{opt}/L) for caissons loaded loaded at angles $\beta = 0$, 15°, 30°, and 45° ($\beta = 0$) when $T = \infty$

s_u = constant	$\beta = 0$		$\beta = 15°$		$\beta = 30°$		$\beta = 45°$	
L/D	F	L_{opt}	F	L_{opt}	F	L_{opt}	F	L_{opt}
1	8.58	0.6	8.90	0.4	9.60	0.3	9.87	0.1
2	9.81	0.6	9.95	0.5	9.14	0.4	7.63	0.3
3	10.30	0.6	10.17	0.5	8.32	0.4	6.35	0.3
4	10.17	0.6	10.24	0.5	7.64	0.4	5.55	0.3
5	10.05	0.6	10.25	0.5	7.03	0.4	5.03	0.3
6	10.26	0.5	10.24	0.5	6.56	0.4	4.67	0.3
$s_u = -\rho z$	$\beta = 0$		$\beta = 15°$		$\beta = 30°$		$\beta = 45°$	
L/D	F	L_{opt}	F	L_{opt}	F	L_{opt}	F	L_{opt}
1	8.84	0.7	9.15	0.6	10.20	0.4	12.21	0.2
2	9.40	0.7	9.39	0.7	10.33	0.6	10.58	0.5
3	10.11	0.7	10.23	0.7	10.36	0.6	9.23	0.5
4	10.79	0.7	10.71	0.7	9.78	0.6	8.01	0.5
5	11.19	0.7	10.85	0.7	9.26	0.6	7.15	0.5
6	11.45	0.7	10.83	0.7	8.76	0.6	6.52	0.5

Table 5.2.

What is immediately visible in Figure 5.15 is that the load angle significantly affects the optimal load point. For inclined loads, Randolph and House (2002) state that the critical dimension is not the external padeye location (L_F), but the length to the intersection of the loading vector with the caisson centreline (℄ in Figure 5.16). When $\beta = 0$ the loading vector intersects with the caisson centreline at $L_{opt,\beta=0}$. In Figure 5.16 inclined loading vectors are applied to caisson centrelines at $L_{opt,\beta=0}$ for caissons in uniform soil. The optimal load point for an inclined load, $L_{opt,\beta}$, is simply the location at which the load vector crosses the caisson wall. Comparing the L_{opt} values for $\beta = 15°$, 30°, and 45° in Figure 5.16(a) to the FELA-calculated values in Table 5.2, it is shown that this reasoning works well for a caisson with $L/D = 1$. As L/D increases, L_{opt} values from Figure 5.16 compare less favourably with FELA values from Table 5.2. It is interesting that for the range of caisson aspect ratios considered here, Table 5.2 shows that for each load angle, the optimal load point (to the nearest $0.1L$) is independent of caisson aspect ratio when $L/D \geq 2$.

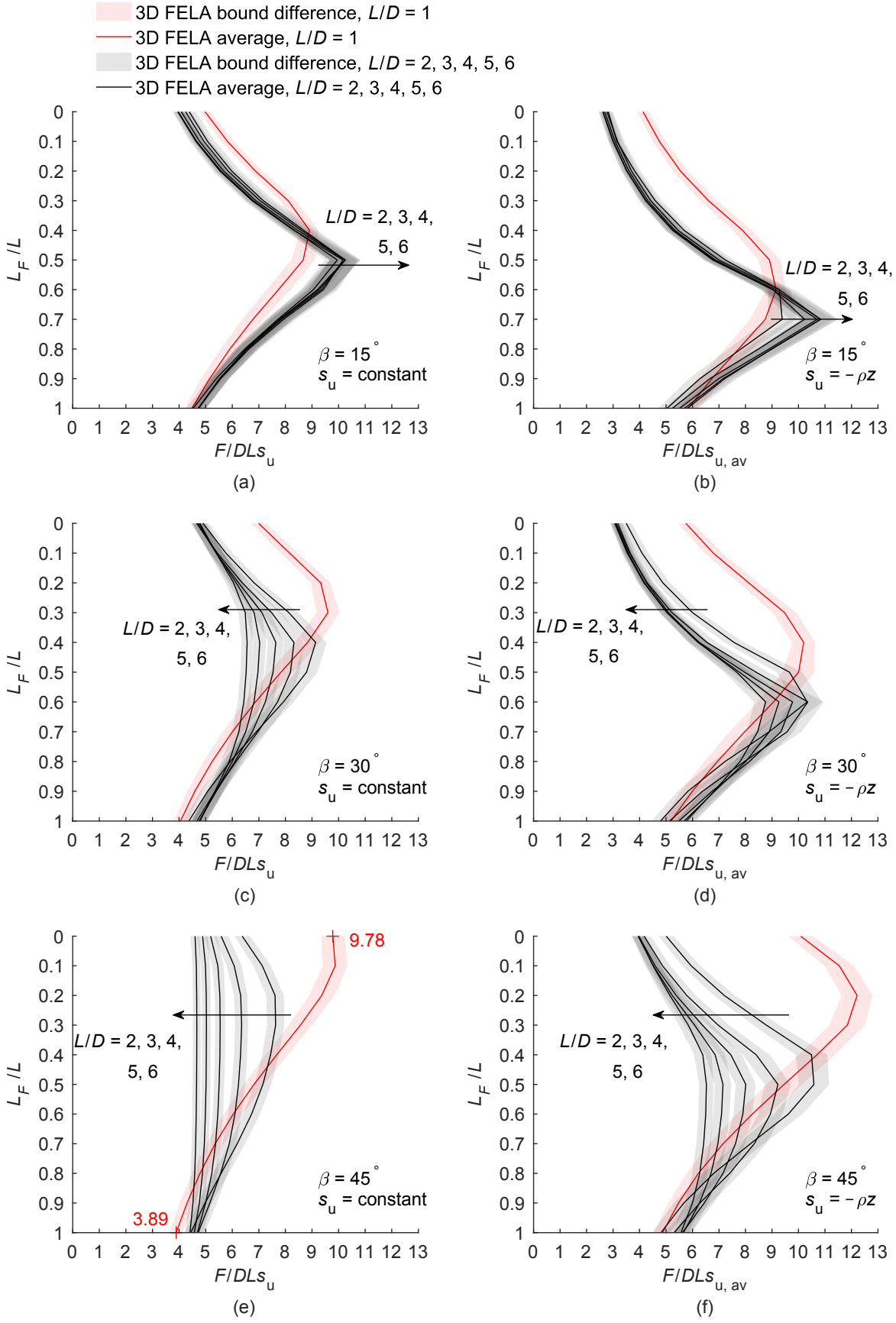

Figure 5.15: Normalised capacities of caissons when loaded at various points along the caisson length. $T = \infty$, $\gamma' =$ any: (a) $\beta = 15°$, $s_u =$ constant; (b) $\beta = 15°$, $s_u = -\rho z$; (c) $\beta = 30°$, $s_u =$ constant; (d) $\beta = 30°$, $s_u = -\rho z$ (e) $\beta = 45°$, $s_u =$ constant; (f) $\beta = 45°$, $s_u = -\rho z$

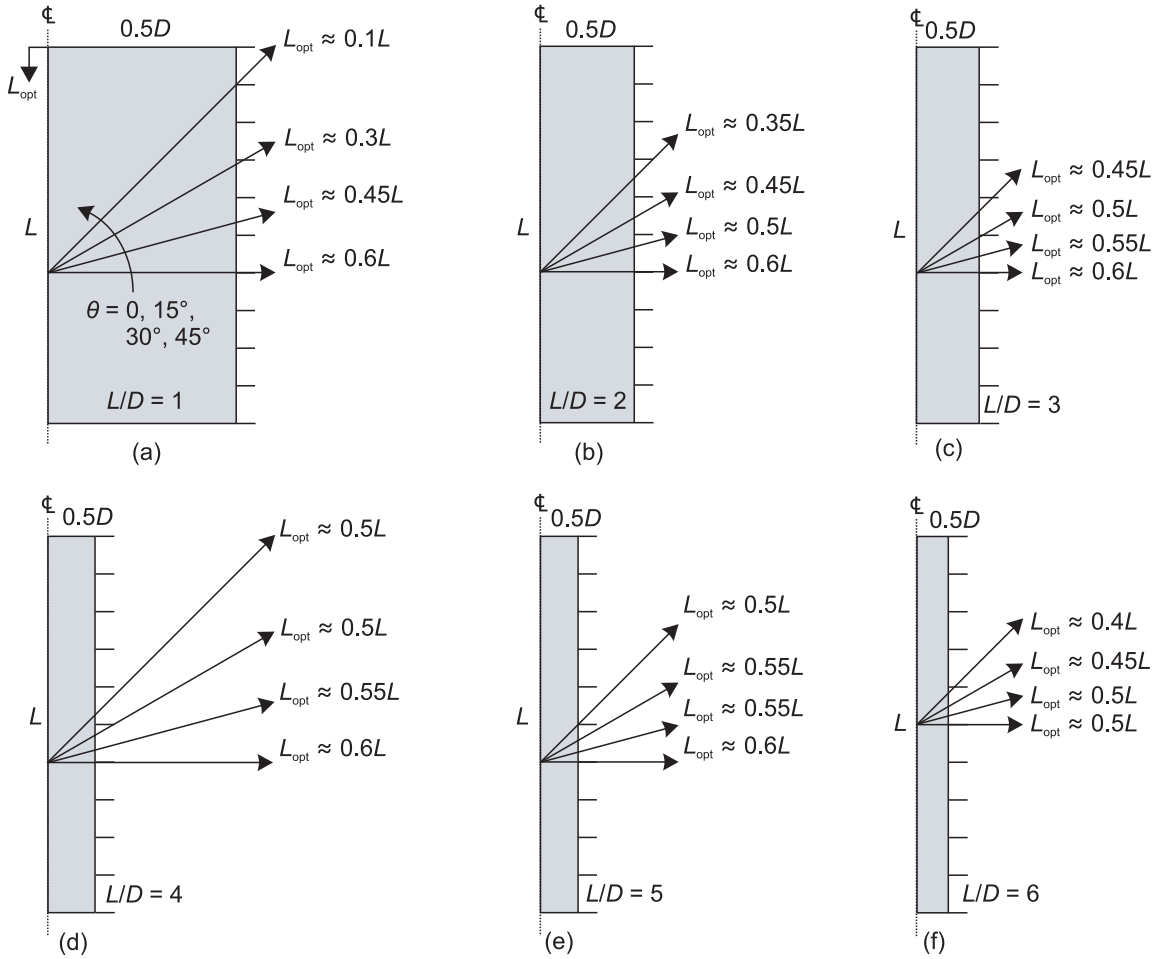

Figure 5.16: Optimal load points found by applying loads at the caisson centreline (℄) at $L_{\text{opt},\beta=0}$. s_u = constant, $T = \infty$, $\gamma' =$ any: (a) $L/D = 1$; (b) $L/D = 2$; (c) $L/D = 3$; (d) $L/D = 4$; (e) $L/D = 5$; (f) $L/D = 6$

From Figure 5.15 it is shown that the capacity curve is quite different for $L/D = 1$ than for $L/D \geq 2$. Considering a caisson with $L/D = 1$, it is shown in Figure 5.15 (and Table 5.2) that increasing the load angle beyond 15° results in an increased capacity when compared with horizontal loading. The mechanisms for caissons with $L/D = 1$ in uniform soil loaded at L_{opt} (shown in Figure 5.17(a) and (b)) are very similar although the optimal attachment point is marginally higher when $\beta = 15°$. In both cases the caisson is translating in the direction of the load, with active and passive wedges of soil developing next to the caisson walls. There is no soil mobilised below the caisson. When $\beta = 30°$ (Figure 5.17(c)) the caisson is still translating in the direction of the load but soil is now also mobilised below the caisson. This resembles a partial reverse end bearing mechanism. When $\beta = 45°$ the reverse end bearing component of

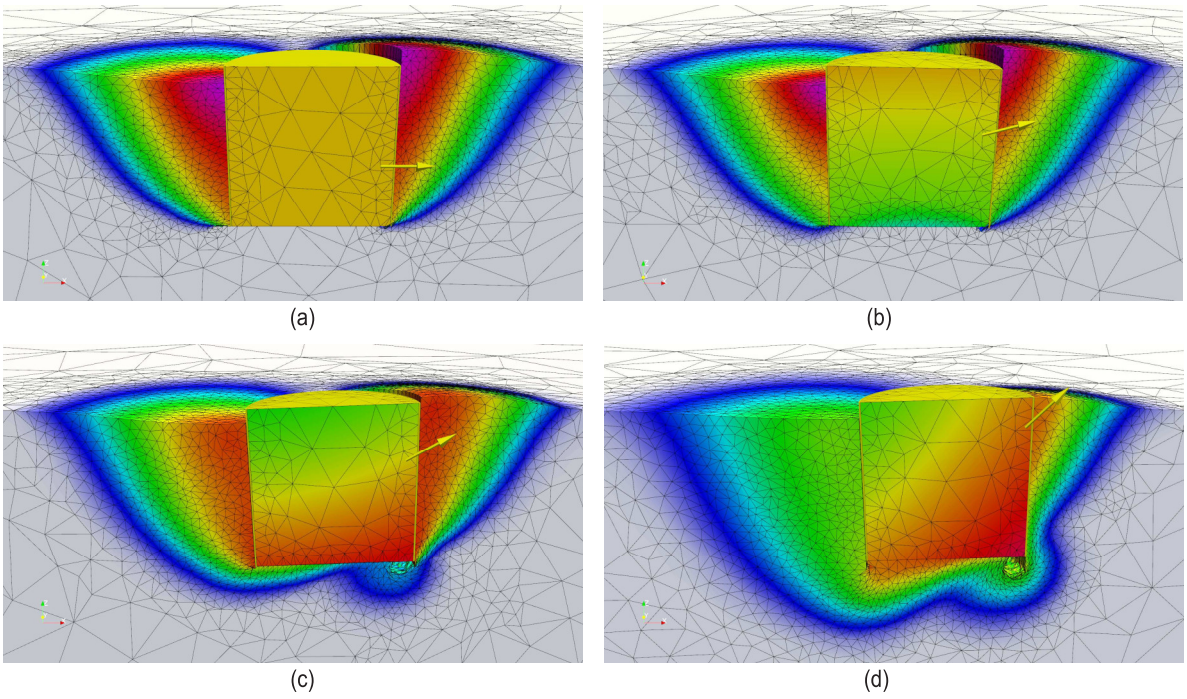

Figure 5.17: Failure mechanisms of caissons with $L/D = 1$ loaded at $L_F = L_{opt}$. s_u = constant, $T = \infty$, γ' = any: (a) $\beta = 0$, $L_{opt} = 0.6L$; (b) $\beta = 15°$, $L_{opt} = 0.4L$; (c) $\beta = 30°$, $L_{opt} = 0.3L$; (d) $\beta = 45°$, $L_{opt} = 0.1L$. Deformation and shading show UB velocity magnitudes and directions

the mechanism is more obvious (Figure 5.17(d)) and this mechanism yields a higher capacity than the active and passive wedge mechanism formed when $\beta = 0$ (Figure 5.17(a)).

For caissons with $L/D \geq 2$, the maximum normalised capacity reduces as the load angle increases (Table 5.2). By comparing Figure 5.5(a) and (b) to Figure 5.15(a) and (b) it is shown that a 15° inclination of the load makes very little difference to the caisson capacity (at any L_F) when compared with a horizontally loaded caisson. This was also noted by Aubeny et al. (2003a). It is shown in Figure 5.15(c) and (e) for uniform soil and (d) and (f) for NC soil that when $\beta = 30°$ and 45° the maximum normalised capacity reduces as caisson aspect ratio increases. When $\beta = 45°$ The capacity of a caisson in uniform soil with $L/D = 6$ does not vary significantly as L_F is varied, but the capacity varies by a factor of 2.5 depending on L_F for a caisson with $L/D = 1$ (Figure 5.15(e)).

The failure mechanisms for a caisson with $L/D = 1$ in uniform soil loaded at $\beta = 45°$ at the mudline and at the caisson base vary considerably (comparing Figure 5.18(a) and (b)). When loaded at the mudline, the mechanism involves a reverse end bearing component and is similar

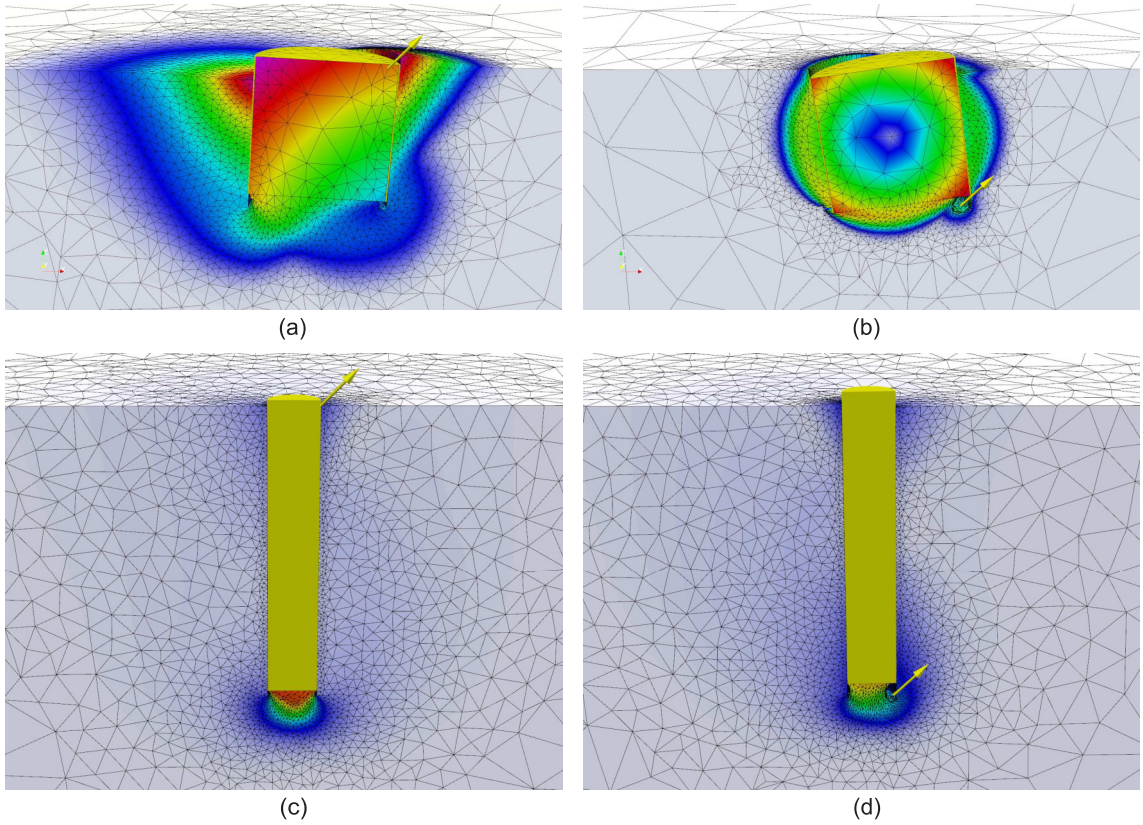

Figure 5.18: Failure mechanisms of caissons loaded at $\beta = 45°$. s_u = constant, $T = \infty$, $\gamma' =$ any. Deformation and shading show UB velocity magnitudes and directions: (a) $L/D = 1$, $L_F = 0$; (b) $L/D = 1$, $L_F = L$; (c) $L/D = 6$, $L_F = 0$; (d) $L/D = 6$, $L_F = L$

to Figure 5.17(d). When loaded at the caisson base, the caisson rotates counter-clockwise and the mechanism is similar to that of a caisson loaded horizontally at its base (Figure 5.8(a)). As the mechanisms are so different it is understandable that the corresponding capacities are also quite different ($9.78DLs_u$ when loaded at the mudline and $3.89DLs_u$ when loaded at the caisson base, shown in Figure 5.15(e)). For this caisson aspect ratio and loading direction, the load location significantly affects caisson capacity.

The mechanisms for a caisson with $L/D = 6$ loaded at $\beta = 45°$ at the mudline and at the caisson base are shown in Figure 5.18(c) and (d). These mechanisms are somewhat similar as in both cases the caisson translates predominantly upwards at failure and a reverse end bearing mechanism is visible at the caisson base. For these two load points the capacities are reasonably close: $4.60DLs_u$ when loaded at the mudline compared with $4.41DLs_u$ when loaded at the caisson base. These values are also close to the maximum capacity, namely $4.67DLs_u$ at $L_{opt} = 0.3L$ (Table 5.2), and it can be concluded that load location does not

effect capacity in this case. The effect of load location on caisson capacity in NC soil when $\beta = 45^\circ$ is also reduced as L/D increases, when compared with a horizontally loaded caisson (comparing Figure 5.5(b) and Figure 5.15(f)).

Capacities obtained using plane strain and 3D FELA are compared for caissons with $L/D = 1$, 3, and 6 in Figure 5.19 ((a), (c), and (e) for uniform soil and (b), (d), and (f) for NC soil). As for a horizontally loaded caisson, when $\beta = 15^\circ$ the plane strain capacities become increasingly inaccurate as L/D increases for both soil strength profiles (Figure 5.19(a) and (b)). However the optimal load point for a caisson under inclined loading can be estimated reasonably accurately by using a plane strain analysis.

When $\beta = 45^\circ$ the capacities obtained using a plane strain analysis are closer to the 3D capacities than when the caisson is horizontally loaded (comparing Figure 5.6(a) and (b) to Figure 5.19(e) and (f)). The maximum capacity is still underestimated by $\sim$30% when compared with the 3D capacity. Unlike a horizontally loaded caisson, the capacities compare most favourably when the caisson is loaded at its base. As L_F decreases from L to zero, the difference between the plane strain and 3D capacities increases.

5.5.2 Contact breaking allowed between caisson and soil

This section considers the effect of contact breaking between the external caisson wall and the soil for a caisson loaded at inclinations $\beta = 15^\circ$, 30°, and 45°. Capacities of a caisson with $L/D = 1$ loaded at various points along the caisson length are shown in Figure 5.20(a), (c), and (e) for uniform soil and Figure 5.20(b), (d), and (f) for NC soil. Capacities of caissons with $L/D = 3$ and 6 are shown in Figure 5.21 and Figure 5.22 respectively. Maximum caisson capacities and corresponding optimal load points for all caissons with $T = 0$ in weightless soil are summarised in Table 5.3. Table 5.4 shows the percentage reduction in the capacity of a caisson with $T = 0$ in weightless soil when compared to a caisson with $T = \infty$ (in which case capacity is independent of soil weight).

From Table 5.4, it can be seen that as the load inclination increases the reduction in capacity due to contact breaking reduces in uniform soil, but remains approximately the same in NC soil. A caisson with $L/D = 1$ undergoes a 30 – 40% reduction in capacity when $T = 0$

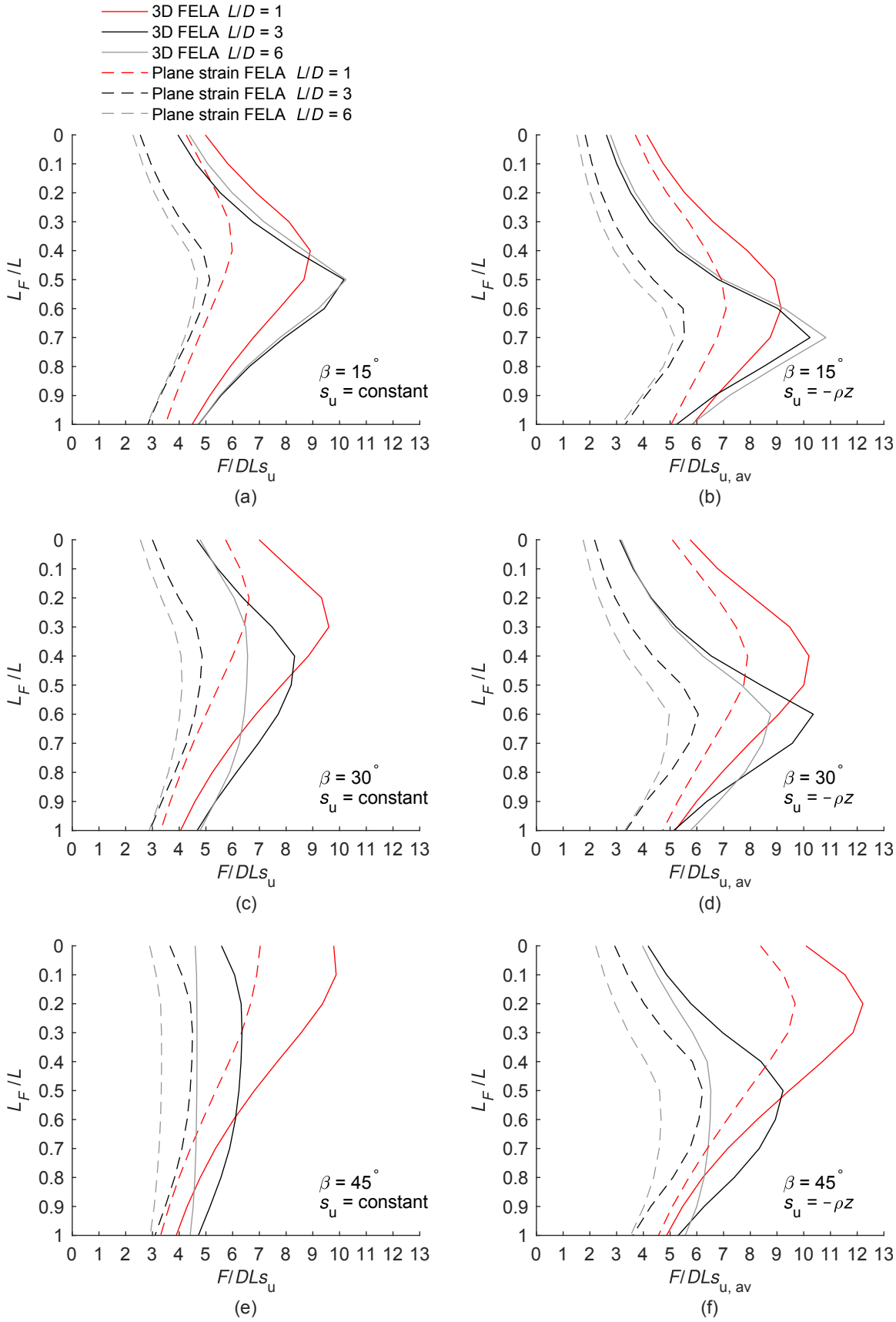

Figure 5.19: Normalised capacities of caissons modelled in 3D and plane strain when loaded at intervals of $0.1L$ along the caisson length. $T = \infty$, $\gamma' =$ any: (a) $\beta = 15°$, $s_u =$ constant; (b) $\beta = 15°$, $s_u = -\rho z$; (c) $\beta = 30°$, $s_u =$ constant; (d) $\beta = 30°$, $s_u = -\rho z$; (e) $\beta = 45°$, $s_u =$ constant; (b) $\beta = 45°$, $s_u = -\rho z$

Table 5.3: Maximum capacities (F in table = $F/DLs_{u,av}$) and corresponding optimal load points to the nearest $0.1L$ (L_{opt} in table $= L_{opt}/L$) for caissons loaded loaded at angles $\beta = 0$, 15°, 30°, and 45° ($\beta = 0$) when $T = 0$ and $\gamma' = 0$

s_u = constant	$\beta = 0$		$\beta = 15°$		$\beta = 30°$		$\beta = 45°$	
L/D	F	L_{opt}	F	L_{opt}	F	L_{opt}	F	L_{opt}
1	5.20	0.6	5.34	0.4	5.89	0.3	6.77	0.0
2	5.67	0.6	5.78	0.5	5.81	0.4	3.69	0.3
3	6.19	0.6	5.95	0.5	5.63	0.5	4.99	0.4
4	6.60	0.6	6.11	0.5	5.61	0.5	4.68	0.4
5	6.96	0.6	6.36	0.6	5.46	0.5	4.30	0.4
6	7.28	0.6	6.58	0.6	5.28	0.5	3.96	0.4
$s_u = -\rho z$	$\beta = 0$		$\beta = 15°$		$\beta = 30°$		$\beta = 45°$	
L/D	F	L_{opt}	F	L_{opt}	F	L_{opt}	F	L_{opt}
1	5.66	0.8	5.87	0.6	6.52	0.5	7.91	0.2
2	5.55	0.7	5.71	0.7	6.31	0.6	7.15	0.5
3	5.82	0.7	5.98	0.7	6.40	0.6	6.54	0.5
4	6.21	0.7	6.29	0.7	6.24	0.6	6.27	0.6
5	6.47	0.7	6.52	0.7	6.14	0.7	5.84	0.6
6	6.75	0.7	6.71	0.7	6.11	0.7	5.45	0.6

Table 5.4: Percentage reduction in capacity of caissons with $T = 0$, $\gamma' = 0$ when compared with $T = \infty$, $\gamma' =$ any

	s_u = constant				$s_u = -\rho z$			
L/D	$\beta = 0$	$\beta = 15°$	$\beta = 30°$	$\beta = 45°$	$\beta = 0$	$\beta = 15°$	$\beta = 30°$	$\beta = 45°$
1	39%	40%	39%	31%	36%	36%	36%	35%
2	42%	42%	36%	52%	41%	39%	39%	32%
3	40%	41%	32%	21%	42%	42%	38%	29%
4	35%	40%	27%	16%	42%	41%	36%	22%
5	31%	38%	22%	15%	42%	40%	34%	18%
6	29%	36%	20%	15%	41%	38%	30%	16%

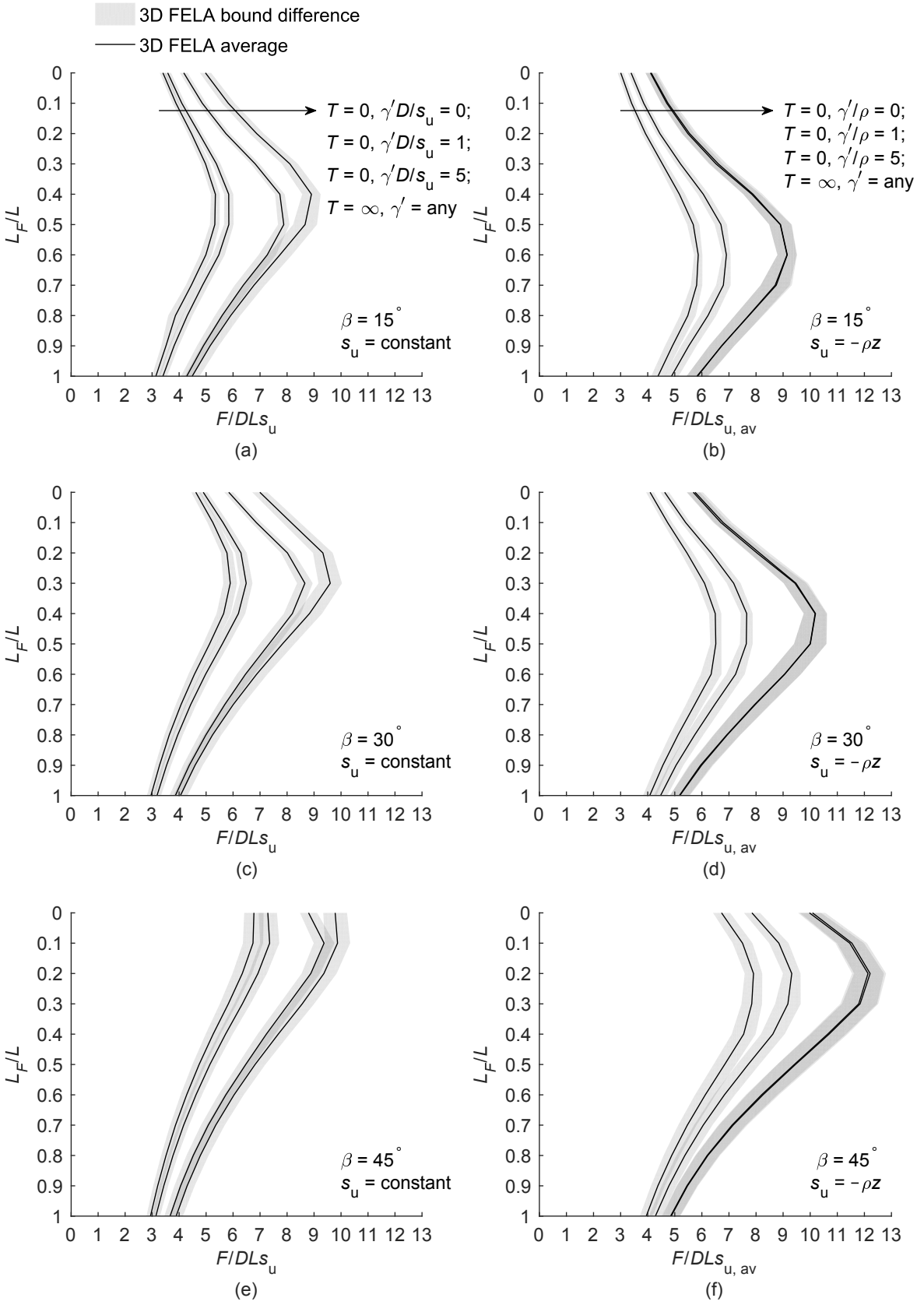

Figure 5.20: Normalised capacities of a caisson with $L/D = 1$ when loaded at various points along the caisson length showing the effect of contact breaking: (a) $\beta = 15°$, $s_u = \text{constant}$; (b) $\beta = 15°$, $s_u = -\rho z$; (c) $\beta = 30°$, $s_u = \text{constant}$; (d) $\beta = 30°$, $s_u = -\rho z$; (e) $\beta = 45°$, $s_u = \text{constant}$; (f) $\beta = 45°$, $s_u = -\rho z$

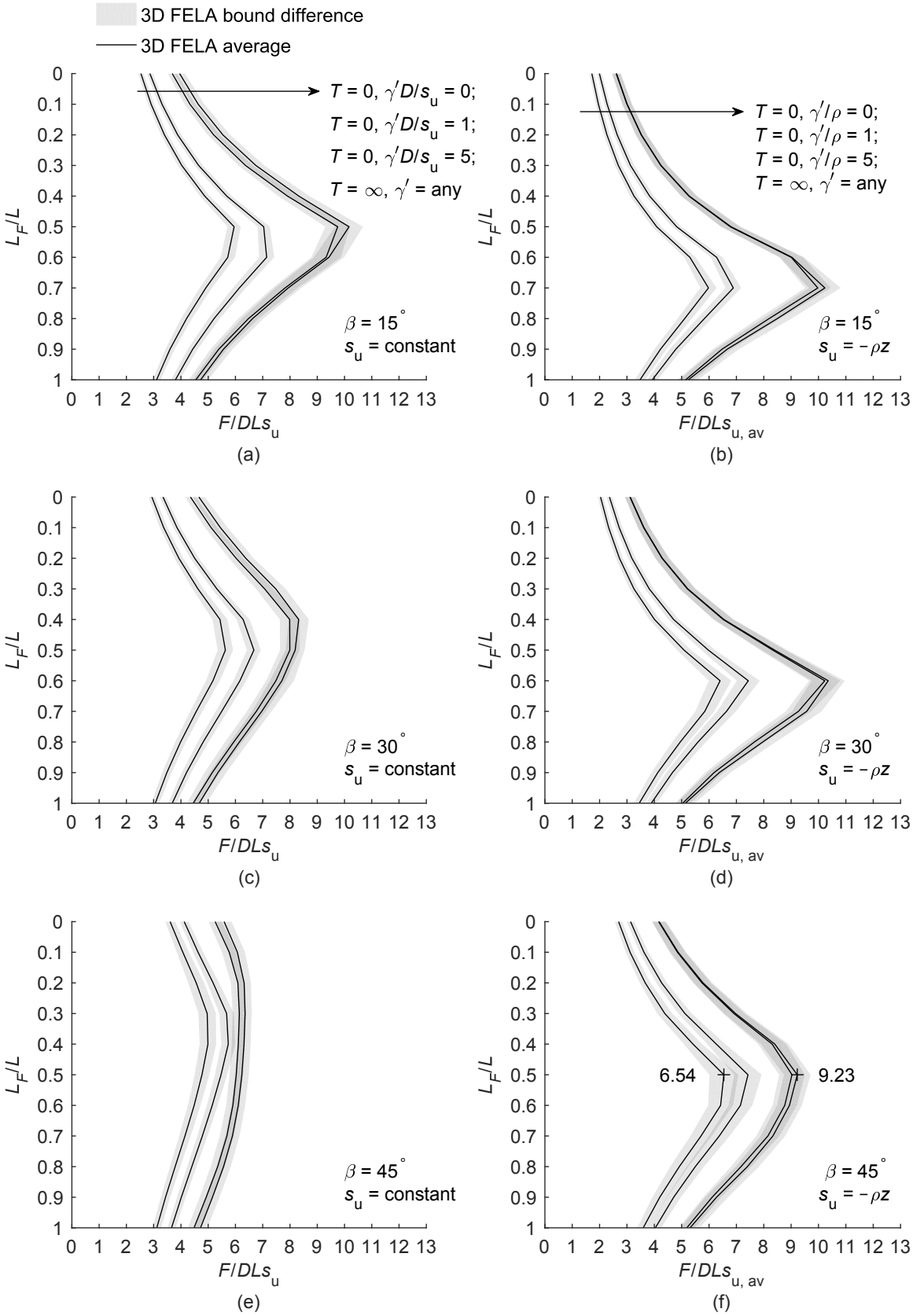

Figure 5.21: Normalised capacities of a caisson with $L/D = 3$ when loaded at various points along the caisson length showing the effect of contact breaking : (a) $\beta = 15°$, $s_u = \text{constant}$; (b) $\beta = 15°$, $s_u = -\rho z$; (c) $\beta = 30°$, $s_u = \text{constant}$; (d) $\beta = 30°$, $s_u = -\rho z$; (e) $\beta = 45°$, $s_u = \text{constant}$; (f) $\beta = 45°$, $s_u = -\rho z$

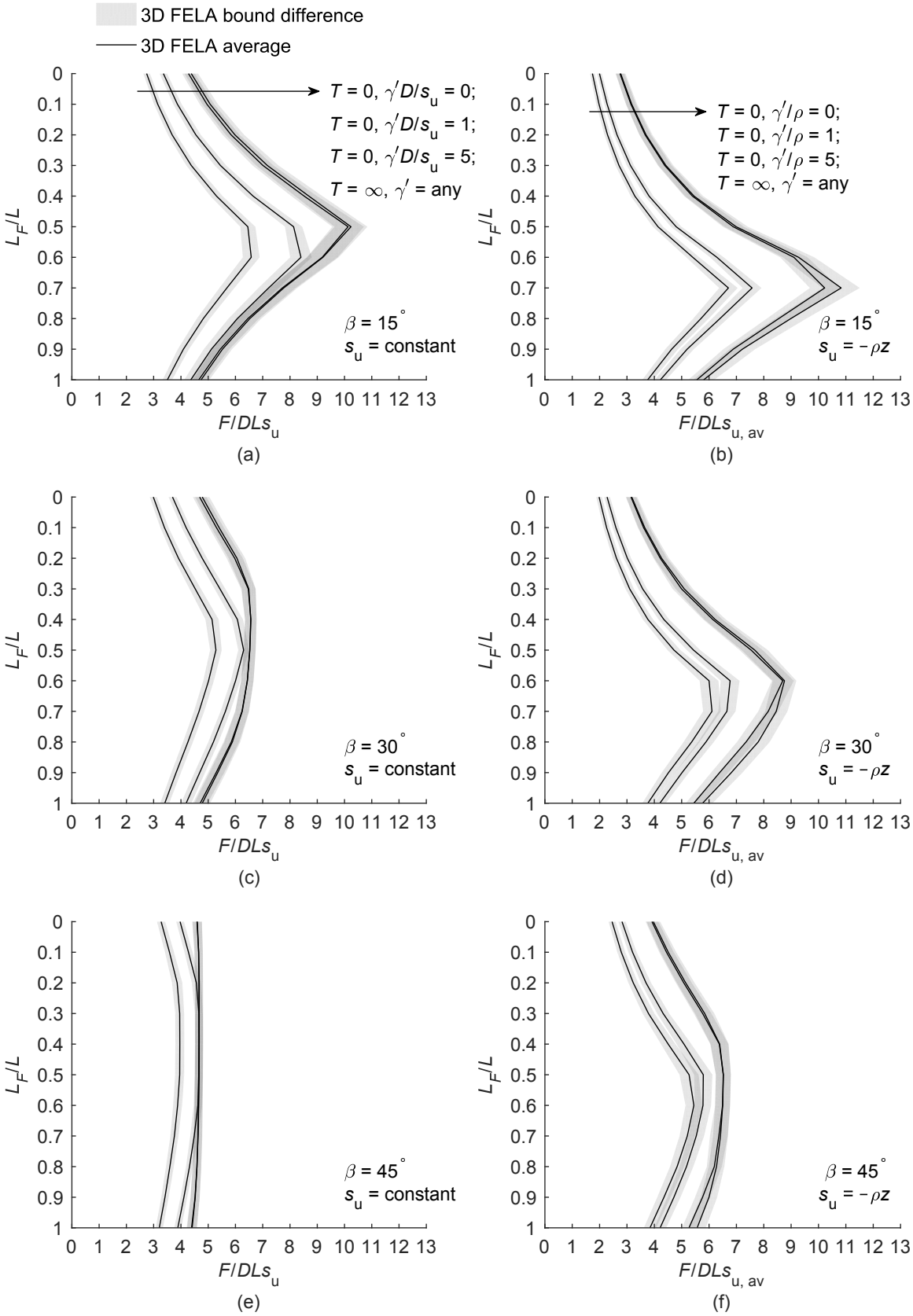

Figure 5.22: Normalised capacities of a caisson with $L/D = 6$ when loaded at various points along the caisson length showing the effect of contact breaking : (a) $\beta = 15°$, $s_u = \text{constant}$; (b) $\beta = 15°$, $s_u = -\rho z$; (c) $\beta = 30°$, $s_u = \text{constant}$; (d) $\beta = 30°$, $s_u = -\rho z$; (e) $\beta = 45°$, $s_u = \text{constant}$; (f) $\beta = 45°$, $s_u = -\rho z$

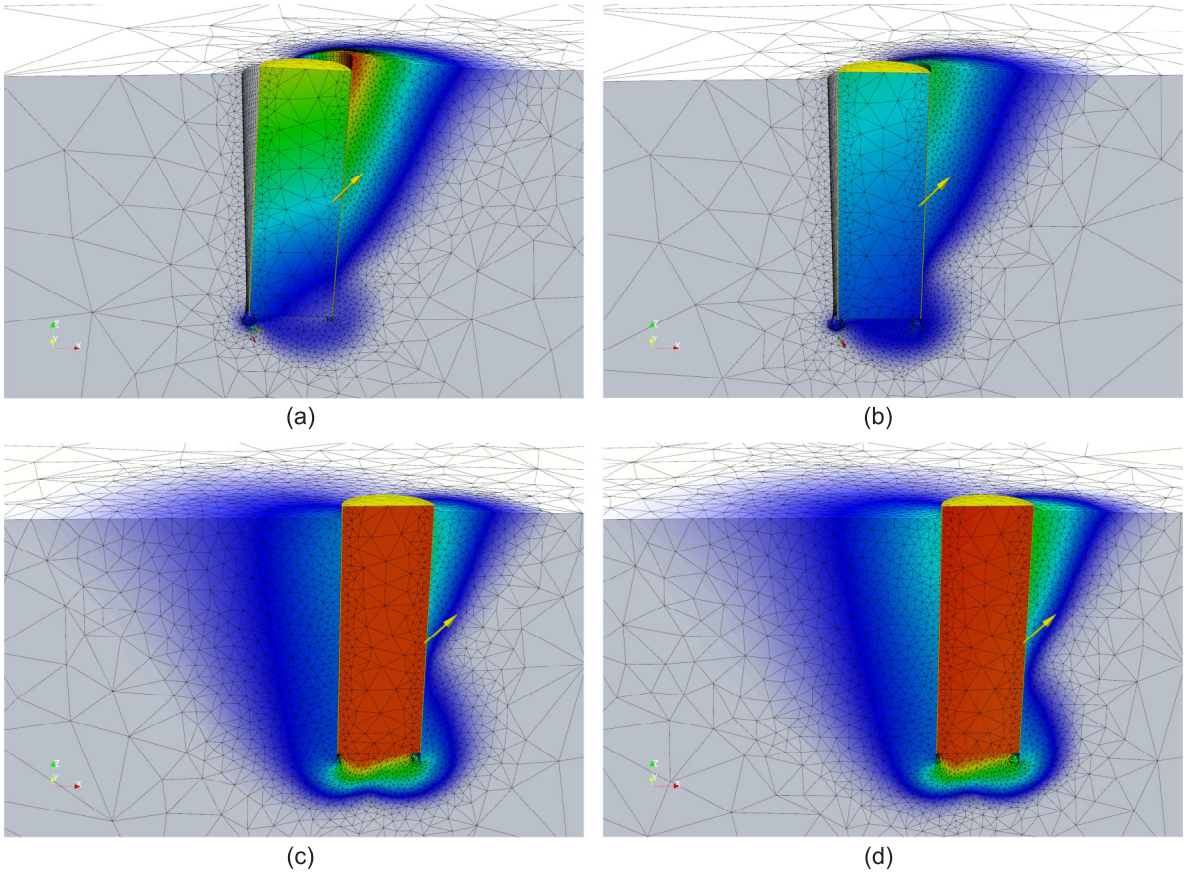

Figure 5.23: Failure mechanism of a caisson with $L/D = 3$ loaded at $L_F = L_{\text{opt}} = 0.5L$ and $\beta = 45°$. $s_u = -\rho z$. Deformation and shading show UB velocity magnitudes and directions: (a) $T = 0$, $\gamma'/\rho = 0$; (b) $T = 0$, $\gamma'/\rho = 1$; (c) $T = 0$, $\gamma'/\rho = 5$; (d) $T = \infty$, $\gamma' =$ any

(Figure 5.21 and Table 5.4). Figure 5.20 shows that the trend of the capacity as L_F is varied remains approximately the same when $T = 0$, as when $T = \infty$ and as such L_{opt} does not significantly change when $T = 0$ compared with $T = \infty$.

A caisson in weightless, NC soil with $L/D = 3$ loaded at $\beta = 45°$ and $L_{\text{opt}} = 0.5L$ fails as shown in Figure 5.23(a). A deep gap opens up behind the caisson, and the corresponding capacity is $6.54DLs_{u,av}$ (shown in Figure 5.21(f)). When normalised soil weight $\gamma'/\rho = 1$ is added to the model, the mechanism does not change significantly (comparing Figure 5.23(b) to (a)), but the capacity rises to $7.42DLs_{u,av}$. A gap cannot be seen in the mechanism for a caisson when $\gamma'/\rho = 5$ (Figure 5.23(c)). The mechanism is almost identical to that when $T = \infty$, as are the corresponding capacities, $8.73DLs_{u,av}$ when $T = 0$ and $\gamma'/\rho = 5$ and $9.23DLs_{u,av}$ when $T = \infty$ (Figure 5.21(f)).

A caisson in relatively light NC soil ($\gamma'/\rho = 1$) with $L/D = 3$ loaded at $\beta = 45°$, below its

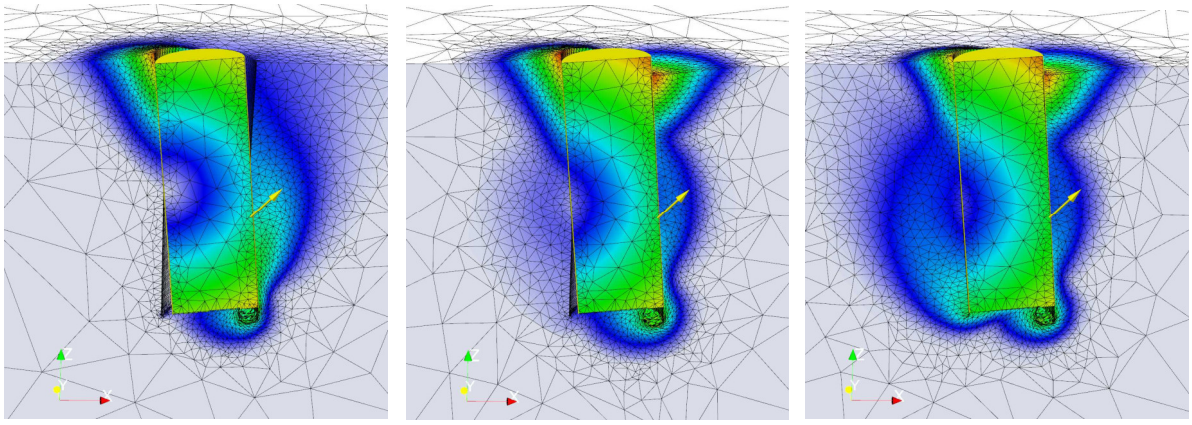

Figure 5.24: Failure mechanism of a caisson with $L/D = 3$ loaded at $L_F/L = 0.8$ and $\beta = 45°$. $s_u = -\rho z$. Deformation and shading show UB velocity magnitudes and directions: (a) $T = 0$, $\gamma'/\rho = 1$; (b) $T = 0$, $\gamma'/\rho = 5$; (c) $T = \infty$, $\gamma' =$ any

optimal point ($L_F/L = 0.8$), fails as shown in Figure 5.24(a), with deep gaps behind the base of the caisson and at the mudline in front of the caisson. It should be noted that for undrained analysis a gap can only open if there is a flow path, perhaps arising from preferential drainage at the caisson/soil interface, that allows water to fill the void. Assuming that a gap can open up at the base of the caisson is, as such, conservative. If the soil weight to strength ratio is increased, the extent of gapping at the base of the caisson is reduced and no gap opens at the mudline (Figure 5.24(b)). The mechanism when $T = \infty$ is shown in Figure 5.24(c). The mechanisms in Figure 5.24(a) and (c) correspond to capacities of $5.5DLs_{u,av}$ and $7.4DLs_{u,av}$ respectively (Figure 5.21(f)) which shows a reduction in capacity when gapping occurs.

5.6 Case study

3D FELA was applied to a recent design of a spar mooring anchor in layered clay soil (Subsea 7, personal communication, 2015). The design parameters are summarised in Table 5.5, and the soil strength profile is shown in Figure 5.25. The stepped soil strength profile was modelled in 3D FELA as four separate soil layers, each with a linear strength variation $s_u = s_{um} - \rho z$, shown in Figure 5.25. An approximate NC soil strength profile was also fitted to the stepped soil profile, and from this, an average soil shear strength over the length of the caisson was determined as $s_{u,av} = 29$ kPa.

Table 5.5: Input parameters for caisson case study

Diameter of caisson (D)	6 m
Length of caisson (L)	18.5 m
Padeye location (L_F)	12 m
Load inclination from horizontal	30°
Submerged pile weight ($F_{z,\,\mathrm{dead}}$)	1200 kN
Submerged soil unit weight (γ')	6 kN/m^3
Internal wall/soil roughness (α_i)	0.5
Outer wall/soil roughness (α_o)	0.6
Wall/soil interface tension (T)	∞
Cap/soil interface tension (T_cap)	0, ∞

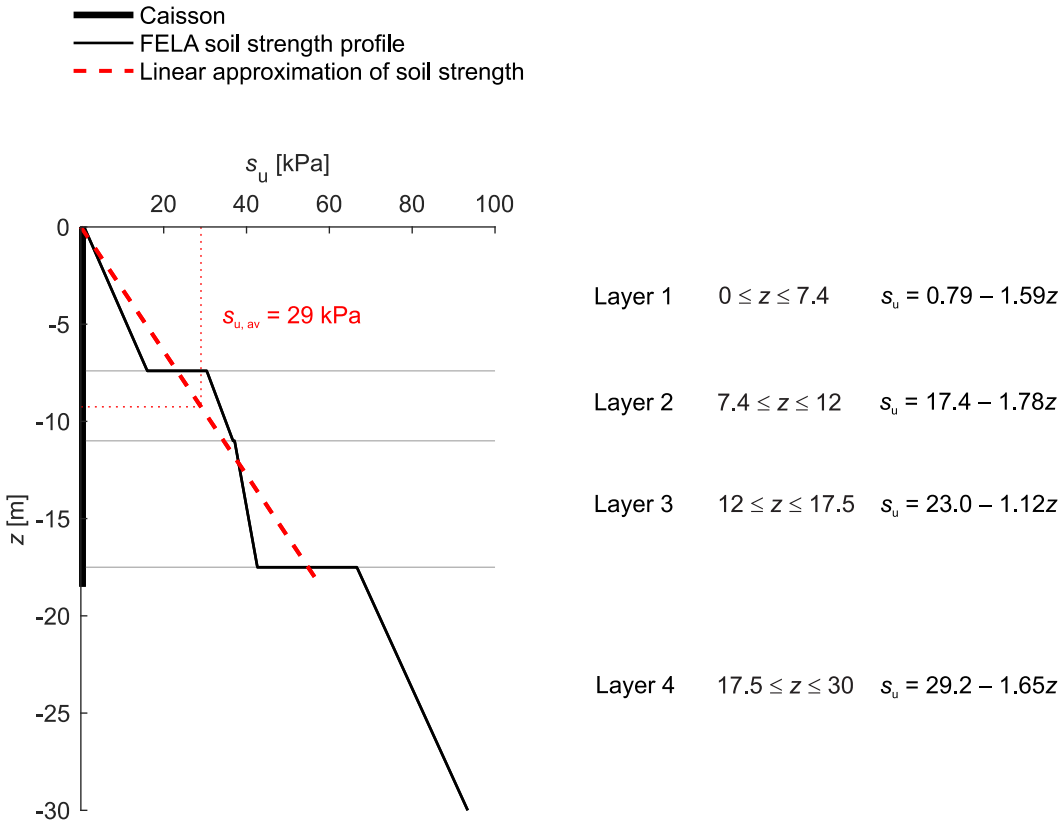

Figure 5.25: Soil strength profile used in caisson case study

Table 5.6: ULS ($T_{cap} = \infty$, soil strength safety factor = 1.3) and ALS ($T_{cap} = 0$, soil strength safety factor = 1.0) capacities and bracketing errors

	ULS		ALS	
Elements	Average (kN)	Error (%)	Average (kN)	Error (%)
10 000	25 768	14.2	19 135	3.0%
25 000	25 593	7.4	—	—
45 000	25 510	5.8	—	—

Ultimate limit state (ULS) and accidental limit state (ALS) caisson capacities were determined. For both cases, gapping was prevented at the wall/soil interface ($T = \infty$). The internal wall/soil roughness factor was modelled as $\alpha_i = 0.5$ and the outer wall/soil roughness factor was modelled as $\alpha_o = 0.6$. For ULS calculations a material safety factor of 1.3 was applied to the soil strength. For ALS calculations, it was assumed that the seals at the caisson top cap might allow water to leak, thus preventing the development of negative excess pore water pressures, and allowing a gap to form at the cap/soil interface. This was modelled as a no-tension interface at the cap, $T_{cap} = 0$.

Capacities found at each 3D FELA solution iteration, for both ULS and ALS design cases, are presented in Table 5.6. For ULS cases, it is clear that the capacity estimate does not change significantly as the mesh is refined (although the bracketing error reduces). This is an advantageous consequence of inaccuracies in both the LB and UB analyses, which provides a representative foundation capacity in an analysis time of under two minutes. In contrast, use of an initial overly coarse mesh in conventional FEA results in an overestimation of the capacity, which is not representative of the capacity found using a refined mesh. However, when using FELA, mesh refinement is still necessary in this instance to confirm the accuracy of the solution. This is more computationally expensive; the ULS capacity found using FELA and a refined mesh ($\sim$45 000 elements) was found in $\sim$20 minutes (LB and UB analyses were solved in series on a 3.1 GHz machine with 32 GB RAM).

Capacity charts derived in Section 5.5.1 (specifically Figure 5.15(d)) can also be used to estimate ULS capacity. For this case study, $L/D \approx 3$ ($18.5/6 = 3.08$), and the caisson is loaded at $L_F/L = 0.65$ ($12/18.5$). From Figure 5.15(d), the capacity is $\sim 10 D L s_{u,av}$.

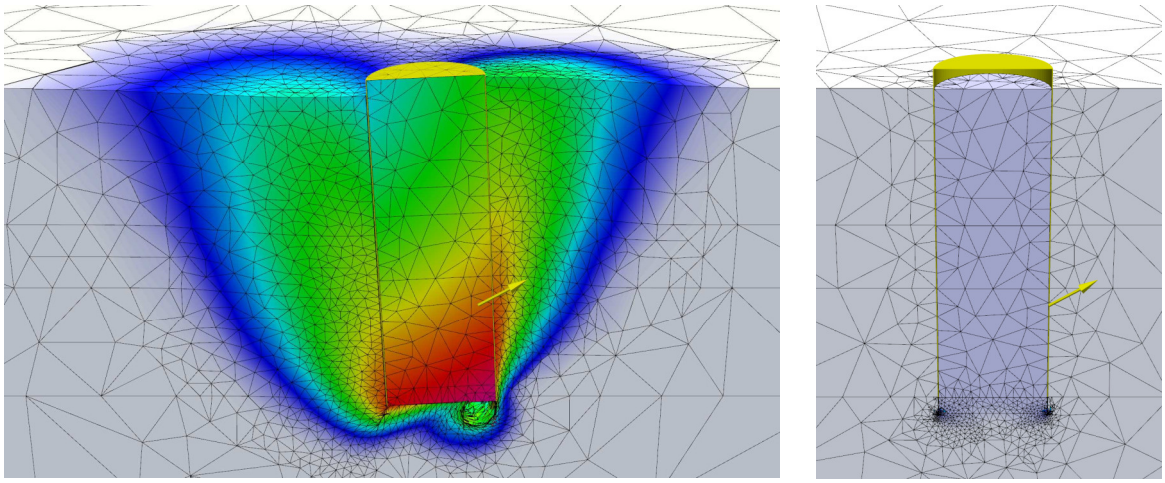

(a) (b)

Figure 5.26: Case study failure mechanisms: (a) ULS ($T_{\text{cap}} = \infty$); (b) ALS ($T_{\text{cap}} = 0$). Deformation and shading show UB velocities

Applying the material factor of safety (1.3), this gives a capacity $F = 10 \times 6 \times 18.5 \times 29/1.3 = 24\ 762$ kPa, which delivers a very accurate capacity assessment in this case (only 3% lower than the capacity calculated directly using 3D FELA (25 510 kPa, from Table 5.6)).

The ALS capacity was bracketed to $\pm 3\%$ after the first iteration of the solution (Table 5.6), deeming mesh refinement unnecessary. The ULS and ALS failure mechanisms are shown in Figure 5.26(a) and (b) respectively. When the cap is sealed (ULS, Figure 5.26(a)), the trapped soil plug moves rigidly with the caisson, which is translating and slightly rotating counter-clockwise; the mechanism involves a large body of soil. However, when the cap is not sealed (ALS, Figure 5.26(b)), the caisson moves vertically at failure and a gap forms at the cap/soil interface. The soil plug is not mobilised, and the capacity is primarily derived from wall/soil interface shearing.

5.7 Summary

This chapter has focused on the analysis of offshore suction caissons in clay, where undrained capacity is critical for preliminary design. Rigorous 3D limit load analyses were carried out using FELA. Parameters such as caisson length to diameter aspect ratio, soil strength profile and submerged unit weight, load attachment location and angle, and wall/soil contact breaking

were studied in detail. Loading was applied to caissons at a range of attachment points along the caisson length. Four load angles from horizontal to 45° above horizontal were considered. Attention was given to generating capacity charts which locate the optimal attachment point and thus the maximum capacity of the caisson. Parameters that affect the optimal attachment point were identified.

A summary of the results is presented in Figure 5.27. Caisson maximum capacities in uniform and NC soil, with and without contact breaking, are shown. The capacities in Figure 5.27 are normalised by $D^2 s_{u,av}$ (instead of $DL s_{u,av}$ used previously in this chapter) to highlight the increase in capacity as caisson length increases (for a given caisson diameter). The corresponding L_{opt} for each capacity is provided in Tables 5.2 and 5.3. Figure 5.27 shows that there is a reduction in the maximum capacity achievable as β increases. It also shows that increasing caisson length (aspect ratio) to add capacity is more beneficial when a horizontal load is applied ($\beta = 0$); when β increases the additional capacity gained with a larger aspect ratio decreases.

It has been shown that for a horizontally loaded caisson, the optimal loading location is generally independent of aspect ratio over the range considered here ($L/D = 1-6$). In uniform soil the optimal location (to the nearest $0.1L$) is $0.6L$ from the mudline and in NC soil it is $0.7L$ from the mudline. The optimal load location is, however, affected by the loading angle. The optimal loading point for a caisson with $L/D = 1$ under inclined loading is the point where a load vector applied at the caisson centreline at $L_{opt,\beta=0}$ crosses the caisson wall (Figure 5.16(a)). For caissons with $L/D \geq 2$, the optimal loading point was found to be largely independent of aspect ratio, and values of L_{opt} for caissons under inclined loading are summarised in Table 5.2.

Capacities found using a simple UB based method outlined in Aubeny et al. (2003a) provide a reasonably accurate estimate of caisson capacity under horizontal loading. The effectiveness of using plane strain analyses to identify 3D caisson failure mechanisms has also been explored. It was found that in many instances, in particular when $L/D > 1$ and when loading is applied away from the mudline, the failure mechanism obtained from a plane

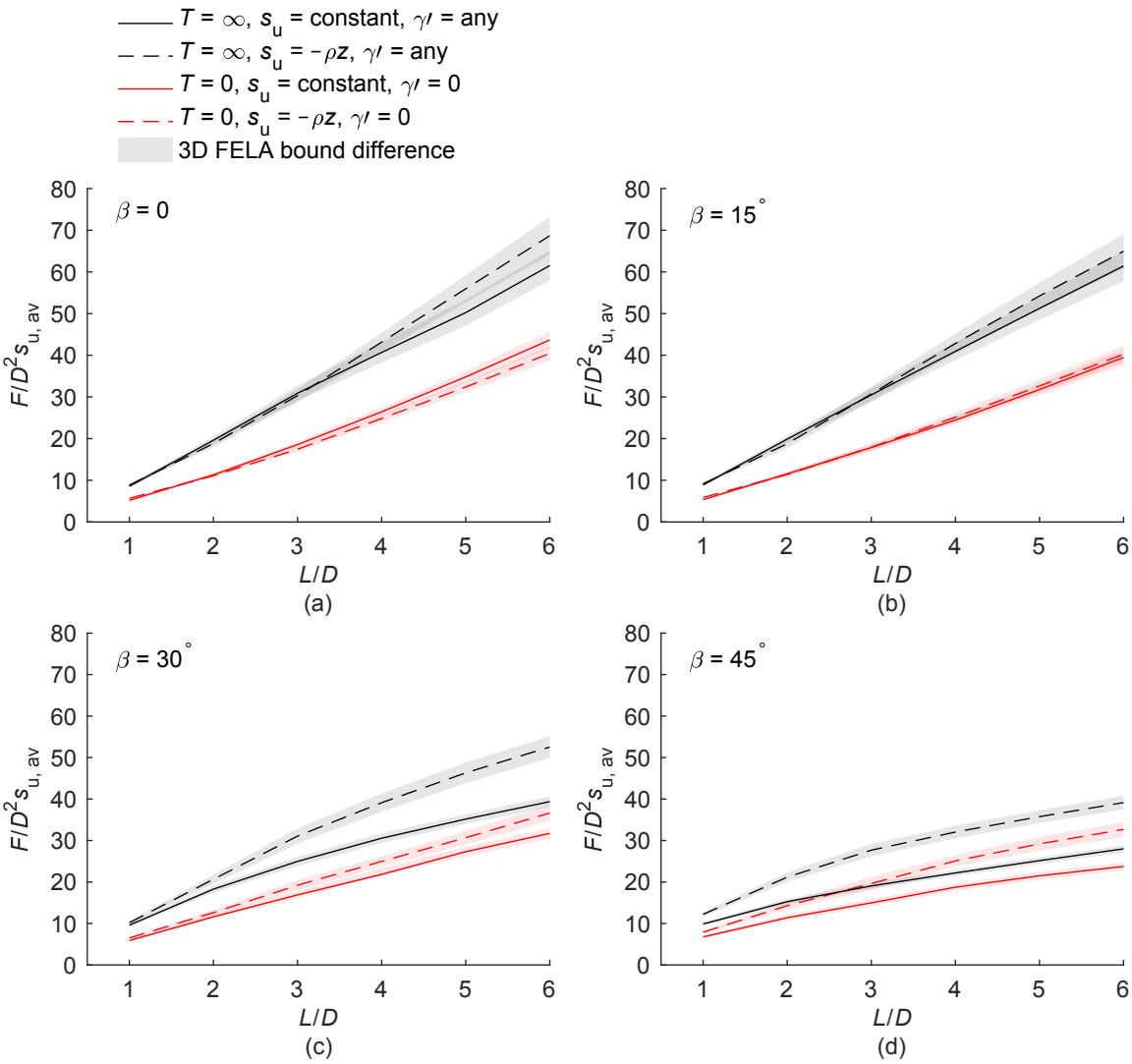

Figure 5.27: Normalised maximum capacities of caissons (F) when loaded optimally in uniform (s_u = constant) and NC soil ($s_u = -\rho z$), with and without contact breaking (T): (a) $\beta = 0$; (b) $\beta = 15°$; (c) $\beta = 30°$; (d) $\beta = 45°$

strain analysis is not representative of the 3D failure mechanism. However, as the loading angle increases the appropriateness of a plane stain analysis increases. This is because the failure mechanism comprises less out of plane soil flow around; it is more akin to a planar reverse end bearing mechanism.

It has been shown that as the aspect ratio L/D increases, the maximum normalised capacity of a caisson loaded horizontally in uniform soil approaches that of a circular pile section translating horizontally. In NC soil, when $L/D \geq 4$ the capacity marginally exceeds that of a circular pile section translating horizontally when the average soil strength $s_{u,av}$ is used for

normalisation (Figure 5.11).

Contact breaking between the caisson and the soil can lead to significant reductions in holding capacity (up to 40%). The reduction in capacity was found to be dependent on the weight to strength ratio of the soil. A gap is more likely to open when the soil is relatively light, resulting in a lower capacity than when a caisson is in relatively heavy soil. The location of the optimal load point does not change significantly when contact breaking can occur between the caisson and the soil. This is in line with Supachawarote (2006), where it was also found that the optimal load point is similar for cases with and without a gap forming behind the caisson.

A case study used 3D FELA to investigate the capacity of a suction anchor in layered clay under ULS ($T_{\text{cap}} = \infty$) and ALS ($T_{\text{cap}} = 0$) design conditions. Under ULS conditions, the capacity obtained using a coarse mesh discretisation was found to give a good estimate of that obtained when using a more refined mesh, but with a significantly quicker analysis time. The ULS capacity was also estimated by approximating an NC soil strength profile and using the relevant capacity chart (Figure 5.15(d)). The ALS capacity was closely bracketed using a coarse 3D FELA mesh, as the mechanism primarily involved wall/soil interface shearing.

Chapter 6

Hybrid mudmat–pile foundations

6.1 Introduction

This chapter considers hybrid foundations comprising a mudmat with four corner piles. It has been noted in the literature that the rotational fixity of the mudmat/pile connection (pile head) can significantly affect foundation capacity (Won et al., 2015; Hossain et al., 2015b). This study compares capacities obtained for three idealised connection types: fixed, fully pinned, and horizontally pinned with vertical movement allowed. Two soil strength profiles are considered: uniform soil and normally consolidated soil (strength proportional to depth).

In the first section, plane strain FELA is used to verify the number of facets needed to accurately model a pile section under combined lateral and torsional loading. Following this, uniaxial vertical, horizontal, moment, and torsional capacities of mudmat and hybrid foundations are determined using UB FELA for the three pile head fixity conditions. The contributions of the constituent foundation parts (mudmat base, mudmat sides, pile base, pile sides) to the total hybrid foundation capacity are analysed. Pile length and pile diameter are varied in order to quantify their effect on foundation capacity.

In some cases a simplified analytical approach can accurately estimate hybrid foundation capacity. FELA results are compared with capacity predictions found using a simplified approach outlined in Dimmock et al. (2013), and other simplified methods for predicting foundation capacity are presented.

Finally, a case study considers a hybrid foundation under six degree-of-freedom loading, and compares the design load factor found using LB and UB 3D FELA with the design load

factor obtained using displacement FEA (undertaken by Subsea 7, personal communication, 2015). FELA is also used to quantify a reduction in capacity due to an inclined seabed.

6.2 Problem overview

The notation and sign conventions adopted are shown in Figure 6.1. Certain dimensionless groups were kept constant throughout the analysis: the mudmat length to breadth aspect ratio (L/B), the mudmat embedment ratio (d/B), and the eccentricity of the pile edge from the mudmat edge (e/B). The variable parameters considered in detail are the pile length, H, and pile diameter, D. The pile diameter was maintained at a base value $D/B = 0.175$ in analyses where the pile length was varied, and similarly the pile length was maintained at a base value $H/B = 1$ in analyses where the pile diameter was varied. These base values are typical encountered in design (Subsea 7, personal communication, 2016). The full set of parameters considered is listed in Table 6.1.

It was assumed that interior skirts justify treating the mudmat as a rigid embedded foundation. The corner piles were also modelled as rigid bodies, assuming a plugged pile response. The mudmat/pile connection (pile head) was modelled as fixed, fully pinned, or horizontally pinned. A fixed connection prevents any relative translation or rotation between the pile head and the mudmat, a fully pinned connection only prevents relative translation, and a horizontally pinned connection only prevents horizontal translation (the pile is free to move vertically relative to the mudmat). The pinned pile head connections were modelled at skirt base level ($z = -d$).

Table 6.1: Hybrid foundation dimensionless geometric parameters. Bold values indicate base values

Dimensionless group	Values considered
L/B	2
D/B	0, 0.125, 0.15, **0.175**, 0.2
H/B	0, 0.25, 0.5, 0.75, **1**, 1.25
d/B	0.05
e/B	0.025

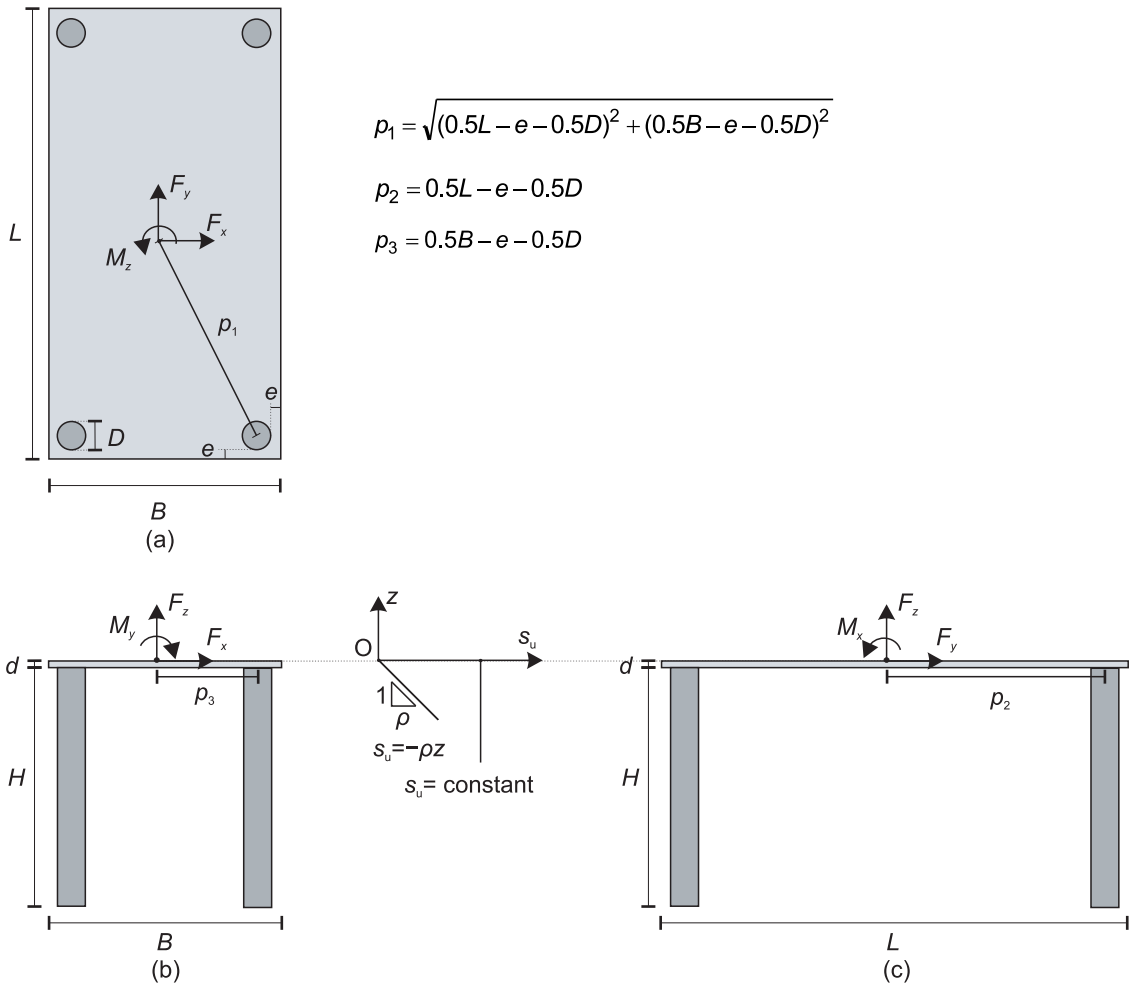

Figure 6.1: Notation used for hybrid foundation analysis showing soil strength profiles and eccentricities of pile heads from the mudmat centre: (a) plan view; (b) front elevation view; (c) side elevation view

As shown in Figure 6.1, two soil strength profiles were considered: soil with uniform undrained shear strength (s_u = constant) and soil with no mudline strength but a linear increase in strength with depth ($s_u = -\rho z$, where $\rho = B$), which is referred to as normally consolidated soil. The mudmat sides were assumed to be fully smooth ($\alpha = 0$) and the mudmat base fully rough ($\alpha = 1$). The pile sides and base were also assumed to be fully rough ($\alpha = 1$). Unlimited tension capacity was assumed at all soil/foundation interfaces. The soil was modelled as weightless because when contact breaking is suppressed ($T = \infty$), soil weight has a negligible effect on the computed horizontal and torsional capacities.

Ultimate uniaxial foundation capacities F_{x0}, F_{y0}, F_{z0}, M_{x0}, M_{y0}, and M_{z0} were determined using 3D UB FELA. As discussed in Section 3.2.3, rigid bodies can be connected in UB

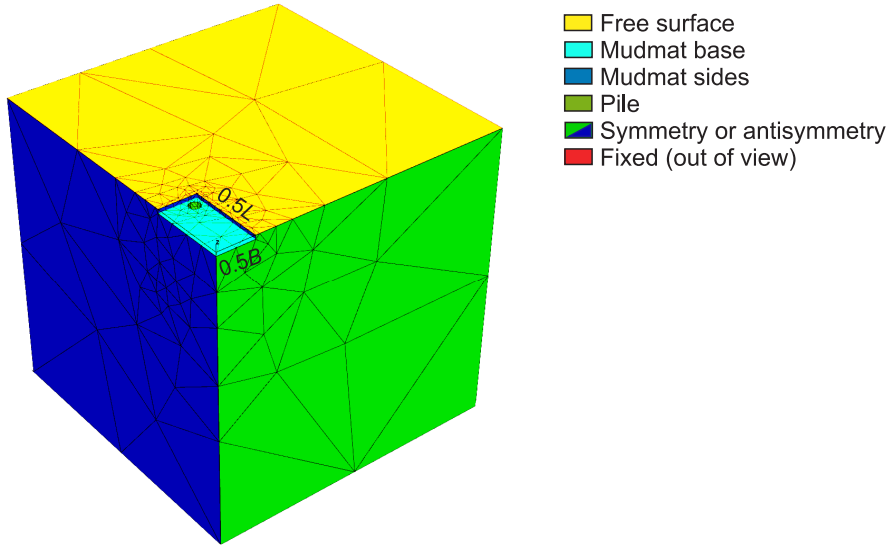

Figure 6.2: Meshed soil domain ($5B \times 5B \times 5B$) exploiting symmetry (quarter model)

OxLim analyses by specifying relative translational and rotational degrees of freedom as free or fixed. Symmetry and/or antisymmetry allowed for one quarter of the soil domain to be analysed in all cases. An initial (unrefined) FELA mesh showing boundary conditions applied to the model is shown in Figure 6.2. Additional planes that rise at 45° from the base of the mudmat to the mudline were prescribed in the otherwise unstructured mesh (downwards fans were not added at the mudmat base as these would intersect with the corner piles). Four iterations of adaptive mesh refinement were undertaken for each analysis and the final refined mesh contained ~40 000 elements.

6.3 Model assumptions and validation

Plane strain FELA was used to determine the number of facets required to accurately discretise a rough circular pile section under combined horizontal and torsional loading. An additional exercise considered the number of facets required to discretise a circular pile section with interface roughness factors $\alpha = 0$, 0.25, 0.5, 0.75, and 1 when subjected to pure torsional loading. The pile cross-sections were modelled as regular N-sided polygons that inscribe a true circular pile (of diameter, D). The number of facets required to accurately capture rough ($\alpha = 1$) circular pile response under combined $F_x - M_z$ loading was considered for piles

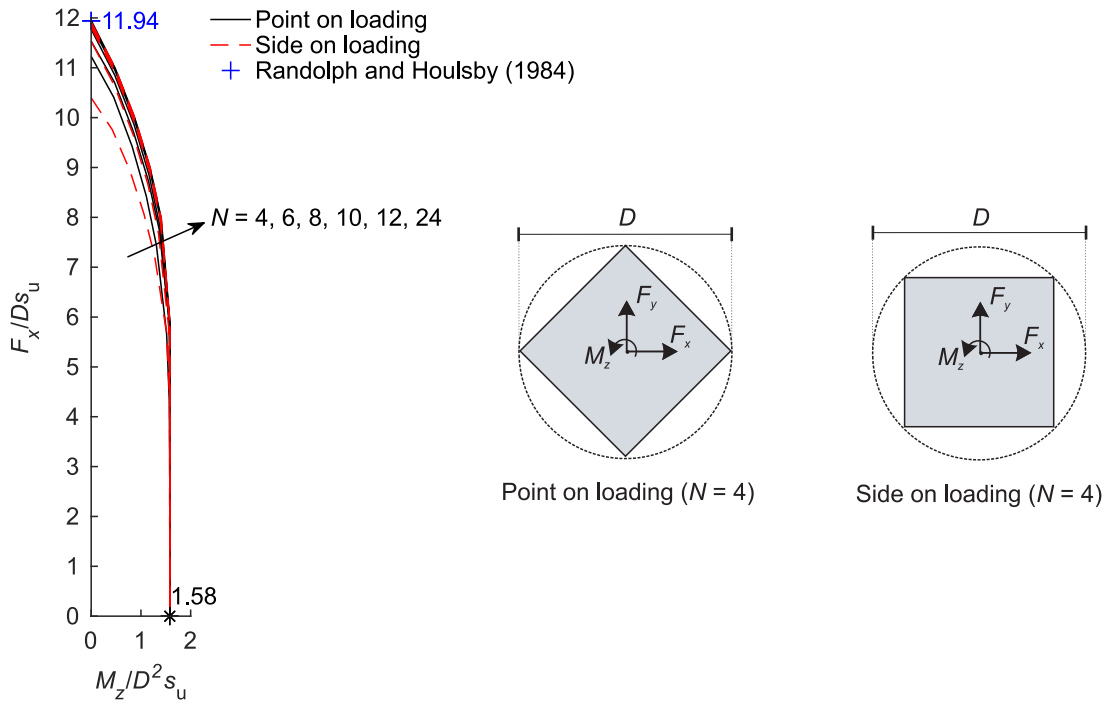

Figure 6.3: Capacity of a fully rough ($\alpha = 1$) N-sided pile section under combined $F_x - M_z$ loading

comprising polygons with $N = 4$, 6, 8, 10, 12, and 24 sides. The piles were loaded at two extreme orientations: 'point on' and 'side on' (see Figure 6.3).

Figure 6.3 shows that even a fairly coarse polygonal discretisation with $N = 12$ allows for an accurate estimation of the lateral and torsional capacities for a rough pile. For F_x loading, the previously benchmarked UB capacity of a circular pile translating laterally in cohesive soil (Randolph and Houlsby, 1984) is shown to compare favourably with the corresponding FELA capacity for $N \geq 12$ at both pile orientations. Fully rough pile sections under pure F_x point on and side on loading fail as shown in Figure 6.4(a) and (b) respectively. These mechanisms and the capacities in Figure 6.3 are virtually identical when $N \geq 12$ and closely match the deformation mechanism described by Randolph and Houlsby (1984) and shown in Figure 6.4(c).

Under M_z loading, the FELA capacities obtained for all values of N ($1.58D^2 s_u$) only marginally overestimate the theoretical torsional capacity for a rough circular pile ($\pi D^2 s_u/2 = 1.57D^2 s_u$). Failure mechanisms for a square pile ($N = 4$) and piles with $N = 12$ and $N = 24$ under pure M_z are shown in Figure 6.5(a). A segment of rigidly rotating soil can

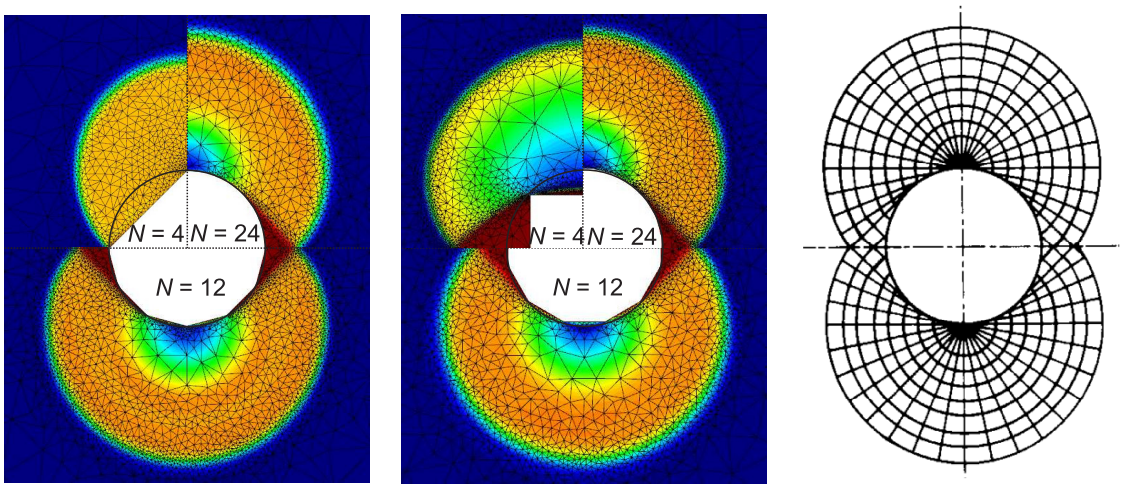

Figure 6.4: Failure mechanisms for fully rough ($\alpha = 1$) pile sections under pure F_x loading. Contoured by velocity magnitude: (a) oriented 'point on'; (b) oriented 'side on'; (c) deformation mechanism from Randolph and Houlsby (1984)

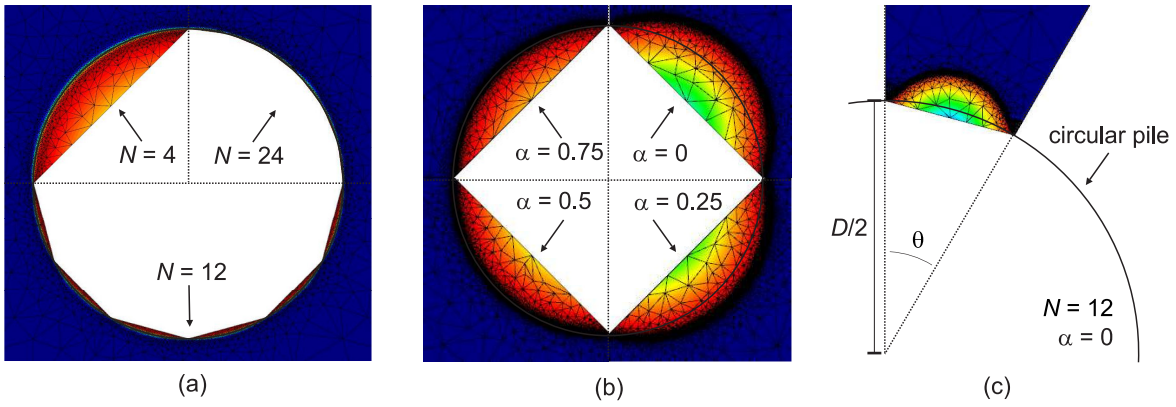

Figure 6.5: Failure mechanisms for pile sections under pure M_z loading. Contoured by velocity magnitude: (a) rough pile ($\alpha = 1$), various N; (b) $N = 4$, various α; (c) smooth pile ($\alpha = 0$), one segment of $N = 12$ polygon

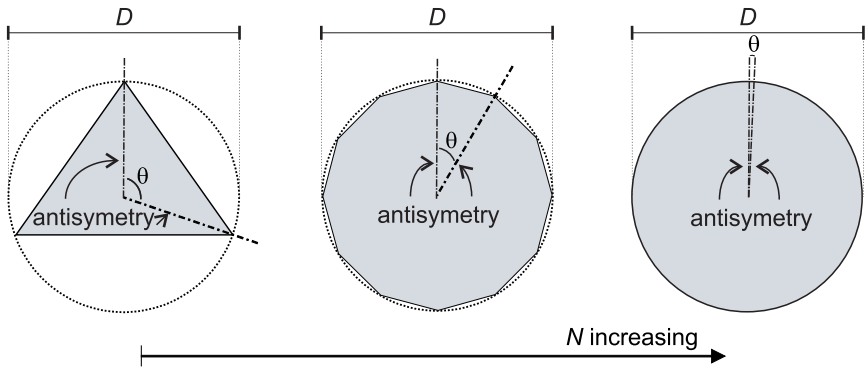

Figure 6.6: Planar segments of piles modelled under torsional loading

be seen between the facets of the polygon and the circle that it inscribes. The circular slip line in the soil is identical for all values of N, which leads to the identical M_z capacities in Figure 6.3.

The effect of pile roughness on the number of facets required to accurately represent a circular pile section under lateral loading has been calibrated in Section 3.5.2. In this section it is calibrated for a pile under pure torsional loading. In order to investigate this effect the ultimate torsional capacity (M_{z0}) of pile sections with a range of interface roughness factors was found. Plane strain FELA was used to model a domain segment of angle $\theta = 2\pi/N$ which contains a single facet of the pile (see Figure 6.6). Antisymmetry boundary conditions were applied at $\theta = 0$ and $\theta = 2\pi/N$.

Figure 6.7 shows tightly bracketed capacities ($\pm 0.25\%$) of the pile sections with a range of roughness factors. It is clear that any number of facets can be used to model a fully rough pile under torsion (also shown in Figure 6.3). However, if the pile is not fully rough many more facets are needed to accurately approximate a circular pile. Figure 6.7(b) highlights some potentially large approximation errors when $N \leq 16$ and $\alpha < 1$. For example a pile with $N = 15$ and $\alpha = 0.25$ has a torsional capacity that is twice the theoretical value for a circular pile ($0.79D^2 s_u$ compared with $0.39D^2 s_u$).

Consideration of the failure mechanisms in Figure 6.5(b) and (c) helps to illustrate the cause of the high calculated capacities at low α and N. Figure 6.5(b) shows that the slip line of a smooth square pile ($N = 4$, $\alpha = 0$) does not follow the shape of the circular pile (unlike when $N = 4$ and $\alpha = 1$, Figure 6.5(a)). It extends deeper into the soil domain and has a

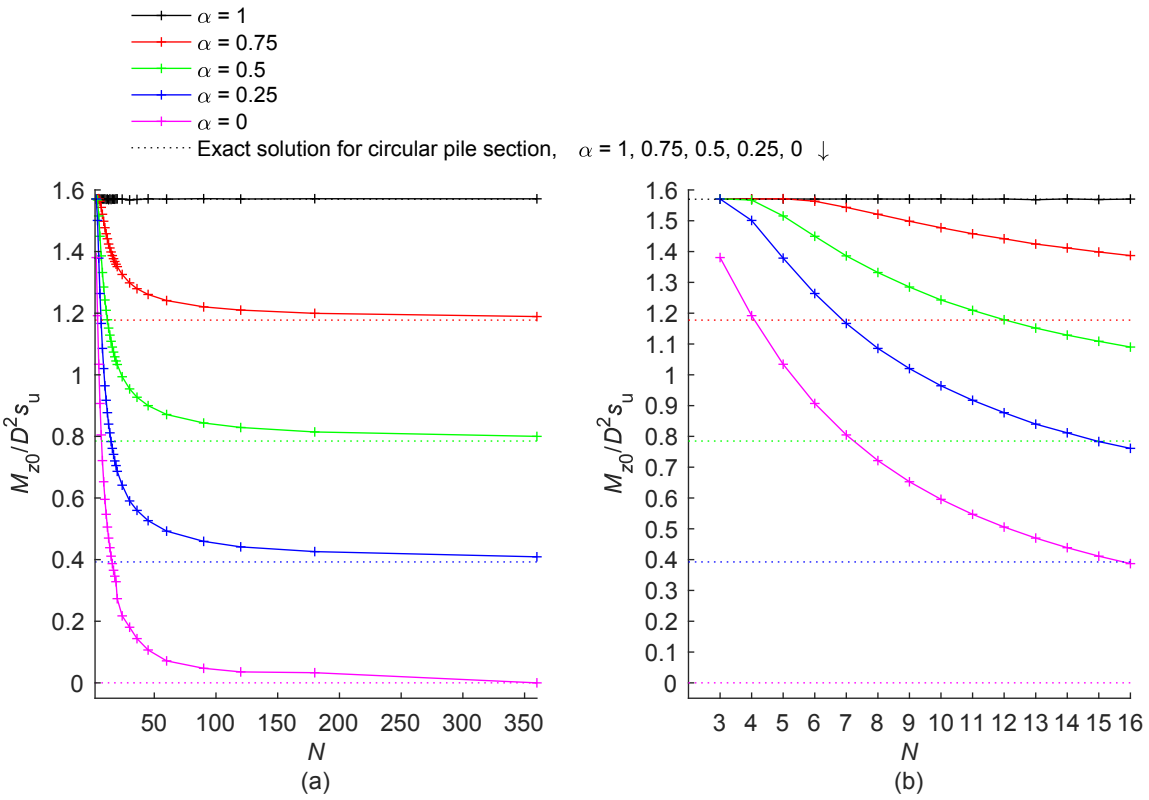

Figure 6.7: Ultimate torsional capacity (M_{z0}) of polygonal pile sections with various interface roughness factors: (a) full range of facet numbers N ; (b) zoomed view showing $N \leq 16$

centre of rotation somewhere between the pile centre the pile edge. There is, as such, relative slip between the pile and the soil block. The corresponding pile capacity is $1.19D^2 s_u$, which is only 24% lower than the capacity of a rough square pile. When $N = 12$ the mechanism becomes shallower but still comprises segments of rigidly rotating soil adjacent to the pile (Figure 6.5(c)). The corresponding capacity is surprisingly high ($0.51D^2 s_u$) considering that a smooth circular pile has no torsional capacity and a fully rough circular pile has a torsional capacity of $1.57D^2 s_u$.

This study of hybrid foundations considers only fully rough ($\alpha = 1$) piles and as such a 12-sided polygonal cross-section can accurately model the pile section (Figures 6.3 and 6.7). A consequence of this discretisation is that the area of the 12 sided polygon used is marginally smaller than the circular pile represented (0.05% smaller) which causes a very slight underestimation of the base shear resistance and bearing capacity of the piles. More facets would be required in order to accurately model a pile that is not fully rough, as highlighted in Figure 6.7.

6.4 Horizontal and torsional capacities

The contributions of the constituent components of a hybrid foundation (mudmat base, mudmat sides, pile base, and pile sides) to the total foundation capacity were first evaluated for foundations under uniaxial horizontal and torsional loading (F_x, F_y, M_z). The effect of pile length, and subsequently pile diameter, on foundation capacity was quantified.

First, the pile diameter was maintained at $D/B = 0.175$ and the pile length was varied. Figure 6.8 shows foundation component contributions to the ultimate horizontal and torsional capacities of foundations for various pile head fixities. It is immediately apparent that under horizontal and torsional loading, vertical pile restraint does not affect pile capacity (comparing columns in Figure 6.8 for fully pinned and horizontally pinned piles). However, rotational restraint significantly affects foundation capacity (comparing columns in Figure 6.8 for fixed and pinned piles).

In uniform soil, a mudmat without piles ($H/B = 0$) has slightly more capacity when loaded by F_x than by F_y due to the mudmat aspect ratio and slight embedment. Figure 6.8(a) shows the ultimate horizontal capacity F_{x0} of a foundation with fixed piles of various lengths. The capacity derived from the mudmat base increases considerably when $H/B = 0.75$ compared with when $H/B = 0.5$. The failure mechanisms for both of these foundation geometries are shown in Figure 6.9. In Figure 6.9(a) ($H/B = 0.5$) the foundation is translating at failure. There is minimal interaction between the soil failure mechanisms associated with the mudmat and the piles, and the capacity of the hybrid foundation could be estimated by summing analytical solutions for a mudmat under horizontal loading (Murff et al., 2010) and for a finite length pile/caisson undergoing translation without rotation (Aubeny et al., 2003a). The capacity of the hybrid foundation was calculated as $3.07BLs_u$ using FELA, and as $3.05BLs_u$ using this simplified approach. Figure 6.9(b) ($H/B = 0.75$) shows that the foundation 'rolls' about the y-axis under F_z loading. By comparison with Figure 6.9(a), there is no lateral soil flow around the full length of the pile. The mudmat is pushing down into the soil (rather than just across) thus increasing the contribution of the mudmat base to the total capacity. The unlimited-tension interface between the mudmat and

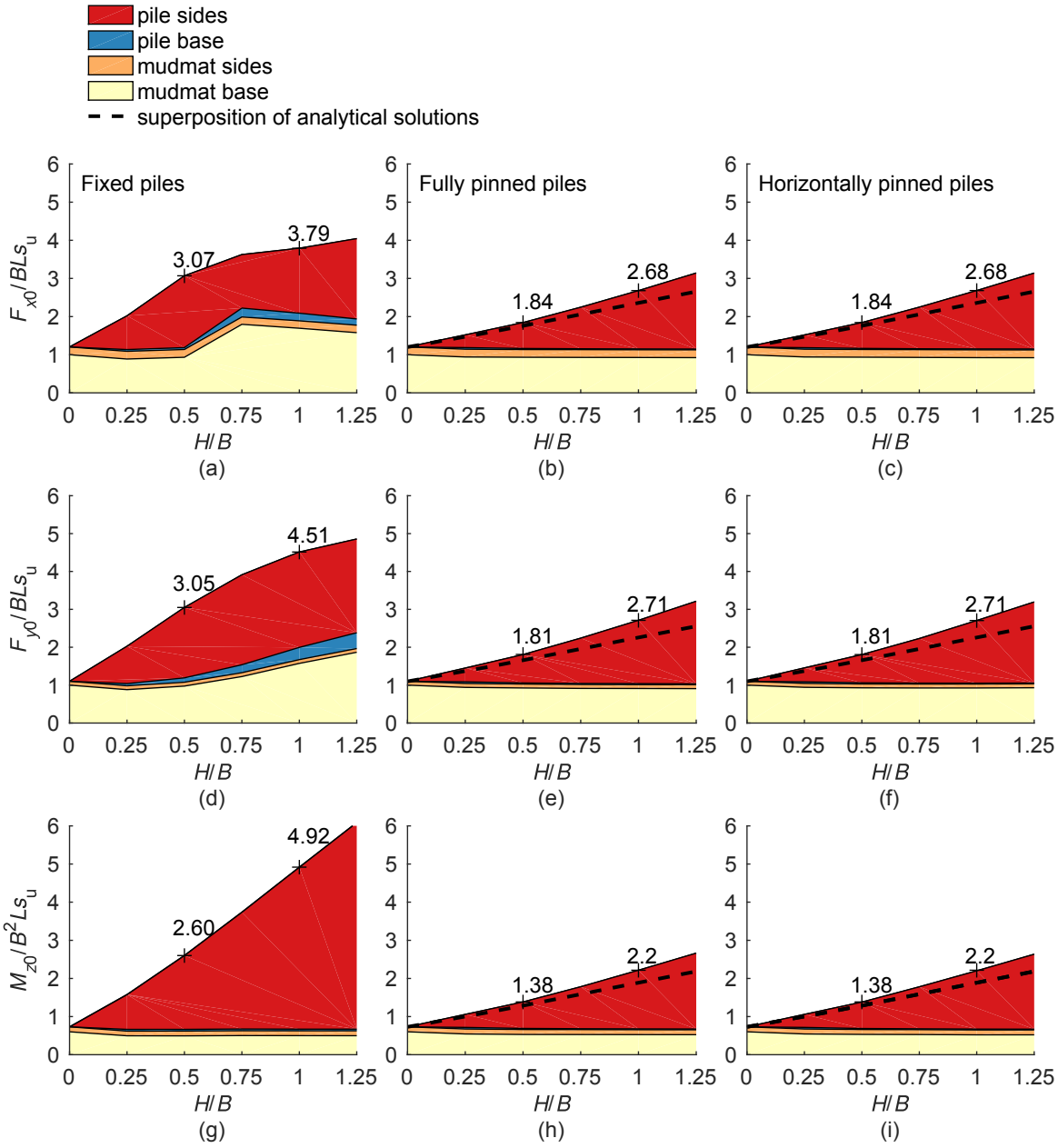

Figure 6.8: Ultimate uniaxial capacities F_{x0}, F_{y0}, and M_{z0} for a hybrid foundation with a range of pile lengths in uniform soil split into component contributions: (a) F_{x0}, fixed piles ; (b) F_{x0}, fully pinned piles; (c) F_{x0}, horizontally pinned piles; (d) F_{y0}, fixed piles; (e) F_{y0}, fully pinned piles; (f) F_{y0}, horizontally pinned piles; (g) M_{z0}, fixed piles; (h) M_{z0}, fully pinned piles; (i) M_{z0}, horizontally pinned piles

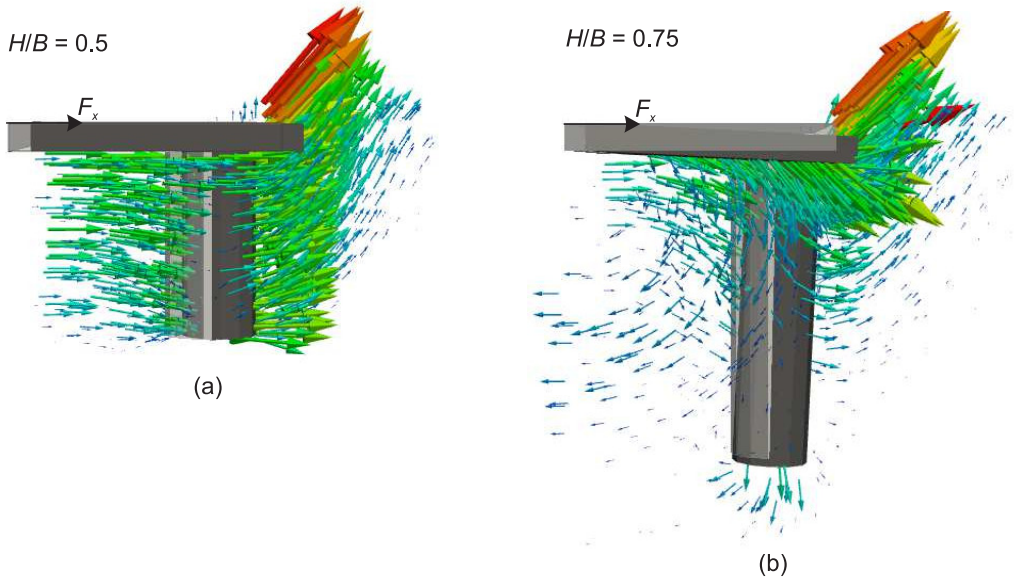

Figure 6.9: Failure mechanisms for hybrid foundations with fixed piles in uniform soil under F_x loading: (a) $H/B = 0.5$; (b) $H/B = 0.75$. Original foundation position drawn in light grey

the soil means that the other half of the foundation (out of view in Figure 6.9(b)) pulls soil up and across as it rotates about the y-axis. The simple decoupled analytical approach described above would not be valid in this case.

The same trend in capacity with pile length can be seen for foundations with fixed piles loaded by F_y. However, due to the aspect ratio of the mudmat, failure does not involve 'pitching' about the x-axis until higher values of H/B (comparing Figure 6.8(d) to (a)). A hybrid foundation with fixed piles under pure M_z loading does not rotate about the x- or y-axes at failure (Figure 6.10(a)) and the overall capacity of the foundation increases almost linearly with additional pile length (Figure 6.8(c)).

For fully pinned piles (and horizontally pinned piles), relative rotation can occur at the pile head and the mudmat does not rotate about the x- or y-axes at failure. Figure 6.11 shows slices through the failure mechanism along the pile centreline for foundations with fixed and fully pinned piles under F_x loading. Figure 6.11(a) and (b) show that the response of fixed piles is dependent on the pile length (also shown in Figure 6.9). The pinned pile behaviour is independent of pile length (Figure 6.11(c)) and is similar to that of a pile or caisson loaded at the mudline (as described by Randolph and House (2002)); the pile rotates at failure and the mechanism can be idealised as a soil wedge extending downward from the mudline (cf.

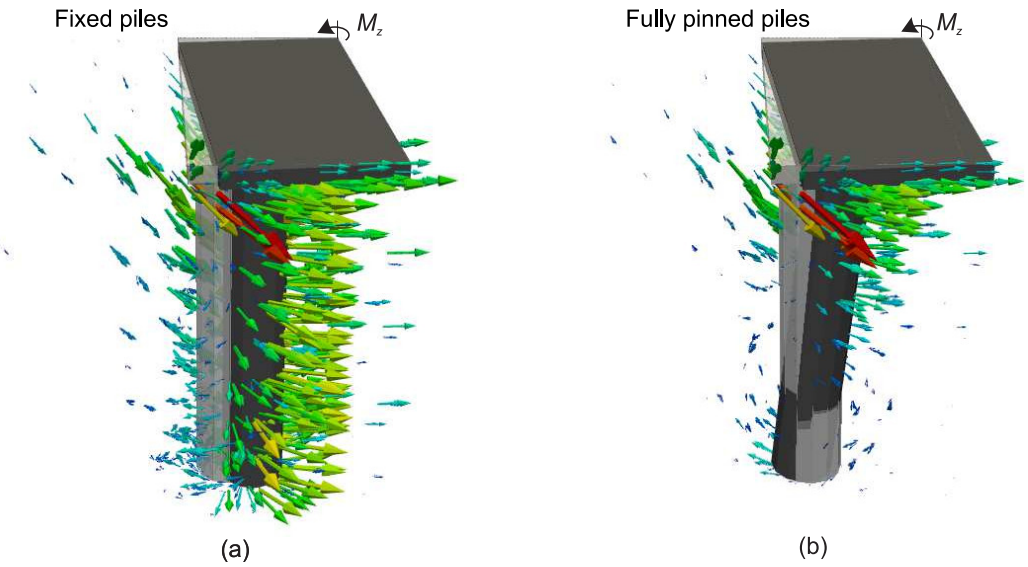

Figure 6.10: Failure mechanisms for hybrid foundations with $H/B = 1$ under M_z loading in uniform soil: (a) fixed piles; (b) fully pinned piles. Original foundation position drawn in light grey

Murff and Hamilton, 1993), with a spherical shearing surface below this which encompasses the pile. The failure mechanism for a hybrid foundation with fully pinned piles under M_z loading is shown in Figure 6.10(b). When compared to a foundation with fixed piles (Figure 6.10(a)), the mudmat mechanism is the same but the pile mechanism matches that for a pile loaded horizontally at the mudline (also shown in Figure 6.11(c)). This shows that pinned pile behaviour is essentially the same irrespective of F_x, F_y or M_z loading.

When the pile heads are fully pinned (or horizontally pinned), for all pile lengths there is minimal interaction between the soil failure mechanisms induced by the mudmat and the piles, for all pile lengths. The overall foundation capacity can be estimated by summing analytical solutions for the capacity of a mudmat under pure horizontal or pure torsional loading (Murff et al., 2010) and for a pile or caisson loaded at the mudline (Aubeny et al., 2003a). Under pure torsion each pile acts at a lever arm to the centre of the foundation, p_1, defined in Figure 6.1. The dashed lines in Figure 6.8 for fully pinned and horizontally pinned piles show that the superposition of these analytical approximations provides a reasonable estimation of the total capacity, although conservatism in the approach increases with increasing pile length.

Figure 6.12 shows the variation of the uniaxial horizontal and torsional capacities with

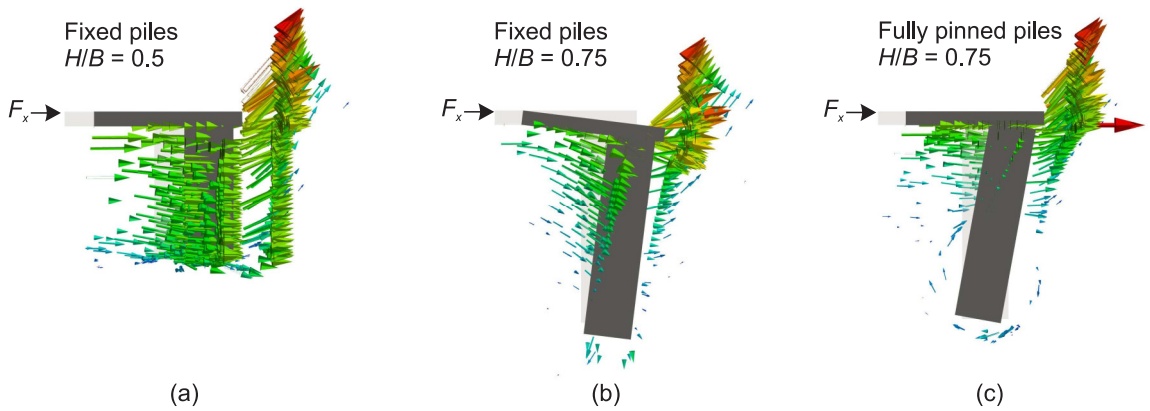

Figure 6.11: Failure mechanisms for hybrid foundations in uniform soil under F_x loading. Cross-section at pile centre: (a) fixed piles, $H/B = 0.5$; (b) fixed piles, $H/B = 0.75$; (c) fully pinned piles, $H/B = 0.75$. Original foundation position drawn in light grey

pile length for hybrid foundations in normally consolidated soil. The contribution from the shallowly embedded mudmat is, unsurprisingly, very low, and the capacity of the hybrid foundation is derived primarily from the piles. However, as was the case in uniform soil, a foundation with fixed piles and $H/B > 0.5$ rotates about the x- or y-axes when loaded horizontally, and this increases the contribution of the mudmat to the overall capacity (Figure 6.12(a) and (d)). Just as in uniform soil, there is no significant capacity difference between foundations with fully pinned piles and those with horizontally pinned piles.

For a foundation with pinned piles in normally consolidated soil, Figure 6.12 shows that the capacity contributed by the mudmat is negligible, irrespective of pile length. Capacities obtained using the analytical approach taken by Dimmock et al. (2013) are shown in Figure 6.12 for fully pinned and horizontally pinned piles. This approach ignores the capacity of the mudmat and uses the Aubeny et al. (2003a) method to find approximate UB capacities of the piles. Figure 6.12 shows that this approach works reasonably well and only marginally underestimates the total capacity when compared with 3D FELA.

It is evident from Figure 6.8 and Figure 6.12 that the capacity of a hybrid foundation is much larger when the piles are fixed than when they are pinned. The capacity of a foundation in uniform soil under F_y loading with fixed $H/B = 0.5$ piles is $3.05BLs_u$ (Figure 6.8(d)). The same foundation with pinned piles has 40% lower capacity, $1.81BLs_u$ (Figure 6.8(e)). Even if the pile length is doubled (to $H/B = 1$) for the foundation with pinned piles, the capacity

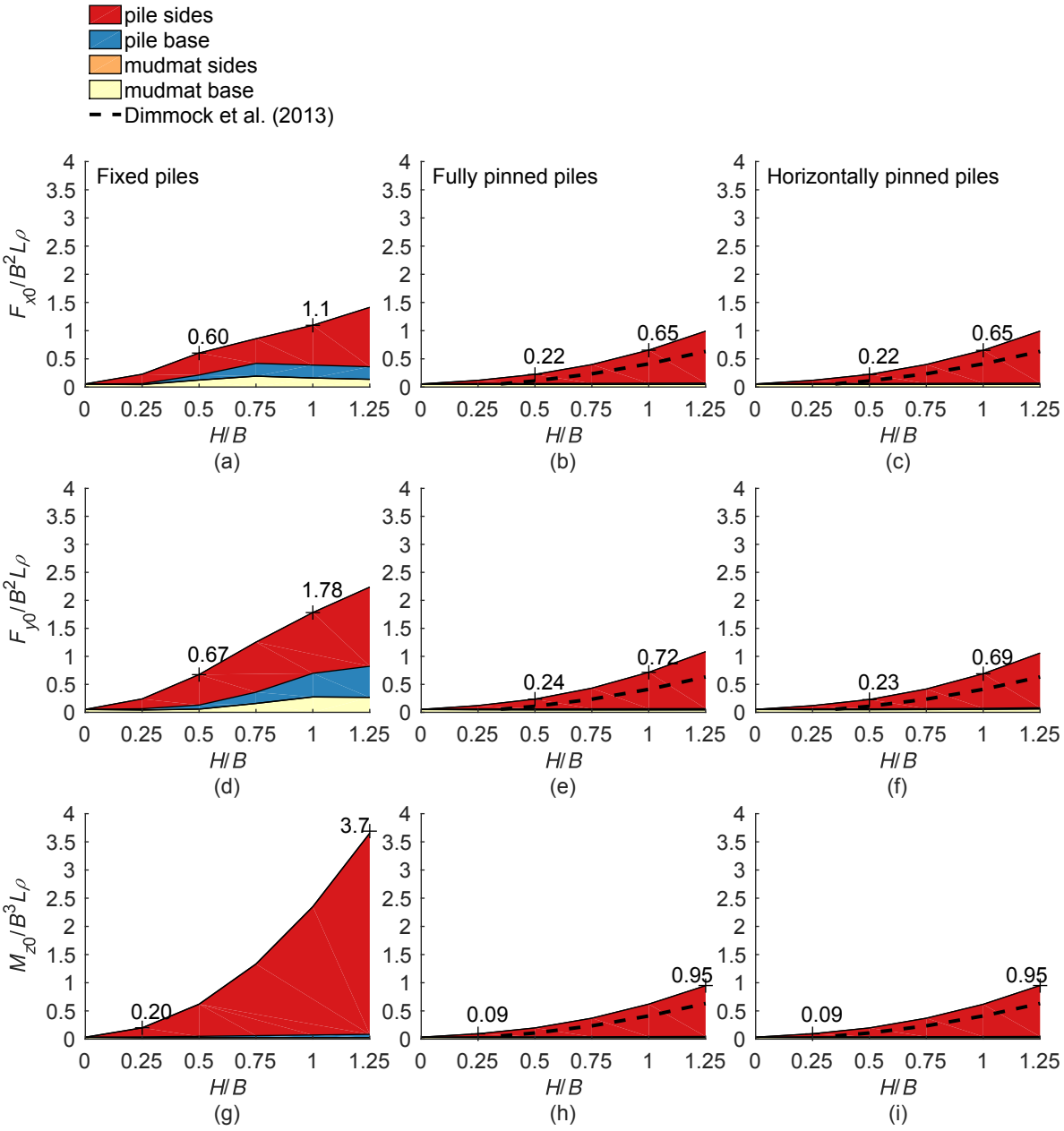

Figure 6.12: Ultimate uniaxial capacities F_{x0}, F_{y0}, and M_{z0} for a hybrid foundation with a range of pile lengths in normally consolidated soil split into component contributions: (a) F_{x0}, fixed piles ; (b) F_{x0}, fully pinned piles; (c) F_{x0}, horizontally pinned piles; (d) F_{y0}, fixed piles; (e) F_{y0}, fully pinned piles; (f) F_{y0}, horizontally pinned piles; (g) M_{z0}, fixed piles; (h) M_{z0}, fully pinned piles; (i) M_{z0}, horizontally pinned piles

is still lower than that with fixed $H/B = 0.5$ piles ($2.71BLs_u$ compared with $3.05BLs_u$). The difference between the capacities of pinned pile and fixed pile foundations is largest under torsional loading.

In normally consolidated soil, see Figure 6.12, the capacity of a foundation under F_y loading with fixed $H/B = 0.5$ piles is $0.67B^2L\rho$. The same foundation with pinned piles has a capacity that is over 60% lower ($0.24B^2L\rho$). If the pile length is doubled (to $H/B = 1$) for the foundation with pinned piles then the capacity is marginally higher ($0.72B^2L\rho$) than that with fixed piles of length $H/B = 0.5$ because the additional pile length is in stronger soil. The biggest difference between the capacities of foundations with pinned and fixed piles is, again, under M_z loading. A foundation with pinned $H/B = 0.25$ piles has an M_{z0} capacity $\sim$55% lower than the same foundation with fixed piles. The difference between the capacities increases as the pile length increases; a foundation with pinned $H/B = 1.25$ piles has a capacity $\sim$75% lower than the equivalent foundation with fixed piles (see Figure 6.12(g) and 6.12(h)).

For the next part of the parametric study, the pile length was fixed at $H/B = 1$ and the pile diameter was varied. Table 6.2 shows uniaxial horizontal and torsional capacities of a mudmat foundation (no piles) and hybrid foundations with horizontally pinned, fully pinned, and fixed piles, of various diameters in uniform soil (s_u = constant) and normally consolidated soil ($s_u = -\rho z$). The capacities of foundations with horizontally pinned piles and fully pinned piles are very similar.

For a hybrid foundation with pinned piles there is no significant difference between the capacities under F_x or F_y loading. When the pile diameter is increased by 60% ($D/B = 0.125$ to $D/B = 0.2$) there is only a 10% increase in F_x capacity for fully pinned piles ($2.44BLs_u$ to $2.78BLs_u$). A hybrid foundation with fixed piles shows larger relative increases in F_x, F_y, and M_z capacity as the pile diameter is increased, but these increases are still relatively modest (no more than 25% as D/B increases from 0.125 to 0.2).

For foundations in normally consolidated soil, an increase in pile diameter results in a proportionally larger increase in capacity when compared with uniform soil. However, the

Table 6.2: Uniaxial F_{x0}, F_{y0}, and M_{z0} capacities for hybrid foundations with a range of pile diameters in uniform soil (s_u = constant) and normally consolidated soil ($s_u = -\rho z$)

		s_u = constant			$s_u = -\rho z$		
	D/B	F_{x0} (BLs_u)	F_{y0} (BLs_u)	M_{z0} (B^2Ls_u)	F_{x0} $(B^2L\rho)$	F_{y0} $(B^2L\rho)$	M_{z0} $(B^3L\rho)$
No piles	0	1.20	1.10	0.73	0.06	0.05	0.03
Horiz. pinned piles	0.125	2.43	2.38	1.99	0.53	0.55	0.51
	0.15	2.56	2.55	2.10	0.59	0.62	0.56
	0.175	2.66	2.68	2.19	0.64	0.69	0.61
	0.2	2.76	2.80	2.25	0.69	0.76	0.65
Fully pinned piles	0.125	2.44	2.39	2.01	0.53	0.56	0.51
	0.15	2.57	2.60	2.12	0.59	0.66	0.57
	0.175	2.68	2.71	2.22	0.65	0.72	0.62
	0.2	2.78	2.81	2.29	0.69	0.79	0.66
Fixed piles	0.125	3.44	3.96	4.11	0.86	1.40	1.90
	0.15	3.63	4.25	4.57	0.98	1.59	2.18
	0.175	3.79	4.51	4.92	1.08	1.78	2.35
	0.2	3.92	4.76	5.14	1.18	1.98	2.47

capacity increases much more rapidly when the pile length (rather than the pile diameter) increases, due to the higher average soil strength along the length of the pile (as discussed above and shown in Figure 6.12).

6.5 Overturning moment capacities

The contributions of the constituent components of a hybrid foundation to the total foundation capacity were evaluated for foundations under uniaxial moment loading (M_x or M_y). The effect of pile length, and subsequently pile diameter, on foundation capacity was quantified. Figure 6.13 shows the effect of pile length on the uniaxial capacities M_{x0} and M_{y0} for foundations in uniform soil, for various pile head fixities. It is clear that fixed piles and fully pinned piles give a different response to moment loading, and furthermore that the use of horizontally pinned piles has no beneficial effect on the moment capacity of a mudmat alone (piles need vertical restraint to be beneficial to mudmat capacity).

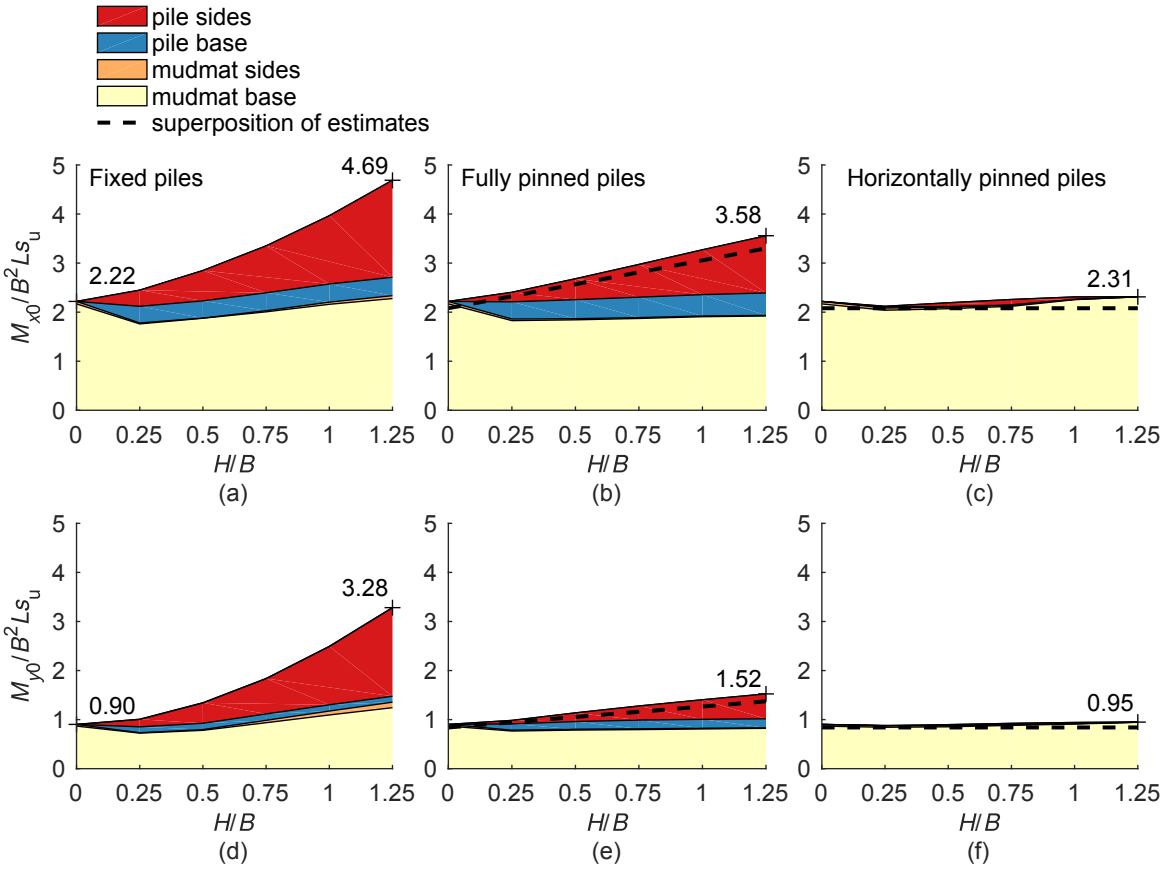

Figure 6.13: Ultimate uniaxial capacities M_{x0} and M_{y0} for a hybrid foundation with a range of pile lengths in uniform soil split into component contributions: (a) M_{x0}, fixed piles; (b) M_{x0}, fully pinned piles; (c) M_{x0}, horizontally pinned piles; (d) M_{y0}, fixed piles; (e) M_{y0}, fully pinned piles; (f) M_{y0}, horizontally pinned piles

Due to the aspect ratio of the mudmat the capacity M_{x0} is over twice M_{y0} ($2.22B^2Ls_u$ compared with $0.90B^2Ls_u$). There is a linear increase in capacity with additional pile length for foundations with pinned piles (Figure 6.13(b) and (e)) but the increase is nonlinear, and larger, for foundations with fixed piles (Figure 6.13(a) and (d)). The failure mechanisms in Figure 6.14(a) and (b) show that fixed piles rotate at failure, which causes the sides of the piles to bear into the soil. As pile length increases, the length of pile bearing into the soil, and the lever arm from the bearing force to the centre of rotation of the foundation, both increase. This gives rise to the non-linear increase in moment capacity as pile length increases (Figure 6.13(a) and (d)). The mechanism extends deeper into the soil domain when the foundation is under M_x loading compared with M_y loading, due to the aspect ratio of the mudmat, and this is clearly shown in the mechanisms for foundations with horizontally pinned

piles (Figure 6.14(e) and (f)). In this case, no capacity is provided by the piles and the failure mechanism resembles a simple 'scoop' mechanism (Bransby and Randolph, 1998).

There is less interaction between the pile and mudmat mechanisms when piles are fully pinned compared with fixed (comparing Figure 6.14(a) and (c) with (b) and (d)). In this case the mudmat mechanism resembles the scoop mechanism shown in Figure 6.14(e) and (f). The piles are moving vertically at failure and the vectors in Figure 6.14(c) and (d) show vertical bearing at the pile base. As the pile translates vertically there is pile/soil interface shearing along the rough pile walls. The pile bearing and shear resistance act at lever arms to the rotation centre p_2 and p_3 for M_x and M_y loading respectively (p_2 and p_3 are defined in Figure 6.1). Figure 6.13(b) and (e) shows that the capacities attributed to pile end bearing are independent of pile length (as the soil strength, pile base area, and lever arm remain the same) but the capacity attributed to the pile sides increases linearly with pile length. The overall pile contribution to capacity under M_x is roughly twice that under M_y as the lever arm p_2 is roughly twice p_3.

The most simple mechanism for hybrid foundations under moment loading is when the pile head is horizontally pinned. As previously mentioned, the mechanism resembles a plane strain simple scoop mechanism. The scoop mechanism for a strip footing of width B yields a capacity $0.69B^2 s_u$, which underestimates the rectangular mudmat moment capacities by $\sim$35% ($M_{x0} = 1.1BL^2 s_u$ and $M_{y0} = 0.90B^2 L s_u$). For a rectangular mudmat with $L/B = 2$, the uniaxial capacities $M_{x0} = 1.02B^2 L s_u$ and $M_{y0} = 0.84BL^2 s_u$ have previously been found using 3D FEA (Feng et al., 2014) and 3D UB FELA (Martin et al., 2015). These capacities compare favourably with the capacities of foundations with horizontally pinned piles (of any length) in Figure 6.13(c) and (f) (note that M_{x0} capacities are normalised by $B^2 L s_u$ and not $BL^2 s_u$ in Figure 6.13).

As already discussed, the mudmat and pile response is somewhat decoupled when the piles are fully pinned (mechanisms shown in Figure 6.14(c) and (d)). The combined mudmat and pile end bearing contribution to the overall moment capacity is roughly equal to the mudmat capacities found by Feng et al. (2014) and Martin et al. (2015) ($M_{x0} = 1.1BL^2 s_u$ and

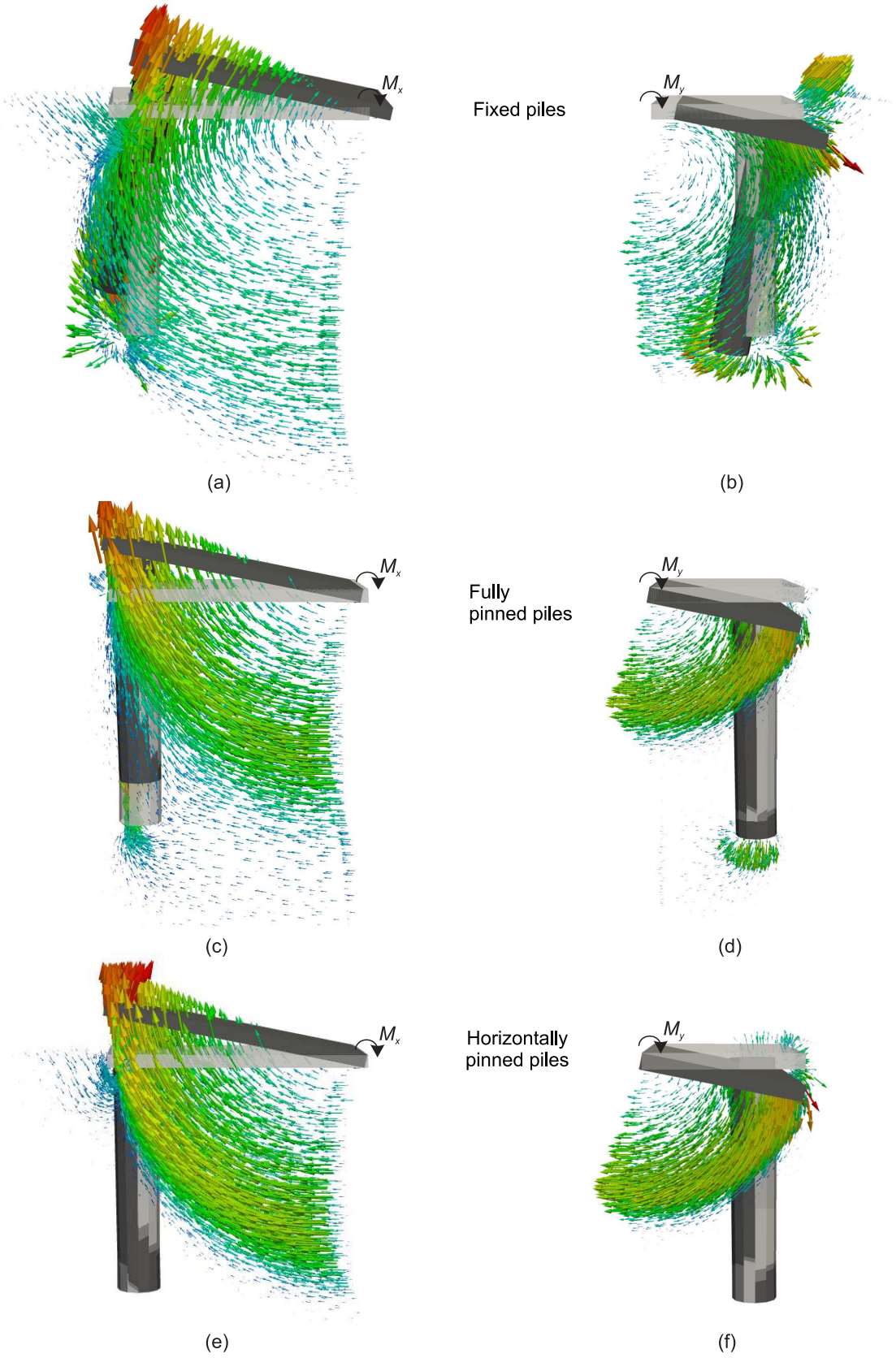

Figure 6.14: Failure mechanisms for hybrid foundations with $H/B = 1$ in uniform soil: (a) M_{x0}, fixed piles; (b) M_{y0}, fixed piles; (c) M_{x0}, fully pinned piles; (d) M_{y0}, fully pinned piles; (e) M_{x0}, horizontally pinned piles; (e) M_{y0}, horizontally pinned piles. Original foundation position drawn in light grey

$M_{y0} = 0.90B^2Ls_u$). The contribution of the pile sides to the overall moment capacity can be estimated for each pile as the pile/soil interface shear capacity times the lever arm to the foundation centre, $p_2\alpha\pi DL$ and $p_3\alpha\pi DL$ for M_x and M_y loading respectively. Superposition of the mudmat and pile side capacities provides an accurate estimate of the FELA UB capacities (dashed lines in Figure 6.13(b) and (e)). A similar approach also using superposition of mudmat and pile capacities was taken by Dimmock et al. (2013). The more complex mechanism for a foundation with fixed piles does not lend itself to an obvious decoupled solution (Figure 6.14(a) and (b)). The approach outlined above would provide a conservative estimate of capacity, particularly when the overturning moment is applied about the foundation's weaker axis.

For a foundation with piles of length $H/B = 1.25$ there is a 23% reduction in M_{x0} capacity if the piles are fully pinned as opposed to fixed ($4.69B^2Ls_u$ compared with $3.58B^2Ls_u$, Figure 6.13(a) and (b)). The capacity reduces to $2.31B^2Ls_u$ if the piles are only horizontally pinned (Figure 6.13(c)). For foundations with $H/B = 1.25$ under M_y loading, the difference in capacities for fixed and fully pinned pile foundations is higher ($3.28B^2Ls_u$ for fixed compared with $1.52LB^2 s_u$ for fully pinned piles).

Figure 6.15 shows the variation of the M_{x0} and M_{y0} capacities with pile length for foundations in normally consolidated soil. The capacity derived from the mudmat base is independent of the pile length, and for all pile head fixity conditions is $0.39B^3L\rho$ and $0.15B^3L\rho$ respectively under M_x and M_y loading. Just as for foundations in uniform soil, no additional moment capacity is gained when horizontally pinned piles are added to the mudmat foundation (Figure 6.15(c) and (f)).

For foundations with fixed and fully pinned piles, the relative contribution of the piles to the total moment capacity is much higher in normally consolidated soil than in uniform soil (comparing Figure 6.15 with Figure 6.13). This is simply because a foundation in normally consolidated soil has piles which are located in relatively stronger soil than the soil in which the mudmat is located. Figure 6.15 shows that the capacity from the pile base increases linearly with depth (as the soil strength at the pile base increases linearly). As fixed piles increase in

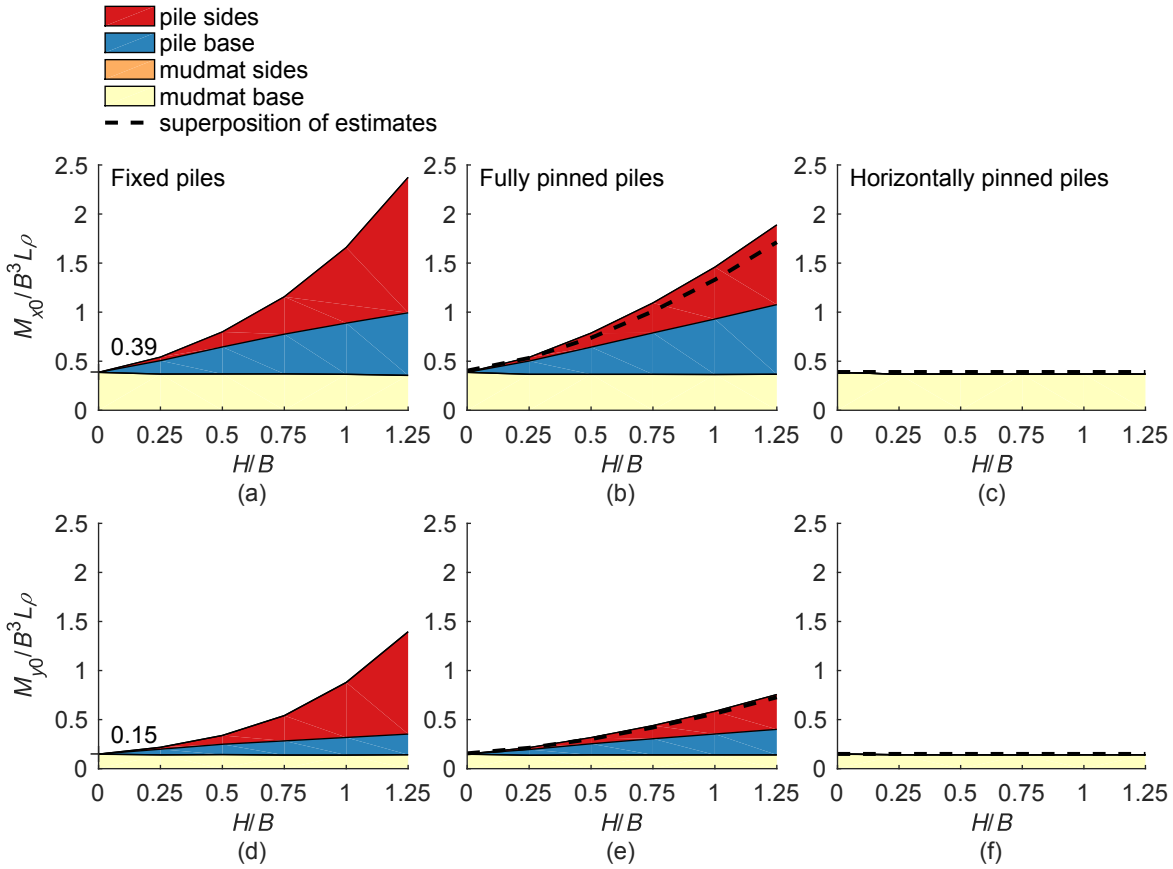

Figure 6.15: Ultimate uniaxial capacities M_{x0} and M_{y0} for a hybrid foundation with a range of pile lengths in normally consolidated soil split into component contributions: (a) M_{x0}, fixed piles; (b) M_{x0}, fully pinned piles; (c) M_{x0}, horizontally pinned piles; (d) M_{y0}, fixed piles; (e) M_{y0}, fully pinned piles; (f) M_{y0}, horizontally pinned piles

length there is a nonlinear increase in moment capacity from the pile wall as the pile lateral bearing area, the force lever arm to the foundation rotation centre, and the average soil strength along the pile length increases. There is also a nonlinear increase in the capacity attributed to fully pinned pile sides as pile length increases. This is because the average shear strength at the pile/soil interface, and the pile surface area are both increasing.

Simple superposition of mudmat and pile capacities can once again be used to estimate the total moment capacity. For a foundation with horizontally pinned piles, the capacity of the mudmat alone is representative of the overall foundation capacity in some cases. The mudmat uniaxial moment capacities M_{x0} and M_{y0} were found using UB FELA to be $0.39B^3L\rho$ and $0.15B^3L\rho$ respectively. The moment capacity derived from shearing at the pile/soil interface for each pile is $p_2\pi DLs_{\mathrm{u,av}}$ and $p_3\pi DLs_{\mathrm{u,av}}$ for M_{x0} and M_{y0} respectively (where $s_{\mathrm{u,av}}$ is

Table 6.3: Uniaxial M_{x0} and M_{y0} capacities for hybrid foundations with a range of pile diameters in uniform soil (s_u = constant) and normally consolidated soil ($s_u = -\rho z$)

		s_u = constant		$s_u = -\rho z$	
	D/B	M_{x0} $(B^2 L s_u)$	M_{y0} $(B^2 L s_u)$	M_{x0} $(B^3 L \rho)$	M_{y0} $(B^3 L \rho)$
No piles	0	2.22	0.90	0.39	0.15
Horiz. pinned piles	0.125	0.95	1.25	0.38	0.15
	0.15	0.95	1.23	0.37	0.14
	0.175	0.94	1.20	0.37	0.14
	0.2	0.94	1.18	0.36	0.14
Fully pinned piles	0.125	3.03	1.28	1.09	0.46
	0.15	3.16	1.35	1.27	0.52
	0.175	3.27	1.41	1.46	0.58
	0.2	3.38	1.46	1.65	0.65
Fixed piles	0.125	3.75	2.29	1.28	0.70
	0.15	3.87	2.40	1.47	0.80
	0.175	3.96	2.49	1.66	0.88
	0.2	4.05	2.55	1.85	0.95

the average shear strength along the length of the pile). In uniform soil the capacity due to end bearing at the pile base was not considered separately, rather it was included with the mudmat capacity. In normally consolidated soil the piles are bearing into relatively stronger soil than the mudmat, and including the contribution of end bearing at the pile base level gives a more accurate representation of the FELA moment capacities. The modified general bearing capacity equation (Equation 2.3) was used to obtain estimates for the pile bearing capacity, where $c_u = s_u$ at $z = -d - H$ and shape and depth factors (as suggested by Skempton (1951)) were used to find bearing capacity factors:

$$N_c = 5.14\,(1.2)\left[1 + \sqrt{0.053 \times \frac{H}{D}}\right] \leq 9 \tag{6.1}$$

Figure 6.15 shows that superposition of capacity estimates gives a good match with the overall moment capacities obtained using FELA.

Finally, the pile length was fixed at $H/B = 1$ and the pile diameter was varied. Table 6.3 shows uniaxial moment capacities of a mudmat foundation (no piles) and hybrid foundations

with horizontally pinned, fully pinned, and fixed piles, of various diameters in uniform soil (s_u = constant) and normally consolidated soil ($s_u = -\rho z$). For horizontally pinned piles, as expected, a longer pile diameter does not result in any increase in capacity. In fact, there is a trivial decrease in capacity, because the mudmat bearing area becomes smaller as the pile diameter increases. For foundations with fixed and fully pinned piles there is a linear increase in capacity with increasing pile diameter, and this increase is larger for M_{x0} compared with M_{y0}. In uniform soil, a 60% increase in pile diameter (from $D/B = 0.125$ to 0.2) leads to a modest $\sim$15% increase in the overall moment capacity. In normally consolidated soil there is a larger increase in capacity when the pile diameter is increased ($\sim$40% increase in capacity when the pile diameter is increased from $D/B = 0.125$ to 0.2).

6.6 Vertical capacity

Figure 6.16 shows the contributions of the constituent components of a hybrid foundation to the uniaxial vertical foundation capacity. In uniform soil the capacity is contributed predominantly by the mudmat. Foundations with fully pinned and fixed piles have essentially equal capacities, and an increase in pile length results in a linear increase in capacity (Figure 6.16(a) and (b)). As expected, there is no contribution from the piles to the foundation capacity when the pile head is free to move vertically relative to the mudmat (pinned against horizontal translation only, Figure 6.16(c)).

The mechanisms in Figure 6.17(a) and (b) for a foundation with fixed or fully pinned piles (of length $H/B = 1$) show that at failure the mudmat and the pile bases are bearing into the soil. The failure mechanism for horizontally pinned piles in Figure 6.17(c) shows that the piles do not move at failure. Dimmock et al. (2013) recommend a simplified design approach where the mudmat alone is assumed to carry the entire vertical load. For foundations in uniform soil, this assumption provides a reasonable estimate of foundation capacity, particularly for foundations with horizontally pinned piles. Dimmock et al. also note that prior to the installation of the piles, the mudmat alone must carry vertical self-weight loads.

The capacities of foundations with pinned and fixed piles can be matched more closely to

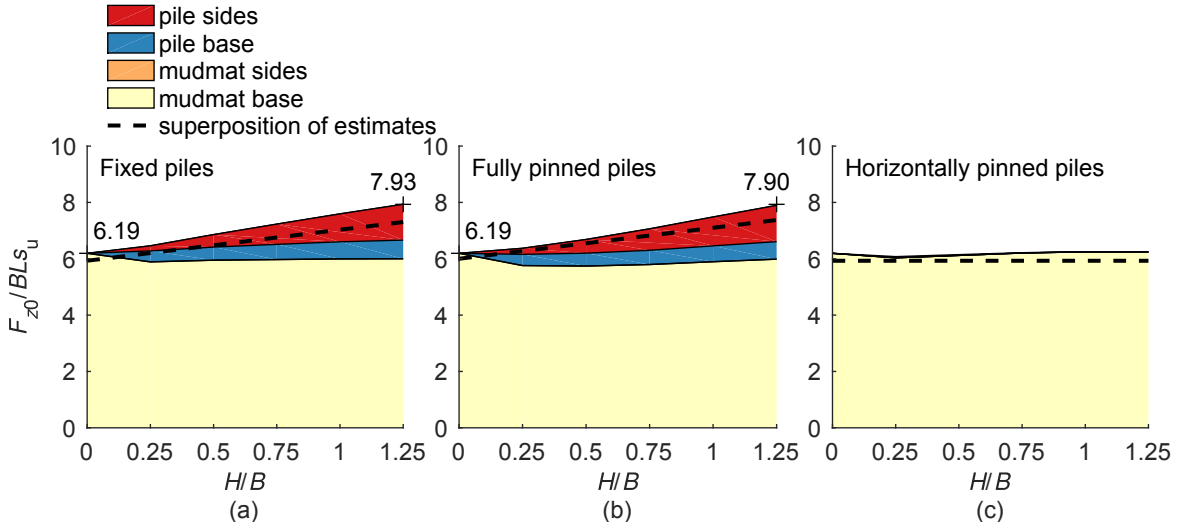

Figure 6.16: Ultimate uniaxial capacities F_{z0} for a hybrid foundation with a range of pile lengths in uniform soil split into component contributions: (a) fixed piles; (b) fully pinned piles; (c) horizontally pinned piles

the FELA capacities by using simple superposition of the estimated mudmat and pile capacities. The combined mudmat and pile base contribution to capacity was estimated using the general bearing capacity equation (Equation 2.3) with N_c found using shape and depth factors for a rectangular embedded foundation, as suggested by Skempton (1951):

$$N_c = 5.14\left(1+\frac{0.2B}{L}\right)\left[1+\sqrt{0.053\times\frac{d}{B}}\right] \leq 9 \tag{6.2}$$

The capacity due to shearing along the pile/soil interface for each pile is πDLs_u. Figure 6.16 shows that combining these capacities provides a reasonable estimate of the vertical capacity, although the method slightly underestimates the UB FELA results.

Figure 6.18 shows that additional pile length results in a large increase in vertical capacity for foundations in normally consolidated soil (provided the pile heads are fixed or fully pinned). Mudmat capacity alone is $0.91B^2L\rho$. When corner piles with length $H/B = 1.25$ are added, the capacity is over 2.5 times higher, at $2.65B^2L\rho$ (Figure 6.18(a) and (b)). The increase in capacity with additional pile length is large because the pile bases are bearing into increasingly stronger soil (than the mudmat base), and the average strength along the pile sides is increasing.

Assuming that only the mudmat contributes to capacity is somewhat conservative in this instance. Superposition of mudmat and pile end bearing and shear capacities provides a more

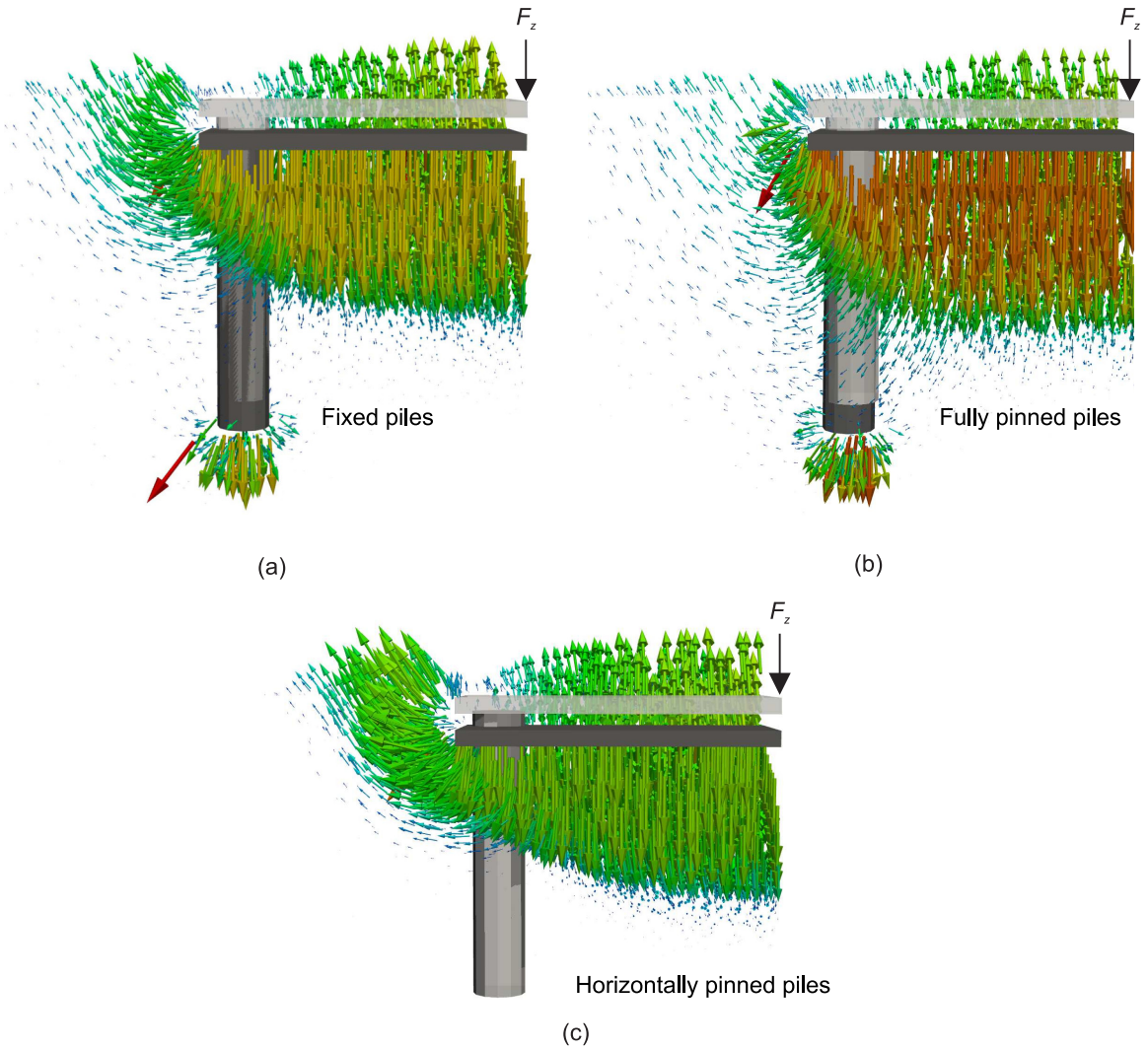

Figure 6.17: Failure mechanisms for hybrid foundations with $H/B = 1$ under F_z downwards loading in uniform soil: (a) fixed piles; (b) fully pinned piles; (c) horizontally pinned piles. Original foundation position drawn lightly

accurate estimate of the overall vertical capacity. An estimate of mudmat capacity was found using the MoC software ABC (Martin, 2004) assuming plane strain conditions. The pile end bearing and shear capacities were calculated in the same way as for a foundation under moment loading (Section 6.5). The superimposed approximate solutions compare favourably with the FELA capacities (Figure 6.18).

Capacities of foundations with a range of pile diameters are shown in Table 6.4. In uniform soil, an increase in diameter results in an almost negligible increase in capacity — when pile diameter increases $\sim$60% the capacity increases $< 10\%$. This is because very little of the overall capacity is contributed by the piles. In normally consolidated soil, an increase in pile

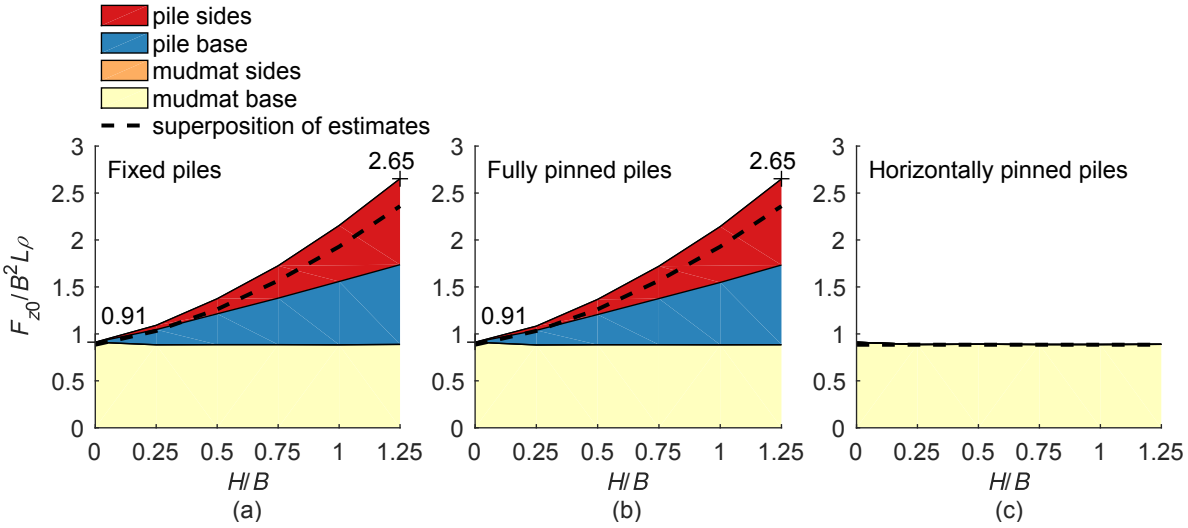

Figure 6.18: Ultimate uniaxial capacity F_{z0} for a hybrid foundation with a range of pile lengths in uniform soil split into component contributions: (a) fixed piles; (b) fully pinned piles; (c) horizontally pinned piles

diameter results in a larger increase in foundation capacity.

Table 6.4: Uniaxial F_{z0} capacities for hybrid foundations with a range of pile diameters in uniform soil (s_u = constant) and normally consolidated soil ($s_u = -\rho z$)

	D/B	s_u = constant (BLs_u)	$s_u = -\rho z$ $(B^2L\rho)$
No piles	0	6.19	0.91
Horiz. pinned piles	0.125	6.31	0.90
	0.15	6.29	0.90
	0.175	6.25	0.89
	0.2	6.22	0.88
Fully pinned piles	0.125	7.16	1.70
	0.15	7.33	1.92
	0.175	7.49	2.15
	0.20	7.65	2.40
Fixed piles	0.125	7.20	1.70
	0.15	7.40	1.92
	0.175	7.60	2.16
	0.2	7.79	2.40

6.7 Case study

A recently completed design of a hybrid foundation with fixed piles under six degree-of-freedom loading was analysed using 3D LB and UB FELA, and compared with 3D displacement FEA undertaken by Subsea 7 (personal communication, 2015). FELA was undertaken for a foundation on flat ground and ground with a slight inclination (5°). The input design parameters are listed in Table 6.5, and the soil strength profiles used in the FELA and FEA models are shown in Figure 6.19. A four-layered soil was implemented in the FEA model, but this was simplified in the FELA model as a heterogeneous soil profile, $s_u = s_{um} - \rho z$.

A rough interface ($\alpha = 1$) with unlimited tension capacity ($T = \infty$) was modelled at the mudmat base and pile bases (where there is a soil/soil interface). The mudmat sides and pile sides were modelled as half-rough ($\alpha = 0.5$). Unlimited tension was modelled at the pile sides ($T = \infty$) and a no-tension interface ($T = 0$) was modelled at the mudmat sides.

The design loads are shown in Table 6.6 (for sign conventions see Figure 6.1). On inclined

Table 6.5: Input parameters for hybrid foundation case study

Mudmat breadth (L)	8 m
Mudmat length (B)	17 m
Mudmat skirt embedment (d)	0.3 m
Pile length (H)	9.7 m
Pile diameter (D)	1.5 m
Pile offset from mudmat edge (e)	0.25 m
Mudline strength (s_{um})	0.69 kPa
Vertical strength gradient (ρ)	0.93 kPa/m
Pile/mudmat connection	fixed
Submerged soil unit weight (γ')	4.5 kN/m^3
Seabed inclination (ξ)	0, 5°

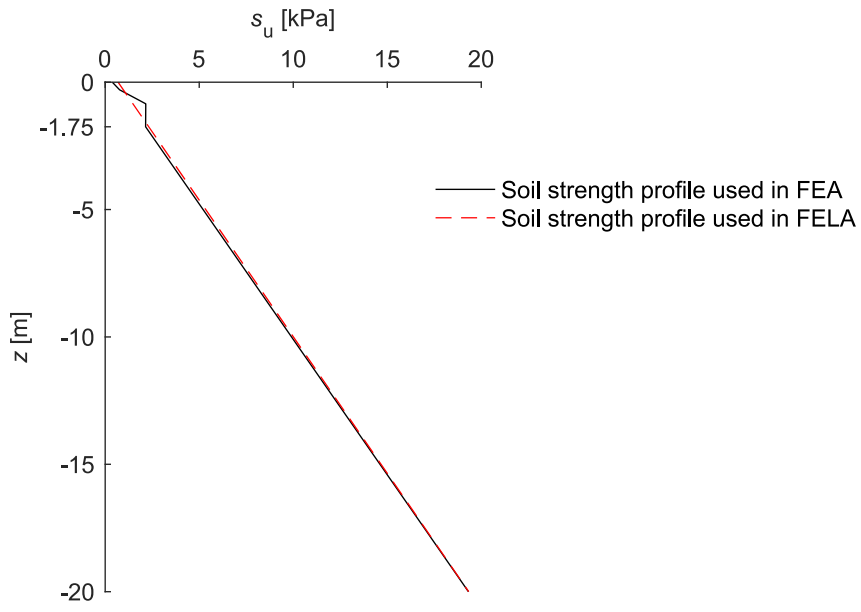

Figure 6.19: Soil strength profiles used in hybrid foundation case study

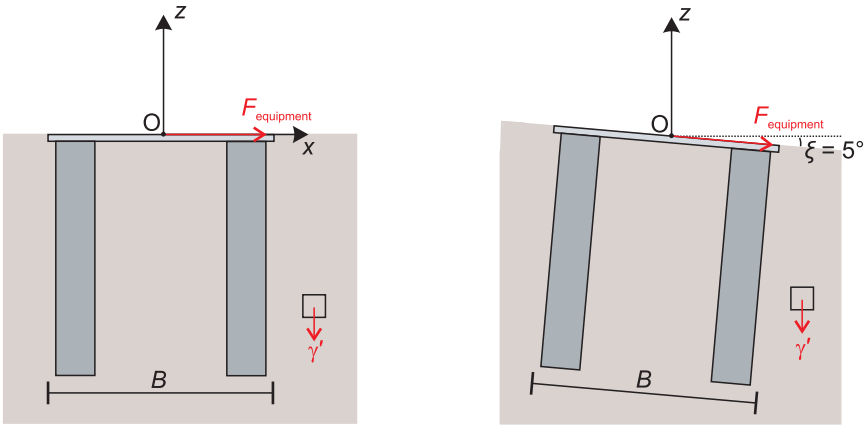

Figure 6.20: Case study loading in the plane $y = 0$: (a) flat ground; (b) ground inclined $\xi = 5°$

Table 6.6: Loading and and soil weight

ξ	F_x (kN)	F_y (kN)	F_z (kN)	M_x (kNm)	M_y (kNm)	M_z (kNm)	γ'_z (kN/m^3)	γ'_x (kN/m^3)
0	200	269	-1974	-3498	1033	-2576	-4.5	0
5°	372	269	-1967	-3498	1033	-2576	-4.48	0.39

ground, the piles were installed perpendicular to the seabed to ensure that the mudmat skirt penetrates fully into the soil, as shown in Figure 6.20(b). As the ground inclination in this case is quite small (5°), equipment on the mudmat was not levelled, and horizontal loads from the connected equipment are applied parallel to the seabed (Figure 6.20(b)). Partly for this reason, and partly due to the somewhat complicated foundation geometry, inclined ground was modelled in OxLim by manipulating the vertical loads, rather than changing the geometry, and updating the forces such that,

$$\begin{aligned} \gamma'_z &= \gamma' \cos(\xi) \\ \gamma'_x &= \gamma' \sin(\xi) \\ F_z &= F_z \cos(\xi) \\ F_x &= F_x - F_z \sin(\xi) \end{aligned} \tag{6.3}$$

Plaxis 3D (Plaxis, 2016) was used by Subsea 7 to undertake displacement FEA. The soil was modelled as a linear elastic–perfectly plastic Tresca material. The problem domain was discretised as an unstructured mesh of 10-noded tetrahedra. Zero-thickness elements were used to model foundation/soil interface shear and tension behaviour. Manual mesh refinement

was undertaken until the solution converged; the final mesh comprised 110 000 elements. Poisson's ratio was set to $\nu_u = 0.49$ (simulating near incompressibility) and Young's modulus was set to $E_u = 1000\,s_u$. Load factors at each solution increment were found using a 'phi-c reduction approach' (see Plaxis, 2016). This approach considers the load factor as the ratio of the soil strength to the computed minimum soil strength required for equilibrium,

$$\mathrm{LF} = \frac{s_u}{s_{u,\,\mathrm{equilibrium}}} \tag{6.4}$$

FELA analyses were undertaken for polygonal pile discretisations $N = 12$ and 24. For analyses where $N = 12$, the initial mesh comprised ∼15 000 elements and three iterations of automated adaptive mesh refinement were performed (to ∼30 000, ∼45 000, and ∼65 000 elements). For analyses where $N = 24$, the initial mesh comprised ∼25 000 elements, and again three iterations of mesh refinement were performed. Load factors obtained for foundations on flat ground using both pile discretisations are shown in Table 6.7. There is no significant difference between the capacities when $N = 12$ and 24. The large bracketing error (∼10%) for both pile discretisations, even for analyses with a large number of elements (65 000), highlights the complexity of the problem.

Similar to the caisson design case study in Section 5.6, the load factor obtained using a coarse mesh is found to give a good estimate of the load factor when a more refined mesh is analysed (1.53 and 1.56 for coarse and fine meshes respectively when $N = 12$, Table 6.7). However, the analysis time for a coarse mesh was under 2 minutes, while analysis of a fine mesh (65 000 elements) took just under 40 minutes (LB and UB analyses solved in series on a 3.1 GHz machine with 32 GB RAM). Load factors found at each FELA mesh refinement iteration (when $N = 12$) and FEA load factors are shown to compare favourably in Figure 6.21. The rigid–plastic FELA load factors are independent of the foundation displacement, in contrast to FEA load factors, which are shown in Figure 6.21 at incremental foundation displacements. Failure appears to onset when the FEA load factor ≈ 1.4.

3D FELA was subsequently used to quantify the reduction in capacity caused by an inclined seabed, for a foundation with a pile discretisation $N = 12$. Suitably adjusted loading was applied to model the sloping seabed, as outlined in Table 6.6. After three iterations of

Table 6.7: Load factors and bracketing errors for flat ground ($\xi = 0$)

	$N = 12$					$N = 24$			
Elements	LB	UB	Average	% Error	Elements	LB	UB	Average	% Error
10 000	1.22	1.84	1.53	20.1	25 000	1.26	1.89	1.57	20.1
30 000	1.32	1.76	1.54	14.1	30 000	1.34	1.80	1.57	14.8
45 000	1.37	1.74	1.55	11.7	45 000	1.39	1.76	1.57	11.7
65 000	1.39	1.71	1.56	10.4	65 000	1.42	1.73	1.58	10.1

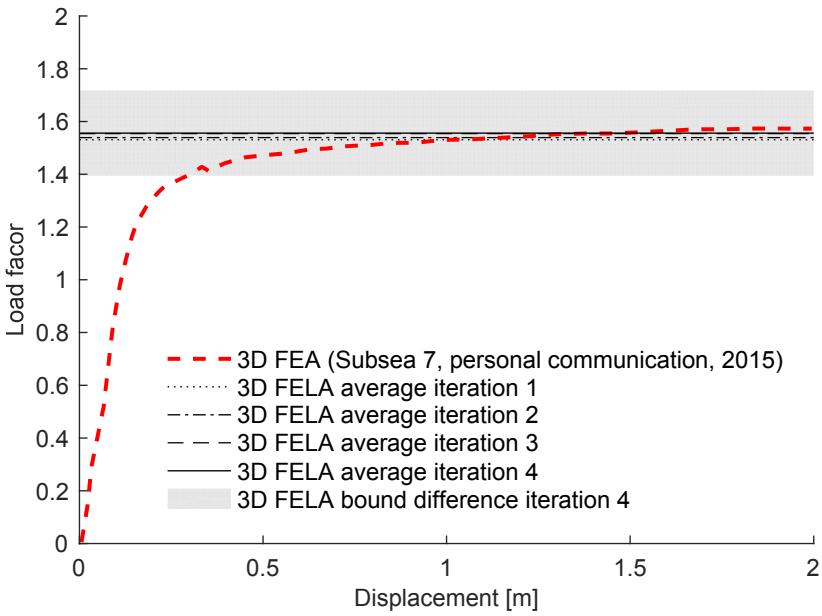

Figure 6.21: Capacity on flat ground found ($\xi = 0$) using FELA ($N = 12$) and FEA

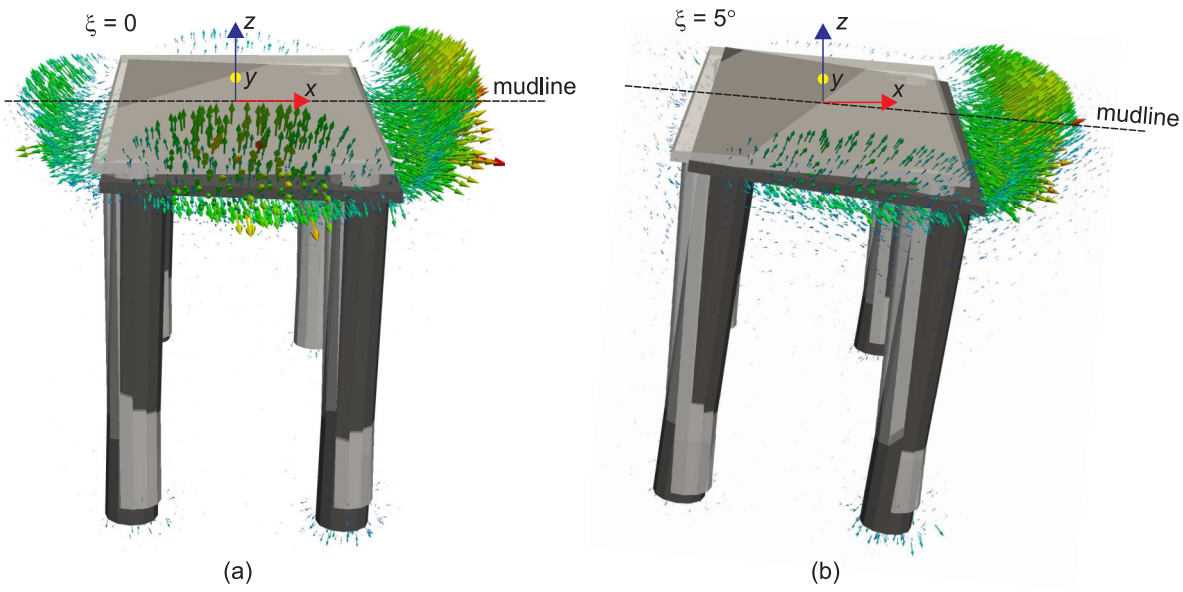

Figure 6.22: Case study failure mechanism: (a) flat ground ($\xi = 0$; (b) inclined ground ($\xi = 5°$))

adaptive mesh refinement, a load factor of 1.39 ($\pm 11\%$) was found. This shows $\sim$10% capacity reduction due to the sloping seabed. Failure mechanisms for the foundation on flat ground and on sloping ground are shown in Figure 6.22. On flat ground, the mechanism is largely dominated by the vertical load, although the mudmat also pivots slightly about a point towards its back left corner. On sloping ground, the mechanism becomes more one-sided, and the effect of a near doubling of the force tangential to the seabed is clearly visible (for F_x loads see Table 6.6 and Equation 6.3). Parallels can be drawn between the mechanisms in Figure 6.22 and those for a planar mudmat on inclined ground under vertical loading (Figure 4.12); in both cases a more one sided mechanism becomes dominant on inclined ground and signals a significant reduction in capacity.

6.8 Summary

It has been shown that for a rough circular pile section under combined horizontal and torsional loading, a rather coarse ($N = 12$) polygonal discretisation of the pile is sufficient to capture the failure envelope accurately. Under pure torsion a rough square pile has the same capacity as a circular pile that it inscribes. A polygonal approximation of a smooth pile requires many more facets in order to accurately capture behaviour under torsional loading.

The capacities of hybrid mudmat–pile foundations under uniaxial vertical, horizontal, moment, and torsional loads have been studied using 3D FELA (UB only). The capacities contributed by the constituent components of hybrid foundations (mudmat base, mudmat sides, pile base, and pile sides) under uniaxial loads have been determined. The effects of pile length, pile diameter, and pile head fixity have been quantified by means of parametric studies. For each load case considered, a change in pile length had a much more significant effect on foundation capacity when compared with a similar relative change in pile diameter.

Hybrid foundations with fully pinned piles and horizontally pinned piles have equal capacities when subjected to horizontal or torsional loading. For a foundation with pinned piles the capacity contributed by the mudmat does not change as the pile length increases, and the soil failure mechanism shows little interaction between the mudmat and the piles. Irrespective of global horizontal or torsional loading, the pile failure mechanism is that of a pile loaded horizontally at the mudline. The analytical approach adopted by Dimmock et al. (2013), which ignores the capacity contributed by the mudmat, was shown to work reasonably well for foundations in normally consolidated soil. In uniform soil, it was shown that a more accurate capacity estimate can be obtained by including an analytical approximation of the mudmat contribution to the hybrid foundation capacity. The behaviour of a hybrid foundation with fixed piles is more complex. When loaded horizontally, this type of foundation may roll or pitch at failure. Whether the foundation slides or rotates is dependent on the relative length (H/B) of the piles.

Under moment loading, the addition of horizontally pinned piles to a mudmat does not increase its capacity. A foundation in uniform soil with fully pinned piles shows a linear increase in moment capacity as pile length increases. As for a foundation under horizontal or torsional loading, there is little interaction between the soil failure mechanism induced by the mudmat and the piles. The mudmat scoops a segment of soil, while the piles bear vertically downwards or upwards. The overall moment capacity with fully pinned piles can be estimated by combining the mudmat moment capacity with vertical pile capacities (due to both interface shearing at the pile wall/soil interface and end bearing) acting at a lever arm

from the load reference point. The failure mechanism under moment loading is more complex for a foundation with fixed piles, and the superposition of easily calculated mudmat and pile capacities is less appropriate, particularly when the foundation is loaded about its weaker axis.

Under vertical loading, the capacities of hybrid foundations with fully pinned and fixed piles are equal under vertical loading, for all pile lengths. In uniform soil the capacity is predominantly contributed by the mudmat, and increasing pile length results in a relatively small increase in capacity. In normally consolidated soil, mudmat capacity can be improved substantially through the addition of fully pinned or fixed piles.The vertical capacity of a hybrid foundation with fixed piles or fully pinned piles can be estimated by summing suitable approximations of the mudmat and pile bearing capacities.

This chapter concluded with a complex design case which considered a hybrid foundation under six degree-of-freedom loading on flat and inclined ground. On flat ground, the average capacity obtained using 3D FELA corresponded well with the capacity obtained using FEA. However, the complexity of the problem was highlighted by a large bracketing error ($\pm 10\%$), even for analysis of a mesh containing 65 000 elements. It was shown that the load factor obtained using a coarse mesh gave a good estimate of that found when a more refined mesh was analysed, but with a substantially shorter analysis time. A sloping seabed caused a 10% reduction in capacity, and induced additional rotation of the foundation at failure.

Chapter 7

Conclusions

This thesis has investigated the ultimate capacity of several types of foundation founded on offshore clay under various loading conditions. The primary analysis tool has been the relatively novel 3D finite element limit analysis (FELA) software, OxLim. OxLim has been benchmarked against analytical solutions, proving itself as an accurate analysis tool. Insight into capacities of a range of offshore foundations has been provided through a series of parametric studies. Failure mechanisms have been interpreted to assist understanding of foundation behaviour. Case studies have demonstrated that 3D FELA with adaptive mesh refinement can be usefully applied to realistic foundation designs. The following sections list the key findings from each study undertaken. Areas for future research are also highlighted.

7.1 Main findings

7.1.1 Finite element limit analysis

- 3D FELA with adaptive mesh refinement has been shown to be a viable alternative to conventional FEA for a range of offshore design problems.

- The method has been used to find rigorous lower and upper bound capacities of shallow foundations, caisson foundations, and hybrid mudmat–pile foundations, in undrained clay. The method is capable of modelling large-scale problems with mesh discretisations that exceed 60 000 elements. Six degree-of-freedom limit load analyses have been undertaken for complex foundation geometries, in soil with various strength profiles (homogeneous, heterogeneous, stepped), with attention also given to modelling

foundation/soil interface properties.

- A key advantage of combining LB and UB FELA is that a quantifiable error measure is associated with the solution. In some instances, the error found when using a coarse mesh was sufficiently small that mesh refinement was not needed. Design case studies have highlighted that a quick initial capacity estimate can be found using a coarse mesh, as this capacity is usually very similar to that found after several iterations of mesh refinement.

7.1.2 Shallow rectangular foundations

7.1.2.1 Foundations on sloping ground

- The vertical capacity of a mudmat on sloping ground can be significantly less than that of an equivalent footing on flat ground. Foundation embedment can offset this reduction, while also providing improved horizontal capacity. Analysis of a recent mudmat design showed that a seabed slope of only 5° caused an 18% reduction in vertical capacity — this is enough to warrant consideration in design.

7.1.2.2 Rectangular mudmats

- The gradual reduction in capacity with increasing lateral eccentricity of a horizontal force was quantified. Under combined horizontal and torsional loading, failure mechanisms were shown to change from pure translation to combined translation and twisting, depending on the level of embedment. The reduction in capacity due to eccentric loading can be reduced by embedding a mudmat, particularly when the horizontal force is aligned with the longer side of the mudmat.

- There is no reduction in capacity due to a horizontal force applied at a height above the mudmat until a critical height is reached, whereupon the capacity reduces rapidly. The critical height is lower when the horizontal force is aligned parallel to the shorter side of the mudmat. The failure mechanisms presented show a change from pure translation to combined translation and rotation once the critical height has been reached.

- A vertical dead load up to half of the ultimate vertical capacity can be applied to the mudmat with minimal effect on the live load capacity for horizontal loading in conjunction with practically feasible levels of torsional and moment loading.

7.1.2.3 Perforated footings

- For embedded foundations, the Tapper et al. (2015) design formula is conservative for foundations with large perforation ratios, particularly in soil with high strength heterogeneity. A modification to this design formula has been proposed which provides better estimates of bearing capacity factors found using 3D FELA.

7.1.3 Suction caissons

- A horizontally loaded suction caisson has an optimal load attachment point that is independent of the length to diameter aspect ratio over the range considered here ($L/D = 1-6$). The optimal location (to the nearest $0.1L$) is $0.6L$ from the mudline for caissons in uniform soil and $0.7L$ from the mudline for caissons in normally consolidated soil. The optimal load point location varies with the load angle. For a given load angle, the optimal location is largely independent of aspect ratio for caissons with $L/D = 2-6$.

- Capacity was significantly reduced (by up to 40%) when contact breaking was permitted at the wall/soil interface. The reduction in capacity can be attributed to gapping at the wall/soil interface, and is dependent on the weight-to-strength ratio of the soil, with gapping more likely to occur in a relatively light soil.

- Failure mechanisms obtained using a plane strain analysis are often not representative of 3D failure mechanisms, as lateral soil flow around the caisson is often a prominent mechanistic feature. However, as the load inclination from the horizontal increases, the effectiveness of a plane stain analysis increases.

7.1.4 Hybrid mudmat–pile foundations

- The addition of corner piles to a mudmat can lead to a significant increase in capacity when compared with the mat alone.

- When subjected to horizontal or torsional loading, hybrid foundations with fully pinned piles and horizontally pinned piles have equal capacities. An analytical approach adopted by Dimmock et al. (2013) provides an accurate estimate of capacity for foundations with pinned piles in normally consolidated soil, but is somewhat conservative in uniform soil. For this case the inclusion of an analytical approximation of the mudmat's contribution to the hybrid foundation capacity improves the accuracy of the analytical approach.

- Under moment loading, piles must be restrained against vertical movement (relative to the mudmat) to contribute to the total foundation capacity. A foundation with fully pinned piles gives rise to soil failure mechanisms induced by the mudmat and the piles that are essentially decoupled, and the moment capacity can be estimated by summing capacities attributed to these independent failure mechanisms.

- Vertical capacities of hybrid foundations with fixed piles and fully pinned piles are equal. Fixed or fully pinned pile foundations have a capacity in uniform soil that is predominantly contributed by the mudmat, and a simple analysis method that neglects pile capacity (from Dimmock et al. (2013)) is appropriate. In normally consolidated soil the total vertical capacity is better approximated by including both the mudmat and pile capacities.

7.2 Areas for future research

The FELA code used in this thesis is under active development. Connectivity between rigid bodies (used in Chapter 6) is a recently added feature that shows much potential. This feature could be used to model pile (or caisson) foundations modelled as a series of rigidly connected

pile segments. Capacity contributions could be found for each pile segment, which could facilitate the production of '$p-y$' style curves.

This thesis considered foundations on undrained clay (acting as a purely cohesive material). Further research is needed for foundations in sand, or sand/clay layered soil.

FELA is a relatively simple plastic technique that is limited by a number of assumptions. A useful extension of this research could consider effects that cannot be handled using limit analysis, for example, cyclic loading, rate effects, and installation effects. This would require the use of displacement FEA rather than FELA.

Specific extensions to studies undertaken in this thesis are subsequently listed.

7.2.1 Analysis of mudmats

- The main study of planar mudmat capacity on inclined ground considered soil with uniform strength. Analysis of foundations with a range of embedment depths, in soil with strength that varies with depth, would provide further insight. This research could also be extended to consider 3D rectangular mudmat capacity on inclined ground.

- Capacity analysis of rectangular mudmats with a length to breadth aspect ratio of 2 could be extended to include mudmats with a range of aspect ratios. Also, the effect of soil strength heterogeneity on mudmat capacity under combined horizontal, torsional, moment, and vertical loading needs further consideration.

- Perforated mudmats were only considered under vertical loading. Examination of embedded foundations with large perforations under combined loading is needed.

7.2.2 Analysis of caissons

- The methodology used for the analysis of suction caissons could be extended to consider caissons used as foundations for offshore wind turbines, where horizontal loading is applied above the mudline.

- This research considered load angles from horizontal to 45° above horizontal. A further study should be undertaken that considers load angles greater than 45°.

- The results have highlighted that a caisson with a length to diameter aspect ratio equal to 1 behaves somewhat differently to caissons with aspect rations greater than 2. A more detailed analysis of caissons with embedment aspect ratios ranging from $L/D = 0.5 - 2$ might provide interesting results.

7.2.3 Analysis of hybrid mudmat–pile foundations

- An obvious extension of the current research is a systematic study that considers hybrid foundations under combined loading. This could be achieved by following the methodology adopted for a rectangular mudmat under combined loading, as set out in Section 4.3.2.

- Hybrid foundations may have slender piles, which should not be considered as fully rigid. An extension of the current research which uses an FEA technique capable of modelling elastic piles would be useful.

- Achieving a fully fixed pile head connection is unlikely to be achievable in practice. Field data, or laboratory testing, of hybrid foundation pile heads would provide necessary information on realistically achievable pile head fixity conditions.

7.3 Final comments

While 3D FELA is not a new analysis method, previous implementations were restricted to simple cases where multiple planes of symmetry could be exploited, and these analyses generally contained less than 6 000 elements (e.g. Martin and Makrodimopoulos, 2008; Krabbenhøft et al., 2008)). What this thesis has shown is that 3D FELA is now capable of handling real design problems that may not contain symmetric planes, and that these problems can be analysed using over 60 000 elements, if needed.

This development is partly due to the advancement of optimisation software. Commercial software (e.g. MOSEK (2014)) is now proficient at handling large SOCP problems, and further improvements in the speed and robustness of optimisation algorithms are likely.

Adaptive mesh refinement over successive solution iterations has led to efficient tightening of FELA bounds. Analysis of an initial coarse mesh has also, somewhat unexpectedly, proven to be extremely advantageous. It allows for a quick capacity approximation to be ascertained, and this quick approximation has been found to give a good estimate of the capacity obtained when a more refined mesh is analysed. For determining if 3D FELA will emerge as a design tool, this is a key finding. What has been presented in this thesis is a quick analysis method which can be used to inform a design at an early stage, and the results can subsequently be confirmed by (adaptive) mesh refinement.

FELA also has much academic merit, in that the method produces rigorously bounded capacities. The bounded capacities in this thesis can be used as benchmarks for future FELA and FEA studies. Also, the overall approach of 3D FELA with adaptive mesh refinement has been shown to produce sufficiently tight bounds for use in design practice, and this approach is ready to be used for the analysis of a wide range of foundations, under manifold loading conditions.

References

Abdi, R., de Buhan, P., and Pastor, J. (1994). Calculation of the critical height of homogenized reinforced soil wall: a numerical approach. *Int. J. Numer. Anal. Methods Geomech.*, 18:485–505.

Advanced Geomechanics (2001). Suction pile analysis code: AGSPANC users' manual.

Alwis, W. (2000). Discrete element slip model of plasticity. *Eng. Struct.*, 23:1494–1504.

American Petroleum institute (API) (2000). Recommended practice for planning, designing and constructing fixed offshore platforms — working stress design (API RP 2A—WSD). 21st edition.

American Petroleum Institute (API) (2011). Geotechnical and foundation design considerations. In *API RP 2GEO*. Washington DC.

Anderheggen, E. and Knöpfel, H. (1972). Finite element limit analysis using linear programming. *Int. J. Solids Struct.*, 8(12):1413–1431.

Andersen, E. D., Roos, C., and Terlaky, T. (2003). On implementing a primal-dual interior-point method for conic quadratic optimization. *Math. Program. Ser. B*, 95(2):249–277.

Andersen, K. H. and Jostad, H. P. (1999). Foundation design of skirted foundations and anchors in clay. In *Proc. Offshore Technol. Conf.* OTC-10824.

Andersen, K. H., Murff, J. D., Randolph, M., Clukey, E. C., Erbrich, C. T., Jostad, H., Hansen, B., Aubeny, C. P., Sharma, P., and Supachawarote, C. (2005). Suction anchors for deepwater applications. In Cassidy, M. J. and Gourvenec, S. M., editors, *Front. Offshore Geotech.*, volume 1, pages 1–30. Taylor & Francis, Perth, Australia.

Arup (2009). *Design Yearbook 2009*.

Aubeny, C. P., Han, S. W., and Murff, J. D. (2003a). Inclined load capacity of suction caissons. *Int. J. Numer. Anal. Methods Geomech.*, 27(14):1235–1254.

Aubeny, C. P., Han, S. W., and Murff, J. D. (2003b). Suction caisson capacity in anisotropic, purely cohesive soil. *Int. J. Geomech.*, 3(2):225–235.

Aubeny, C. P., Murff, J. D., and Moon, S. K. (2001). Lateral undrained resistance of suction caisson anchors. *Int. J. Offshore Polar Eng.*, 11(3):211–219.

Ayachit, U. (2015). *The ParaView guide: a parallel visualization application*.

Belytschko, T. and Hodge, P. (1970). Plane stress limit analysis by finite elements. *J. Eng. Mech. Div.*, 96:931–944.

Bisbos, C., Makrodimopoulos, A., and Pardalos, P. (2005). Second-order cone programming approaches to static shakedown analysis in steel plasticity. *Optim. Methods Softw.*, 20(1):25–52.

Bottero, A., Negre, R., Pastor, J., and Turgeman, S. (1980). Finite element method and limit analysis theory for soil mechanics problems. *Comput. Methods Appl. Mech. Eng.*, 22:131–149.

Bransby, M. F. and Randolph, M. F. (1998). Combined loading of skirted foundations. *Géotechnique*, 48(5):637–655.

Bransby, M. F. and Randolph, M. F. (1999). The effect of embedment depth on the undrained response of skirted foundations to combined loading. *Soils Found.*, 39(4):19–33.

Brinch Hansen, J. (1970). A revised and extended formula for bearing capacity. *Danish Geotech. Inst.*, (Bulletin No. 28):5–11.

Carter, J. P. and Taiebat, H. A. (2005). A failure surface for caisson foundations in undrained soils. In Cassidy, M. J. and Gourvenec, S. M., editors, *Front. Offshore Geotech.*, pages 289–295. Taylor & Francis.

Chakraborty, M. and Kumar, J. (2015). Lower-bound axisymmetric formulation for geomechanics problems using nonlinear optimization. 06014024(8):1–8.

Chen, J., Yin, J.-h., and Lee, C. F. (2004). Rigid finite element method for upper bound limit analysis of soil slopes subjected to pore water pressure. *J. Eng. Mech.*, 130(8):886–893.

Chen, Z., Wang, J., Wang, Y., Yin, J.-H., and Haberfield, C. (2001a). A three-dimensional slope stability analysis method using the upper bound theorem Part II: numerical approaches, applications and extensions. *Int. J. Rock Mech. Min. Sci.*, 38(3):379–397.

Chen, Z., Wang, X., Haberfield, C., Yin, J.-h., and Wang, Y. (2001b). A three-dimensional slope stability analysis method using the upper bound theorem Part I : theory and methods. *Int. J. Rock Mech. Min. Sci.*, 38:369–378.

CIMNE (2006). GiD version 8.0 reference manual.

Ciria, H. and Peraire, J. (2004). Computation of upper and lower bounds in limit analysis using second-order cone programming and mesh adaptivity. In *9th ASCE Spec. Conf. Probabilistic Mech. Struct. Reliab.*, pages 1–13, Albuquerque.

Clancy, P. and Randolph, M. F. (1996). Simple design tools for piled raft foundations. *Géotechnique*, 46(2):313–328.

Clukey, E. C., Aubeny, C. P., and Murff, J. D. (2004). Comparison of analytical and centrifuge model tests for suction caissons subjected to combined loads. *J. Offshore Mech. Arct. Eng.*, 126(4):364–367.

Dassault Systèmes Simulia Corp. (2014). *Abaqus 6.14-1 user manual*.

Davis, E. H. and Booker, J. R. (1973). The effect of increasing strength with depth on the bearing capacity of clays. *Géotechnique*, 23(4):551–563.

Deng, W., Carter, J. P., and Taiebat, H. (2001). Prediction of the lateral capacity of suction caissons. In Desai, C. S., editor, *10th Int. Conf. Int. Assoc. Comput. Methods Adv. Geomehanics*, pages 33–38, Rotterdam.

Dimmock, P., Clukey, F., Randolph, M., Murff, D., and Gaudin, C. (2013). Hybrid subsea foundations for subsea equipment. *J. Geotech. Geoenvironmental Eng.*, 139(12):2182–2192.

DNV (Det Norske Veritas) (1992). Classification notes No. 30.4, Foundations.

Drucker, D., Prager, W., and Greenburg, H. (1952). Extended limit design theory for continuous media. *Q. Appl. Math.*, 9:381–389.

Dunne, H. P. and Martin, C. M. (2017a). Capacity analysis of suction caissons used in catenary mooring systems. In *Proc., 19th Int. Conf. Soil Mech. Geotech. Eng. ICSMGE 2017*, Seoul.

Dunne, H. P. and Martin, C. M. (2017b). Capacity of rectangular mudmat foundations on clay under combined loading. *Géotechnique*, 67(2):168–180.

Dunne, H. P., Martin, C. M., Muir, L., Brown, N., and Wallerand, R. (2015). Undrained bearing capacity of skirted mudmats on inclined seabeds. In Meyer, V., editor, *Front. Offshore Geotech. III*, pages 783–788. CRC Press.

Dunne, H. P., Martin, C. M., and R, W. (2017). Limit analysis of hybrid foundations on clay under combined horizontal and torsional loading. In *8th Offshore Site Investig. Geotech. Int. Conf. –Smarter Solut. Futur. offshore Dev.*, London.

Eason, G. and Shield, R. T. R. (1960). The plastic indentation of a semi-infinite solid by a perfectly rough circular punch. *Zeitschrift für Angew. Math. und Phys. ZAMP*, 11(1):33–43.

Eltaher, A., Rajapaksa, Y., and Chang, K. T. (2003). Industry trends for design of anchoring systems for deepwater offshore structures. In *Offshore Technol. Conf.*, Houston, Texas. OTC-15265.

Feng, X., Gourvenec, S. M., Randolph, M. F., Wallerand, R., and P., D. (2015). Effect of a surficial crust on mudmat capacity under fully three-dimensional loading. *Géotechnique*, 65(7):590–603.

Feng, X., Randolph, M. F., and Gourvenec, S. M. (2017). An analytical solution for the undrained horizontal–torsional resistance of mudmats. *Géotechnique*, 67(4):325–337.

Feng, X., Randolph, M. F., Gourvenec, S. M., and Wallerand, R. (2014). Design approach for rectangular mudmats under fully three-dimensional loading. *Géotechnique*, 64(1):51–63.

Finnie, I. M. S. and Morgan, N. (2004). Torsional loading of subsea structures. In *Proc. 14th Int. Offshore Polar Eng. Conf.*, volume 1, pages 326–333.

Fu, D., Gaudin, C., Tian, Y., Cassidy, M. J., and Bienen, B. (2017). Uniaxial capacities of skirted circular foundations in clay. *J. Geotech. Geoenvironmental Eng.*, 143(7):04017022.

Georgiadis, K. (2010a). An upper-bound solution for the undrained bearing capacity of strip footings at the top of a slope. *Géotechnique*, 60(10):801–806.

Georgiadis, K. (2010b). The influence of load inclination on the undrained bearing capacity of strip footings on slopes. *Comput. Geotech.*, 37(3):311–322.

Gerber, T. M. and Rollins, K. M. (2009). Behavior of a nine-pile group with and without a pile cap. In Iskander, M., Laefer, D., and Hussein, M., editors, *Contemp. Top. Situ Testing, Anal. Reliab. Found.*, pages 530–537, Reston, VA. American Society of Civil Engineers.

Gilbert, M. and Smith, C. (2013). Identification of rotational failure mechanisms in cohesive media using discontinuity layout optimisation. *Géotechnique*, 63(14):1194–1208.

Gottardi, G. and Butterfield, R. (1993). On the bearing capacity of surface footings on sand under general planar loading. *Soils Found.*, 33(3):68–79.

Gottardi, G., Houlsby, G., and Butterfield, R. (1999). The plastic response of circular footings on sand under general planar loading. *Géotechnique*, 50(4):117–129.

Gourvenec, S. M. (2007). Failure envelopes for offshore shallow foundations under general loading. *Géotechnique*, 57(9):715–728.

Gourvenec, S. M. (2008). Effect of embedment on the undrained capacity of shallow foundations under general loading. *Géotechnique*, 58(3):177–185.

Gourvenec, S. M. and Barnett, S. (2011). Undrained failure envelope for skirted foundations under general loading. *Géotechnique*, 61(3):263–270.

Gourvenec, S. M. and Mana, D. S. K. (2011). Undrained vertical bearing capacity factors for shallow foundations. *Géotechnique Lett.*, 1(4):101–108.

Gourvenec, S. M. and Randolph, M. F. (2003). Effect of strength non-homogeneity on the shape of failure envelopes for combined loading of strip and circular foundations on clay. *Géotechnique*, 53(6):575–586.

Gourvenec, S. M., Randolph, M. F., and Kingsnorth, O. (2006). Undrained bearing capacity of square and rectangular footings. *Int. J. Geomech.*, 6(3):147–157.

Gourvenec, S. M. and Steinepreis, M. (2007). Undrained limit states of shallow foundations acting in consort. *Int. J. Geomech.*, 7(3):194–205.

Green, A. P. (1954). The plastic yielding of metal junctions due to combined shear and pressure. *J. Mech. Phys. Solids*, 2(3):197–211.

Gzodev, A. (1960). Determination of the collapse load for statically determinate systems undergoing plastic deformations (Translation by R.M. Haythornthwaite). *Int. J. Mech. Sci.*, 1(4):332–335.

Hawksbee, S. J., Gilbert, M., and Smith, C. C. (2014). Upper bound limit analysis of 3D problems using discontinuity layout optimisation. In *Proc. 11th World Congr. Comput. Mech.*, pages 3–4, Barcelona, Spain.

Hawksbee, S. J., Smith, C. C., and Gilbert, M. (2013). Application of discontinuity layout optimization to three-dimensional plasticity problems. *Proc. R. Soc. A Math. Phys. Eng. Sci.*, 469(2155):20130009–20130009.

Hazell, E. C. J. and Martin, C. M. (2005). Bearing capacity of parallel strip footings on non-homogeneous clay. In Gourvenec, S. and Cassidy, M., editors, *Front. Offshore Geotech.*, pages 427–433. Taylor & Francis, Perth.

Hill, R., Lee, E. H., and Tupper, S. J. (1947). The Theory of Wedge Indentation of Ductile Materials. *Proc. R. Soc. A Math. Phys. Eng. Sci.*, 188(1013):273–289.

Hossain, M. K., Shi, H., Abdalla, B., Audibert, J., Swearingen, S., and Fu, L. (2015a). FEA based design approach for hybrid subsea foundations clump weight pin-piles. In *Proceedigns 25th Int. Ocean Polar Eng. Conf.*, pages 900–904.

Hossain, M. K., Shi, H., Abdalla, B., and Markella, K. S. (2015b). Understanding hybrid subsea foundation design. In *Proc. ASME 34th Int. Conf. Ocean. Offshore Arct. Eng.*, pages 1–6, Newfoundland. ASME.

Houlsby, G. T. and Puzrin, A. M. (1999). The bearing capacity of a strip footing on clay under combined loading. *Proc. R. Soc. A Math. Phys. Eng. Sci.*, 455(1983):893–916.

ISO (International Organisation for Standardisation) (2003). *ISO 19901-4: Petroleum and natural gas industries – Specific requirements for offshore structures – Part 4: Geotechnical and foundation design considerations*. Geneva, Switzerland, 1st edition.

Jostad, H. and Andersen, K. (2015). Calculation of undrained holding capacity of suction anchors in clays. In Meyer, V., editor, *Front. Offshore Geotech. III*, pages 263–268. CRC Press, Oslo.

Kawai, T. (1977). New discrete models and their application to seismic response analysis of structures. *Nucl. Eng. Des.*, 48(1978):207–229.

Kay, S. and Palix, E. (2010). Caisson capacity in clay: VHM resistance envelope – Part 2: VHM envelope equation and design procedures. In White, D. J., editor, *Front. Offshore Geotech. II*, pages 741–746. CRC Press.

Kay, S. and Palix, E. (2011). Caisson capacity in clay : VHM resistance envelope – Part 3: extension to shallow foundations. In *Proc. ASME 2011 30th Int. Conf. Ocean. Offshore Arct. Eng. OMAE2011*, pages 1–10.

Keaveny, J., Hansen, S., Madshus, C., and Dyvic, R. (1994). Horizontal capacity of large scale model anchor. In *Proc. Thirteen. Intern. Conf. Soil Mech. Found.*, pages 677–680, New Delhi, India.

Keawsawasvong, S. and Ukritchon, B. (2016). Finite element limit analysis of pullout capacity of planar caissons in clay. *Comput. Geotech.*, 75:12–17.

Kennedy, J., Oliphant, J., Maconochie, A., Stuyts, B., and Cathie, D. (2013). CAISSON: A Suction Pile Design Tool. In *Vol. 6 Polar Arct. Sci. Technol. Offshore Geotech. Pet. Technol. Symp.*, page V006T10A030. ASME.

Kennedy, J., Oliphant, J., Maconochie, A., Stuyts, B., and Cathie, D. (2015). Suction anchor geotechnical design practice: A case study. In *Front. Offshore Geotech. III*, pages 283–288. CRC Press.

Krabbenhøft, K., Lyamin, A., Hjiaj, M., and Sloan, S. (2005). A new discontinuous upper bound limit analysis formulation. *Int. J. Numer. Methods Eng.*, 63(7):1069–1088.

Krabbenhøft, K., Lyamin, A., and Krabbenhøft, J. (2015). Optum computational engineering (OptumG2). www.optumce.com.

Krabbenhøft, K., Lyamin, A. V., and Sloan, S. W. (2007). Formulation and solution of some plasticity problems as conic programs. *Int. J. Solids Struct.*, 44(5):1533–1549.

Krabbenhøft, K., Lyamin, A. V., and Sloan, S. W. (2008). Three-dimensional Mohr-Coulomb limit analysis using semidefinite programming. *Commun. Numer. Methods Eng.*, 24(11):1107–1119.

Kumar, J. and Chakraborty, M. (2014). Upper-bound axisymmetric limit analysis using the Mohr–Coulomb yield criterion, finite elements, and linear optimization. *J. Eng. Mech.*, 140(1982):06014012.

Kusakabe, O., Kimura, T., and Yamaguchi, H. (1981). Bearing capacity of slopes under strip loads on the top surfaces. *Soils Found.*, 21(4):29–40.

Li, A., Merifield, R., and Lyamin, A. (2009). Limit analysis solutions for three dimensional undrained slopes. *Comput. Geotech.*, 36(8):1330–1351.

Li, H. and Yu, H. (2005). Kinematic limit analysis of frictional materials using nonlinear programming. *Int. J. Solids Struct. 2005*, 42:4058–4076.

Lim, K., Li, A., and Lyamin, A. (2015). Three-dimensional slope stability assessment of two-layered undrained clay. *Comput. Geotech.*, 70(2015):1–17.

LimitState Ltd (2016). LimitState:GEO version 3.1 user manual.

Liu, F. and Zhao, J. (2013). Limit analysis of slope stability by rigid finite-element method and linear programming considering rotational failure. *Int. J. Geomech.*, 13(6):827–839.

Lyamin, A. V., Salgado, R., Sloan, S. W., and Prezzi, M. (2007). Two- and three-dimensional bearing capacity of footings in sand. *Géotechnique*, 57(8):647–662.

Lyamin, A. V. and Sloan, S. W. (2002a). Lower bound limit analysis using non-linear programming. *Int. J. Numer. Methods Eng.*, 55(5):573–611.

Lyamin, A. V. and Sloan, S. W. (2002b). Upper bound limit analysis using linear finite elements and non-linear programming. *Int. J. Numer. Anal. Methods Geomech.*, 26(2):181–216.

Lyamin, A. V. and Sloan, S. W. (2003). Mesh generation for lower bound limit analysis. *Adv. Eng. Softw.*, 34(6):321–338.

Lysmer, J. (1970). Limit analysis of plane problems in soil mechanics. *J. Soil Mech. Found. Div.*, 96(4):1311–1334.

Maier, G. (1969). Shakedown theory in perfect elastoplasticity with associated and nonassociated flow-laws: a finite element, linear programming approach. *Meccanica*, 4(3):250–260.

Makrodimopoulos, A. and Martin, C. M. (2006). Lower bound limit analysis of cohesive-frictional materials using second-order cone programming. *Int. J. Numer. Methods Eng.*, 66(4):604–634.

Makrodimopoulos, A. and Martin, C. M. (2007). Upper bound limit analysis using simplex strain elements and second-order cone programming. *Int. J. Numer. Anal. Methods Geomech.*, 31(6):835–865.

Mana, D. S. K., Gourvenec, S., and Martin, C. M. (2013). Critical skirt spacing for shallow foundations under general loading. *J. Geotech. Geoenvironmental Eng.*, 139(9):1554–1566.

Mandel, J. (1963). Interférence plastique de foundations superficielles. In *Proc. Int. Conf. Soil Mech.*, pages 267–280, Budapest.

Martin, C., Dunne, H., Wallerand, R., and Brown, N. (2015). Three-dimensional limit analysis of rectangular mudmat foundations. In Meyer, V., editor, *Front. Offshore Geotech. III*, pages 789–794. CRC Press, Oslo, Norway.

Martin, C. M. (1994). *Physical and numerical modelling of offshore foundations under combined loads*. DPhil thesis, University of Oxford.

Martin, C. M. (2003). New software for rigorous bearing capacity calculations. In *BGA Int. Conf. Found. Innov. Obs. Des. Pract.*, pages 581–592. Thomas Tellford, Dundee.

Martin, C. M. (2004). User guide for ABC – analysis of bearing capacity version 1.0.

Martin, C. M. (2005). Exact bearing capacity calculations using the method of characteristics. In *Proc. 11th Int. Conf. IACMAG*, Turin, Italy.

Martin, C. M. (2011). The use of adaptive finite-element limit analysis to reveal slip-line fields. *Géotechnique Lett.*, 1(2):23–29.

Martin, C. M. and Makrodimopoulos, A. (2008). Finite-element limit analysis of Mohr–Coulomb materials in 3D using semidefinite programming. *J. Eng. Mech.*, 134(4):339–347.

Martin, C. M. and Randolph, M. F. (2006). Upper-bound analysis of lateral pile capacity in cohesive soil. *Géotechnique*, 56(2):141–145.

Martin, C. M. and White, J. D. (2012). Limit analysis of the undrained bearing capacity of offshore pipelines. *Géotechnique*, 62(9):847–863.

McDonald, S., Suroor, H., Malachowski, J., Wang, Q., and Qi, X. (2014). Analysis of subsea structures subject to significant torsion. In *Proc. 33rd Int. Conf. Ocean. Offshore Arct. Eng.*, pages OMAE2014–24192, San Francisco, California.

Meyerhof, G. G. (1951). The ultimate bearing capacity of foudations. *Géotechnique*, 2(4):301–332.

Michalowski, R. L. (1989). Three-dimensional analysis of locally loaded slopes. *Géotechnique*, 39(1):27–38.

Michalowski, R. L. (2001). Upper-bound load estimates on square and rectangular footings. *Géotechnique*, 51(9):787–798.

Michałowski, R. L. and Dawson, E. M. (2002). Three-dimensional analysis of limit loads on Mohr-Coulomb soil. *Found. Civ. Environ. Eng.*, 1.

Michalowski, R. L. and Drescher, A. (2009). Three-dimensional stability of slopes and excavations. *Géotechnique*, 59(10):839–850.

Mokwa, R. L. and Duncan, J. M. (2003). Rotational restraint of pile caps during lateral loading. *J. Geotech. Geoenvironmental Eng.*, 129(9):829–837.

MOSEK ApS (2014). *The MOSEK C optimizer API manual, version 7.1*.

Murff, J., Aubeny, C., and Yang, M. (2010). The effect of torsion on the sliding resistance of rectangular foundations. In *Front. Offshore Geotech. II*, pages 439–443. CRC Press, Perth, Australia.

Murff, J. and Miller, T. (1977). Stability Of offshore gravity structure foundations by the upper bound method. In *Offshore Technol. Conf.*, Houston, Texas. OTC-2896.

Murff, J. D. and Hamilton, J. M. (1993). P-ultimate for undrained analysis of laterally loaded piles. *J. Geotech. Eng.*, 119(1):91–107.

Nagtegaal, J. C., Parks, D. M., and Rice, J. R. (1974). On numerically accurate finite element solutions in the fully plastic range. *Comput. Methods Appl. Mech. Eng.*, 4(2):153–177.

Nouri, H., Biscontin, G., and Aubeny, C. P. (2014). Undrained sliding resistance of shallow foundations subject to torsion. *J. Geotech. Geoenvironmental Eng.*, 140(8):04014042.

Palix, E., Willems, T., and Kay, S. (2010). Caisson capacity in clay: VHM resistance envelope – Part 1. In *Front. Offshore Geotech. II*, pages 753–758. CRC Press.

Pastor, J. (1978). Analyse limite: détermination numérique de solutions statiques complètes. Application au talus vertical. *J. Mécanique appliquée*, 2:167–196.

Pastor, J., Thai, T.-H., and Francescato, P. (2000). New bounds for the height limit of a vertical slope. *Int. J. Numer. Anal. Methods Geomech.*, 24(2):165–182.

Pastor, J., Turgeman, S., and Boehler, J. P. (1990). Solution of anisotropic plasticity problems by using associated isotropic problems. *Int. J. Plast.*, 6(2):143–168.

Plaxis (2016). Plaxis 3D reference manual. Technical report.

Potts, D. M. and Zdravković, L. (1999). *Finite Element Analysis in Geotechnical Engineering: Volume One - Theory*. Thomas Telford Ltd, Bath, 1st edition.

Potts, D. M. and Zdravković, L. (2001). *Finite Element Analysis in Geotechnical Engineering: Volume two - Application*. Thomas Telford Publishing, Bath, 1st edition.

Poulos, H. G. (1994). An approximate numerical analysis of pile-raft interaction. *Int. J. Numer. Anal. Methods Geomech.*, 18(2):73–92.

Poulos, H. G. (2001). Piled raft foundations: design and applications. *Géotechnique*, 51(2):95–113.

Prandtl, L. (1920). Über die Härte plastischer Körper. *Nachrichten von der Gesellschaft der Wissenschaften zu Göttingen, Math. Klasse*, pages 75–85.

Puzrin, A. M. and Randolph, M. F. (2003). New planar velocity fields for upper bound limit analysis. *Int. J. Solids Struct.*, 40(13-14):3603–3619.

Python Software Foundation (2016). Python. www.python.org.

Randolph, M. F. and Houlsby, G. T. (1984). The limiting pressure on a circular pile loaded laterally in cohesive soil. *Géotechnique*, 34(4):613–623.

Randolph, M. F. and House, A. R. (2002). Analysis of suction caisson capacity in clay. In *Offshore Technol. Conf.*, Houston, Texas. OTC-14236.

Randolph, M. F. and Puzrin, a. M. (2003). Upper bound limit analysis of circular foundations on clay under general loading. *Géotechnique*, 53(9):785–796.

Salgado, R., Lyamin, a. V., Sloan, S. W., and Yu, H. S. (2004). Two- and three-dimensional bearing capacity of foundations in clay. *Géotechnique*, 54(5):297–306.

Shen, Z., Feng, X., and Gourvenec, S. (2017). Effect of interface condition on the undrained capacity of subsea mudmats under six-degree-of-freedom loading. *Géotechnique*, 67(4):338–349.

Shen, Z., Feng, X., and Gourvenec, S. M. (2016). Undrained capacity of surface foundations with zero-tension interface under planar V-H-M loading. *Comput. Geotech.*, 73:47–57.

Shewchuk, J. R. (1996). Triangle: engineering a 2D quality mesh generator and Delaunay triangulator. In Lin, M. C. and Manocha, D., editors, *Appl. Comput. Geom. Towar. Geom. Eng.*, pages 203–222. Springer-Verlag.

Shiau, J. S., Merifield, R. S., Lyamin, A. V., and Sloan, S. W. (2011). Undrained Stability of Footings on Slopes. *Int. J. Geomech.*, 11(5):381–390.

Shield, R. T. (1955). On the plastic flow of metals under conditions of axial symmetry. *Proc. R. Soc. A Math. Phys. Eng. Sci.*, 233(1193):267–287.

Si, H. (2013). *TetGen user manual, version 1.5*.

Skempton, A. (1951). The bearing capacity of clays. In *Proc. Build. Res. Congr.*, pages 180–189, London.

Sloan, S. and Kleeman, P. (1995). Upper bound limit analysis using discontinuous velocity fields. *Comput. Methods Appl. Mech. Eng.*, 127(1-4):293–314.

Sloan, S. W. (1988). Lower bound limit analysis using finite elements and linear programming. *Int. J. Numer. Anal. Methods Geomech.*, 12(1):61–77.

Smith, C. and Gilbert, M. (2007). Application of discontinuity layout optimization to plane plasticity problems. *Proc. R. Soc. A Math. Phys. Eng. Sci.*, 463(2086):2461–2484.

Sturm, J. F. (1999). Using SeDuMi 1.02, a Matlab toolbox for optimization over symmetric cones. *Optim. Methods Softw.*, 11(1-4):625–653.

Subsea 7 (2013). Shallow foundation analysis study. Technical report.

Subsea 7 (2017). Subsea 7 web page. www.subsea7.com.

Sukumaran, B., McCarron, W. O., Jeanjean, P., and Abouseeda, H. (1999). Efficient finite element techniques for limit analysis of suction caissons under lateral loads. *Comput. Geotech.*, 24(2):89–107.

Supachawarote, C. (2006). *Inclined Load Capacity of Suction Caisson in Clay*. DPhil thesis, University of Wesern Australia.

Taiebat, H. and Carter, J. P. (2004). Effects of torsion on caisson capacity in clay. In *Proc. 9th Aust. New Zeal. Conf. Geomech.*, pages 130–136, Auckland, New Zealand.

Taiebat, H. A. and Carter, J. P. (2000). Numerical studies of the bearing capacity of shallow foundations on cohesive soil subjected to combined loading. *Géotechnique*, 50(4):409–418.

Taiebat, H. A. and Carter, J. P. (2005). Interaction of forces on caissons in undrained soils. In *Proc. 15th Int. Offshore Polar Eng. Conf.*, volume 8, pages 625–632, Seoul, Korea.

Tan, F. S. C. (1990). *Centriufge and numerical modelling of conical footings on sand*. DPhil thesis, University of Cambridge.

Tani, K. and Craig, W. (1995). Bearing capacity of circular foundations on soft clay of strength increasing with depth. *Soils Found.*, 35(4):21–35.

Tapper, L. (2013). *Bearing capacity of perforated offshore foundations under combined loading*. DPhil thesis, University of Oxford.

Tapper, L., Martin, C. M., and Byrne, B. W. (2014). Undrained bearing capacity of circular footings on Tresca soil using adaptive finite element analysis. In Hicks, M. A., Brinkgreve, R. B. J., and Rohe, A., editors, *Numer. Methods Geotech. Eng.*, pages 699–704. CRC Press, London.

Tapper, L., Martin, C. M., Byrne, B. W., and Lehane, B. (2015). Undrained vertical bearing capacity of perforated shallow foundations. In *Front. Offshore Geotech. III*, pages 813–818. CRC Press, Oslo.

Terzaghi, K. (1943). *Theoretical Soil Mechanics*. John Wiley & Sons, Inc., Hoboken, NJ, USA.

Tütüncü, R. H., Toh, K. C., and Todd, M. J. (2003). Solving semidefinite-quadratic-linear programs using SDPT3. *Math. Program.*, 95(2):189–217.

Ukritchon, B. and Keawsawasvong, S. (2016). Undrained pullout capacity of cylindrical suction caissons by finite element limit analysis. *Comput. Geotech.*, 80(9):301–311.

Ukritchon, B., Whittle, A. J., and Sloan, S. W. (1998). Undrained Limit Analyses for Combined Loading of Strip Footings on Clay. *J. Geotech. Geoenvironmental Eng.*, 124(3):265–276.

van Dijk, B. (2015). Caisson capacity in undrained soil: Failure envelopes with internal scooping. In Meyer, V., editor, *Front. Offshore Geotech. III*, volume 1, pages 337–342. CRC Press.

Vesic, A. S. (1975). Bearing capacity of shallow foundations. In Winterkorn, H. F. and Fang, H., editors, *Found. Eng. Handb.* Van Nostrand Reinhold, New York, 1st edition.

Vulpe, C. (2015). Design method for the undrained capacity of skirted circular foundations under combined loading: effect of deformable soil plug. *Géotechnique*, 65(8):669–683.

White, D., Cheuk, C., Springman, S., Bolton, M., Joray, D., and Maconochie, A. (2005). An investigation into the vertical bearing capacity of perforated mudmats. In Gourvenec, S. and Cassidy, M., editors, *Front. Offshore Geotech.*, pages 459–465. Taylor & Francis, Perth.

Won, J., Audibert, J. M. E., Swearingen, S., Suroor, H., and Thioulouse, F. (2015). Effect of pile head restraint on subsea hybrid foundation response. In *Proc. 25th Int. Ocean Polar Eng. Conf.*, pages 886–893, Kona, Big Island, Hawaii.

Yang, H., Shen, Z., and Wang, J. (2003). 3D lower bound bearing capacity of smooth rectangular surface footings. *Mech. Res. Commun.*, 30(5):481–492.

Yu, H. S., Sloan, S. W., and Kleeman, P. W. (1994). A quadratic element for upper bound limit analysis. *Eng. Comput.*, 11(3):195–212.

Yu, S., Zhang, X., and Sloan, S. W. (2016). A 3D upper bound limit analysis using radial point interpolation meshless method and second-order cone programming. *Int. J. Numer. Methods Eng.*, 108(13):1686–1704.

Yun, G. and Bransby, M. F. (2007). The undrained vertical bearing capacity of skirted foundations. *Soils Found.*, 47(3):493–505.

Yun, G., Maconochie, A., Oliphant, J., and Bransby, F. (2009). Undrained capacity of surface footings subjected to combined V-H-T loading. In *Proc. 19th Int. Offshore Polar Eng. Conf.*, volume 1, pages 9–14, Osaka, Japan.

Zdravković, L. and Potts, D. (2005). Parametric finite element analyses of suction anchors. In *Front. Offshore Geotech.*, pages 297–302. Taylor & Francis.

Zdravković, L., Potts, D. M., and Jardine, R. J. (2001). A parametric study of the pull-out capacity of bucket foundations in soft clay. *Géotechnique*, 51(1):55–67.

Zhang, J. H., Chen, Z. Y., and Li, F. (2010). Three dimensional limit analysis of suction bucket foundations. *Ocean Eng.*, 37(8-9):790–799.

Zouain, N., Herskovits, J., Borges, L. A., and Feijóo, R. A. (1993). An iterative algorithm for limit analysis with nonlinear yield functions. *Int. J. Solids Struct.*, 30:1397–1417.

Appendix A

UINTER user subroutine

This appendix gives further details of, and provides the source code for, the UINTER subroutine described in Section 3.3.1. The subroutine was used as part of analysis undertaken in Abaqus/Standard 6.14 – 1 (Dassault Systèmes Simulia Corp., 2014); it defines the constitutive behaviour at a foundation/soil interface. The subroutine was called by Abaqus at each contact pair in each iteration of the solution. It specifically models available shear strength (αs_u) and allows for tension breaking ($T = 0$) at a foundation/soil interface. It is called in the Abaqus input file under *SURFACE INTERACTION and requires four inputs from the user;

- the soil normal stiffness, k_n,
- the soil shear stiffness, k_s,
- the interface shear strength, αs_u, and
- a 'switch', t, identifying if $T = 0$ or $T = \infty$.

In all analyses undertaken, k_n and k_s were set to $1000 s_u$, as this was the stiffness of the soil domain. The interface shear strength, αs_u, can be set to any value, values of $0 \leq \alpha \leq 1$ were used in analyses in this thesis. If the tension capacity switch is set equal to zero ($t = 0$) then a zero tension interface is modelled. An input $t = 1$ specifies that the interface mimics an interface modelled in OxLim. In this case, 'phantom' shear stresses can still exist in the soil after a gap has formed at the foundation/soil interface (see Section 3.2.3). Any other t input

models a full tension interface. Inputs are required from Abaqus at each increment of the solution, namely;

- a vector containing the relative positions of each constraint point on the soil with respect to the closest point on the foundation, $\mathbf{R}$ ($[2 \times 1]$ in a plane strain analysis, $[3 \times 1]$ in a 3D analysis), and
- a vector containing the incremental relative displacement between the two points, $\mathbf{r}$ ($[2 \times 1]$ in a plane strain analysis, $[3 \times 1]$ in a 3D analysis).

The subroutine supplies Abaqus with;

- the stress vector, $\boldsymbol{\sigma}$, ($[2 \times 1]$ in a plane strain analysis, $[3 \times 1]$ in a 3D analysis).
- the interface stiffness matrix, $\mathbf{K}$, ($[2 \times 2]$ in a plane strain analysis, $[3 \times 3]$ in a 3D analysis).

To determine $\boldsymbol{\sigma}$ and $\mathbf{K}$, the following steps are undertaken by the subroutine in a plane strain analysis:

1. $\mathbf{K}$ and $\boldsymbol{\sigma}$ are initialised to zeros.
2. The normal stress is calculated and the stiffness matrix is updated:

$$\sigma_1 = R_1 k_\mathrm{n} \tag{A.1}$$

$$K_{11} = k_\mathrm{n} \tag{A.2}$$

3. A trial shear stress is calculated:

$$\tau_\mathrm{trial} = \tau_0 + k_\mathrm{s} r_2 \tag{A.3}$$

   where τ_0 is the shear stress at the end of the previous increment.

4. If $\tau_\mathrm{trial} \leq \alpha s_\mathrm{u}$, the interface responds elastically and the stress vector and stiffness matrix are updated:

$$\sigma_2 = \tau_\mathrm{trial} \tag{A.4}$$

$$K_{22} = k_\mathrm{s} \tag{A.5}$$

OR

If $\tau_{\text{trial}} > \alpha s_{\text{u}}$, the maximum shear stress has been exceeded by the trial stress and the interface is behaving plastically. The stress vector and stiffness matrix are updated:

$$\sigma_2 = \alpha s_{\text{u}} \tag{A.6}$$

$$K_{22} = 0 \tag{A.7}$$

5. The zero tension switch, t, is inspected. If $t = 0$, full contact breaking is enforced. If $\sigma_1 < 0$, the stress vector and stiffness matrix are updated:

$$\boldsymbol{\sigma} = 0 \tag{A.8}$$

$$\mathbf{K} = 0 \tag{A.9}$$

OR

If $t = 1$, contact breaking which mimics OxLim is enforced. If $\sigma_1 < 0$ the stress vector and stiffness matrix are updated:

$$\sigma_1 = 0 \tag{A.10}$$

$$K_{11} = 0 \tag{A.11}$$

The same methodology is undertaken for a 3D analysis, but in a 3D analysis the shear stresses along two planes are resolved. The FORTRAN code for the UINTER subroutine for a 3D analysis is as follows:

```
!DEC$ FREEFORM

module mymod

implicit none

! real constants

real(8), parameter :: zero = 0.0_8
real(8), parameter :: inc = 1.E-7_8
```

```
contains

subroutine main(props,rdisp,drdisp,lopenclose,tau0x,tau0y, &
  statev,ddsddr,stress,tautrialx,tautrialy,dplas0x,dplas0y, &
  taulimx,dplasx, dplasy,taulimy,tautrial,taulim, &
  tautrialxp,tautrialp,taulimxp,taulimyp,tautrialyp)

    real(8) :: tautrialx
    real(8) :: tautrialy
    real(8) :: tautrial
    real(8) :: tau0x
    real(8) :: tau0y
    real(8) :: dplas0x
    real(8) :: dplas0y
    real(8) :: dplasx
    real(8) :: dplasy
    real(8) :: taulimx
    real(8) :: taulimy
    real(8) :: taulim

    real(8) :: tautrialxp
    real(8) :: tautrialp
    real(8) :: taulimxp
    real(8) :: taulimyp
    real(8) :: tautrialyp

    integer :: i
    integer :: j

    real(8), intent(inout) :: statev(:)
    real(8), intent(in) :: props(:)
    real(8), intent(in) :: rdisp(:)
    real(8), intent(in) :: drdisp(:)
    integer, intent(out) :: lopenclose
    real(8), intent(out) :: ddsddr(3,3)
    real(8), intent(out) :: stress(:)

        lopenclose = 1

        ! state variables saved between increments
        tau0x = statev(1)
        dplas0x = statev(2)
        tau0y = statev(3)
        dplas0y = statev(4)

        do i = 1 , 3
```

```
      stress(i) = zero
      do j = 1 , 3
          ddsddr(i,j)=zero
      end do
  end do

  ! normal direction
  ddsddr(1,1)=props(1)
  stress(1) = props(1) * rdisp(1)

  ! trial stress
  tautrialx = tau0x + (props(2)*drdisp(2))
  tautrialy = tau0y + (props(2)*drdisp(3))
  tautrial = sqrt((tautrialx**2) + (tautrialy**2))

  taulimx = props(3)*tautrialx/tautrial
  taulimy = props(3)*tautrialy/tautrial
  taulim = props(3)

  ! shear direction

  if (tautrial <= taulim) then ! elastic contact
      stress(2) = tautrialx
      statev(1) = tautrialx
      statev(2) = dplas0x

      stress(3) = tautrialy
      statev(3) = tautrialy
      statev(4) = dplas0y

      ddsddr(2,2)= props(2)
      ddsddr(3,3)= props(2)

  else ! plastic contact

      stress(2) = taulimx
      statev(1) = taulimx
      dplasx = dplas0x + drdisp(2)
      statev(2) = dplasx

      stress(3) = taulimy
      statev(3) = taulimy
      dplasy = dplas0y + drdisp(3)
      statev(4) = dplasy

      tautrialxp = taulimx + inc
      tautrialp = sqrt((tautrialxp**2) + (taulimy**2))
```

```
            taulimxp = props(3)*tautrialxp/tautrialp
            taulimyp = props(3)*taulimy/tautrialp

            ddsddr(2,2) = (taulimxp - taulimx)/inc*props(2)
            ddsddr(3,2) = (taulimyp - taulimy)/inc*props(2)

            tautrialyp = taulimy + inc
            tautrialp = sqrt((taulimx**2) + (tautrialyp**2))
            taulimyp = props(3)*tautrialyp/tautrialp
            taulimxp = props(3)*taulimx/tautrialp

            ddsddr(2,3) = (taulimxp - taulimx)/inc*props(2)
            ddsddr(3,3) = (taulimyp - taulimy)/inc*props(2)

        end if

        if (props(4) == 0) then  ! T = 0
            if (stress(1) < zero) then
                do i = 1 , 3
                    stress(i) = zero
                    do j = 1 , 3
                        ddsddr(i,j)=zero
                    end do
                end do
            end if

        else if (props(4) == 1) then
! T = 0, shear stress neq 0
            if (stress(1) < zero) then
                ddsddr(1,1)=zero
                stress(1)=zero
            end if
        end if

end subroutine main

end module mymod

! interface with Abaqus

subroutine UINTER(STRESS,DDSDDR,DVISCOUS,DSTRUCTURAL, &
        FLUX,DDFDDT,DDSDDT,DDFDDR,STATEV,SED,SFD,SPD, &
        SVD,SCD,PNEWDT,RDISP,DRDISP, &
        TEMP,DTEMP,PREDEF,DPRED,TIME,DTIME,FREQR, &
        CINAME,SLNAME,MSNAME, &
        PROPS,COORDS,ALOCALDIR,DROT,AREA,CHRLNGTH,NODE, &
        NDIR,NSTATV,NPRED,NPROPS,MCRD,KSTEP,KINC,KIT, &
```

```
      LINPER,LOPENCLOSE,LSTATE,LSDI,LPRINT)

      use mymod, only: zero, inc, main

      include 'aba_param.inc'

      dimension STRESS(NDIR),DDSDDR(NDIR,NDIR),FLUX(2), &
        DDFDDT(2,2),DDSDDT(NDIR,2),DDFDDR(2,NDIR), &
        STATEV(NSTATV),RDISP(NDIR),DRDISP(NDIR), &
        TEMP(2),DTEMP(2),PREDEF(2,NPRED),DPRED(2,NPRED), &
        TIME(2),PROPS(NPROPS),COORDS(MCRD),ALOCALDIR(3,3), &
        DROT(2,2),DVISCOUS(NDIR,NDIR),DSTRUCTURAL(NDIR,NDIR)

      call main(props,rdisp,drdisp,lopenclose tau0x, &
       tau0y,statev,ddsddr,stress,tautrialx,tautrialy, &
      dplas0x,dplas0y,taulimx,dplasx,dplasy,taulimy, &
      tautrial,taulim,tautrialxp,tautrialp,taulimxp, &
      taulimyp,tautrialyp)

end subroutine uinter
```